THE OBSERVABILITY OF JETS IN COSMIC AIR SHOWERS

Hans Montanus

Dutch title: *De observeerbaarheid van jets in atmosferische lawines veroorzaakt door kosmische deeltjes.*

ISBN: 978-94-028-0549-9

This work is part of the research programme 'promotiebeurs voor leraren' of the Netherlands Organisation for Scientific Research (NWO). It was carried out at the National Institute for Subatomic Physics (Nikhef).

THE OBSERVABILITY OF JETS IN COSMIC AIR SHOWERS

ACADEMISCH PROEFSCHRIFT

ter verkrijging van de graad van doctor
aan de Universiteit van Amsterdam
op gezag van de Rector Magnificus
prof. dr. ir. K.I.J. Maex
ten overstaan van een door het College voor Promoties ingestelde commissie,
in het openbaar te verdedigen in de Agnietenkapel
op dinsdag 25 april 2017, te 14.00 uur

door

Johannes Martinus Cornelis Montanus
geboren te Loon op Zand

Promotiecommissie:

Promotores:	prof. dr. P.M. Kooijman	Universiteit van Amsterdam
	prof. dr. J.W. van Holten	Unversiteit Leiden
Copromotor:	dr. J.J.M. Steijger	FOM-instituut Nikhef
Overige leden:	prof. dr. J.J. Engelen	Universiteit van Amsterdam
	prof. dr. F.L. Linde	Universiteit van Amsterdam
	prof. dr. S.C.M Bentvelsen	Universiteit van Amsterdam
	prof. dr. ir. E.N. Koffeman	Universiteit van Amsterdam
	prof. dr. R.J.M. Snellings	Universiteit Utrecht
	dr. C.W.J.P. Timmermans	Radboud Universiteit Nijmegen
	dr. D.B.R.A. Fokkema	Vrije Universiteit Amsterdam

Faculteit der Natuurwetenschappen, Wiskunde en Informatica

Voor

Daniële, Jenny en Romy

Contents

1 Introduction

1.1 Cosmic rays

Already in 1785 de Coulomb found that his equipment suffered from discharging [1]. If ions in the atmosphere were responsible, there had to be an unknown source of ionizing radiation. After the discovery of radioactivity in 1896 by Becquerel [2] it was generally believed that radioactive elements in the ground caused the ionization of the air. However, experiments by Wulf in 1909 and Pacini in 1911 showed that a part of the ionization had to be due to sources other than the Earth's radioactivity [3, 4]. The history of cosmic rays literally took off in 1912 when Hess discovered with his balloon experiments that an electroscope discharged more rapidly at large altitudes [5]. He attributed it to radiation of extra-terrestrial origin [6]. After that, several experiments were conducted to study the nature of these 'cosmic rays' [7–9]. In 1927 Clay found evidence for cosmic rays being deflected by the geomagnetic field, which implied the cosmic rays to be charged [10, 11]. From the difference between the intensities of cosmic rays coming from the east and the west, the so-called east-west effect, it was found by Rossi in 1934 that most cosmic rays have a positive charge [12]. Nowadays it is known that 99 % of the cosmic rays are nuclei (ionized atoms with positive charge) and 1 % are electrons. A very small fraction of the cosmic rays are gamma particles. The nuclei include essentially all of the elements of the periodic table: about 89 % hydrogen (protons), 10 % helium (alpha particles) and 1 % heavier elements. The observed energies of cosmic particles ranges from somewhat greater than their mass-equivalent to $3 \cdot 10^{20}$ eV. Particles with energy smaller than 10^{10} eV originate mainly from the Sun. Particles with energy between 10^{10} eV and 10^{16} eV are attributed to sources in our Milky-Way galaxy. From there the origin gradually shifts to extragalactic origin. Beyond 10^{18} eV cosmic particles are thought to be of extragalactic origin. The interaction of cosmic particles with the cosmic microwave background sets a limit to the energy of cosmic rays, the GZK limit [13, 14]. The GZK limit implies that cosmic rays coming

from a distance larger than 50 Mpc can not have an energy larger than $5 \cdot 10^{19}$ eV. The flux of cosmic particles decreases with energy, see Figure 1.1. The flux is proportional to $E^{-\gamma}$, where γ is about 2.7 before the 'knee', about 3 beyond the knee, larger than 3 after the '2nd knee' and smaller than 3 beyond the 'ankle'.

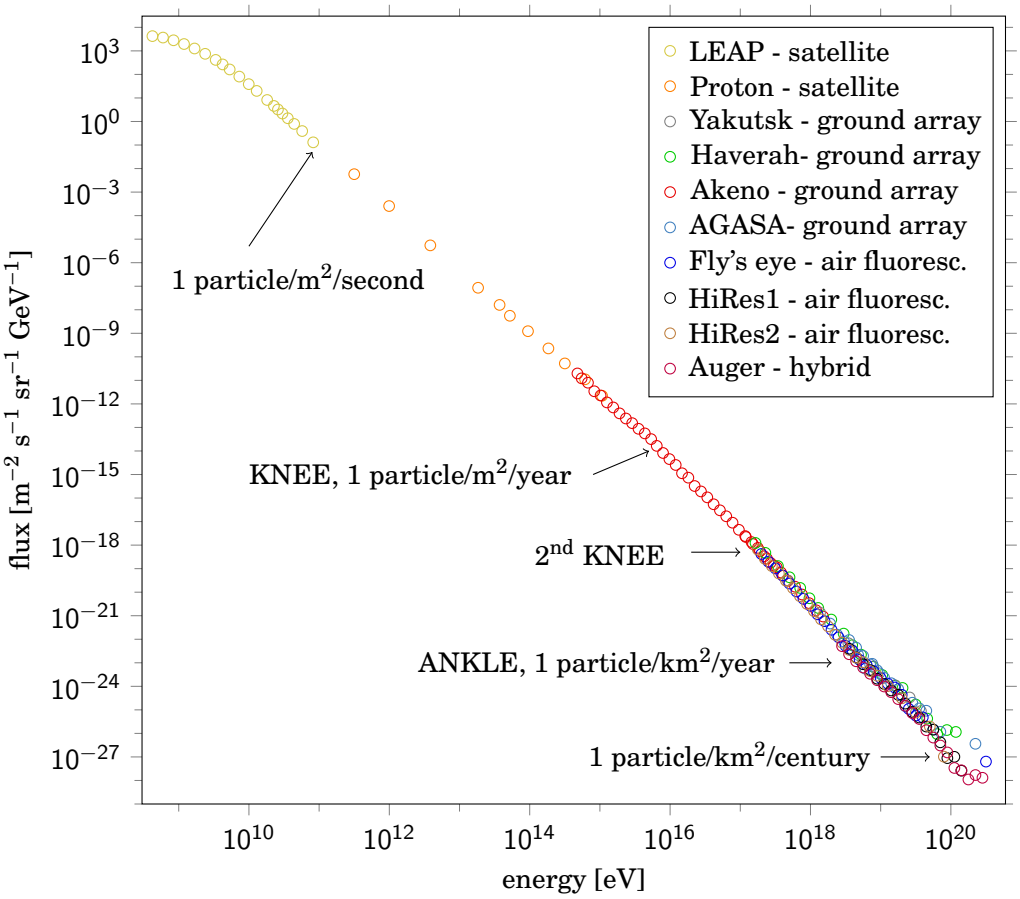

Figure 1.1: Cosmic ray energy spectrum from several experiments, see [15–17] and references therein.

The sources of cosmic rays are a subject of ongoing debate and continuous research. For galactic cosmic rays supernova remnants are regarded as candidates. For extragalactic cosmic rays one thinks of active galactic nuclei and of gamma-ray bursts, extremely energetic flashes of gamma rays released by collapsing stars, two merging stars or a star merging with a black-hole. For the determination of cosmic ray sources one usually considers showers with energy larger than $5 \cdot 10^{19}$ eV since the paths through the universe of cosmic rays with such a large energy are less deflected by magnetic fields. An astronomical object is considered a 'hotspot' if its celestial coordinates coincides, within measurement uncertainties, with an anisotropy in the density of origins of ultra high energy cosmic rays. The active galaxy Centaurus A, at a distance of 3.4 Mpc, is an example [18, 19]. Another example is possibly the starburst galaxy M82 or the blazer Mrk 180 [20, 21].

1.2 Cosmic air showers

While conducting his experiment for the east-west effect Rossi observed that many particles arrived simultaneously at separate detectors placed apart from each other [12]. The same phenomenon was detected independently by Auger in 1937 [22]. He recognized that primary cosmic ray particles interact with air nuclei in the atmosphere. The interaction leads to the production of many particles which in turn interact also with air nuclei. The result is a 'shower' of particles: a cosmic air shower.

The simplest shower to describe is an electromagnetic shower as, for instance, caused by a gamma ray. Electromagnetic showers are observed with Cherenkov Telescopes of the HESS experiment [23, 24]. When a photon passes the Coulomb field near an atomic nucleus in the atmosphere an electron and a positron can be created; a pair production process. Under the same condition the electron and the positron can radiate photons, the so-called Bremsstrahlung. The photons resulting from Bremsstrahlung can produce an electron positron pair and so on. The cascade of repeated collisions leads to a shower of electrons, positrons and photons.

Figure 1.2: Pair production (left) and bremsstrahlung (right).

Showers are far more likely to be caused by a proton or a heavier nucleus. When such a cosmic ray particle enters the atmosphere, a hadronic interaction will occur with a nucleus of an atom in the air, mostly nitrogen and oxygen. The collision results in the production of secondary particles, mostly pions, some neutrons, but also particles such as kaons. The neutral pions, with a mean lifetime of $8.4 \cdot 10^{-17}$ s, decay almost instantly into two gamma particles, giving rise to electromagnetic sub-showers. The charged pions, with a mean lifetime of 26 ns in rest, can collide with other nuclei, generating new pions. When the energy of a pion is not large enough to survive to the next collision, it will decay into a muon and a neutrino. That is, the positive pion decays into an anti-muon and a muon neutrino and the negative pion decays into a muon and a muon antineutrino:

$$\pi^+ \rightarrow \mu^+ + \nu_\mu \,, \tag{1.1}$$

$$\pi^- \rightarrow \mu^- + \overline{\nu}_\mu \,. \tag{1.2}$$

These are primary decay modes with a probability, branching ratio, close to unity. For both the charged and the neutral pion the other decay modes have very small branching ratios. The

muons, with a lifetime of 2.2 µs, will either survive to the surface of the Earth or decay into an electron and two neutrinos according to the following rules:

$$\mu^- \rightarrow e^- + \overline{\nu}_e + \nu_\mu \,, \tag{1.3}$$

$$\mu^+ \rightarrow e^+ + \nu_e + \overline{\nu}_\mu \,. \tag{1.4}$$

The energy loss of a muon due to Bremsstrahlung is negligible compared to electrons, while an electron resulting from the muon decay will contribute to the electromagnetic component of the shower. The whole of hadronic collisions and electromagnetic sub-showers form a so-called extended air shower (EAS). The shower size, the number of particles, is mainly determined by the photons, electrons, muons and neutrinos. A vertical EAS is shown in Figure 1.3.

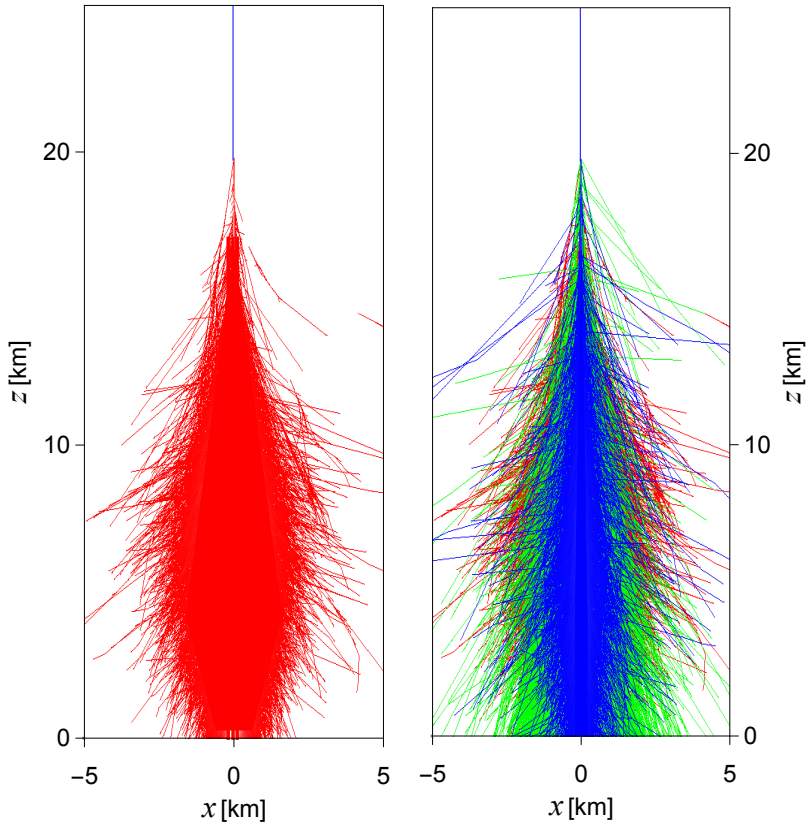

Figure 1.3: Impression of a vertical shower initiated by a 10^{15} eV proton. Left panel: electron trajectories (red). Right panel: Hadron trajectories (blue) plotted on top of the muon trajectories (green) plotted on top of the electron trajectories (red).

1.3 Jets in cosmic air showers

Quarks are elementary particles which carry an electric charge and a color charge. There are six types of quarks, known as flavors: d, u, s, c, b and t. In units of electron charge, the u, c and t quarks have electric charge $\frac{2}{3}$, the other quarks have electric charge $-\frac{1}{3}$. Each quark also has one of the three color charges red, green or blue. Quarks only appear in composite colorless particles: mesons and baryons (and possibly exotic composites like the pentaquark). Mesons and baryons, which are sensitive for the strong interactions, are called hadrons. Mesons consist of a quark-antiquark pair or of a linear combination of such pairs. The pion π^+, for instance, consists of a u and a $\overline{\mathrm{d}}$ quark, while the π^0, for instance, is a $(\mathrm{u}\overline{\mathrm{u}} - \mathrm{d}\overline{\mathrm{d}})/\sqrt{2}$ combination. Mesons are not stable, they decay by means of the strong or weak forces into mesons and leptons with smaller mass. The charged pion, for instance, decays into a μ and a ν_μ. Baryons consists of three quarks. A stable baryon is the proton p. It consists of a u, u and d quark. Another well known baryon is the neutron n which is a udd combination. On the basis of properties as spin, isospin, charge and strangeness mesons and baryons can be arranged in octets, nonets and decuplets [25].

Protons and the neutrons are the nucleons of which all the nuclei consist. The quarks in a nucleon are bounded tightly together by the strong force. Although the nucleons as a whole are colorless, there still is some exchange of gluons and pions, which supplies the nuclear force, the force which binds the nucleons to a nucleus. The nuclear force therefore is, so to say, a residual strong force. For radii larger than 1 fm the nuclear force is determined by the Yukawa potential $V \propto -\frac{g^2}{r}e^{-\mu r}$. Because of the exponential factor $e^{-\mu r}$ the Yukawa potential rapidly decreases. The Yukawa potential prevents the protons from repelling each other by the electric Coulomb force for distances smaller than about 2 fm. For the quarks inside a nucleon the potential is $V \propto \frac{\alpha_\mathrm{s}}{r} - kr$, where the strong coupling constant α_s depends on the virtuality Q^2 of the interaction. This leads to a the running coupling constant:

$$\alpha_\mathrm{s} = \frac{12\pi}{(11n_\mathrm{g} - 2n_\mathrm{f})\ln\left[\frac{Q^2}{\Lambda^2}\right]} \quad \text{if } Q^2 >> \Lambda^2 \,, \tag{1.5}$$

where $\Lambda \approx 0.2\,\mathrm{GeV}$ and where n_f and n_g are the number of quark flavors respectively the number of quark colors. For large energies the strong coupling constant is small, $\alpha_\mathrm{s} << 1$, leading to asymptotic freedom. The value of the strong coupling constant is often expressed at the M_Z energy: $\alpha(M_Z^2) \approx 0.12$. When a large amount of energy is transferred to a nucleon in a collision, the small coupling constant causes the quarks to behave as free quarks initially.

The linear factor kr in the quark potential causes a large attractive force between quarks. The force does not decrease with distance. This has severe consequences when a lepton or a quark (of a hadron) collides hard against a target quark inside a nucleon. Independent of the

amount of energy the target quark can not be kicked out of the nucleon, quark confinement. Instead, new quark pairs and gluons are created in between the initial position of the target quark and its 'kick-out' position: fragmentation. When a proton collides against a proton, a process which we will take as the basis for a cosmic ray proton colliding against a nucleus of a nitrogen or oxygen atom in the atmosphere, a main QCD process occurs with the production of quarks and, mostly soft, gluons.

If a small momentum transfer is involved with the collision of two nucleons, one speaks about soft QCD. The processes (elastic, minimum bias, and diffraction) are described by phenomenological models whose parameters are verified from collider experiments. For large momentum transfer one speaks about hard QCD. In the latter case the small value of strong coupling allows for perturbative QCD. The multiparton interaction leads to a production of a large number of gluons and quarks. The splittings are described by the DGLAP equations [26–28]. The gluon radiation leads to angles between the two partons after a splitting. That is, the partons obtain a transverse momentum p_{T}. The quarks created during the collision rearrange to mesons and baryons, the hadronization. These 'final' hadrons will have a momentum with a large component in the transverse direction. The bunch of new hadrons created this way can move in a direction close to the initial quark or diquark, a so-called jet. In Figure 1.4 a schematic example is given of two jets in, for convenience, $e^- e^+ \rightarrow q\overline{q}$ scattering.

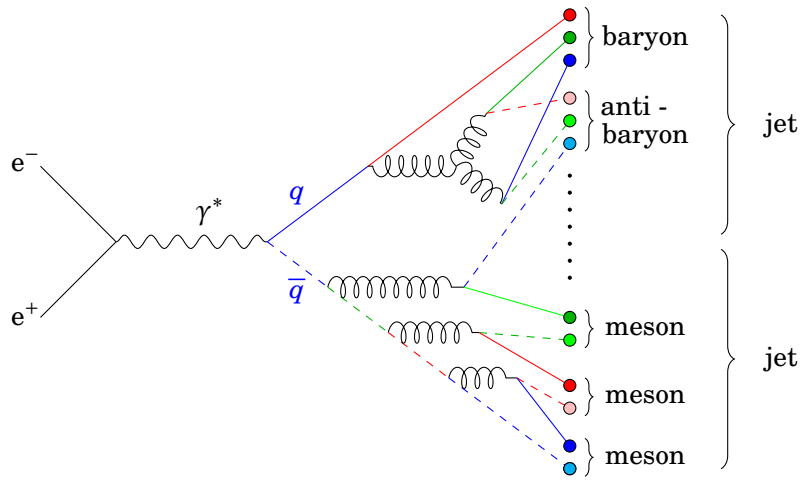

Figure 1.4: Fragmentation and hadronization in deep inelastic electron positron scattering.

Because of the quark structure of hadrons jets occur relatively often in hard collisions. An example of a dijet event in a proton-proton collision detected with ATLAS at CERN is shown in Figure 1.5. Although less frequently events with three or more jets can occur as well.

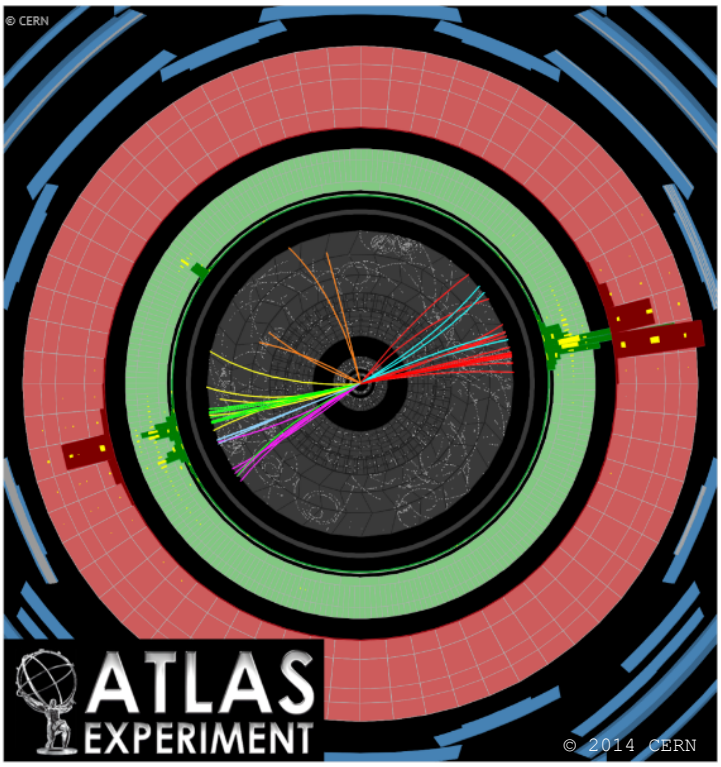

Figure 1.5: A dijet event in a p-p collision as detected with ATLAS.

In a collider the protons collide with opposite but equally large velocities, the center of mass (CM) frame is at rest. In a cosmic air shower the incoming cosmic ray has a velocity almost equal to the speed of light while the target nucleon in an atom in the atmosphere can be considered at rest. The Lorentz transformation from the CM frame to the fixed target (FT) frame causes the transversal jets to be close to the core of the shower, see Figure 1.6.

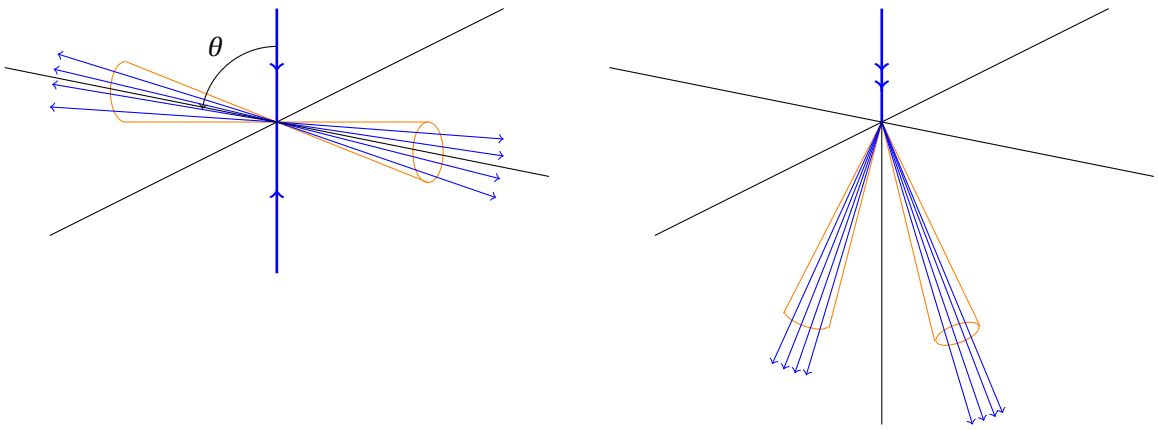

Figure 1.6: Dijet event in the CM frame (left) and in the FT (right).

The transversality of the direction of a jet is described by the angle θ, see Figure 1.6. If $\theta = \frac{\pi}{2}$ the jet cone is completely transverse. For the collision in the FT frame the jet cone has a large component parallel to the shower axis. At the altitude of observation the two jets cause density fluctuation with respect to the density of the main shower. An impression of the density pattern in a shower with two jets is shown in Figure 1.7.

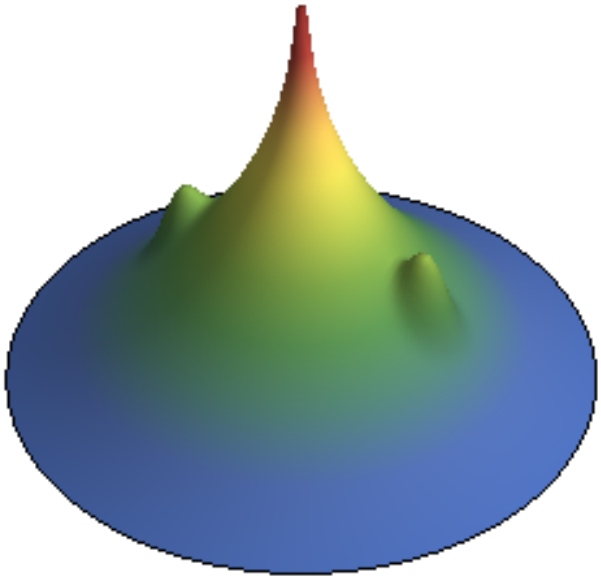

Figure 1.7: Impression of the lateral density, not to scale, plotted in vertical direction, with two density fluctuations caused by a di-jet for the hypothetical situation where the lateral density is smooth.

With an array of detectors one can try to reconstruct a jet fluctuation from the detector signals. The investigation of jets in cosmic air showers requires insight in the evolution of the shower in the atmosphere, the distribution of particles at observation level, the reconstruction of showers on the basis of detected signals and the relativistic kinematics of jets. Next to the simulation of cosmic air showers it also requires the simulation of the hadronic interaction in the first collision of the cosmic ray with the nucleus of an atom in the atmosphere. The collision is comparable to a proton-proton collision. The simulation of proton-proton scattering with large p_{T} jets will be performed with version 8.212 of PYTHIA [29–31]. PYTHIA is a Monte Carlo event generator for e-e, e-p and p-p interactions based on leading order matrix elements. On the basis of the splitting functions it simulates the branching of the quarks and gluons to a scale where perturbative QCD is valid. As soon as the quarks and gluons become more separated, all at the fm-scale, α_{s} becomes large and the QCD process is no longer perturbative. The interaction process factorizes in two parts: the hard process and the fragmentation part. PYTHIA contains a package JETSET which takes care of the fragmentation according to the Lund string model and the hadronization to 'final' particles, particles with a lifetime longer than 10^{-8} s.

1.4 Longitudinal profile

After the first collision of a cosmic ray with a nucleus in the atmosphere the shower size grows. Initially the growth is approximately exponential. However, with each collision the energy of the secondary particles is smaller than the energy of the incoming particle. When the energy falls below the critical energy, which is the energy for which the ionization losses are equal to the radiation losses, the electron will be absorbed or scattered out of the shower. This will slow down the growth of the electromagnetic shower. After reaching a maximum the number of particles will decrease. The longitudinal profile is the evolution of the number of particles during its passage through the earth's atmosphere. Since the interactions in the shower depend on the atmospheric depth met by the traveling shower particles, the number of particles is usually plotted against atmospheric depth. The atmospheric depth X at an altitude z is given by $X(z) = \int_z^\infty \rho(r)\mathrm{d}r$. In Figure 1.8 an example is given of the longitudinal profile of electrons of a vertical shower initiated by a 10^{15} eV proton. The first interaction is around $70\,\mathrm{g\,cm^{-2}}$, which is at an altitude of 22 km. The example shower size reaches a maximum of about $7 \cdot 10^5$ electrons around $550\,\mathrm{g\,cm^{-2}}$, which is at an altitude of 5 km.

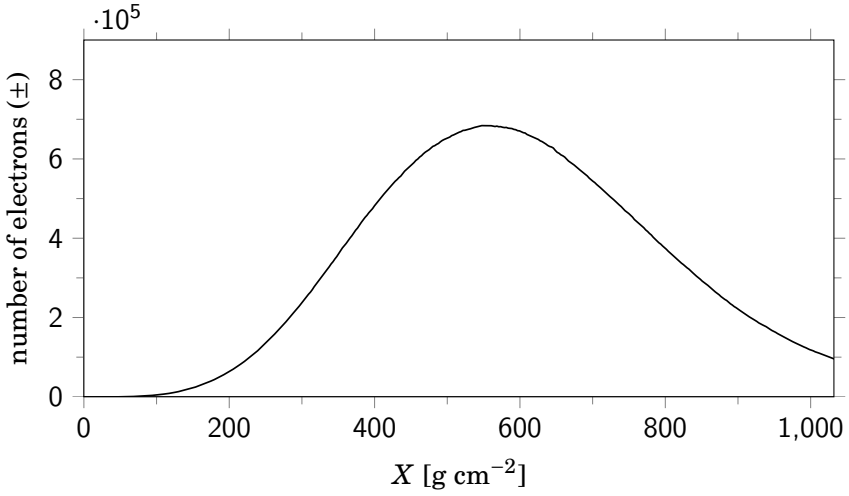

Figure 1.8: The number of electrons of a vertical shower initiated by a 10^{15} eV proton plotted against atmospheric depth.

About 10^5 electrons survive to the surface of the Earth ($z = 0$), where the atmospheric depth is about $1030\,\mathrm{g\,cm^{-2}}$. The evolution of the longitudinal profile differs from shower to shower. The atmospheric depth of the first interaction as well as the atmospheric depth between the successive interactions is a matter of probability. The average value, the interaction length is related to the cross section and depends on the energy of the interaction. In Figure 1.9 an impression is given of the different evolutions of showers with the same initial condition: all vertical shower initiated by a 10^{15} eV proton.

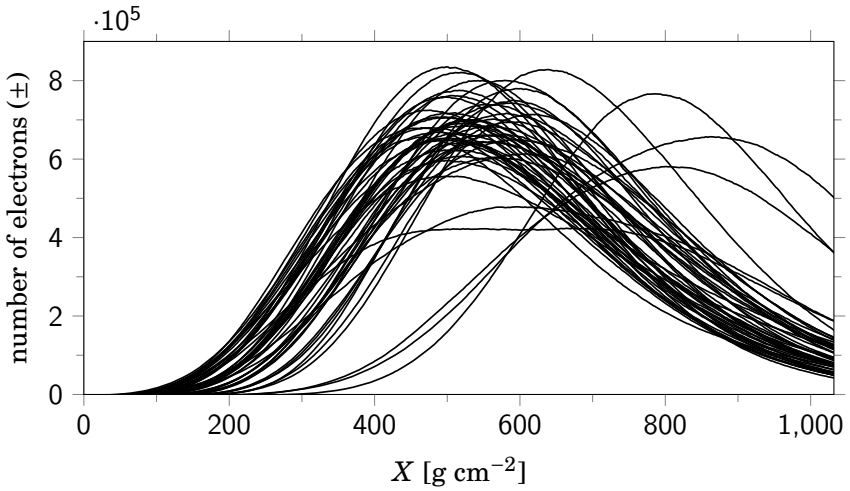

Figure 1.9: The number of electrons of 50 vertical showers initiated by a 10^{15} eV proton plotted against atmospheric depth. Three of the showers developed slowly; the maximum is around $800\,\mathrm{g\,cm^{-2}}$. For one shower shows the maximum shower size is constant for a large interval of atmospheric depth

.

For Figures 1.8 and 1.9 the showers were simulated, without thinning, by means of AIRES-2-8-4a [32] with SIBYLL 2.1 [33] for the hadronic interactions. It shows how the different evolutions causes the number of electrons at ground level to range from $3 \cdot 10^4$ through $5 \cdot 10^5$

A simple model for the longitudinal evolution of the electromagnetic cascade has been given by Heitler [34]. It predicts well the depth of maximum shower size as a function of energy of the primary cosmic particle. The longitudinal evolution is described far more accurately by a system of diffusion equations [35–38]. In Chapter 2 intermediate models for the electromagnetic shower will be considered. The Heitler model has been applied to the hadronic cascade by Matthews [39]. The prediction for the elongation rate, the change of the depth of shower maximum with the logarithm of the energy, is based on the first generation of γ's. In Chapter 2 the Heitler-Matthews model is extended to the full hadronic cascade. The longitudinal evolution of the number of gamma's, electrons, muons and hadrons in a hadronic shower is shown in Figure 1.10. The shower of Figure 1.10 and all Monte Carlo showers hereafter are simulated without thinning with CORSIKA-v7.4 [40], with QGSJET-II-04 [41] + GHEISHA [42] for the hadronic interactions. For the shower of Figure 1.10 there are at ground level about $5 \cdot 10^5$ gamma's, $1 \cdot 10^5$ electrons, $1 \cdot 10^4$ muons and $8 \cdot 10^2$ hadrons (mainly pions). For small showers most of the electrons will be absorbed in the atmosphere, only some muons will reach the surface of the Earth. For extensive air showers the number of electrons that reach the Earth exceeds the number of muons. Since low energy showers occur far more often than high energy showers, the net result is that there are about four times more muons than electrons at sea level, see Fig. 7.9 of [43]. The muon rate at sea level is $100\,\mathrm{s^{-1}\,sr^{-1}\,m^{-2}}$.

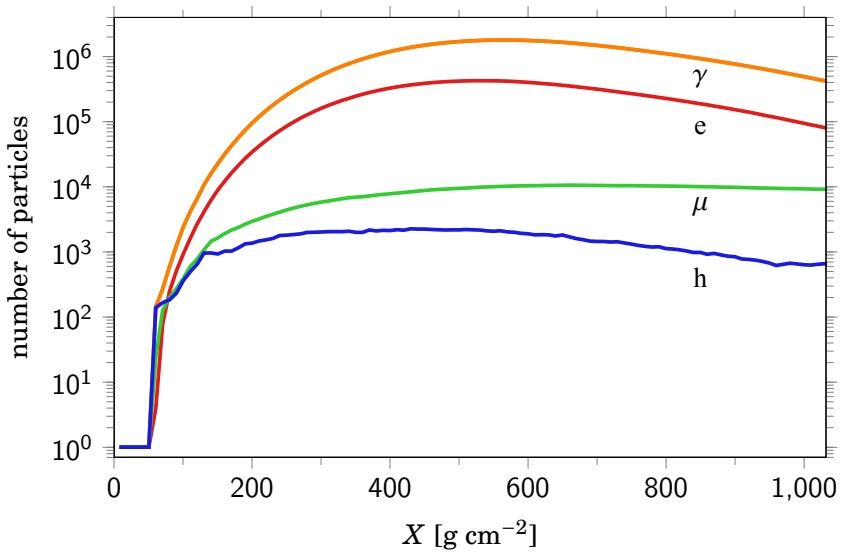

Figure 1.10: The longitudinal development of the number of gamma's (orange), electrons (red), muons (green) and hadrons (blue) of a vertical shower initiated by a 10^{15} eV proton versus atmospheric depth.

1.5 Lateral density

While the cosmic air shower develops in the longitudinal direction it also develops in the direction perpendicular to the shower axis, the lateral direction. The lateral spread in an EAS is the result of both hadronic interactions and electromagnetic interactions. The transverse momentum in hadronic collisions, the angles between produced particles in pair-production, bremsstrahlung and decays, deflections due to Coulomb interactions and Compton scattering all cause the shower front to expand in the lateral direction. Since less energetic particles will lag behind the more energetic particles the thickness of the shower front will increase. The shower front can be imagined as a slightly curved 'pancake' moving with nearly the speed of light. An impression of the front of a vertical shower is shown in Figure 1.11. The radius of curvature for this shower front is about 10 km.

Particles reaching the ground are distributed over a large area. The number of particles per square meter, the lateral density, is large near the center and decreases with the distance to the core. The lateral density depends on the energy of the primary cosmic ray, the identity of the cosmic ray and the inclination of the shower. The larger the energy the larger the lateral density. The larger the mass number of a cosmic nucleus the larger the probability it will collide with an atom in the air. As a consequence the depth of maximum shower size is smaller for an iron initiated shower than for a proton initiated shower of the same energy. As a further consequence the iron initiated shower is more attenuated at the moment of arrival at the ground, which leads to a smaller lateral density.

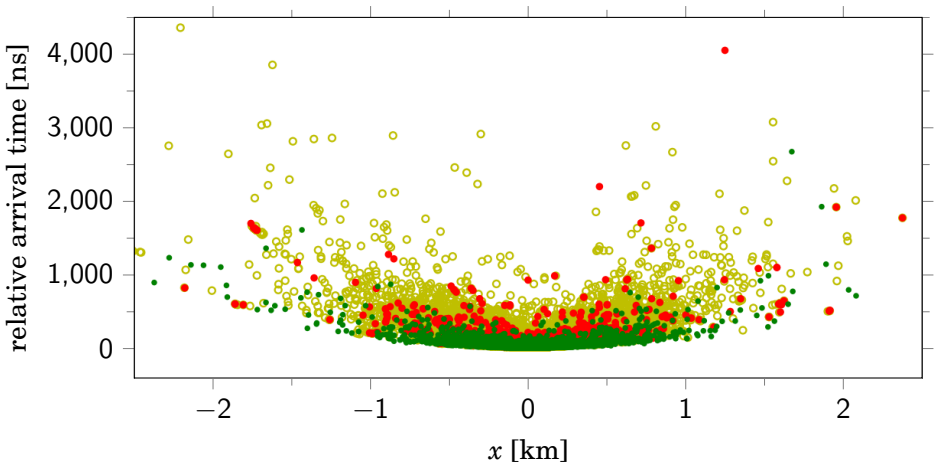

Figure 1.11: An impression of the front of a 10^{15} eV proton initiated vertical shower, the muons (green) plotted on top of the electrons (red) plotted on top of the gamma's (yellow).

The inclination of the shower has a large effect on the lateral density. Inclined showers are more attenuated because the slant depth is $\cos^{-1}\theta$ times the vertical depth, with θ the zenith angle. The attenuation mainly concerns the electrons. The horizontal density of electrons and the density of muons for an inclined shower therefore differ substantially from the one of a vertical shower. The horizontal density is of interest since shower detectors are usually placed in a, more or less, horizontal plane. For two different zenith angles the horizontal density of electrons, muons and their sum are plotted for a 10^{16} eV shower in Figure 1.12.

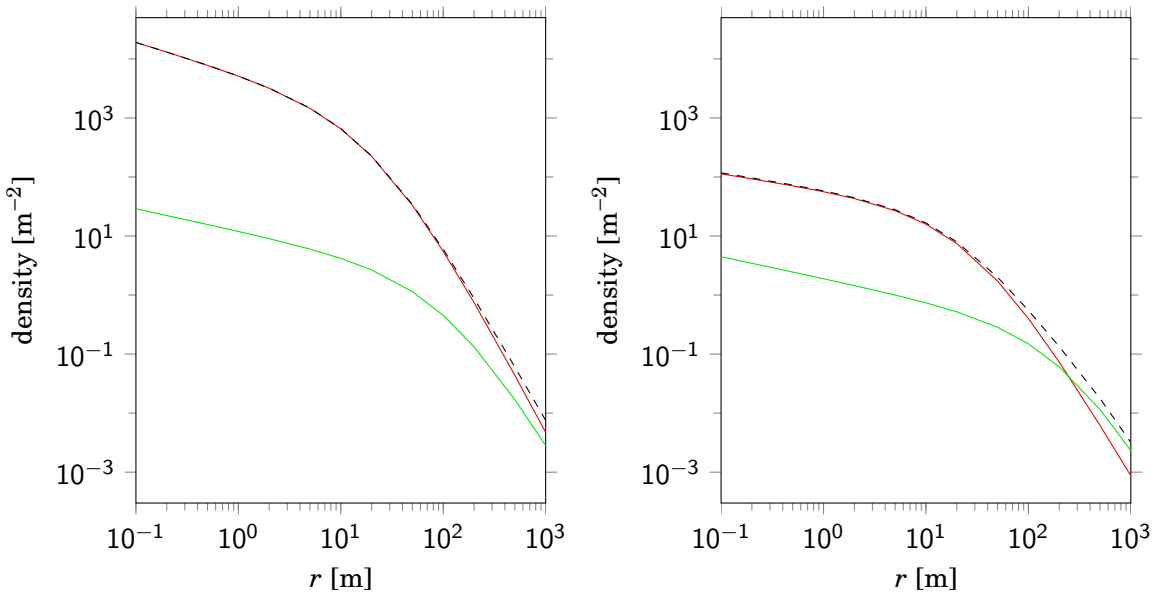

Figure 1.12: The horizontal density of electrons (red), muons (green) and the sum of them (black dashed) versus distance to the shower core for a 10^{16} eV proton shower with 0° (left) and with 45° (right).

For the vertical situation, left panel of Figure 1.12, the shower size of charged particles is mainly determined by the electrons for radii smaller that 300 m. Near the core the electron density is about 400 times larger than the muon density. For $\theta = 45°$, right panel of Figure 1.12, the sum density already starts to deviate from the electron density around a radius of 100 m in the horizontal plane. Near the core the electron density of the inclined shower is far smaller than for the vertical situation, while the muon density is less influenced by the inclination.

For a vertical shower the horizontal density depends only on the radius; the iso-density contours are circles. The projection of the inclined shower front on the horizontal plane causes the iso-density contours to be stretched to ellipses. Moreover, since the early part of the shower is less attenuated than the late part, the centers of the iso-density contours are shifted. Both require the horizontal density to be described as a function of the radius r and the polar angle α. In Chapter 3 different aspects of the lateral density will be considered. A polar density function, parameterized by energy and inclination will be derived.

1.6 HiSPARC

There are different ground-based methods to detect cosmic air showers. The relativistic velocity of charged shower particles in the atmosphere causes Cherenkov radiation, electromagnetic radiation emitted when a charged particle passes through a medium at a speed larger than the phase velocity of light in that medium. The shower particles can excite nitrogen molecules in the air. The de-excitation of nitrogen molecules produces fluorescent light. The advantage is that Cherenkov light and fluorescent light provide information about the longitudinal development of a shower. The disadvantage is that both can be detected only during clear, moonless nights. Another type of ground-based detector is the water Cherenkov detector. When a charged particle of the shower enters a tank filled with water it will radiate Cherenkov light which can be detected. A common method to detect charged particles of a shower is by means of a scintillator. Scintillation light is generated when a shower particle traverses a layer of scintillation material. Scintillator detectors are employed by the HiSPARC experiment.

HiSPARC is a large scale cosmic ray experiment [44]. It has two goals. One is to offer an opportunity for high school students and teachers to participate in scientific research. The other is to conduct scientific studies on cosmic rays. It consists of a network of more than 100 detection stations. About 90 % of them are located in the Netherlands, the others in England and Denmark. Most stations are positioned on the roofs of high schools participating in the HiSPARC project. The positions of stations is therefore determined by the geographical location of the participating high schools rather than by a predetermined pattern. The locations of HiSPARC stations in the Netherlands are shown in Figure 1.13.

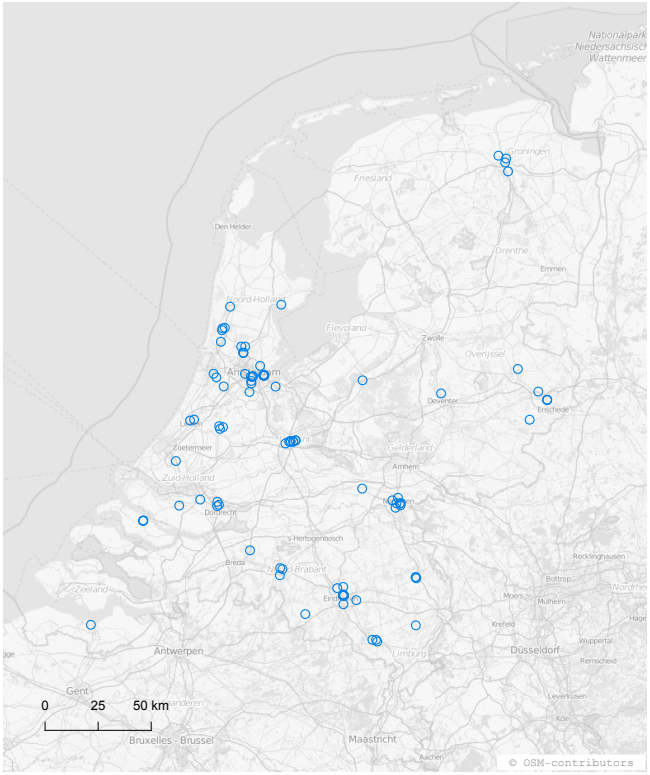

Figure 1.13: Locations of the HiSPARC stations in the Netherlands.

A particular role is played by the stations at Science Park Amsterdam (SPA). Momentarily it consists of 11 stations of which 10 are positioned on the roofs of scientific institutes. Each station at SPA consists of 4 scintillator detectors. Since they are distributed over an area of about 300 acres an extensive shower can cause signals in a number of stations. From the set of signals the direction and size of the shower can be derived. The locations of the stations at SPA are shown in Figure 1.14. The SPA station are numbered 501 through 511in the order of their historical appearance.

When an electron or a muon traverses a scintillation detector it may result in a signal. An isolated detector signal is not recorded; only if a signal is received from a second detector of the same station within 1.5 µs after the first signal, then the time and size of the signals are recorded and stored as an 'event' in the Event Summary Database (ESD).

In Chapter 4 a description is given of the energy loss of electrons and muons in scintillator material and of the way the energy deposit is converted to a digital signal value. This is mainly hardware. The software, i.e. the Python package SAPPHiRE [45, 46], a framework developed for the analysis of HiSPARC data, and the application of the shower simulation program CORSIKA [47] are described also in Chapter 4.

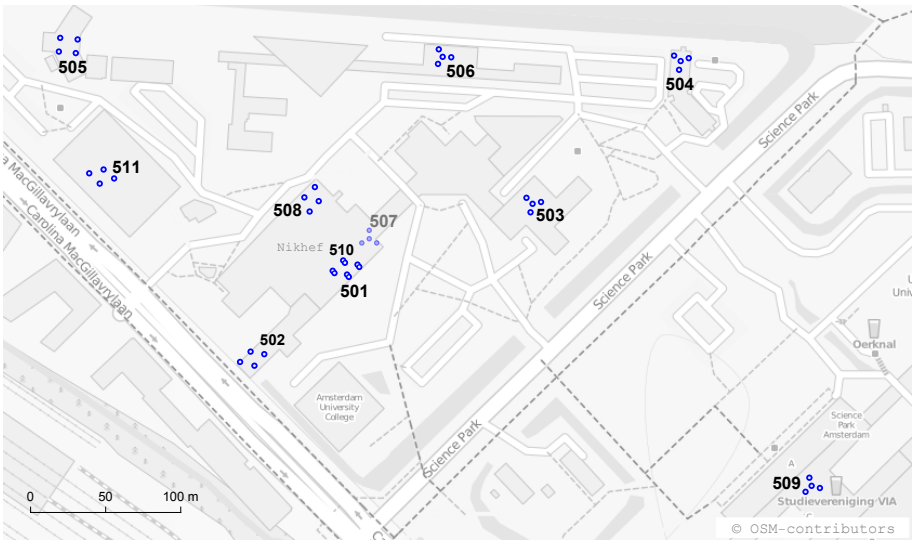

Figure 1.14: Locations of HiSPARC station detectors at Science Park Amsterdam. Station 507 has been bleared to express its indoor location at floor level.

1.7 Reconstruction methods

Events that are within a certain window of time simultaneous, a 'coincidence', are regarded to belong to the same shower. The differences between the times of arrival at different stations increase in general with the inclination of a shower. If at least three stations participate in a coincidence the direction of a shower, i.e. the zenith angle θ and the azimuth angle ϕ, can be reconstructed from the arrival time differences. A small complication is that the SPA stations are not exactly in a horizontal plane. For three stations, with different altitudes, participating in a coincidence an analytical expression is derived for the direction of the shower. For three or more stations, all in a horizontal plane, an analytical expression is derived by means of regression. For more than three stations with different altitude the latter result is applied in an iterative procedure. A description of the direction reconstruction methods and a theoretical derivation of the uncertainty are given in Chapter 5.

More complicated is the reconstruction of the core of the shower. The situation can be compared with the intensity of a light bulb. Three photometers at different positions are sufficient for the determination of the position of a light bulb if its intensity is known. If the intensity of the light bulb is not known, as the energy of a shower is not known a priori, a fourth photometer is required. In case of a shower one seeks the core position for which the lateral density function fits best with the signals. To avoid a large number of trials an estimation of the core position is desired. A method based on radical axes is described in Chapter 6. The energy of the shower is determined from the best fitting lateral density function. Direction and energy reconstructions and other analyses of HiSPARC data are presented in Chapter 7.

1.8 Jet rates and jet simulation

The probability that a cosmic ray proton collides inelastically with a nucleon in the atmosphere is determined by the cross section $\sigma^{\text{inel}}_{\text{p-air}}$. The larger the cross section the smaller the interaction length, the mean free path between two successive collisions. The relation between interaction length in units of atmospheric depth and the cross section is given by

$$\lambda\,[\mathrm{g\,cm^{-2}}] = \frac{A}{N_A \cdot \sigma[\mathrm{cm^2}]}\ , \tag{1.6}$$

where A is the mass number, $A_{\text{air}} \approx 14.5\,\mathrm{g\,mol^{-1}}$, and N_{A} is the Avogadro constant, $N_{\text{A}} = 6.022 \cdot 10^{23}\,\mathrm{mol^{-1}}$. For the cross section in millibarn, $1\,\mathrm{mb} = 10^{-27}\,\mathrm{cm^{-2}}$, the relation reduces to

$$\lambda\,[\mathrm{g\,cm^{-2}}] = \frac{24100}{\sigma[\mathrm{mb}]}\ . \tag{1.7}$$

The cross section for p-air collisions grows approximately linearly with the logarithm of the proton energy from $3.3 \cdot 10^2$ mb for $10^{13.5}$ eV to $4.3 \cdot 10^2$ mb for 10^{16} eV.

As for p-p collisions the hard scattering of a high energy cosmic proton with the nucleus of an atom in the atmosphere will give rise to jets. The ratio of a jet cross section and the cosmic ray collision cross section determines the probability for the jet to occur in the first interaction. This as well as the relativistic kinematics of jets is described in Chapter 8.

The collision of a cosmic proton with a nucleus of an atom of the atmosphere of the Earth is simulated by a p-p collision with PYTHIA. The output of PYTHIA, particles and their momentums, is used as input for the shower simulator CORSIKA. The output of CORSIKA, the positions of electrons and muons at the desired observation level, is used as input for a Monte Carlo program. The latter throws the electrons and muons on a large square array of detectors and inspects all the detector signals for the largest fluctuation. To ascribe a fluctuation to a jet it has to be significantly larger than the Poisson variations. In another program the positions of the largest fluctuations are compared with the expected positions of the imposed jets. The whole simulation is described in Chapter 9. The simulation results are analyzed in Chapter 10. The important simulation results are the effective areas and the effective areas per observational jet. They are tabulated in Appendices A and B. The effective areas per observational jet are translated to observational jet rates. The latter are tabulated in Appendix C. In Chapter 11 the HiSPARC data for the SPA cluster is analyzed for large fluctuations. Conclusions concerning the observation of jets at sea level are drawn in the final section of Chapter 11.

2 Longitudinal profile

2.1 Electromagnetic cascade

According to the Heitler model each particle (electron, gamma) will split into two particles of half the energy after traveling a fixed distance. This distance is equal to $\lambda_r \ln 2$, where λ_r is the radiation length. The radiation length is the mean distance over which an electron loses all but e^{-1} of its energy by bremsstrahlung and $\frac{7}{9}$ of the mean free path for pair production by a photon [48]. For air $\lambda_r = 37\,\mathrm{g\,cm^{-2}}$ [49]. After the first collision there will be 2 particles, after the second collision there are 4 particles and so on. After n collisions, at atmospheric depth $n\lambda_r \ln 2$, there will be 2^n particles each with energy $E_0 \cdot 2^{-n}$, where E_0 is the energy of the primary cosmic ray. The cascade continues until the energy of a particle is decreased to the critical value E_c at which the bremsstrahlung and ionization rates are equal. For air $E_c \approx 84\,\mathrm{MeV}$ [49]. Beyond the critical value the energy losses will be dominated by ionization instead of radiation and the particle is considered lost for the shower. According to the Heitler model the shower stops when $n > n_c$, where

$$n_c = \ln(E_0/E_c)/\ln 2 \,. \tag{2.1}$$

Although $n_c \lambda_r \ln 2$ is a good prediction for the depth of maximum shower size, the shape of the shower profile is far from realistic.

The longitudinal evolution is described accurately by a system of diffusion equations [35–37]. For the so-called *Approximation A*, complete screening and the neglect of collision losses, it can be written as

$$\frac{\partial n_{e\pm}}{\partial t} = -A' n_{e\pm} + B' n_\gamma \tag{2.2}$$

and

$$\frac{\partial n_\gamma}{\partial t} = C' n_{e\pm} - \sigma_0 n_\gamma \ . \tag{2.3}$$

In these equations t is the atmospheric depth in units of radiation length

$$t = \frac{X}{\lambda_r} \tag{2.4}$$

and A', B' and C' are integral operators:

$$A' n_{e\pm}(E,t) = \int_0^1 \left[n_{e\pm}(E,t) - \frac{1}{1-v} n_{e\pm}\left(\frac{E}{1-v}, t\right)\right] \phi(v) \mathrm{d}v \ , \tag{2.5}$$

$$B' n_\gamma(E,t) = 2 \int_0^1 n_\gamma\left(\frac{E}{u}, t\right) \frac{\psi(u)}{u} \mathrm{d}u \ , \tag{2.6}$$

$$C' n_\gamma(W,t) = \int_0^1 n_{e\pm}\left(\frac{W}{v}, t\right) \frac{\phi(v)}{v} \mathrm{d}v \ , \tag{2.7}$$

where

$$\psi(u) = u\phi\left(\frac{1}{u}\right) = \frac{4}{3}u^2 - \frac{4}{3}u + 1 + 2b\left(u^2 - u\right) \ . \tag{2.8}$$

In the latter $b = \left(18 \ln\left[183 Z^{-1/3}\right]\right)^{-1} \approx 0.0122$ is very small in comparison to the other coefficients. $A' n_{e\pm}$ consists of two integrals. The first one,

$$\int_0^1 n_{e\pm}(E,t)\phi(v)\mathrm{d}v = n_{e\pm}(E,t) \int_0^1 \phi(v)\mathrm{d}v \ , \tag{2.9}$$

represents the decrease of electrons with energy E due to bremsstrahlung. The latter integral is logarithmically divergent at $v \to 0$; the infrared divergence. The other part of $A' n_{e\pm}$, representing the increase of electrons with energy E due to bremsstrahlung of electrons with larger energy, also is divergent. However, both divergences cancel each other, leaving a finite value for the net change of electrons with a certain energy. $B' n_\gamma$ represents the increase of electrons due to pair production. $C' n_\gamma$ represents the increase of gamma's due to bremsstrahlung of electrons. Finally, $\sigma_0 n_\gamma$ represents the decrease of gamma's due to pair production, where

$$\sigma_0 = \int_0^1 \psi(u)\mathrm{d}u = \frac{7}{9} - \frac{1}{3}b \approx 0.77 \tag{2.10}$$

in units of radiation length. That is, the interaction length of pair production is $\frac{9}{7}$ times the radiation length: $\lambda_{\mathrm{pair}} = \frac{9}{7}\lambda_r$.

The system of equations is solved by means of a Mellin transform and a saddle point approximation. For a clear exposure see for instance [50]. The solution can be described by to the

Greisen function:

$$N_{\mathrm{e}} = \frac{0.37}{\sqrt{n_{\mathrm{c}}}} \cdot e^{t(1-1.5\ln s)} \,, \tag{2.11}$$

where

$$s = \frac{3t}{t + 2t_{\max}} \tag{2.12}$$

is the age parameter with

$$t_{\max} = n_{\mathrm{c}} \ln 2 \,. \tag{2.13}$$

For a 10^{15} eV shower the longitudinal profile according to the Heitler model and the Greisen function are shown in Figure 2.1.

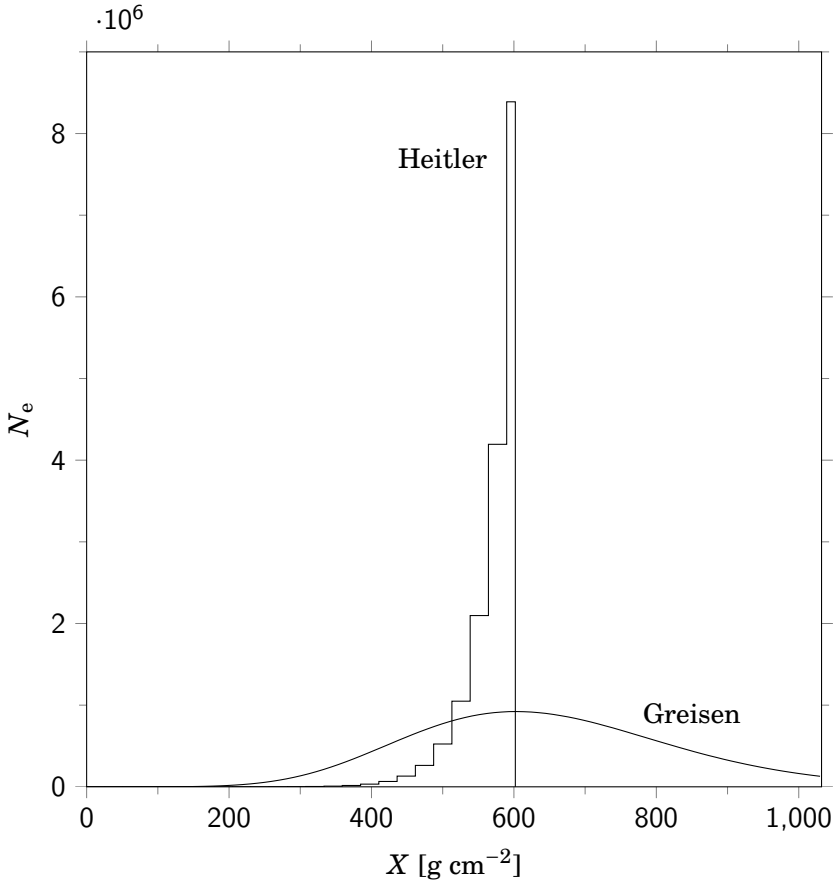

Figure 2.1: Longitudinal shower profile according the Heitler model and the Greisen function.

Realistic profiles for the electromagnetic shower can also be obtained from intermediate models. The analysis has been published [51]. The publication is shown hereafter.

2.2 Hadronic cascade

The main difference between electromagnetic and hadronic interactions is the multiplicity of secondary particles. In electromagnetic cascades bremsstrahlung and pair production are interactions where two particles are produced, while a hadronic interaction of a proton or an iron nucleus with a nucleus of the air many particles are produced. Depending on the energy the incoming particle the hundreds of secondary particles may be produced. The multiplicity increases with atomic number. Since this results in a less energy per secondary particle the depth of maximum shower size is smaller for an iron primary than for a proton primary.

The Heitler model can also be applied to hadronic cascades [39]. As for electromagnetic cascades the energy is regarded to be equally divided among the secondary particles. It leads to predictions of too small a depth of maximum. On the basis of the first generation the prediction for the elongation rate, $\mathrm{d}X_{\mathrm{max}}/\mathrm{d}\log_{10}E_0$, seems right. By means of a semi-analytical approach the Heitler-Matthews model can be extended to the second and further generations of the hadronic cascade. Then the predictions for both the depth of maximum and the elongation rate are too small. A more realistic, non-equal division of the energy, which is hard to model, will increase the prediction of both the depth of maximum and the elongation rate. The analysis has been published [52]. The publication is shown hereafter.

2.3 Summary

For the longitudinal evolution of the electromagnetic shower four models have been considered. The simplest one is the Heitler model: fifty-fifty energy splittings at fixed increments of atmospheric depth. The next to simplest one is an intermediate model where the depths of interaction are stochastically determined. With a small modification by means of a parameter X_0 the corresponding longitudinal profile is a Gaisser-Hillas function. A more accurate intermediate model is obtained when the the fifty-fifty splittings are stretched to non-equal energy divisions in splittings, while each splitting still occurs with the same probability. The corresponding longitudinal profile is a Gaussian in Age function. If the model is further stretched to physical probabilities for the splittings one arrives at the well known model of Rossi and Greisen. A schematic overview is shown in Table 2.1.

model	depths of interaction	energy division	splitting probability	longitudinal profile function
Heitler	●	●	●	Heitler
intermediate 1	○	●	●	Gaisser-Hillas
intermediate 2	○	○	●	Gaussian in Age
Rossi-Greisen	○	○	○	Greisen

Table 2.1: Model properties and the corresponding longitudinal profiles. • = fixed, ○ = stochastic.

For the longitudinal evolution of hadronic showers the Heitler-Matthews model is based on the first interaction. With suitable descriptions of interaction length and multiplicity as functions of energy the Heitler-Matthews model has been extended to the full hadronic cascade. The latter under predicts both the depth of maximum shower size and the elongation rate. The under prediction is a consequence of the tacitly assumed homogeneous energy distribution over the secondary particles. An inhomogeneous energy distribution over the secondary particles increases both the depth of maximum shower size and the elongation rate.

Recently, the extension of the Heitler-Matthews model has been utilized to calculate the muon production depths by means of a branching model for hadronic air showers [53].

3 Lateral density

3.1 Lateral density function

To reconstruct the core and the energy of the cosmic ray the detector signals have to be fitted along a lateral density function (LDF). The LDF is a function of the radial distance r to the core of the shower and depends on the energy of the primary and the zenith angle. It also depends on the individual development of the shower. However, for reconstructions it is difficult to take individual deviations into account. We therefore restrict to average LDF's. The basic LDF is the Nishimura-Kamata-Greisen (NKG) function [38, 54].

$$\rho(r) = c(s) \cdot N_{\mathrm{e}} \left(\frac{r}{r_0}\right)^{s-2} \left(1 + \frac{r}{r_0}\right)^{s-4.5} , \tag{3.1}$$

where $c(s)$ is the normalization factor

$$c(s) = \frac{\Gamma(4.5-s)}{2\pi r_0^2 \Gamma(s)\Gamma(4.5-2s)} \tag{3.2}$$

and where r_0 is the Molière radius:

$$r_0 = \lambda_{\mathrm{r}} \frac{E_{\mathrm{s}}}{E_{\mathrm{c}}} . \tag{3.3}$$

with $E_{\mathrm{s}} = m_{\mathrm{e}} c^2 \sqrt{\frac{4\pi}{\alpha}} \approx 21.2$ MeV. The parameter E_{s} is known as the scale energy. The age parameter s is given by

$$s = \frac{3X}{X + 2X_{\max}} \tag{3.4}$$

with X is the atmospheric depth. As we saw before, the value of $X_{\max}$ is equal to $\lambda_{\mathrm{r}} \ln(E_0/E_{\mathrm{c}})$. The number of electrons (+ and -) at ground level, which is the altitude of the detectors, is denoted as N_{e}. For positive arguments in the Gamma functions the age parameter should satisfy

the condition $0 < s < 2.25$. Since $s = 1$ at $X = X_{\max}$ the value of the age parameter at ground level is $s \approx 1.5$ for 1 PeV showers.

To derive the NKG function a system of equations, as already derived by Landau [55], had to be solved. It reads:

$$\frac{\partial n_{e\pm}}{\partial t} + \vec{\theta} \cdot \vec{\nabla}_r n_{e\pm} = -A' n_{e\pm} + B' n_\gamma + \frac{E_s^2}{4E^2} \vec{\nabla}_\theta^2 n_{e\pm} + E_c \frac{\partial n_{e\pm}}{\partial E} \tag{3.5}$$

and

$$\frac{\partial n_\gamma}{\partial t} + \vec{\theta} \cdot \vec{\nabla}_r n_\gamma = C' n_{e\pm} - \sigma_0 n_\gamma \ , \tag{3.6}$$

where t is the atmospheric depth in units of radiation length: $t = X/\lambda_r$ and where $\vec{r}$ and $\vec{\theta}$ are the two dimensional lateral and angular deviations of the particle densities respectively. Without the spatial variations, i.e. without the second term on the left hand side of the Equations 3.5 and 3.6, and without the Coulomb scattering and collision losses, i.e. without the third and fourth term on the right hand side of Equation 3.5, the system reduces to the Equations 2.2 and 2.3 as considered for the longitudinal development. The fourth term on the right hand side of Equation 3.5 represents the collision losses. The third term on the right hand side of Equation 3.5 represents the Coulomb scattering.

Most LDF's are modifications of the NKG function [56]. The following LDF was used for the KASCADE experiment [57]:

$$\rho(r) = N_e \cdot c(s) \cdot \left(\frac{r}{r_0}\right)^{s-\alpha} \left(1 + \frac{r}{r_0}\right)^{s-\beta} \ , \tag{3.7}$$

where

$$c(s) = \frac{\Gamma(\beta - s)}{2\pi r_0^2 \Gamma(s - \alpha + 2)\Gamma(\alpha + \beta - 2s - 2)} \tag{3.8}$$

is the normalization constant. Although the parameters r_0 and s play a similar role as the Molière radius and the shower age in the original NKG function, they are rather fit parameters now. Optimum agreement with the KASCADE data was obtained for $\alpha = 1.5$, $\beta = 3.6$ and $r_0 = 40\,\text{m}$ for the electron density and $\alpha = 1.5$, $\beta = 3.7$ and $r_0 = 420\,\text{m}$ for the muon density. The parameter s should satisfy the condition $0.5 < s < 1.55$. Since the numerical relation with shower age is lost the fit parameter s is called the shape or form parameter [57].

For the present analysis the following LDF will be used initially for the lateral density in the horizontal plane of observation:

$$\rho(r) = N \cdot c(s) \cdot \left(\frac{r}{r_0}\right)^{s_1} \left(1 + \frac{r}{r_0}\right)^{s_2} \ , \tag{3.9}$$

where

$$c(s) = \frac{\Gamma(-s_2)}{2\pi r_0^2 \Gamma(s_1+2)\Gamma(-s_1-s_2-2)} \,. \tag{3.10}$$

This LDF will be applied to the electron density, the muon density and the combined density of both muons and electrons. The latter is of particular interest since electrons and muons have a practically identical energy loss in scintillator detectors. The values of the parameters r_0, s_1 and s_2 for electrons differs from the ones for muons and the ones for the combined density.

3.2 Polar averaged density

The values of the parameters r_0, s_1 and s_2 also depend on the zenith angle of the shower. The relation will be analyzed on the basis of showers simulated with CORSIKA, all without thinning. The horizontal observation level was set to 10 m; the average altitude of the HiSPARC detectors at SPA. The energy cuts are 0.3 GeV for hadrons and muons and 3 MeV for electrons and gamma's. To obtain a radial LDF the simulated densities are polar averaged for radii within 1000 m. The polar averaged density is binned with a bin width of 1 m (1000 bins). To the binned density a χ^2-fit is applied with the LDF 3.9. In Figure 3.1 the polar averaged electron density, muon density and combined density together with the fit curves are shown for three different showers with energy 10^{15}, 10^{16} and 10^{17} eV, all with zenith angle 15°. In Figure 3.2 similar plots are shown for four different showers with energy 10^{15}, 10^{16}, 10^{17} and 10^{18} eV, all with zenith angle 45°. The figures show that electron and muon densities accurately follow the LDF 3.9. The combined density follows the LDF well for zenith angle 15°, while for zenith angle 45° the LDF underestimates the combined density for radii larger than about 300 m. The deviation is caused by the relatively large muon component. To obtain an accurate LDF for the combined density, the LDF 3.9 has to be modified. Before we turn to the modification we first consider the difference between the polar averaged density and the polar density.

3.3 Polar density

When an inclined air shower strikes a horizontal plane the lateral density in the horizontal plane is elliptic. That is, the iso-density contours are ellipses with the angle of the semi-major axis equal to the azimuth angle. At the same time the horizontal density is decreased by a factor $\cos\theta$ because of the projection. In this section the consequences of polar averaging of an elliptic density for the parameter values are investigated. Without loss of generality the azimuth angle will be conveniently taken equal to zero in the following analysis. Secondly, we will denote the density in the horizontal plane as ν to distinguish it from the density ρ in the plane perpendicular to the shower direction. An elliptic density at a position in the horizontal plane with with polar coordinates r and α is $\cos\theta$ times the density in the front plane at a

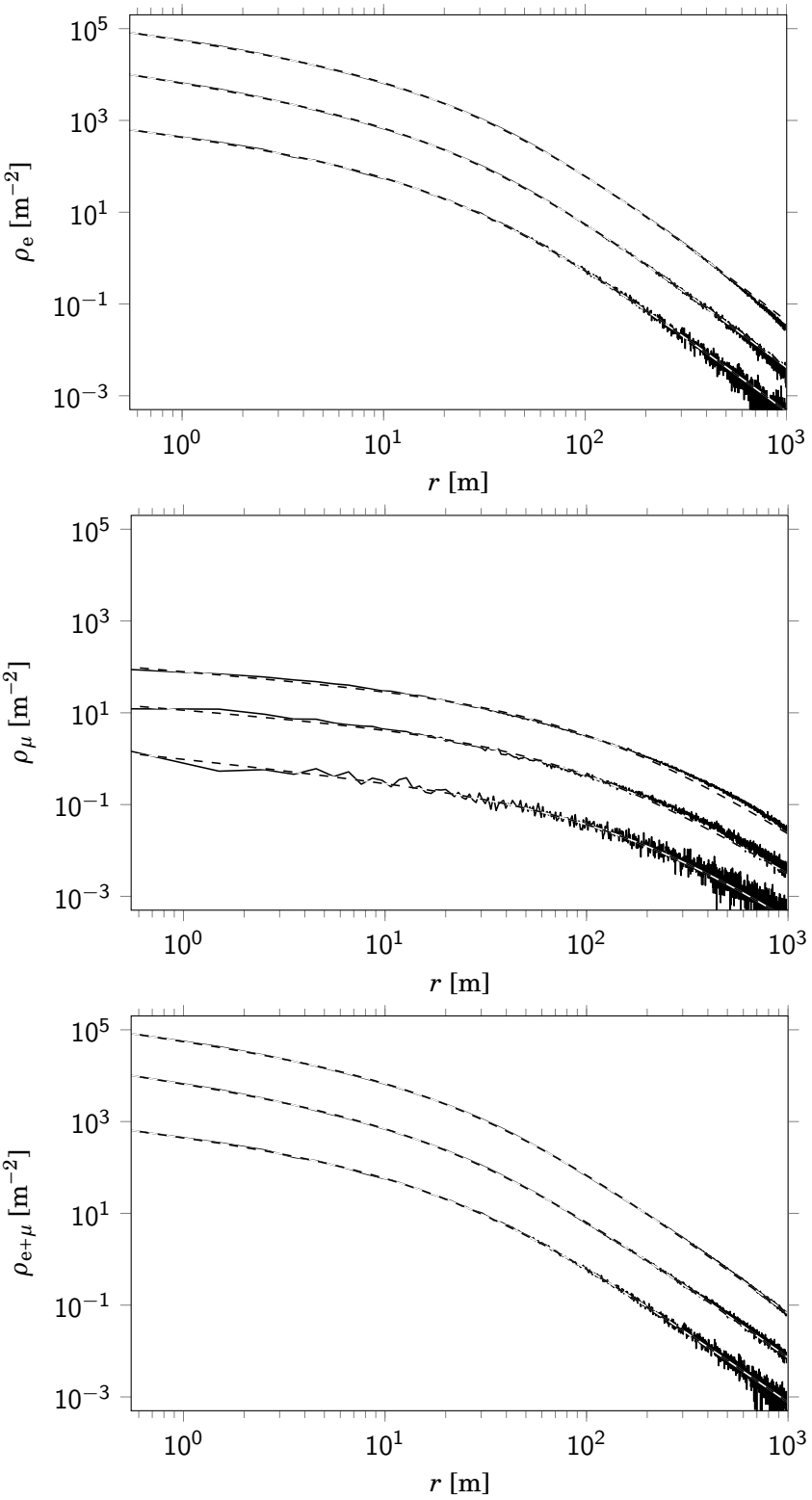

Figure 3.1: Polar averaged electron density (upper panel), muon density (middle panel) and combined density (lower panel) for showers with zenith angle 15° and, in ascending order in the plots, energies 10^{15}, 10^{16} and 10^{17} eV. The dashed curves are the χ^2-fits with the LDF as given in the text.

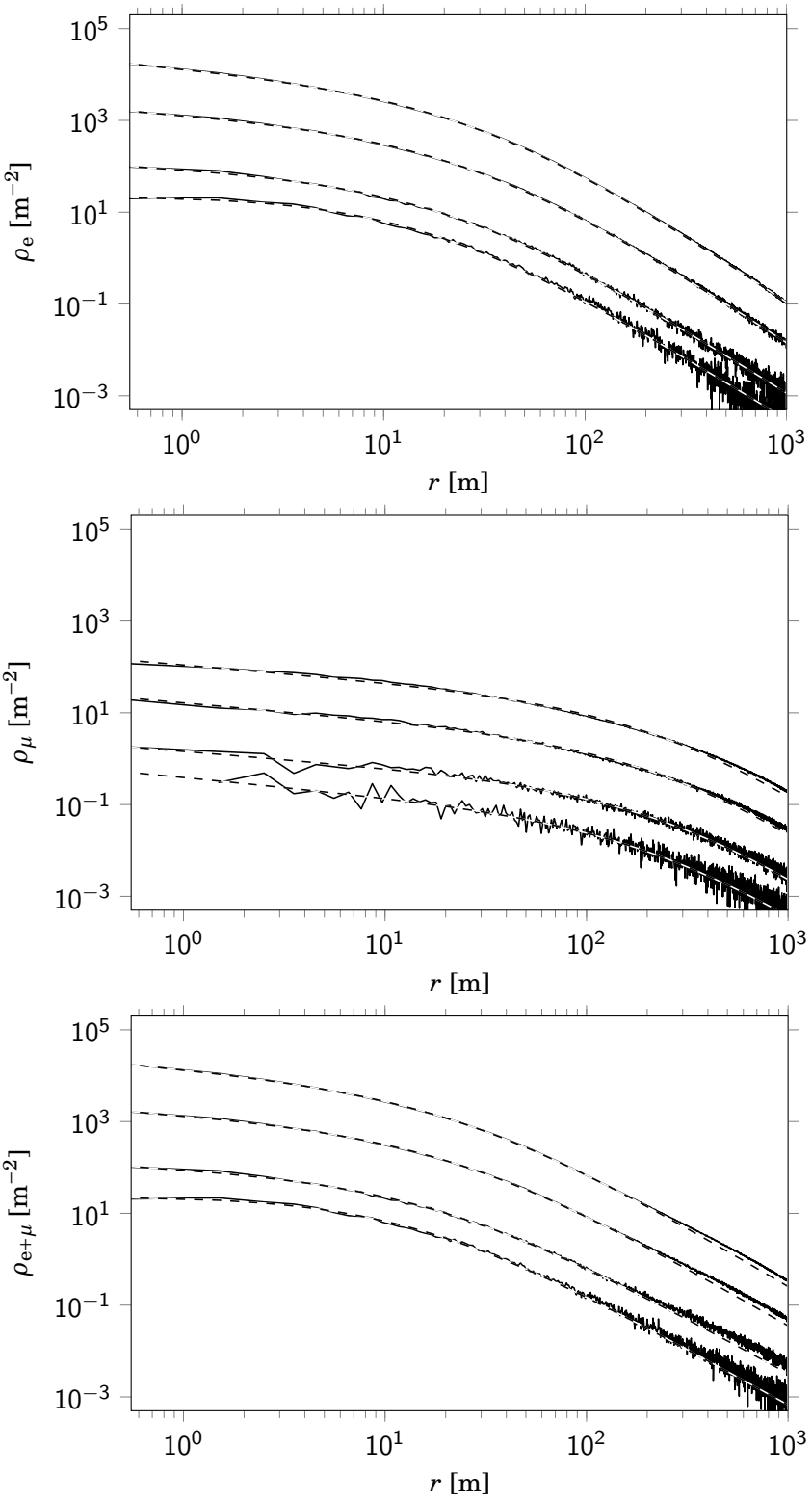

Figure 3.2: Polar averaged electron density (upper panel), muon density (middle panel) and combined density (lower panel) for showers with zenith angle 45° and, in ascending order in the plots, energies 10^{15}, 10^{16}, 10^{17} and 10^{18} eV. The dashed curves are the χ^2-fits with the LDF as given in the text.

radius k, where k is given by [58].

$$k = r\sqrt{1-\sin^2\theta\cos^2\alpha}\ . \tag{3.11}$$

The $\cos\theta$ is from the projection. In short

$$\nu(r,\alpha) = \rho(k)\cos\theta \tag{3.12}$$

For the LDF 3.9 the corresponding elliptic horizontal density for an air shower with zenith angle θ is given by

$$\nu(r,\alpha) = N\cdot\cos\theta\cdot c(s)\cdot\left(\frac{k}{r_0}\right)^{s_1}\left(1+\frac{k}{r_0}\right)^{s_2}\ , \tag{3.13}$$

where k is as given by Equation 3.12.

First the consequences of the substitution of Equation 3.11 for the number of particles will be considered. For a polar symmetric density ρ in the plane of the shower front the number of particles N follows from the surface integral of the density:

$$N = \int_0^{2\pi}\int_0^{\infty}\rho(k)k\,\mathrm{d}k\,\mathrm{d}\alpha = 2\pi\int_0^{\infty}\rho(k)k\,\mathrm{d}k\ . \tag{3.14}$$

For the number of particles in the horizontal plane, N_h we have

$$N_\mathrm{h} = \int_0^{2\pi}\int_0^{\infty}\nu(r,\alpha;\theta)r\,\mathrm{d}r\,\mathrm{d}\alpha\ . \tag{3.15}$$

By means of Equation 3.12 this is

$$N_\mathrm{h} = \cos\theta\int_0^{2\pi}\int_0^{\infty}\rho(k)r\,\mathrm{d}r\,\mathrm{d}\alpha\ , \tag{3.16}$$

where k is a function of r and α as given by Equation 3.11. A change of variables $r\rightarrow k$ leads to the following integral

$$N_\mathrm{h} = \cos\theta\int_0^{2\pi}\int_0^{\infty}\frac{\rho(k)k}{1-\cos^2\alpha\sin^2\theta}\,\mathrm{d}k\,\mathrm{d}\alpha\ . \tag{3.17}$$

The integral can be evaluated exactly. To this end the following Taylor series is considered

$$\frac{1}{1-\cos^2\alpha\sin^2\theta} = \sum_{n=0}^{\infty}\cos^{2n}\alpha\sin^{2n}\theta\ . \tag{3.18}$$

By means of partial integration it follows

$$\int_0^{2\pi}\cos^{2n}\alpha\,\mathrm{d}\alpha = \frac{2n-1}{2n}\int_0^{2\pi}\cos^{2n-2}\alpha\,\mathrm{d}\alpha = 2\pi\sum_{n=0}^{\infty}\frac{(2n)!}{2^n n!}\ . \tag{3.19}$$

Hence,

$$\int_0^{2\pi} \frac{1}{1-\cos^2\alpha\sin^2\theta}\,\mathrm{d}\alpha = 2\pi\sum_{n=0}^{\infty}\frac{(2n)!}{2^n n!}\sin^{2n}\theta\ . \tag{3.20}$$

The latter is the Taylor series of $2\pi/\sqrt{1-\sin^2\theta}$. As a consequence the following identity is obtained:

$$\int_0^{2\pi} \frac{1}{1-\cos^2\alpha\sin^2\theta}\,\mathrm{d}\alpha = \frac{2\pi}{\cos\theta} \tag{3.21}$$

By means of this identity the integration over α leads to

$$N_\mathrm{h} = 2\pi\int_0^{\infty}\rho(k)k\,\mathrm{d}k\ . \tag{3.22}$$

From the comparison with Equation 3.14 we obtain

$$N_\mathrm{h} = N\ . \tag{3.23}$$

As expected, the number of particles is conserved by the projection.

Second the consequences of the substitution Equation 3.11 for the polar averaged density will be considered. The polar averaged density will be denoted as $<\nu>_\alpha$ to distinguish it from the true horizontal density ν. For the polar averaged density it holds

$$<\nu>_\alpha = \frac{1}{2\pi}\int_0^{2\pi}\nu(r,\alpha;\theta)\mathrm{d}\alpha = \frac{\cos\theta}{2\pi}\int_0^{2\pi}\rho(k;\theta)\mathrm{d}\alpha\ . \tag{3.24}$$

With k as given by Equation 3.11 and ρ as given by Equation 3.9 this is, explicitly,

$$<\nu>_\alpha = N\cdot c(s)\cdot\frac{\cos\theta}{2\pi}\int_0^{2\pi}\left(\frac{r\sqrt{1-\sin^2\theta\cos^2\alpha}}{r_0}\right)^{s_1}\left(1+\frac{r\sqrt{1-\sin^2\theta\cos^2\alpha}}{r_0}\right)^{s_2}\mathrm{d}\alpha\ . \tag{3.25}$$

This integral is evaluated numerically for different r. The result is compared to the density ρ we started with. For $r_0 = 30\,\mathrm{m}$, $s_1 = -0.592+0.229\theta$ and $s_2 = -3.157+0.222\theta$ the ratio of $<\nu>_\alpha$ and $\rho\cos\theta$ is plotted for zenith angles 0° through 52.5° in steps of 7.5°, see Figure 3.3. The expressions given for r_0, s_1 and s_2 are applied just because we will arrive at them at the end of this section. For other values for the parameters, $r_0 = 40\,\mathrm{m}$, $s_1 = -0.5$ and $s_2 = -3$ for instance, the curves in Figure 3.3 are practically identical.

The polar averaged density overestimates the projected density $\rho\cos\theta$. The corrected density function is obtained by dividing the polar averaged density by the ratio shown in Figure 3.3. This method is applied to a set of simulated showers. The energies of the simulated showers are 10^{15}, 10^{16}, 10^{17} and 10^{18} eV. The zenith angles of the showers range from 7.5° through 60° in steps of 7.5°. The parameters r_0, s_1 and s_2 are determined for 10 simulated showers for each of the energy-zenith angle entries considered. For the largest energy considered, 10^{18} eV, the

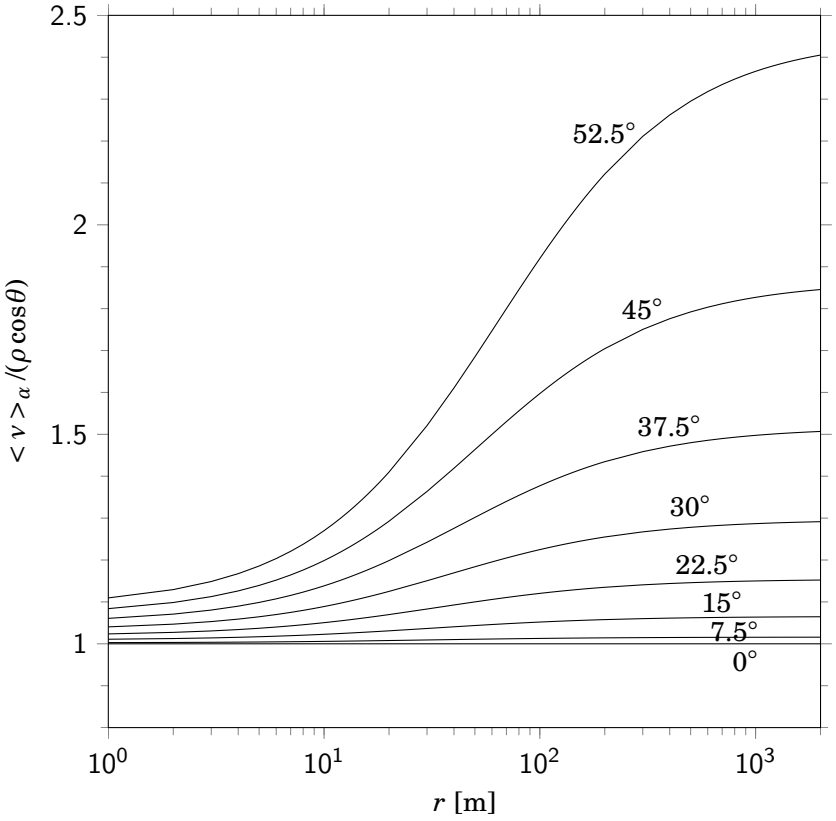

Figure 3.3: The ratio of polar average density and horizontal density for zenith angles 0° through 52.5° in steps of 7.5° for parameter values as given in the text.

library of simulated showers was at the moment of the investigation limited to 10 showers for zenith angle 60°, 10 for zenith angle 52.2°, 8 for zenith angle 45°, 5 for zenith angle 37.5° and none for smaller zenith angles. The set of showers was initially intended for another purpose and the parameters were determined without the correction for the polar averaging. Since the polar averaged densities for electrons and for muons are accurately described by the LDF 3.9 we apply the correction to the sum of them. The result is fitted with a modified LDF. For the modification we take inspiration from the Greisen function [59]. That is, we multiply the LDF by $(1+\frac{r}{g\cdot r_0})$. With this modification the LDF we will apply is

$$\rho_{e+\mu} = N_{e+\mu}\cdot c\cdot\left(\frac{r}{r_0}\right)^{s_1}\left(1+\frac{r}{r_0}\right)^{s_2}\left(1+\frac{r}{g\cdot r_0}\right). \tag{3.26}$$

For this LDF the normalization constant is given by

$$c = \frac{g\Gamma(-s2)}{2\pi r_0^2\Gamma(s_1+2)\Gamma(-s_1-s_2-3)\cdot[2+s_1-g\cdot(3+s_1+s_2)]}. \tag{3.27}$$

In the original Greisen function $g = 11.4$. It is found empirically that good fits with the three parameters, r_0, s_1 and s_2 are obtained if g is taken equal to $11.4\cos^2\theta$. The results are shown in Figure 3.4.

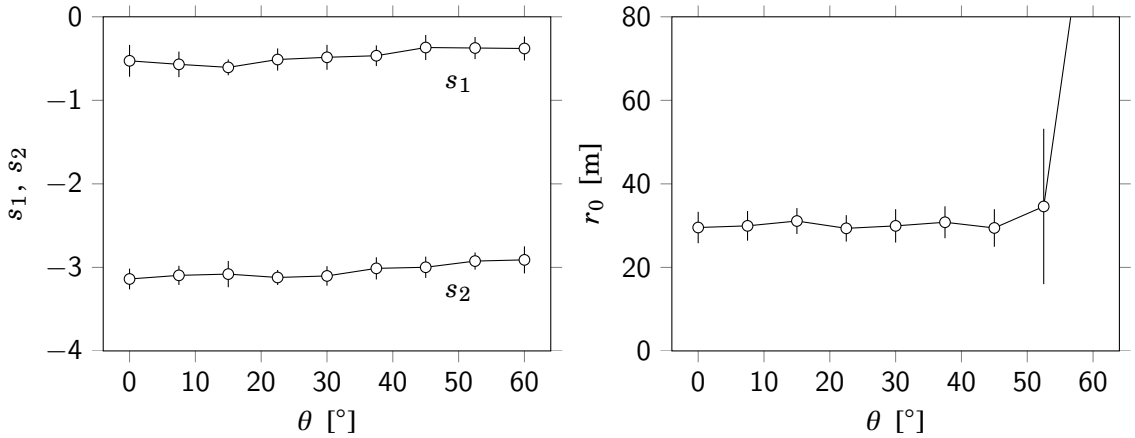

Figure 3.4: The parameters s_1 and s_2 (left panel) and r_0 (right panel) versus zenith angle.

The variation of the parameters with zenith angle is very small. This implies that the density perpendicular to the shower direction is practically concentrical. As far as the parameters vary with zenith angle the relation is almost linear, except for r_0 which tends to larger values and larger variations in the neighborhood of 60°. For $\theta \leq 52.5°$ the parameter r_0 is approximately a constant equal to 30 m. Linear approximations for the other parameters are:

$$s_1 = -0.592 + 0.229\theta \tag{3.28}$$

and

$$s_2 = -3.157 + 0.222\theta\ , \tag{3.29}$$

with θ in radians. These equations were therefore used for the plots in Figure 3.3.

3.4 The shift in elliptic densities

The lateral density of inclined showers are approximately concentrical in the plane perpendicular to the shower axis. The projection on a horizontal plane of observation leads to elliptic iso-density contours. After the early part of an inclined air shower reaches a horizontal surface the late part of the shower will attenuate further because of atmospheric attenuation. As a consequence the center of the elliptic horizontal density will be shifted with respect to the shower core. This effect can be modeled. The analysis has been published [60]. The publication is shown hereafter.

3.5 Summary

The horizontal combined density of an inclined air shower is described by

$$\nu_{e+\mu}(r,\alpha) = N_{e+\mu} \cdot \cos\theta \cdot c \cdot \left(\frac{k}{r_0}\right)^{s_1} \left(1+\frac{k}{r_0}\right)^{s_2} \left(1+\frac{k}{g \cdot r_0}\right) , \tag{3.30}$$

where the normalization constant is given by Equation 3.27, where s_1 and s_2 slightly depend on θ as given by Equation 3.28 and Equation 3.29 respectively, where is taken $r_0 = 30\,\mathrm{m}$ and $g = 11.4 \cdot \cos^2\theta$ and where k is related to r as given by Equation 3.11. The main conclusion of the shift analysis is that the shift can be accounted for by modifying Equation 3.11 to

$$k = -Sr\cos\alpha\sin(2\theta) + r\sqrt{1-\cos^2\alpha\sin^2\theta} , \tag{3.31}$$

where S is a constant, $S \approx 0.058$.

The shift has little consequences for the total number of particles. The surface integral is now given by

$$N_h = \cos\theta \int_0^{2\pi} \int_0^{\infty} \frac{\rho(k)k}{(-S\cos\alpha\sin(2\theta) + \sqrt{1-\cos^2\alpha\sin^2\theta})^2} \,\mathrm{d}k\,\mathrm{d}\alpha . \tag{3.32}$$

The integral

$$I = \int_0^{2\pi} \frac{1}{(-S\cos\alpha\sin(2\theta) + \sqrt{1-\cos^2\alpha\sin^2\theta})^2} \,\mathrm{d}\alpha \tag{3.33}$$

is evaluated numerically. For $S = 0.058$ the result of the numerical evaluation is

$$I = \frac{2\pi}{\cos\theta}\left(1+\mu(\theta)\right) , \tag{3.34}$$

where $\mu(\theta)$ grows from 0 for $\theta = 0$ to 0.02 for $\theta = 90°$. In good approximation $\mu \approx 0.0205\sin^2\theta$. For the situation with a shift we thus find that the number of particles in the horizontal plane is slightly larger than in the front plane:

$$N_h \approx N \cdot \left(1 + 0.0205\sin^2\theta\right) . \tag{3.35}$$

That $N_h > N$ for the shifted density does not have to be a surprise. If the attenuation decreases the number of particles at the late part of the shower to, say, half its value, then the reverse process implies an increase of the number of particles at the early part of the shower to twice its value. On average the number of particles in the horizontal plane will then be 25 % larger than in the front plane. In reality the differences are not that large. As follows from Equation 3.35 the difference is smaller than 1 % for $\theta < 45°$. The factor $\mu(\theta)$ is therefore negligible for polar averaging.

4

HiSPARC equipment

4.1 HiSPARC hardware

The HiSPARC experiment is intended to study cosmic-rays by detecting extensive air showers, for educational as well as scientific purposes. The HiSPARC project consists of a network of over 100 detection stations positioned on the roofs of high schools or other buildings. Each detector consists of a plastic scintillator of 100 cm× 50 cm×2 cm. The detection area therefore is 0.5 m^2. The scintillator is glued to a plastic 'fishtail' light guide. The narrow end of the light guide is glued to a plastic connection socket which in turn is connected, with transparent double-sided tape, to a photo multiplier tube (PMT). In Figure 4.1 a schematic impression of a HiSPARC detector is shown.

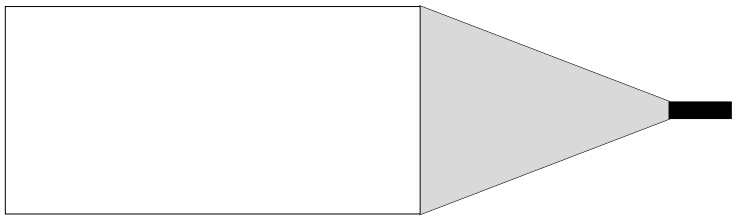

Figure 4.1: Schematic detector layout: scintillator (white), light guide (gray) and PMT (black).

Most stations consists of two detectors, some of four. Each station is provided with a global positioning system (GPS) receiver. The stations at the Science Park Amsterdam (SPA) cluster have four detectors. Some stations have three detectors arranged at the corners of an equilateral triangle with 10 m sides and with the fourth detector in the barycenter, see left side of Figure 4.2. Other stations have the detectors arranged in a 60° diamond with 10 m sides, see right side of Figure 4.2.

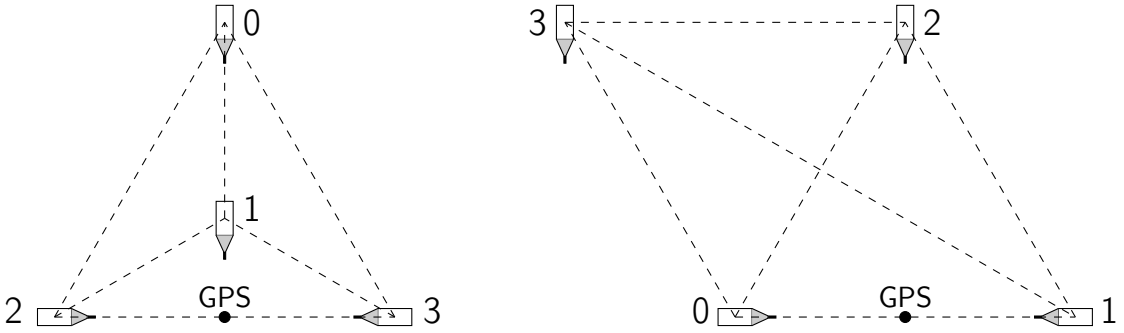

Figure 4.2: Schematic layout for the triangle station (left) and the diamond station (right). The black dot is the position of the GPS receiver.

The scintillator and the light guide are wrapped in silver foil and then in plastic pond liner.

Figure 4.3: Taping silver foil around a detector. Photo courtesy of A.P.L.S. de Laat.

The complete detector is placed in a ski-box on the roof of a building. After the connection with a power and signal cable it is ready for use.

The scintillator consists of polyvinyltoluene (the base) doped with anthracene (the fluor). When a charged particle passes the scintillator it will lose energy to the base by ionization. The absorbed energy will be re-emitted in the form of light. For a minimum ionizing particle (MIP) on average 123 photoelectrons are detected at the PMT.

Figure 4.4: Ski-boxes on the roof of a building at SPA. Photo courtesy of A.P.L.S. de Laat.

4.2 Data acquisition

A HiSPARC-II or HiSPARC-III unit supplies the high voltage for the PMT and acquires the signal from the PMT. Each HiSPARC-II or HiSPARC-III unit controls two PMT's. So, for four-detector stations two units are required. One unit is connected to a GPS detector for time stamping a PMT signal. The PMT signal is converted with a 4096 channel Analog Digital Converter (ADC) to a digital value. The signal range is between +0.133 V and -2.222 V. This is about 0.57 mV per ADC count. For a single MIP the modal pulse height is 220 ADC counts or 125 mV. A HiSPARC unit houses a 200 MHz digital clock. The HiSPARC units contain four ADC's, two for each channel. For each PMT the conversion occurs in the one channel on the leading and in the second channel on the trailing edge of a clock pulse. In this way the two ADC's alternately sample every 5 ns, with a 2.5 ns offset between the two. The PMT signal in each channel is therefore sampled with an effective frequency of 400 MHz. From the moment the first particles of a cosmic air shower front strike a detector it takes, depending on the size of the shower, hundreds of nanoseconds until the last particle has passed the scintillator. Because the effective sampling period of 2.5 ns is much smaller, the time evolution of the sampled signal, the trace, more or less represents the shape of the shower front.

Every detector of a station can register a trace. A single trace, that is a trace in one of the four detectors of a station, may be caused by a background muon which should not be stored. As soon as two high signals of more than 70 mV or three signals larger than 30 mV are detected in a station, the station is 'triggered' and the signals are considered to be due to an air shower and registered as an 'event'. About 99 % of the events are triggered by the 'two high' threshold. The traces of detector 0 through 3 are usually colored black, red, green and blue respectively. In Figure 4.5 an example is shown.

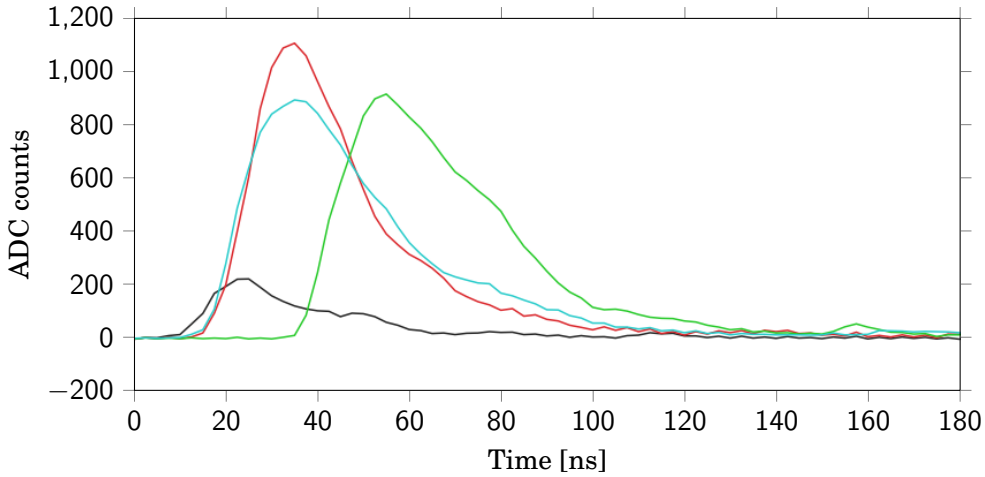

Figure 4.5: Traces of an event with a signal in all four scintillator plates of SPA station 506 at 2015-07-28 00:00:17.

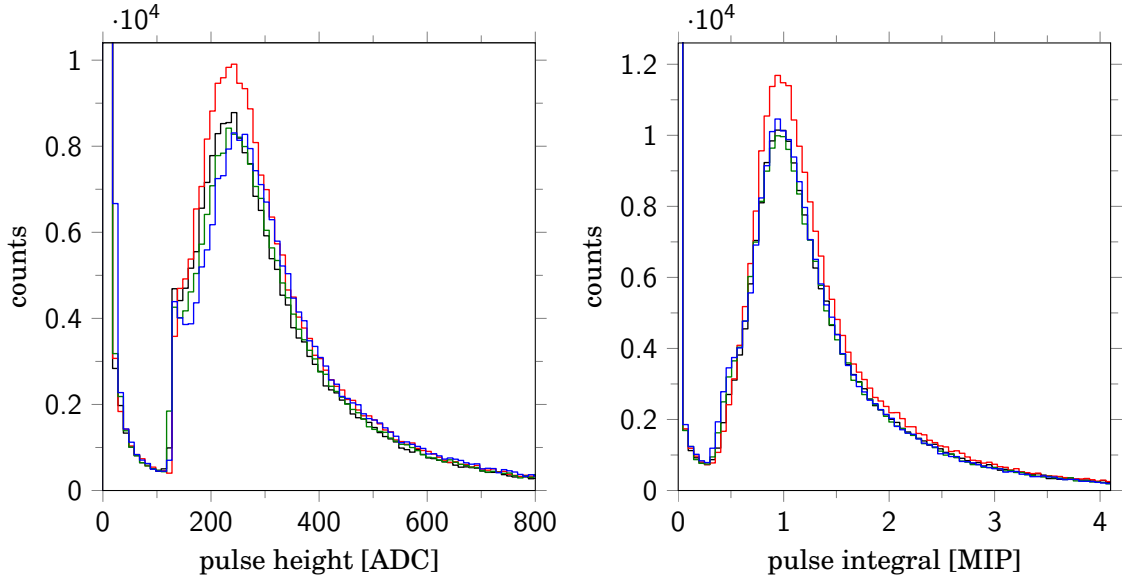

Figure 4.6: Pulse height (left) and pulse integral (right) distributions for the four detectors 0 (black), 1 (red), 2 (green) and 3 (blue) of station 501. Data taken between 2014-09-12 00:00:00 and 2014-09-19 00:00:00. In the pulse height diagram the 70 mV trigger level causes the vertical 'jump' at 125 ADC counts. The part of the distribution left of the jump is caused by the small energy losses of gammas.

Pulse height and pulse integral distributions for station 501 at SPA are shown in Figure 4.6. The peak of the pulse height diagram is at about 240 ADC counts, which corresponds to 135 mV PMT signal. The peak of the pulse integral distribution is in the neighborhood of 2800 ADC ns. As will be shown further on the peak is related to the most probable energy loss of a single particle, a so-called minimum ionizing particle (MIP). The pulse integral therefore is usually expressed in units of MIP where 1 MIP corresponds to the pulse integral value of the peak of the pulse integral distribution.

The whole process is controlled by a LabView program running on a personal computer dedicated to a station. A Python monitor program controls the local storage as well as the transfer of the data to the central data storage at Nikhef. There the data is adapted and made accessible, for instance via the public database. The status of the HiSPARC stations is monitored by a Nagios network control system [61]. In case of a malfunctioning detector or station, the problems can be solved by the local user or remotely by the central HiSPARC administration. Finally, some stations are equipped with a weather station supplying weather data like temperature, air pressure and humidity. For these stations the weather data are also registered, stored and sent to the central data storage.

4.3 HiSPARC software

For a quick look there is the HiSPARC Public Database [62]. It gives an overview of all the stations, their names and numbers, the clusters they reside in. For each station it gives by day an event histogram, pulse height histogram, pulse integral histogram and, if available, data about the air pressure and temperature. It also gives, for each station, information of the actual status and the history of PMT voltages, PMT currents, timing offsets and Global Positioning System (GPS) positions. Also a coincidence histogram, for the full network, can be obtained together with a histogram of the coincidence size, the number of stations participating in the coincidence. Information on clusters, stations, plates, pulse heights, weather, etc., can also be retrieved from the HiSPARC API [63]. Data of events can be downloaded and plotted directly with HiSPARC data retrieval [64]. A user can choose the type of plot, the variables and a function with which to fit the data. The fits are based on linear regression. The fit equation, with the numerical values for the coefficients and the correlation are given below the plot diagram. As an example a histogram of the event rate for station 501 on an arbitrary day is shown in Figure 4.7. The mean value of the event rate, $0.679\,\mathrm{s}^{-1}$, means that about 60 000 events are registered for station 501 per day. As another example a scatter plot of pulse height versus pulse integral is shown in Figure 4.8.

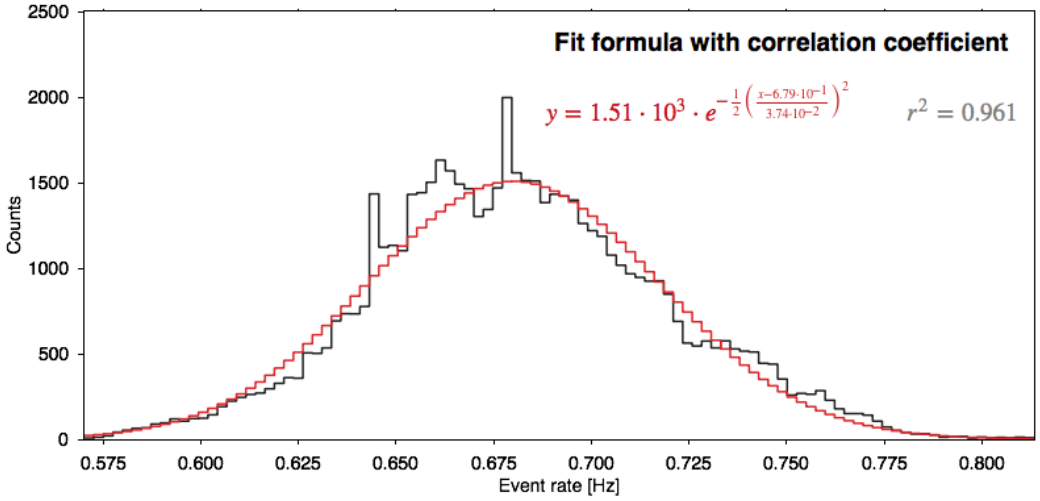

Figure 4.7: Histogram of event rates between 2015-07-28 00:00 and 2015-07-29 00:00 for station 501 and the fit results.

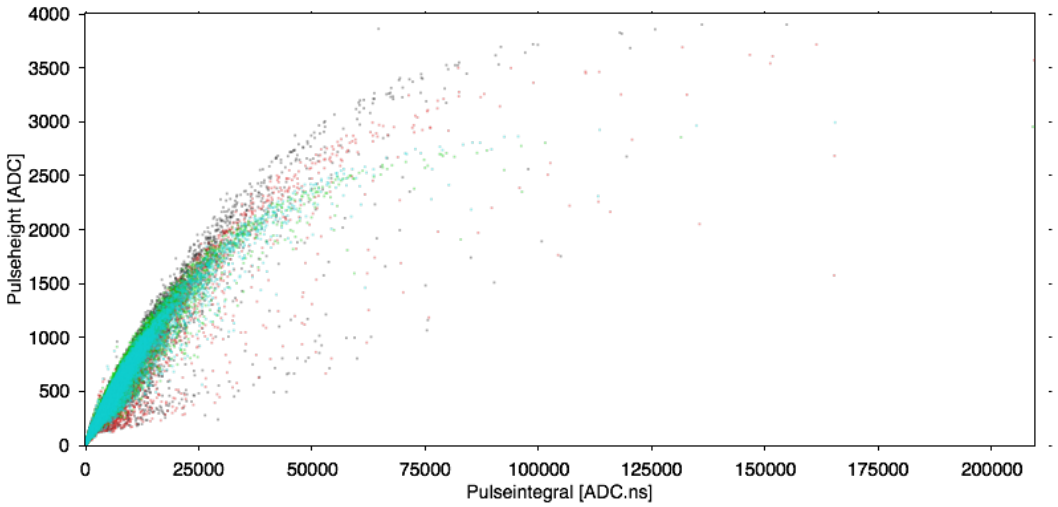

Figure 4.8: Scatter plot of pulse heights versus pulse integrals of events between 2013-08-28 00:00 and 2013-08-29 00:00 for the four detectors of station 501.

Data of events and coincidences can be downloaded by means of a data download form resulting in a CSV file [65]. Most important for data analysis is the Python package SAPPHiRE [45]. It contains

Data download Events and coincidences from the event summary database.

Data analysis Reconstruction of directions and sizes of showers.

Simulations The response of stations to simulated showers.

For the simulations showers can be accessed which have been simulated without thinning with CORSIKA-v7.4. The simulated particles hitting the ground can be thrown on a group of stations. Each simulated shower is used multiple throws. To this end the configuration of detectors is randomly translated and rotated, while the positions of the ground particles are unaltered. For each throw detector signals are synthesized by drawing randomly from an energy loss distribution for each charged lepton that passes a detector. The energy loss distribution implemented in SAPPHiRE is described in the next sections.

4.4 Stopping power

When a charged particle passes through matter it will lose energy by collisions (ionization) and by radiation (bremsstrahlung). The mean rate of energy loss is called the stopping power. Since bremsstrahlung photons leave the scintillator without substantial interaction, we restrict ourselves to the collisions. For electrons and muons incoming with velocity v the collision stopping power is given by the Bethe-Bloch equation [66, 67]:

$$-\langle\frac{\mathrm{d}E}{\mathrm{d}x}\rangle = \frac{K}{2}\frac{Z}{A}\frac{1}{\beta^2}\left[\ln\frac{2m_\mathrm{e}c^2\beta^2\gamma^2T_\mathrm{max}}{I^2} + F - \delta - C^*\right] , \tag{4.1}$$

where E is the energy in MeV and x is the depth in $\mathrm{g\,cm^{-2}}$. Other parameters are the velocity of light c, the relative velocity $\beta = \frac{v}{c}$, the relativistic factor $\gamma = 1/\sqrt{1-\beta^2}$, the electron mass m_e, the mean excitation energy I of the matter, the atomic number Z and the atomic mass A of the matter. The constant K is given by

$$K = 4\pi N_A r_\mathrm{e}^2 m_\mathrm{e} c^2 , \tag{4.2}$$

where N_A is Avogadro's number and r_e is the classical electron radius in cm. Numerically $K \approx 0.307\,\mathrm{MeV\,cm^2}$.

The stopping power is different for muons and electrons in that the quantity F and the maxi-

mum kinetic energy transfer in one collision $T_{\max}$ are different for muons and electrons:

$$F(\gamma) = \begin{cases} -2\beta^2 & \text{, for } \mu^{\pm} \\ \frac{1}{\gamma^2}\left(1-(2\gamma-1)\ln 2+\frac{(\gamma-1)^2}{8}\right) & \text{, for } e^- \\ 2\ln 2-\frac{\beta^2}{12}\left(23+\frac{14}{\gamma+1}+\frac{10}{(\gamma+1)^2}+\frac{4}{(\gamma+1)^3}\right) & \text{, for } e^+ . \end{cases} \tag{4.3}$$

and

$$T_{\max} = \begin{cases} \frac{2m_e c^2\beta^2\gamma^2}{1+2\gamma m_e/m_\mu+(m_e/m_\mu)^2} \approx \frac{2m_e c^2\beta^2\gamma^2}{1+0.00964\gamma} & \text{, for } \mu^{\pm} \\ \\ \frac{m_e c^2(\gamma-1)}{2} & \text{, for } e^{\pm} . \end{cases} \tag{4.4}$$

For $\gamma > 10$ the values of F are close to their limit values:

$$\lim_{\gamma\to\infty} F(\gamma) = \begin{cases} -2 & \text{, for } \mu^{\pm} \\ \frac{1}{8} & \text{, for } e^- \\ 2\ln 2-\frac{23}{12} & \text{, for } e^+ . \end{cases} \tag{4.5}$$

All the other parameters in the stopping power are identical for electrons and muons. The density correction δ is given by

$$\delta = \begin{cases} 2\ln(\hbar\omega_p/I)+2\ln\beta\gamma-1 & \text{, if } \beta\gamma \geq 100 \\ 2\ln(\hbar\omega_p/I)+2\ln\beta\gamma-1+\delta^* & \text{, if } 1<\beta\gamma<100 \\ 0 & \text{, if } \beta\gamma \leq 1 , \end{cases} \tag{4.6}$$

where $\hbar\omega_p$ is the plasma energy. The latter equation is similar to Sternheimer's parameterization [68]. For the factor δ^* we apply

$$\delta^* \approx 0.46\cdot\left(2-\log_{10}(\beta\gamma)\right)^{2.8} , \tag{4.7}$$

on the basis of scintillator data [69]. The plasma energy is given by

$$\hbar\omega_p = 28.816\cdot\sqrt{\rho\cdot\langle Z/A\rangle} , \tag{4.8}$$

where ρ is the density of the material. Polyvinyltoluene molecules consists of carbon, C_{12}^6, and hydrogen, H_1^1, atoms in the ratio 9:10. The corresponding values for Z and A then are $(9\cdot 6+10\cdot 1)/19 \approx 3.37$ and $(9\cdot 12+10\cdot 1)/19 \approx 6.21$ respectively. The Z/A ratio for polyvinyltoluene then equals 0.54. The mean Z/A ratio for polyvinyltoluene based scintillator material will be close to it. Its precise value is 0.54141 [70]. Since the density of polyvinyltoluene is $1.03\,\mathrm{g\,cm^{-3}}$, the plasma energy is 21.5 electronvolt. The mean excitation energy for polyvinyltoluene is $I = 64.7\,\mathrm{eV}$ [71]. With the substitution of these numerical values the density correction is

approximately given by:

$$\delta = \begin{cases} 2\ln\beta\gamma - 3.2 & \text{, if } \beta\gamma \geq 100 \\ 2\ln\beta\gamma - 3.2 + 0.0443 \cdot \left(4.61 - \ln(\beta\gamma)\right)^{2.8} & \text{, if } 1 < \beta\gamma < 100 \\ 0 & \text{, if } \beta\gamma \leq 1\,, \end{cases} \tag{4.9}$$

The parameter C^* is given by $C^* = 2C/Z$, where C is the shell correction given by [67]:

$$\begin{aligned} C = &\left(\frac{0.422377}{(\beta\gamma)^2} + \frac{0.0304043}{(\beta\gamma)^4} - \frac{0.00038106}{(\beta\gamma)^6}\right) \cdot \frac{I^2}{10^6} \\ &+ \left(\frac{3.850190}{(\beta\gamma)^2} + \frac{0.1667989}{(\beta\gamma)^4} - \frac{0.00157955}{(\beta\gamma)^6}\right) \cdot \frac{I^3}{10^9}\,. \end{aligned} \tag{4.10}$$

For polyvinyltoluene this is

$$C \approx \left(\frac{0.0028}{(\beta\gamma)^2} + \frac{0.000058}{(\beta\gamma)^4} - \frac{0.0000020}{(\beta\gamma)^6}\right)\,. \tag{4.11}$$

For $\beta\gamma > 0.2$ the shell correction is practically equal to $0.0028 \cdot (\beta\gamma)^{-2}$. For $\beta\gamma > 1$ it is already of negligible order.

In Figure 4.9 the stopping power is plotted against $\beta\gamma$.

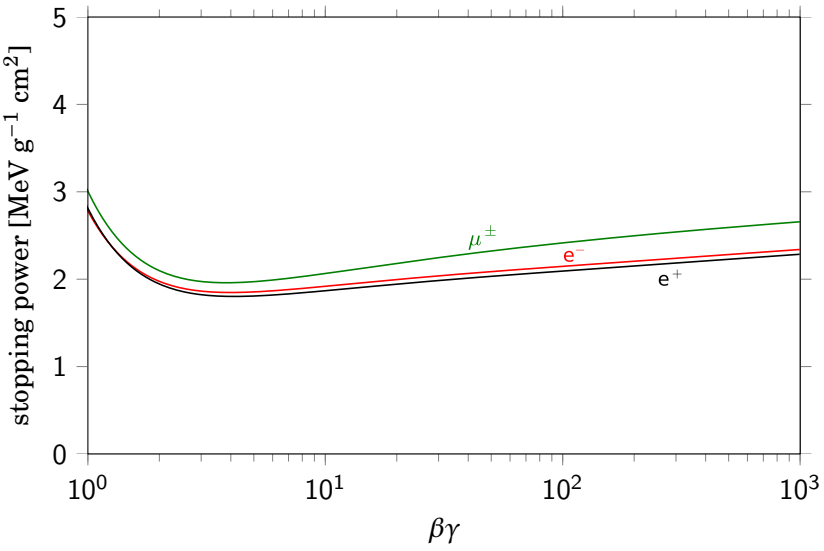

Figure 4.9: Collision stopping power for electrons and muons in polyvinyltoluene according to the Bethe-Bloch equation.

The radiation (bremsstrahlung) stopping power is not shown in Figure 4.9. The total stopping power is practically equal to the collision stopping power for $\beta\gamma < 10$. For $\beta\gamma > 10$ the total stopping power increases with respect to the collision stopping power because of the increas-

ing radiation stopping power. Since the bremstrahlung photons leave the scintillator without substantial interaction, the curves in Figure 4.9 represent the actual average energy deposit in the scintillator. Values for the stopping power for polyvinyltoluene, including bremstrahlung for highly relativistic energies, have been tabulated [72].

The curves in Figure 4.9 are mean energy losses. The energy losses are distributed and the most probable energy losses are smaller than the mean energy losses.

4.5 Energy loss distribution

The mean energy loss is the stopping power times the travelled depth x_0 in $\mathrm{g\,cm^{-2}}$:

$$\bar{\Delta} = -\langle \frac{\mathrm{d}E}{\mathrm{d}x} \rangle x_0 = \xi \left[\ln \frac{2m_e c^2 \beta^2 \gamma^2 T_{\max}}{I^2} + F - \delta - C^* \right] , \tag{4.12}$$

where ξ in MeV is given by

$$\xi = \frac{K}{2} \frac{Z}{A} \frac{1}{\beta^2} x_0 . \tag{4.13}$$

For vertical electrons and muons passing a scintillator plate with thickness 2 cm and density $1.03\,\mathrm{g\,cm^{-3}}$ the depth is $x_0 = 2.06\,\mathrm{g\,cm^{-2}}$. For $\beta \to 1$ the parameter ξ obtains its asymptotic value 0.171 MeV. Of importance is the distribution of energy losses. The description of ionization fluctuations is characterized by the significance parameter κ [73]:

$$\kappa = \frac{\xi}{T_{\max}} . \tag{4.14}$$

In different domains the fluctuations in the energy losses are described by different 'straggling' functions. Usually three domains are distinguished. For $\kappa > 10$ there is a Gaussian distribution of energy losses [74]. This domain does not occur in scintillators with thickness of 2 cm. For $0.01 < \kappa < 10$ the straggling is described by the Vavilov function [75]. For $\kappa < 0.01$ the Landau distribution is of application [76]. In HiSPARC scintillators the value $\kappa = 0.01$ corresponds to the value $\beta\gamma = 68$ for incoming electrons and to the value $\beta\gamma = 4.3$ for incoming muons. This corresponds to an energy of 35 MeV for electrons and of 0.47 GeV for muons. In Figure 4.10 the cumulative fractions of $\beta\gamma$ are shown for electrons and muons at sea level in a simulated shower. For the 10^{15} eV shower the number of electrons and muons is $6.3 \cdot 10^4$ and $1.5 \cdot 10^4$ respectively. For the 10^{16} eV shower the number of electrons and muons is $7.5 \cdot 10^5$ and $7.8 \cdot 10^4$ respectively. Despite the differences in number the cumulative fractions are practical identical. Since the muons among the groundparticles almost all have $\beta\gamma > 4.3$ the Landau distribution is applicable to them. About 50 % of the electrons among the ground particles have $\beta\gamma > 68$ for which a Landau distribution holds. For the electrons with $8 < \beta\gamma < 68$ the energy losses are described by the Vavilov distribution [75]. From inspection by means of the Vavilov distribution

it is found that the energy loss distribution for electrons with $8 < \beta\gamma < 68$ slightly deviates from the Landau distribution, the deviation being smaller for larger $\beta\gamma$. For the Monte Carlo we accept a small deviation in a small percentage of electrons and describe all energy losses with a Landau distribution.

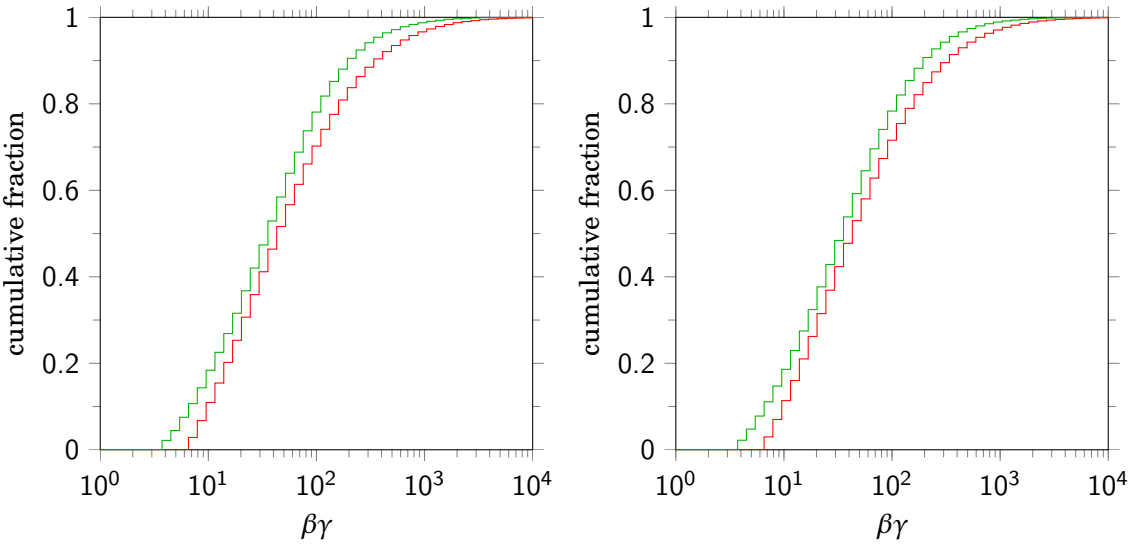

Figure 4.10: Distribution of the $\beta\gamma$ values at sea level for electrons (red) and muons (green) for a vertical 10^{15} eV shower (left) and 10^{16} eV shower (right) with zenith angle 15°.

The Landau probability distribution of energy losses Δ in MeV is given by

$$f(\Delta) = \frac{1}{\xi}\phi(\lambda)\,, \tag{4.15}$$

where ϕ is the universal Landau function. Its argument λ is related to Δ as follows [77]:

$$\lambda = \frac{\Delta - \bar{\Delta}}{\xi} - \ln\left(\frac{\xi}{T_{\max}}\right) - \beta^2 - 1 + C_E\,, \tag{4.16}$$

where C_E is the Euler-Mascheroni constant, $C_E \approx 0.577$. By means of Equation 4.1 the expression for λ can also be written in the form

$$\lambda = \frac{\Delta}{\xi} - \ln\frac{2m_e c^2\beta^2\gamma^2\xi}{I^2} - 1 + C_E - \beta^2 - F + \delta\,. \tag{4.17}$$

The Landau probability density function $\phi(\lambda)$ has a maximum for $\lambda \approx -0.223$ [78]. The corresponding value for the most probable energy loss, Δ_p, then follows from Equation 4.17:

$$\Delta_p = \xi\left(\ln\frac{2m_e c^2\beta^2\gamma^2\xi}{I^2} + 0.200 + F + \beta^2 - \delta\right)\,. \tag{4.18}$$

With the substitution of $F = -2\beta^2$ for muons the latter expression reduces to its familiar form [48]:

$$\Delta_p = \xi \left(\ln \frac{2m_e c^2 \beta^2 \gamma^2 \xi}{I^2} + 0.200 - \beta^2 - \delta \right) , \tag{4.19}$$

Substituting the asymptotic values and approximating β by 1, we obtain the following relation between λ and the energy loss Δ:

$$\lambda = \begin{cases} 5.85\Delta - 20.18 & \text{, for } \mu^{\pm} \\ 5.85\Delta - 22.29 & \text{, for } e^{-} \\ 5.85\Delta - 21.65 & \text{, for } e^{+} . \end{cases} \tag{4.20}$$

For the most probable energy loss we obtain:

$$\Delta_p = \begin{cases} 3.41\,\text{MeV} & \text{, for } \mu^{\pm} \\ 3.77\,\text{MeV} & \text{, for } e^{-} \\ 3.66\,\text{MeV} & \text{, for } e^{+} . \end{cases} \tag{4.21}$$

The original expression for the Landau probability density function ϕ is the following complex integral [76]

$$\phi(\lambda) = \frac{1}{2\pi i} \int_{\sigma - i\infty}^{\sigma + i\infty} e^{u(\lambda + \ln u)} \, \mathrm{d}u \ , \quad \sigma \geq 0 . \tag{4.22}$$

It can be transformed into real integral representations each of which suffers from bad convergence due to oscillations in certain domains of λ [79]. For $\lambda > 0$ we have used the following integral [79]:

$$\phi(\lambda) = \frac{1}{\pi} \int_0^{\infty} e^{-u(\lambda + \ln u)} \sin(\pi u) \, \mathrm{d}u . \tag{4.23}$$

For $\lambda < 0$ we have used [77]:

$$\phi(\lambda) = \frac{1}{\pi} \int_0^{\infty} e^{(-\pi u/2)} \cos(u(\lambda + \ln u)) \, \mathrm{d}u . \tag{4.24}$$

By means of the latter two expressions the energy loss distribution for vertical incidence is plotted in Figure 4.11.

As required for a probability function the area under the Landau probability density curve is equal to unity. The corresponding Landau distribution, the cumulative probability, can be approximated by means of asymptotic series expansions [78]. However, the Landau probability density function has no mean and therefore also no variance. A mean value for the energy loss is obtained if the total energy loss is limited to a maximum: $\Delta_{\max}$ [73].

For highly asymmetric distributions like the Landau distribution one usually describes them with the most probable energy and the full width of half maximum (FWHM) of the distribution.

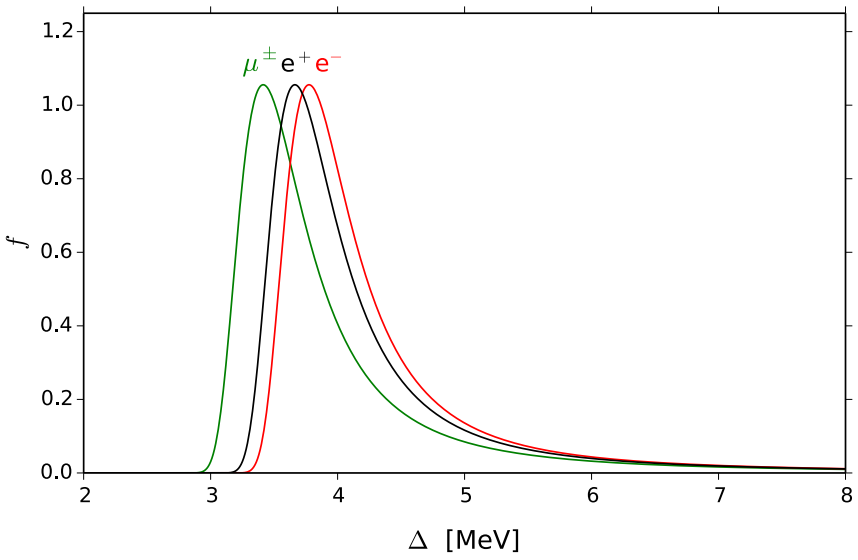

Figure 4.11: Energy loss distribution for vertical electrons and muons for $\kappa < 0.01$.

There are several contributions to the width of the distribution of PMT signals. Approximating the peak of a distribution by a Gauss distribution, the different contributions to the width can be 'added' in the same way as is done for normal distributions: $\sigma = \sqrt{\sigma_1^2 + \sigma_2^2 + \ldots}$. While we keep track of contributions to the width of a distribution, we will translate it each time to the σ of a Gaussian curve. For a Gauss curve the FWHM is about 2.35 times σ. To translate the FWHM of a distribution to a Gauss curve with $\mu = 1\,\text{MIP}$, it is convenient to consider the relative width w, which is the ratio between the FWHM and the most probable energy loss. Simulating signals independent of the particles identity, leads to an estimated FWHM of 0.9. For the relative width we obtain $w \approx 0.24$. For a Gauss curve with $\mu = 1$ this is $\sigma_\Delta = 0.1$.

4.6 The direction of the incident particle

So far, only vertical electrons and muons were considered. For vertical electrons and muons the traveling distance through a scintillator plate with thickness 2 cm and density ρ =1.03 g cm^{-3} is x_0 =2.06 g cm^{-2}. For a non zero angle of incidence the traveling distance changes accordingly: $x = x_0/\cos\theta$. As a consequence ξ, $\bar{\Delta}$ and κ will increase with θ. The energy loss distribution for muons with $\beta\gamma \geq 100$ is shown in Figure 4.12 for three different values of θ. Similar plots hold for the electrons. For increasing angles of incidence the peak is shifted towards larger values and the peak is broadened. Clearly the distribution depends on θ in a way that cannot be neglected. A zenith dependent energy loss is therefore applied in the simulations.

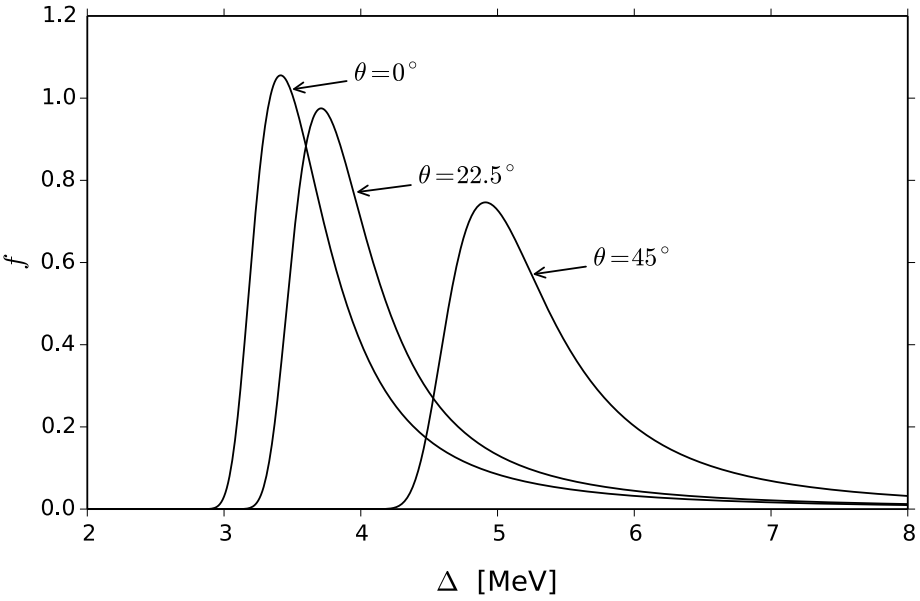

Figure 4.12: Energy loss distributions for muons for three different angles of incidence.

For an estimate of the spread of the signal distribution we mention that a non-zero angle of incidence broadens it for two reasons. The first is the zenith angle of the shower. Assuming the zenith angles to be distributed as [80]

$$N(\theta) \propto \sin\theta \cos^n(\theta)\,, \tag{4.25}$$

where $n \approx 7.5$, the angles of half the maximum of this distribution are at $\theta \approx 6°$ and $\theta \approx 38°$ corresponding to $\cos\theta \approx 0.99$ and $\cos\theta \approx 0.80$ respectively. The corresponding values of ξ ranges between 0.17 and 0.22 MeV. The zenith distribution obtains its maximum for $\theta \approx 22°$, corresponding to $\xi = .18$. Since the height of the peak goes as $\cos\theta$ and the width as $\sec\theta$, this leads to an additional spread of the pulse integral diagram of about $w \approx 0.05/0.18 = 0.28$ or $\sigma_z \approx 0.12$. The second is the angle of incidence of particles within the shower. For a 1 PeV shower with zenith angle 22.5° the distribution of zenith angles of individual electrons and muons is shown in Figure 4.13. The width of the distribution in Figure 4.13 is about 0.1 rad; it leads to an additional spread in $\sec\theta$: $w \approx 0.14$ or $\sigma_\theta \approx .06$. The final width is given by the convolution of the energy loss distribution, the zenith angle distribution and the individual direction distribution: $\sigma = \sqrt{\sigma_\Delta^2 + \sigma_z^2 + \sigma_\theta^2} = \sqrt{0.1^2 + 0.12^2 + 0.06^2} \approx 0.17$.

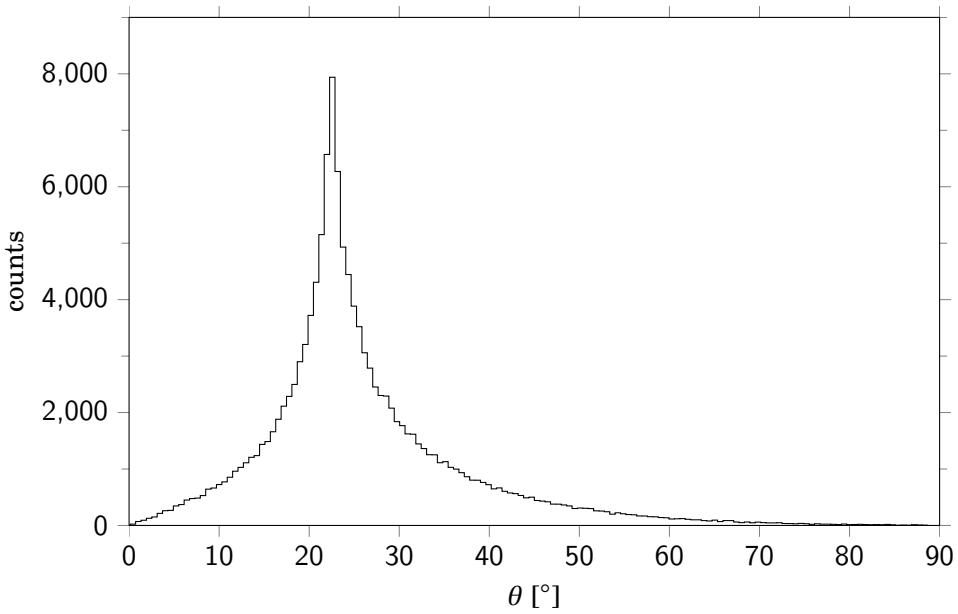

Figure 4.13: The distribution of zenith angles θ of individual electrons and muons for a 1 PeV shower with zenith angle 22.5°.

4.7 Efficiency

The production of one scintillation photon requires about 100 eV [81]. For an energyloss peak around 3.6 MeV this corresponds to 36 000 photons. About 28 % of them, about 10 000 photons, enter the fish tail shaped light guide. The area of the mutual surface of the scintillator and the fish tail is $50 \cdot 2 = 100\,\mathrm{cm}^2$. The area of the opening window of the PMT is $4.4\,\mathrm{cm}^2$. Based on this area the number of photons that will enter the PMT is estimated to be around 440 or 1.2 % of the photons we started with. An estimate of the average transmission efficiency therefore is 1.2 %. In the PMT the 440 photons will give rise to about 123 photo-electrons, because the quantum efficiency is 28 %. Poisson statistics for large numbers predict a spread $\sigma_{\mathrm{PMT}} = \sqrt{N}/N \approx 0.09$. As a consequence the spread in the pulse integral diagram increases to $\sigma = \sqrt{\sigma_\Delta^2 + \sigma_z^2 + \sigma_\theta^2 + \sigma_{\mathrm{PMT}}^2} \approx 0.19$. The 440 photons which enter the PMT are an estimate.

The probability for a scintillation photon to reach the PMT depends on the position of entrance of the incident particle [82]. For 1250 positions the efficiency has been simulated [83]. The transmission efficiency has been experimentally verified [84]. The simulation resulted in a distribution for the number of photons arriving at the PMT, shown in Figure 4.14. A Gaussian fit of the distribution in Figure 4.14 yields $\mu = 425$ and $\sigma = 93$. The relative spread then is $\sigma_\eta = 0.22$ corresponding to a FWHM of 0.52 [81, 83]. This increases the spread in the pulse-integral diagram: $\sigma = \sqrt{\sigma_\Delta^2 + \sigma_z^2 + \sigma_\theta^2 + \sigma_{\mathrm{PMT}}^2 + \sigma_\eta^2} \approx 0.3$. This result is in agreement with actual pulse height and pulse integral diagrams.

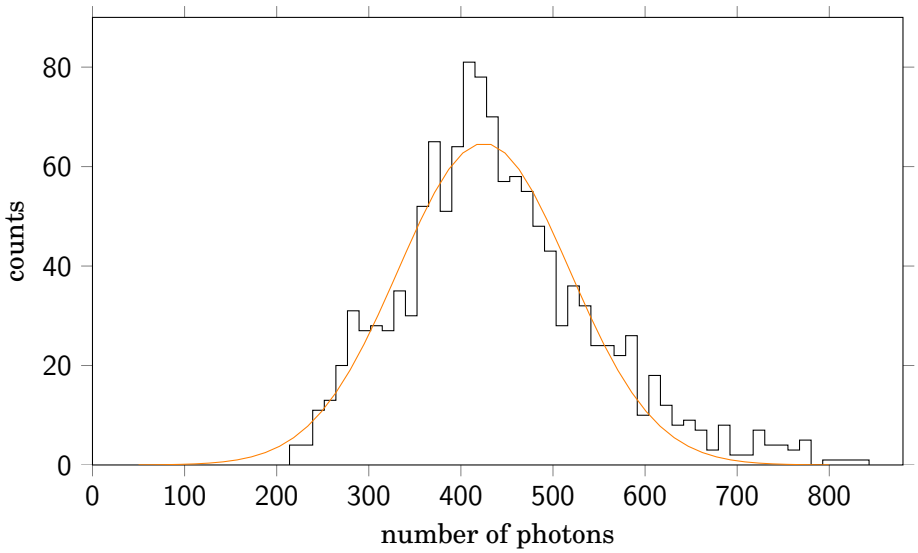

Figure 4.14: Distribution of number of photons which arrive at the PMT and a fit with a Gaussian curve (dashed orange).

4.8 Convolution

A convolution of the energy loss distribution, the quantum efficiency and the transmission efficiency is obtained as follows. The fraction of muons, electrons and positrons in a shower is roughly 20 %, 50 % and 30 %. Therefore a list of 10 000 energy losses is made of which 2000, 5000 and 3000 correspond to the distribution of the muon, electron and positron respectively.

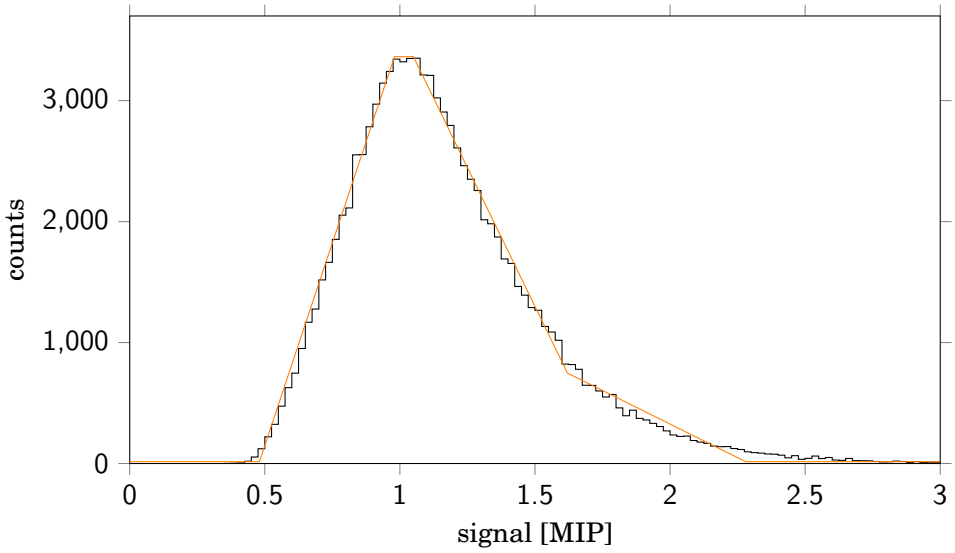

Figure 4.15: Distribution of the convoluted signal and a piecewise linear approximation (dashed orange)

The most probable value of the energy loss is estimated by taking the weighted average of the most probable values for muons, electrons and positrons with the weights in the ratio 0.2 : 0.5 : 0.3. The result is 3.67 MeV. The most probable value for the number of photons reaching the PMT is 425. By dividing the energy losses and photon numbers by 3.67 and 425 respectively, the distributions are normalized such that their most probable values become equal to unity. The unit being a vertical equivalent MIP. A Monte Carlo method is used to determine the full signal response. The result for 100 000 samples is shown in Figure 4.15.

Approximately the distribution in Figure 4.15 is piecewise linear. The linear decomposition of the distribution can be described as

$$\begin{cases} y(x) = 0 & ; \text{ if } 0 < x < 0.48 \\ y(x) = c_1(x-0.48)/(0.98-0.48) & ; \text{ if } 0.48 \le x < 0.98 \\ y(x) = c_2 & ; \text{ if } 0.98 \le x < 1.05 \\ y(x) = c_3(x-1.05)/(1.62-1.05) & ; \text{ if } 1.05 \le x < 1.62 \\ y(x) = c_4(x-1.62)/(2.28-1.62) & ; \text{ if } 1.62 \le x \le 2.28 \\ y(x) = 0 & ; \text{ if } x > 2.28\ , \end{cases} \tag{4.26}$$

where the c_i are numerical constants. The probability distribution of the signal explicitly reads:

$$f(x) = \begin{cases} 0 & ; \text{ if } 0 < x < 0.48 \\ -1.30327 + 2.71514x & ; \text{ if } 0.48 \le x < 0.98 \\ 1.35757 & ; \text{ if } 0.98 \le x < 1.05 \\ 3.32319 - 1.87202x & ; \text{ if } 1.05 \le x < 1.62 \\ 1.00361 - 0.44018x & ; \text{ if } 1.62 \le x \le 2.28 \\ 0 & ; \text{ if } x > 2.28\ . \end{cases} \tag{4.27}$$

The corresponding cumulative probability distribution:

$$F(x) = \begin{cases} 0 & ; \text{ if } 0 < x < 0.48 \\ 0.312785 - 1.30327x + 1.35757x^2 & ; \text{ if } 0.48 \le x < 0.98 \\ -0.991028 + 1.35757x & ; \text{ if } 0.98 \le x < 1.05 \\ -2.02298 + 3.32319x - 0.93601x^2 & ; \text{ if } 1.05 \le x < 1.62 \\ -0.144118 + 1.00361x - 0.22009x^2 & ; \text{ if } 1.62 \le x \le 2.28 \\ 1 & ; \text{ if } x > 2.28\ . \end{cases} \tag{4.28}$$

is shown in Figure 4.16.

The linear decomposition is advantageous for the Monte Carlo since the cumulative probability distribution is an analytic invertible function. For each particle passing a detector the signal is simulated by taking a random number $\mathscr{R}$ between 0 and 1, and convert it to a signal

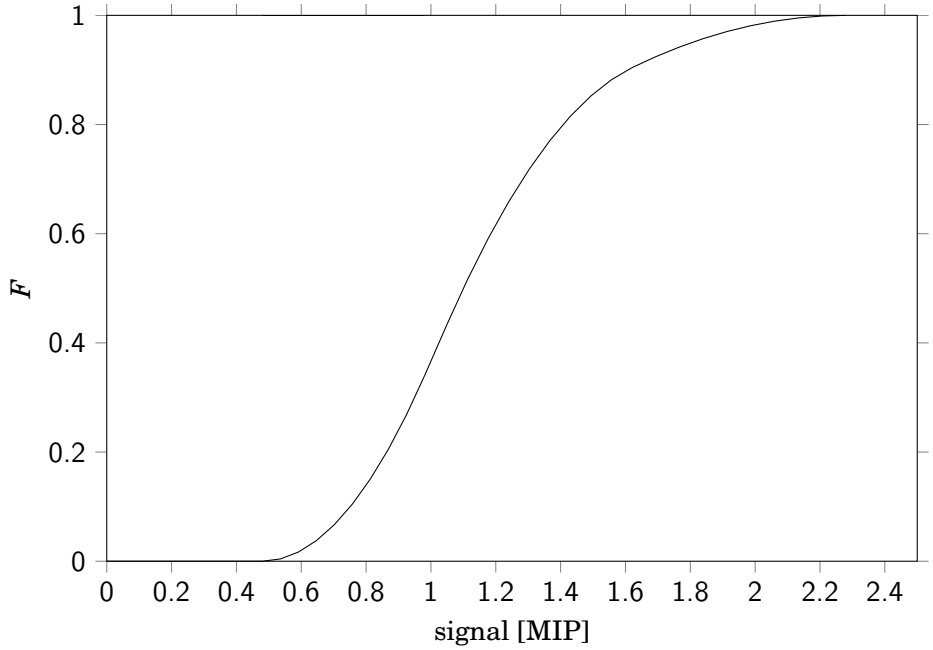

Figure 4.16: Cumulative probability of signals.

x in MIP by means of the inverse of $F(x)$. To be specific,

$$x = \begin{cases} 0.48 + 0.8583\sqrt{\mathscr{R}} & \text{, if } 0 < \mathscr{R} \leq 0.3394 \\ 0.73 + 0.7366\mathscr{R} & \text{, if } 0.3394 < \mathscr{R} \leq 0.4344 \\ 1.7752 - 1.0336\sqrt{0.9267 - \mathscr{R}} & \text{, if } 0.4344 < \mathscr{R} \leq 0.9041 \\ 2.28 - 2.1316\sqrt{1 - \mathscr{R}} & \text{, if } 0.9041 < \mathscr{R} < 1 \,. \end{cases} \tag{4.29}$$

The latter expression holds for the case of vertical incidence. The situation changes for non zero angles of incidence. Then

$$\xi = \frac{0.171}{\cos\theta} \text{ MeV} \,. \tag{4.30}$$

The angle of incidence is obtained from the momentum of the particle:

$$\sec\theta = \frac{p}{p_z} \,. \tag{4.31}$$

As a consequence the Equation 4.29 is transformed to

$$x = \begin{cases} (0.48 + 0.8583\sqrt{\mathscr{R}})\sec\theta & \text{, if } 0 < \mathscr{R} \leq 0.3394 \\ (0.73 + 0.7366\mathscr{R})\sec\theta & \text{, if } 0.3394 < \mathscr{R} \leq 0.4344 \\ (1.7752 - 1.0336\sqrt{0.9267 - \mathscr{R}})\sec\theta & \text{, if } 0.4344 < \mathscr{R} \leq 0.9041 \\ (2.28 - 2.1316\sqrt{1 - \mathscr{R}})\sec\theta & \text{, if } 0.9041 < \mathscr{R} < 1 \,. \end{cases} \tag{4.32}$$

To get an impression of different contributions to the pulse-integral diagram, and to check the foregoing implementation, a small simulation is conducted: 1 PeV showers with different zenith angles and different energies (drawn from the energy spectrum) are randomly thrown on a station with diamond configuration of four detectors. For the events caused by the showers the particle density at a detector is obtained from a NKG function and via Poisson statistics translated to an integer number of particles. The latter is converted to a signal as described above. In this way the distribution of the signal is obtained for each integer number of particles. The result of 1 million throws is shown in Figure 4.17.

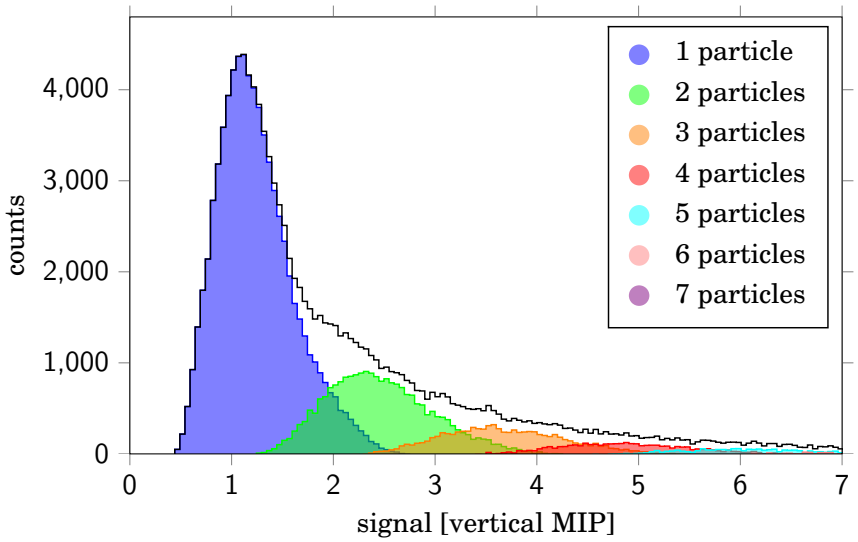

Figure 4.17: Simulated distribution of the detector signals caused by an integer number of particles. The overall distribution (black) shows a 'second peak'.

The main peak is caused by single particle signals. Its width is equal to the expected value $w = 0.7$. The overall distribution is a little wider because of the 2-particle contribution. The overall distribution is comparable to the observed pulse integral diagram in Figure 4.6.

For vertical incidence 1 MIP corresponds to 3.67 MeV. In the diagram the peak position is larger since we simulated with different zenith angles. The peak is therefore larger by a factor 1.07, thus at 3.9 MeV. That is about 15 % larger than the vertical muon peak at 3.41 MeV. In summary, the MIP peak is at about 7 % larger energy than the peak for vertical particles which is on its turn 8 % larger than the vertical muon MIP.

4.9 PMT non-linearity

For large signals the response of a PMT lags behind the ideal response because of saturation [85]. The non-linear response for the type of PMT used for HiSPARC has been measured [86]. For the non-linear relation the following equation is considered:

$$I_0 = I + aI^b \ , \tag{4.33}$$

where I_0 would be the ideal pulse integral for a linear PMT and where I is the pulse integral for a non-linear PMT. As usual the pulse integral is expressed in MIPs.The fit resulted in $a = 3.876 \cdot 10^{-5}$ and $b = 3.871$. The data points and the fit equation are shown in fig. 4.18.

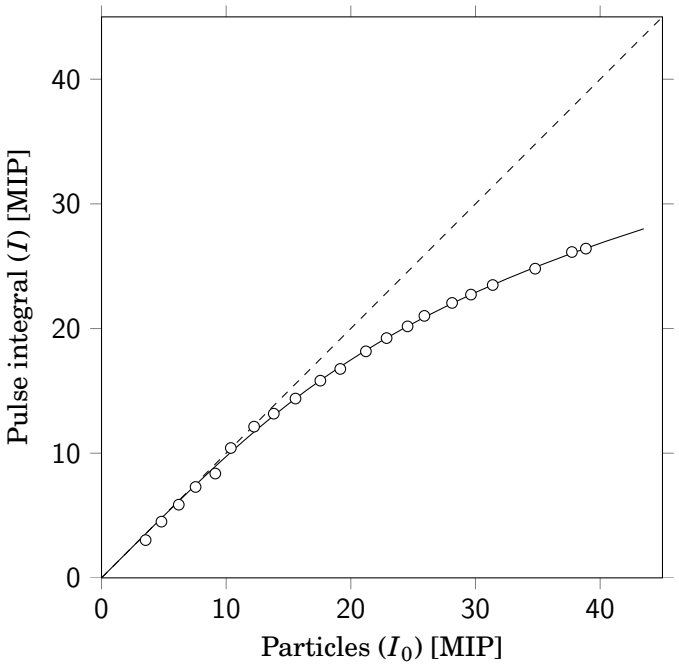

Figure 4.18: The non-linear PMT response (circles) and the fit function (black). The dashed line expresses the ideal linear PMT response.

For shower core reconstructions the detector signals are corrected for the PMT non-linearity.

5 Direction reconstruction

5.1 Detector constellations

If a cosmic air shower triggers at least three detectors of a four detector station, the direction of the shower can be reconstructed from the arrival times of the shower front [82]. At SPA the detectors of a station always have the same altitude. The direction of a shower can also be reconstructed if the shower has caused a coincidence of at least three events. If all the stations participating in such a coincidence would have the same altitude, the situation is comparable to the reconstruction from three or four detectors. The SPA stations do differ in altitude. In that case the algorithm for three stations differs from the algorithm for more than three stations. For every configuration the reconstruction can be achieved by minimizing a χ^2 function. However, for a large number of showers it saves time to apply customized reconstruction methods. As another advantage, analytical methods allow for a theoretical uncertainty analysis.

For the application of fast reconstruction methods different situations will be distinguished. If the shower front is assumed to be flat the methods are:

Flat-2D-3 Reconstruction by means of 3 stations or detectors in a horizontal plane.

Flat-3D-3 Reconstruction by means of 3 stations with different altitude.

Flat-2D-n Reconstruction by means of $n > 3$ stations or detectors in a horizontal plane.

Flat-3D-n Reconstruction by means of $n > 3$ stations with different altitude.

For a curved shower front:

Curved-2D Reconstruction by means of $n > 3$ stations or detectors in a horizontal plane.

Curved-3D Reconstruction by means of $n > 3$ stations with different altitude.

For Flat-2D-3 an analytic expression is obtained in an elementary manner. For Flat-3D-3 a compact analytical expression is derived by means of vector calculus. For Flat-2D-n an analytical expression is derived by means of regression. The regression will be applied repeatedly in an iterative procedure for Flat-3D-n reconstruction. For a curved shower front the methods are based on an iterative application of a regression equation. The described reconstruction methods for curved shower fronts still have to be implemented in SAPPHiRE in due time.

The methods described hold for the situation where the timing uncertainty is assumed to be equal in every detector. In reality, the variation in the thickness of the shower front and therefore the uncertainty grows with the distance to the shower core [82, 87, 88]. In many situations the gain in the accuracy by taking non-constant timing uncertainties is negligible. Even for weighted uncertainties one can still save time by applying the described methods to the first step or first few steps of an iteration and switching to a numerical optimization method for the later steps.

For each direction reconstruction the system of equations have a twofold mathematical ambiguity. In case the detectors are in a horizontal plane one solution corresponds to a shower coming from above and the other to a shower coming from below the horizon. The first one is regarded as the physical solution, while the second one is ignored. For Flat-3D reconstruction the mirror plane may not be (precisely) horizontal. As a consequence there is a small probability that both solutions correspond either to two showers coming from above or to two showers coming from below the horizon. In both cases the solutions are discarded.

Finally, there is also the possibility that no solution for the direction is obtained if the arrival times imply a velocity of the shower front exceeding the speed of light. A reconstruction attempt will then result in complex values for the parameters [89].

5.2 Flat-2D-3

We consider three detecting points (detectors or stations) 0, 1 and 2 in a horizontal ($z = 0$) plane with positions $(x_0, y_0, 0)$, $(x_1, y_1, 0)$ and $(x_2, y_2, 0)$. The unit vector normal to the shower front in the direction of the origin of the shower is denoted by $\mathbf{n} = (n_x, n_y, n_z)$. Furthermore we will assume for the analysis a plane shower front propagating at the velocity of light c. If t_0, t_1 and t_2 are the respective arrival times at the three detection points, the plane of the shower front at $t = 0$ is determined by the points P_0, P_1 en P_2 with coordinates:

$$P_0(x_0 + ct_0 n_x, y_0 + ct_0 n_y, ct_0 n_z)\,, \tag{5.1}$$

$$P_1(x_1 + ct_1 n_x, y_1 + ct_1 n_y, ct_1 n_z) \tag{5.2}$$

and

$$P_2(x_2 + ct_2 n_x, y_2 + ct_2 n_y, ct_2 n_z) \,. \tag{5.3}$$

A plane with normal vector $\mathbf{n} = (n_x, n_y, n_z)$ is given by the equation

$$x n_x + y n_y + z n_z + a = 0 \tag{5.4}$$

for some constant a. For point P_0 in this plane

$$(x_0 + ct_0 n_x) n_x + (y_0 + ct_0 n_y) n_y + (ct_0 n_z) n_z + a = 0 \,. \tag{5.5}$$

Hence,

$$x_0 n_x + y_0 n_y + ct_0 + a = 0 \,. \tag{5.6}$$

For the points P_1 en P_2 in the plane we similarly have

$$x_1 n_x + y_1 n_y + ct_1 + a = 0 \tag{5.7}$$

and

$$x_2 n_x + y_2 n_y + ct_2 + a = 0 \,. \tag{5.8}$$

The difference between Equation 5.7 and Equation 5.6 and between Equation 5.8 and Equation 5.6 respectively read

$$(x_1 - x_0) n_x + (y_1 - y_0) n_y + c(t_1 - t_0) = 0 \tag{5.9}$$

and

$$(x_2 - x_0) n_x + (y_2 - y_0) n_y + c(t_2 - t_0) = 0 \,. \tag{5.10}$$

This system of two equations for n_x en n_y can be solved with the result

$$n_x = \frac{c\Delta t_2 \Delta y_1 - c\Delta t_1 \Delta y_2}{\Delta y_2 \Delta x_1 - \Delta y_1 \Delta x_2} \tag{5.11}$$

and

$$n_y = \frac{c\Delta t_1 \Delta x_2 - c\Delta t_2 \Delta x_1}{\Delta x_1 \Delta y_2 - \Delta x_2 \Delta y_1} \,, \tag{5.12}$$

where $\Delta x_i \equiv x_i - x_0$, $\Delta y_i \equiv y_i - y_0$ and $\Delta t_i \equiv t_i - t_0$. The zenith and azimuth angle follow from

$$\tan\phi = \frac{n_y}{n_x} \tag{5.13}$$

and

$$\cos\theta = \sqrt{1 - n_x^2 - n_y^2} \,. \tag{5.14}$$

5.3 Flat-3D-3

Here we consider a plane shower front arriving at three detecting points with different altitudes. For gravitational waves an analytic expression for the direction has been derived and applied for a particular choice of local coordinates [90, 91]. A general analytic expression can be derived in an elementary way, although the result is rather lengthy [92, 93]. We will present a derivation which results in a compact form of the general analytic expression. To this end we consider three detecting points 0, 1 and 2 at the positions (x_0, y_0, z_0), (x_1, y_1, z_1) and (x_2, y_2, z_2). Again, the unit vector normal to the shower front in the direction opposite to the shower direction is $\mathbf{n} = (n_x, n_y, n_z)$ and the shower front is assumed to move with the speed of light c. If t_0, t_1 and t_2 are the times at which the shower front arrives at the detecting points 0, 1 and 2 respectively, the plane of the shower front at $t = 0$ is determined by the following three points:

$$\mathbf{p_i} = \begin{pmatrix} x_i + ct_i n_x \\ y_i + ct_i n_y \\ z_i + ct_i n_z \end{pmatrix} \quad , \quad i = 0,1,2 \; . \tag{5.15}$$

Two vectors in this plane are

$$\mathbf{s_i} = \mathbf{p_i} - \mathbf{p}_0 = \begin{pmatrix} \Delta x_i + c\Delta t_i n_x \\ \Delta y_i + c\Delta t_i n_y \\ \Delta z_i + c\Delta t_i n_z \end{pmatrix} \quad , \quad i = 1,2 \; . \tag{5.16}$$

Also here $\Delta x_i \equiv x_i - x_0$, $\Delta y_i \equiv y_i - y_0$ and $\Delta t_i \equiv t_i - t_0$.

By means of the vectors

$$\mathbf{d_i} = \begin{pmatrix} \Delta x_i \\ \Delta y_i \\ \Delta z_i \end{pmatrix} \quad , \quad i = 1,2 \tag{5.17}$$

the vectors $\mathbf{s_i}$ can be written as

$$\mathbf{s_i} = \mathbf{d_i} + c\Delta t_i \mathbf{n} \quad , \quad i = 1,2 \; . \tag{5.18}$$

Since the normal vector $\mathbf{n}$ is orthogonal to the plane of the shower front the dot product of $\mathbf{n}$ with vectors in this plane should vanish:

$$\mathbf{s_i} \cdot \mathbf{n} = 0 \; . \tag{5.19}$$

This requirement leads to the following two equations:

$$\begin{aligned} \mathbf{d}_1 \cdot \mathbf{n} &= -c\Delta t_1 \ , \\ \mathbf{d}_2 \cdot \mathbf{n} &= -c\Delta t_2 \ . \end{aligned} \tag{5.20}$$

Together with the condition

$$n^2 = \mathbf{n} \cdot \mathbf{n} = 1 \tag{5.21}$$

we have three equations for the three component vector $\mathbf{n}$. To solve the system for $\mathbf{n}$ we consider the following two vectors:

$$\mathbf{u} := c\Delta t_2 \mathbf{d}_1 - c\Delta t_1 \mathbf{d}_2 \tag{5.22}$$

and

$$\mathbf{v} := \mathbf{d}_1 \times \mathbf{d}_2 \ . \tag{5.23}$$

The vectors have the following properties:

$$\mathbf{u} \cdot \mathbf{v} = 0 \ , \tag{5.24}$$

$$\mathbf{u} \cdot \mathbf{n} = 0 \ , \tag{5.25}$$

$$|\mathbf{u} \times \mathbf{v}| = uv \ , \tag{5.26}$$

$$\mathbf{v} \times \mathbf{n} = \mathbf{u} \quad \rightarrow \quad (\mathbf{v} \cdot \mathbf{n})^2 = v^2 - u^2 \ , \tag{5.27}$$

and

$$\mathbf{n} \cdot (\mathbf{u} \times \mathbf{v}) = u^2 \ . \tag{5.28}$$

The projection of the vector $\mathbf{n}$ onto the orthogonal set ($\mathbf{u}$, $\mathbf{v}$, $\mathbf{u} \times \mathbf{v}$) yields

$$\mathbf{n} = \frac{\mathbf{u} \cdot \mathbf{n}}{u^2}\mathbf{u} + \frac{\mathbf{v} \cdot \mathbf{n}}{v^2}\mathbf{v} + \frac{(\mathbf{u} \times \mathbf{v}) \cdot \mathbf{n}}{(\mathbf{u} \times \mathbf{v})^2}(\mathbf{u} \times \mathbf{v}) \ . \tag{5.29}$$

With the substitution of the foregoing identities it is reduced to its final form

$$\mathbf{n} = \frac{\mathbf{u} \times \mathbf{v} \pm \mathbf{v}\sqrt{v^2 - u^2}}{v^2} \ . \tag{5.30}$$

It can be verified that this expression satisfies the system of Equations 5.20 and 5.21, as it should.

The two solutions for $\mathbf{n}$, one for each sign of the square root, correspond to two shower directions mirrored in the plane of the three detecting points [90]. If both solutions correspond to a shower coming from above (or from below) the horizon, one can not know which is the correct one and both solutions are discarded. Writing the normal vector of the shower front in

spherical coordinates

$$\mathbf{n} = \begin{pmatrix} n_x \\ n_y \\ n_z \end{pmatrix} = \begin{pmatrix} \sin\theta\cos\phi \\ \sin\theta\sin\phi \\ \cos\theta \end{pmatrix} , \tag{5.31}$$

we obtain for the azimuth angle

$$\tan\phi = \frac{n_y}{n_x} = \frac{(\mathbf{u}\times\mathbf{v})_y \pm v_y\sqrt{v^2-u^2}}{(\mathbf{u}\times\mathbf{v})_x \pm v_x\sqrt{v^2-u^2}} . \tag{5.32}$$

Where the sign of the numerator and the sign of the denominator determine the quadrant of the azimuth angle. The zenith angle follows directly from the third component of $\mathbf{n}$:

$$\cos\theta = \frac{(\mathbf{u}\times\mathbf{v})_z \pm v_z\sqrt{v^2-u^2}}{v^2} . \tag{5.33}$$

In case the three detecting points are in a horizontal plane the corresponding analytical expression is obtained by substituting $\Delta z_1 = \Delta z_2 = 0$ and $u_z = v_x = v_y = 0$. The solutions for ϕ and θ then reduce to

$$\tan\phi = \frac{-u_x v_z}{u_y v_z} \tag{5.34}$$

and

$$\sin\theta = \sqrt{\frac{u_x^2+u_y^2}{v_z^2}} \tag{5.35}$$

respectively. These coincide with Equations 5.13 and 5.14. In Equation 5.35 a positive sign is taken for the square root to ensure a positive θ. In Equation 5.34 the sign of the numerator, $-u_x v_z$, and the sign of the denominator, $u_y v_z$ determine the quadrant of the azimuth angle.

5.4 Flat-2D-n

Here we consider a plane shower hitting more than three detecting points. For a reconstructed shower front plane with normal vector $\mathbf{n}$, the points $\mathbf{p_i}$ as given by Equation 5.1 will not lie exactly in the plane $xn_x + yn_y + zn_z + m = 0$. The deviations will be denoted as δ_i :

$$\delta_i = \mathbf{p_i}\cdot\mathbf{n} + m = x_i n_x + y_i n_y + z_i n_z + ct_i + m . \tag{5.36}$$

The optimal solution corresponds to the minimum of the corresponding χ^2 function:

$$\chi^2 = \sum_{i=0}^{k-1}\left(\frac{x_i n_x + y_i n_y + z_i n_z + ct_i + m}{\sigma(t_i)}\right)^2 , \tag{5.37}$$

where k is the number of detecting points hit and where $\sigma(t_i)$ is the timing uncertainty for detector i. In general, the uncertainty σ_t in t_i will depend on the distance r_i of detector i to

the shower core, $\sigma(t_i) = \sigma_t(r_i)$ [87]. To minimize the general χ^2 function one has to resort to a numerical optimization method. As mentioned before, however, we restrict ourselves to the situation where the uncertainty is regarded as a constant: $\sigma(t_i) = \sigma$. Then the optimal plane corresponds to the minimum of the sum of squares of the residuals

$$R^2 = \sum_{i=0}^{k-1} \left(x_i n_x + y_i n_y + z_i n_z + c t_i + m\right)^2 \ , \tag{5.38}$$

If all the detecting points are in a horizontal plane a regression formula can be derived. For this we make use of the fact that for the solution which minimizes

$$R^2 = \sum_{i=0}^{k-1} \left(x_i n_x + y_i n_y + c t_i + m\right)^2 \tag{5.39}$$

the derivatives with respect to the components of the normal vector are zero:

$$\frac{\mathrm{d}R^2}{\mathrm{d}n_x} = 0 \ , \quad \frac{\mathrm{d}R^2}{\mathrm{d}n_y} = 0 \ , \quad \frac{\mathrm{d}R^2}{\mathrm{d}m} = 0 \ . \tag{5.40}$$

For the direction components the solution reads

$$n_x = c\frac{\overline{tx}\left(\overline{y^2} - \overline{y}^2\right) + \overline{xy}\left(\overline{t}\,\overline{y} - \overline{ty}\right) + \overline{x}\,\overline{y}\,\overline{ty} - \overline{t}\,\overline{x}\,\overline{y^2}}{\overline{xy}^2 + \overline{x}^2\,\overline{y^2} + \overline{y}^2\,\overline{x^2} - \overline{x^2}\,\overline{y^2} - 2\overline{x}\,\overline{y}\,\overline{xy}} \tag{5.41}$$

and

$$n_y = c\frac{\overline{ty}\left(\overline{x^2} - \overline{x}^2\right) + \overline{xy}\left(\overline{t}\,\overline{x} - \overline{tx}\right) + \overline{x}\,\overline{y}\,\overline{tx} - \overline{t}\,\overline{y}\,\overline{x^2}}{\overline{xy}^2 + \overline{x}^2\,\overline{y^2} + \overline{y}^2\,\overline{x^2} - \overline{x^2}\,\overline{y^2} - 2\overline{x}\,\overline{y}\,\overline{xy}} \ , \tag{5.42}$$

where we have used the following abbreviations for the means:

$$\overline{a} := \frac{1}{k}\sum_{i=0}^{k-1} a_i \ , \quad \overline{a^2} := \frac{1}{k}\sum_{i=0}^{k-1} a_i a_i \ , \quad \overline{ab} := \frac{1}{k}\sum_{i=0}^{k-1} a_i b_i \ . \tag{5.43}$$

One can transform to relative coordinates with respect to detector 0 and to relative times with respect to the time of arrival at detector 0. Then the x_i, y_i and t_i should be read as Δx_i, Δy_i respectively Δt_i, while the summation runs from 1 through $k-1$. Either way, the direction follows from

$$\tan\phi = \frac{n_y}{n_x} \tag{5.44}$$

and

$$\cos\theta = \sqrt{1 - n_x^2 - n_y^2} \ . \tag{5.45}$$

5.5 Flat-3D-n

For the situation where the stations are not in a horizontal plane, but at different altitudes the normal vector as found from the Flat-2D reconstruction is used as the initial vector for an iterative procedure. That is, we first regard the stations as being positioned in a horizontal plane. This results in a first approximation for the direction. By means of the approximate direction the relative detector coordinates and arrival times are determined as they would have at virtual positions $(x', y', 0)$ in a horizontal plane through station 0:

$$\Delta x'_i = \Delta x_i - \frac{\Delta z_i}{n_z} n_x \,, \tag{5.46}$$

$$\Delta y'_i = \Delta y_i - \frac{\Delta z_i}{n_z} n_y \tag{5.47}$$

and

$$c\Delta t'_i = c\Delta t_i + \frac{\Delta z_i}{n_z} \,. \tag{5.48}$$

For each station i the line through (x_i, y_i, z_i) and normal to the plane of the shower front also goes through the virtual position $(x'_i, y'_i, 0)$. The intersection of this line with the plane of the shower front is identical for the original and primed coordinates. The situation is illustrated in Figure 5.1.

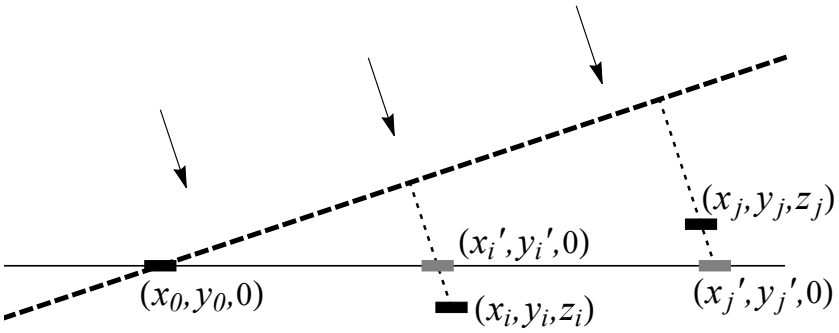

Figure 5.1: The plane of the shower front (dashed), the stations (black) with different altitudes and the virtual station positions (gray) with equal altitude.

New approximations for the direction are found by repeatedly applying the Flat-2D-n reconstructions to the primed quantities. The values for **n** quickly converge. The iterations are repeated until the difference between two successive directions is smaller than 0.001 rad. The iterative regression procedure returns just a single value for the direction. It can therefore only be applied if the mean plane of the stations is close to horizontal, which is actually the case for the SPA stations. Flat-3D-n reconstructions are about three times faster than minimization by means of the SLSQP method of the SCIPY.OPTIMIZE package.

5.6 Reconstruction of curved shower fronts

The accuracy of the reconstructed direction can be improved by taking the curvature of the shower front into account. Although not implemented in SAPPHiRE yet, we already describe a method based on the Flat-2D reconstruction. The method requires the knowledge of the location of the shower core. A method for the reconstruction of the shower core is given in the Chapter 6. The position of the shower core at the horizontal $z = 0$ plane of the stations will be denoted by $\mathbf{p}_c = (x_c, y_c, 0)$. The shower core axis is given by $\mathbf{p}_c + \lambda \mathbf{n}$, with λ a parameter. Curved showers are assumed to be axially symmetric around the shower core axis. The deviation f between the curved front and a flat front, measured in the direction of the shower, is a function of the radial distance r from the core axis: $f = f(r)$, shown schematically in Figure 5.2.

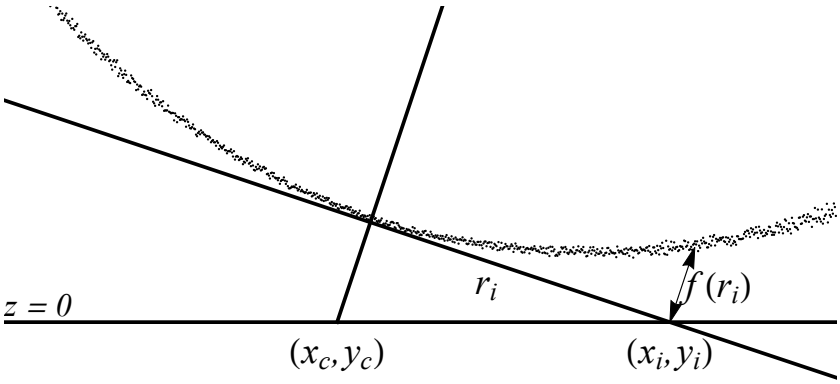

Figure 5.2: Impression of a curved shower front reaching a plane through station i and perpendicular to the shower core. The distance from the core to station i is r_i.

A plane perpendicular to $\mathbf{n}$ that passes through station i with coordinates $(x_i, y_i, 0)$ is given by

$$(x - x_i)n_x + (y - y_i)n_y + z n_z = 0 \; . \tag{5.49}$$

The shower core reaches this plane if $\lambda = (x_i - x_c)n_x + (y_i - y_c)n_y$. This corresponds to the point

$$\begin{pmatrix} x_c + (x_i - x_c)n_x^2 + (y_i - y_c)n_x n_y \\ y_c + (x_i - x_c)n_x n_y + (y_i - y_c)n_y^2 \\ (x_i - x_c)n_x n_z + (y_i - y_c)n_y n_z \end{pmatrix} . \tag{5.50}$$

For the radial vector $\mathbf{r}_i$ between the core and station i we obtain

$$\mathbf{r}_i = \begin{pmatrix} y_{i,c} n_x n_y - x_{i,c}\left(1 - n_x^2\right) \\ x_{i,c} n_x n_y - y_{i,c}\left(1 - n_y^2\right) \\ x_{i,c} n_x n_z + y_{i,c} n_y n_z \end{pmatrix} , \tag{5.51}$$

where $x_{i,c}$ and $y_{i,c}$ are abbreviations for $x_c - x_i$ and $y_c - y_i$ respectively. For the radial distance r_i between the core and station i we obtain

$$r_i = \sqrt{x_{i,c}^2\left(1-n_x^2\right) + y_{i,c}^2\left(1-n_y^2\right) - 2x_{i,c}y_{i,c}n_x n_y} \; . \tag{5.52}$$

The arrival time t_i^* at detector i as it would be in case of a plane shower front is $t_i^* = t_i - f(r_i)/c$. For the corresponding time difference $\Delta t_i^* = t_i^* - t_0^*$ we find

$$\Delta t_i^* = t_i - \frac{f(r_i)}{c} - t_0 + \frac{f(r_0)}{c} = \Delta t_i - \frac{f(r_i)}{c} + \frac{f(r_0)}{c} \; . \tag{5.53}$$

The evaluation Δt_i^* requires the values of r_i and thus of the shower direction $\mathbf{n}$. We start with the Flat-2D reconstruction to obtain a first approximation for $\mathbf{n}$. The Curved-2D reconstruction now just consists in a repetitive use of Flat-2D reconstruction where each time Δt_i replaced by Δt_i^* and where the r_i are obtained from the previous iteration. That is, we correct for the deviation in the timing of a flat and a curved shower front.

Curved-3D reconstruction, finally, is a combination of Curved-2D and Flat-3D reconstruction in that the time differences should be adjusted for both the curvature of the shower front and the altitude differences of the stations. To be specific,

$$\Delta t_i' = \Delta t_i - \frac{f(r_i)}{c} + \frac{f(r_0)}{c} + \frac{\Delta z_i}{n_z} \; . \tag{5.54}$$

5.7 Uncertainty analysis

Timing uncertainties have both instrumental and physical causes. The latter are due to the statistics of individual shower particles hitting a detector. A timing uncertainty σ_t results in a zenith angle uncertainty σ_θ and in an azimuth angle uncertainty σ_ϕ. The relation will be analyzed for a horizontal diamond shaped detector station as shown in Figure 4.2. We will first consider the reconstruction for the situation where the detectors 0, 1 and 2 are hit. These three detectors are at the corners of an equilateral triangle. To obtain a general result, the length a of the side of the triangle will be left unspecified during the analysis. Taking detector 0 as the origin, the coordinates of the detectors 1 and 2 are $(a,0)$ and $(\frac{1}{2}a, \frac{1}{2}a\sqrt{3})$ respectively. The substitution of these sizes into Equations 5.34 and 5.35 leads to the following expressions for the azimuth angle ϕ and zenith angle θ:

$$\phi = \arctan\left(\frac{2\Delta t_2 - \Delta t_1}{\Delta t_1\sqrt{3}}\right) \; , \tag{5.55}$$

$$\theta = \arcsin\left(\frac{2c}{a\sqrt{3}}\sqrt{T_-^2}\right) \; , \tag{5.56}$$

where

$$T_-^2 := \Delta t_1^2 + \Delta t_2^2 - \Delta t_1 \Delta t_2 \ . \tag{5.57}$$

For the uncertainties σ_ϕ and σ_θ we obtain

$$\sigma_\phi^2 = \sum_{i=0}^{2} \left(\frac{\partial \phi}{\partial t_i} \sigma_t \right)^2 = \frac{3\sigma_t^2}{2T_-^2} \ , \tag{5.58}$$

$$\sigma_\theta^2 = \sum_{i=0}^{2} \left(\frac{\partial \theta}{\partial t_i} \sigma_t \right)^2 = \frac{6c^2\sigma_t^2}{3a^2 - 4c^2T_-^2} \ , \tag{5.59}$$

where σ_t is the timing uncertainty. In terms of θ and ϕ:

$$\sigma_\phi = \frac{c\sigma_t\sqrt{2}}{a\sin\theta} \ , \tag{5.60}$$

$$\sigma_\theta = \frac{c\sigma_t\sqrt{2}}{a\cos\theta} \ . \tag{5.61}$$

For small zenith angles the uncertainty of the zenith angle is approximately given by

$$\sigma_\theta = \frac{c\sigma_t\sqrt{2}}{a} \ . \tag{5.62}$$

The uncertainty $\sigma_{\Delta t}$ in the time difference Δt between two detectors is $\sigma_t\sqrt{2}$. So, for the equilateral triangle the expression for the zenith uncertainty is equal to the 'crude' rule [80]:

$$\sigma_\theta = \frac{c\sigma_{\Delta t}}{a} \ . \tag{5.63}$$

The uncertainty in azimuth becomes very large for small zenith angles, eventually growing to infinity in the limit $\theta \to 0°$. Large azimuth uncertainties do not necessarily mean that the reconstructed direction is inaccurate. For the reconstructed direction the solid azimuth angle $\sigma_\phi \sin\theta$ is what matters. The latter remains finite, even independent of the zenith angle: $\sigma_\phi \sin\theta = c\sigma_t\sqrt{2}/a$. The uncertainty of the zenith angle grows to infinity in the limit $\theta \to 90°$. This behavior of the zenith uncertainty can be suppressed with a volumetric detector arrangement [89]. For the uncertainty of the solid angle we obtain

$$\sigma = \sqrt{\sigma_\phi^2 \sin^2\theta + \sigma_\theta^2} = \frac{c\sigma_t\sqrt{2}}{a\cos\theta}\sqrt{1+\cos^2\theta} \ . \tag{5.64}$$

A sampling frequency of 400 MHz corresponds to a time uncertainty $\sigma_t = \frac{2.5}{\sqrt{12}} \approx 0.722\,\text{ns}$. We substitute this minimum time uncertainty and the size $a = 10$ for the model station of Figure 4.2. In degrees the corresponding uncertainties of the zenith angle and the solid angle become

$$\sigma_\theta = \frac{1.75°}{\cos\theta} \ , \quad \sigma = \frac{1.75°}{\cos\theta}\sqrt{1+\cos^2\theta} \ . \tag{5.65}$$

For the uncertainty of the solid azimuth we obtain $\sigma_\phi \sin\theta = 1.75°$. In Figure 5.3 the uncertainties are plotted against the zenith angle.

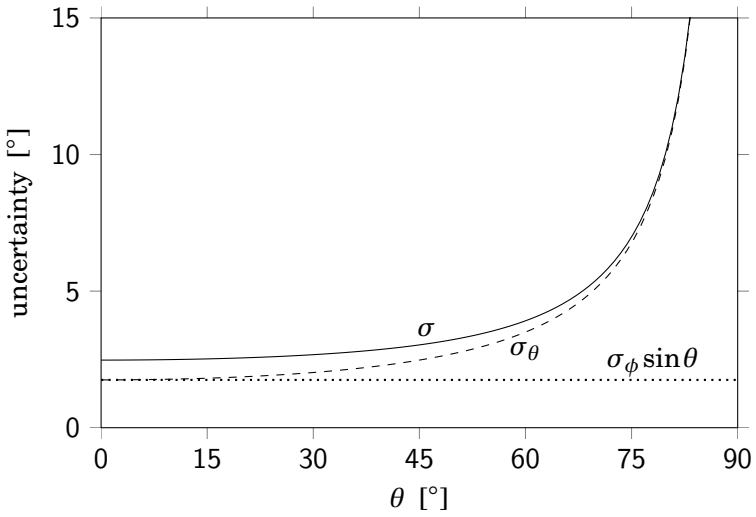

Figure 5.3: Uncertainty of the solid angle (solid), uncertainty σ_θ of the zenith angle (dashed) and $\sigma_\phi \sin\theta$ (dotted) in degrees as a function of zenith angle for an equilateral triangle of detectors.

We also consider the situation where detectors 0, 1 and 3 of the diamond station in Figure 4.2 are hit. Compared to the previous situation detector 0 is now closer to the line connecting detectors 1 and 3. A larger uncertainty can therefore be expected if the azimuth angle of the shower is perpendicular to the line connecting detectors 1 and 3, thus if $\phi = 60°$ or $\phi = -120°$. For the same reason a smaller uncertainty can be expected if the azimuth of the shower is along the line connecting detectors 1 and 3, thus if $\phi = -30°$ or $\phi = 150°$. To derive the uncertainty analytically we have to replace the coordinates of detector 2 by the coordinates $(-\frac{1}{2}a, \frac{1}{2}a\sqrt{3})$ of detector 3. The substitution of the new sizes into Equations 5.34 and 5.35 lead to the following expressions for the azimuth angle ϕ and zenith angle θ:

$$\phi = \arctan\left(\frac{2\Delta t_2 + \Delta t_1}{\Delta t_1 \sqrt{3}}\right) , \tag{5.66}$$

$$\theta = \arcsin\left(\frac{2c}{a\sqrt{3}}\sqrt{T_+^2}\right) , \tag{5.67}$$

where

$$T_+^2 := \Delta t_1^2 + \Delta t_2^2 + \Delta t_1 \Delta t_2 . \tag{5.68}$$

For the uncertainties σ_ϕ and σ_θ we obtain

$$\sigma_\phi^2 = \frac{3\sigma_t^2 T_-^2}{2T_+^4} , \tag{5.69}$$

$$\sigma_\theta^2 = \frac{2c^2\sigma_t^2\left(10T_+^2 - 3T_-^2\right)}{3a^2T_+^2 - 4c^2T_+^4} \,. \tag{5.70}$$

Expressed as functions of the azimuth and zenith angle the uncertainties are:

$$\sigma_\phi = \frac{\sqrt{2}c\sigma_t}{\sqrt{3}a\sin\theta}\sqrt{5 - 2\sqrt{3}\sin(2\phi) + 2\cos(2\phi)} \,, \tag{5.71}$$

$$\sigma_\theta = \frac{\sqrt{2}c\sigma_t}{\sqrt{3}a\cos\theta}\sqrt{5 + 2\sqrt{3}\sin(2\phi) - 2\cos(2\phi)} \,. \tag{5.72}$$

As expected the uncertainties depend on the azimuth for non-equilateral triangles of detectors. For the corresponding uncertainty of the solid angle we obtain

$$\sigma = \frac{\sqrt{2}c\sigma_t}{\sqrt{3}a\cos\theta}\sqrt{10 - \left(5 + 2\cos(2\phi) - 2\sqrt{3}\sin(2\phi)\right)\sin^2\theta} \,. \tag{5.73}$$

Obviously the uncertainties depend on both the zenith and the azimuth. This is the case in general, except for the equilateral triangle where the uncertainty solely depends on the zenith. For $\sigma_t = 0.722$ ns and $a = 10$ the uncertainty of the solid angle in degrees is

$$\sigma = \frac{1.01^\circ}{\cos\theta}\sqrt{10 - \left(5 + 2\cos(2\phi) - 2\sqrt{3}\sin(2\phi)\right)\sin^2\theta} \,. \tag{5.74}$$

The uncertainties in azimuth and zenith in degrees are obtained by replacing $\sqrt{2}c\sigma_t/\sqrt{3}a$ by 1.01°. In Figure 5.4 the solid uncertainties corresponding to the oblate triangle are plotted against the zenith angle.

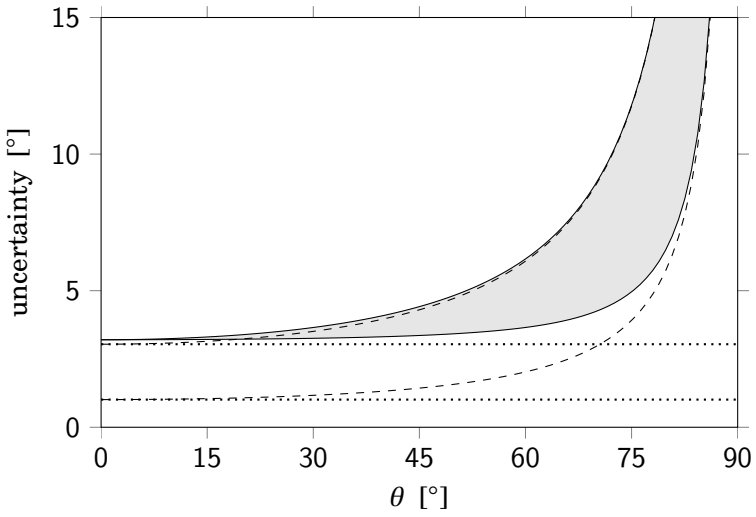

Figure 5.4: Uncertainty range (gray filled) of the solid angle as a function of zenith angle for the oblate triangle of detectors as given in the text. The dashed and dotted curves represent the range of σ_θ respectively $\sigma_\phi \sin\theta$.

The lower curve corresponds to $\phi = -30^\circ$ or $\phi = 150^\circ$ and the upper curve to $\phi = 60^\circ$ or $\phi = -120^\circ$. For other azimuthal angles the curve is in the gray band between these curves. Also shown in Figure 5.4 are the boundaries of σ_θ and $\sigma_\phi \sin\theta$.

For $\theta = 30^\circ$ the uncertainties σ_θ and $\sigma_\phi \sin\theta$ and the corresponding uncertainty of the solid angle are shown in Figure 5.5. As we see, the uncertainty σ_θ obtains a maximum when $\sigma_\phi \sin\theta$

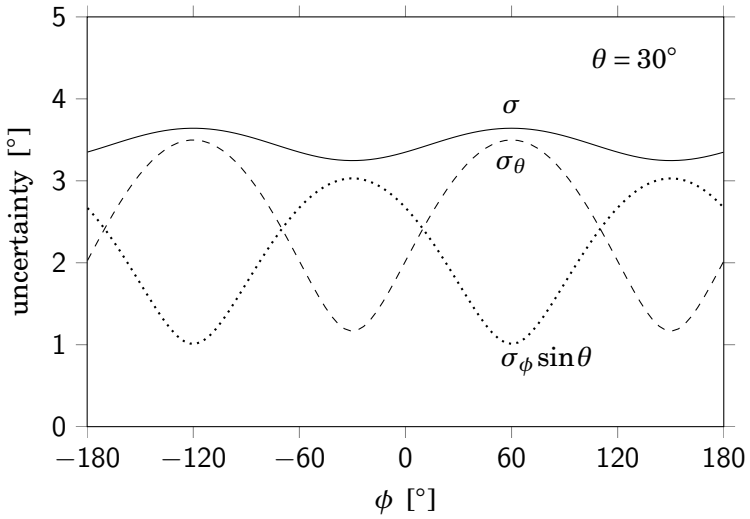

Figure 5.5: Uncertainty of the solid angle (solid), the zenith angle (dashed) and the solid azimuth angle (dotted) for $\theta = 30^\circ$.

obtains a minimum and vice versa. This explains why the gray band is more narrow than the range of the dashed curves and the range of the dotted curves.

6

Core reconstruction

6.1 Introduction

When a cosmic air shower reaches the detectors at the surface of the earth it can leave a signal in one or more detectors. The core of the shower has to be determined out of the pattern of signals. If one takes a guess for the core position, the expected signal ρ_i in detector i will differ from the actual signal w_i. The best core position is obtained by minimizing the function

$$\chi^2 = \sum_{i=1}^{n} \left(\frac{w_i - \rho_i}{\sigma_i} \right)^2 , \tag{6.1}$$

where n is the number of detectors. If density variations follow Poisson statistics $\sigma_i = \sqrt{\rho_i}$. Even in the ideal situation where signals are as expected χ^2 will have several local minima. The presence of several local minima complicates the determination of the core position. A core finding algorithm can benefit if an initial guess for the core position is obtained in an analytical manner. In this chapter a method is described for an estimation of the core position on the basis of the ratio of observed densities. For this the shower size is redundant. Once the core position is estimated further fits with the shower size complete the task. The fits require a lateral density function. Most lateral density functions are modifications of the Nishimura-Kamata-Greisen (NKG) function [38, 56, 94]. The dependence of the density on the distance r to the core is typically governed by

$$\rho(r) \propto \left(\frac{r}{r_0} \right)^a \left(1 + \frac{r}{r_0} \right)^b , \tag{6.2}$$

where r_0 is the Molière radius. The values for a and b depend on the age of the shower. At sea level $a \approx -0.5$ respectively $b \approx -3.0$. As a consequence $\rho(r) \propto r^{-0.5}$ for $r << r_0$ and $\rho(r) \propto r^{-3.5}$ for $r >> r_0$. For the core estimation method the density will be approximated by $\rho(r) \propto r^{-m}$.

6.2 Radical axes

The core estimation method is based on radical axes. To explain the radical axes method we consider five detectors A, B, C, D and E in a horizontal plane. These points have been given the following (x,y) coordinates: $A(0,0)$, $B(70,0)$, $C(100,40)$, $D(70,90)$ and $E(30,80)$. The shower core is taken at $(30,40)$. The coordinates are expressed in m.

First we look at the detectors A, B and C. The detected signals in the detectors are ρ_A, ρ_B and ρ_C respectively. For $\rho(r) \propto r^{-m}$ we obtain for the ratios of the densities at these three detectors:

$$\frac{\rho_A}{\rho_B} = \left(\frac{32}{25}\right)^{\frac{m}{2}} \quad , \quad \frac{\rho_A}{\rho_C} = \left(\frac{49}{25}\right)^{\frac{m}{2}} \quad , \quad \frac{\rho_B}{\rho_C} = \left(\frac{49}{32}\right)^{\frac{m}{2}} \; . \tag{6.3}$$

From the ratios of the densities we derive equations for the coordinates (x,y) of the core position. To this end we substitute

$$\rho_A \propto \left((x-x_A)^2 + (y-y_A)^2\right)^{-m/2} \tag{6.4}$$

and similar expressions for ρ_B and ρ_C. With the given coordinates of the detectors we obtain for the ratio between ρ_A and ρ_B the following:

$$25\left((x-70)^2 + y^2\right) = 32\left(x^2 + y^2\right) \; . \tag{6.5}$$

From the other two ratios we obtain

$$25\left((x-100)^2 + (y-40)^2\right) = 49\left(x^2 + y^2\right) \tag{6.6}$$

and

$$32\left((x-100)^2 + (y-40)^2\right) = 49\left((x-70)^2 + y^2\right) \; . \tag{6.7}$$

Since the expected density ratios have been calculated from the distances the power m has dropped out of the equations. The system of equations (6.5) through (6.7) can be reduced to

$$(x+250)^2 + y^2 = \left(200\sqrt{2}\right)^2 \; , \tag{6.8}$$

$$\left(x + \frac{625}{6}\right)^2 + \left(y + \frac{125}{3}\right)^2 = \left(\frac{175}{6}\sqrt{29}\right)^2 \tag{6.9}$$

and

$$\left(x - \frac{230}{17}\right)^2 + \left(y + \frac{1280}{17}\right)^2 = \left(\frac{1400}{17}\sqrt{2}\right)^2 \tag{6.10}$$

respectively. They describe three different circles, see Figure 6.1.

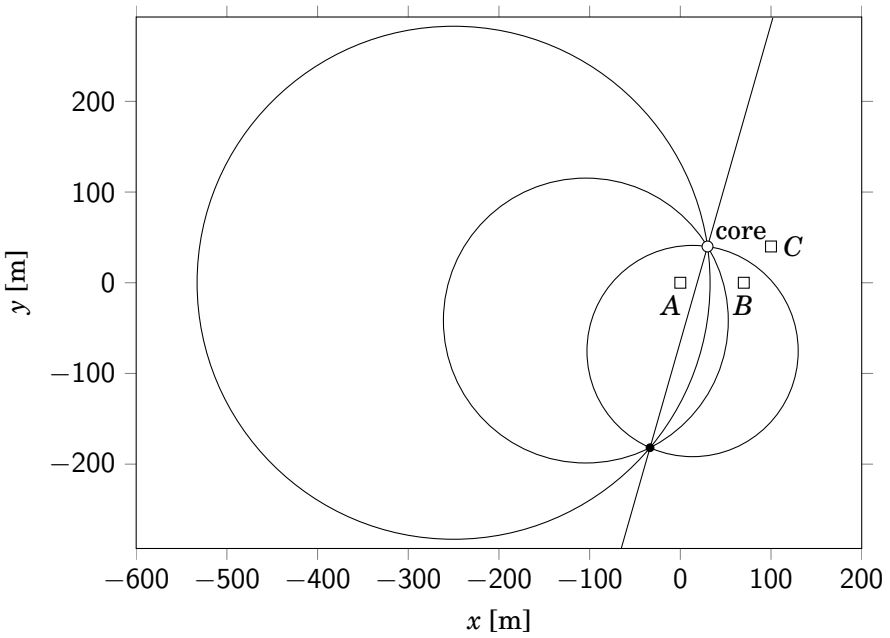

Figure 6.1: Three circles of possible core positions for expected densities in detectors A, B and C, and the radical axis.

Since each circle is determined by a density ratio it will be denoted as density-ratio-circle (DRC). The three DRC's intersect in two points. One of the intersections is at the imposed core position, $(30,40)$. The other intersection is equally possible if one only has access to the signals in A, B and C. The straight line between the two intersections is the radical axis. The DRC's bear properties known from hyperbolic geometry. The DRC's are mapped on themselves when inverted with respect to the circle circumscribing triangle ABC. Also the radical axis is mapped on itself and therefore crosses the center of the circumscribed circle of triangle ABC. To determine the radical axis, which is the essential ingredient of the algorithm, it is sufficient to consider just two of the three DRC's.

Next we consider detectors A, B and D. For the ratios of the densities at these three detectors we obtain:

$$\frac{\rho_A}{\rho_B} = \left(\frac{32}{25}\right)^{\frac{m}{2}} \quad , \quad \frac{\rho_A}{\rho_D} = \left(\frac{41}{25}\right)^{\frac{m}{2}} \quad , \quad \frac{\rho_B}{\rho_D} = \left(\frac{41}{32}\right)^{\frac{m}{2}} \quad . \tag{6.11}$$

From the ratio between ρ_A and ρ_B Equation 6.5 is obtained. New equations are obtained for the other two ratios:

$$25\left((x-70)^2+(y-90)^2\right) = 41\left(x^2+y^2\right) \tag{6.12}$$

and

$$32\left((x-70)^2+(y-90)^2\right) = 41\left((x-70)^2+y^2\right) \ , \tag{6.13}$$

which can be reduced to

$$\left(x+\frac{875}{8}\right)^2+\left(y+\frac{1125}{8}\right)^2=\left(\frac{25}{8}\sqrt{5330}\right)^2 \tag{6.14}$$

and

$$(x-70)^2+(y+320)^2=\left(40\sqrt{82}\right)^2 \tag{6.15}$$

respectively. The three DRC's are shown in Figure 6.2.

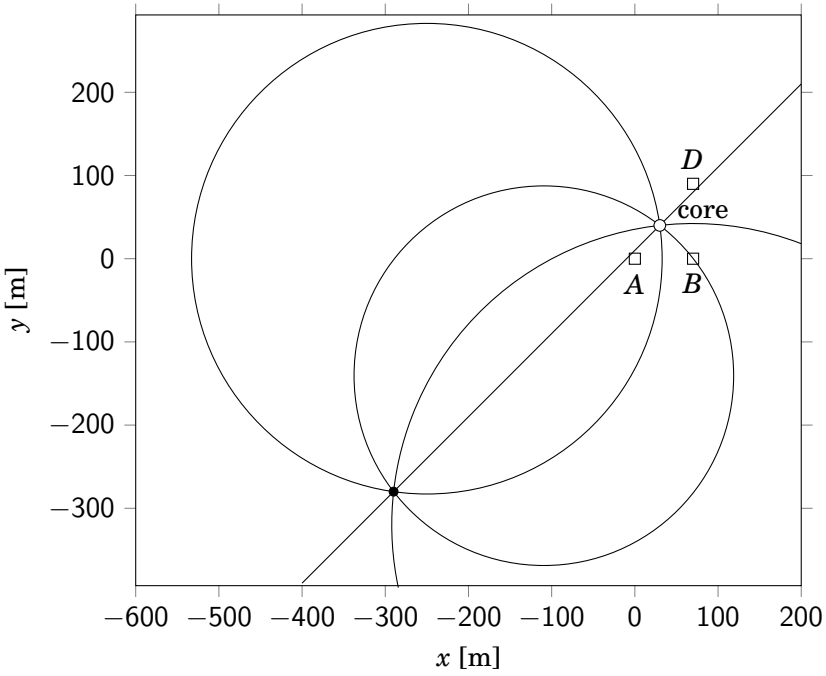

Figure 6.2: Three circles of possible core positions for detectors A, B and D, and the radical axis.

Also here the three DRC's intersect at the imposed core position and at another point. In all case a triple of detectors delivers two intersections of the DRC's. To determine which of the two intersections is the core position a fourth detector is needed, which is not on the circumscribed circle of the other three detectors.

For the other triples of detectors similar figures with three DRC's are obtained. For the quadruple $ABCD$ it results in four radical axes intersecting at the position of the imposed core, see Figure 6.3.

If detector E is also hit there will be $\binom{5}{3}=10$ triples of detector and thus 10 radical axes. If the signals in the detectors would be as expected, all radical axes would intersect in a single point: the position of the imposed core.

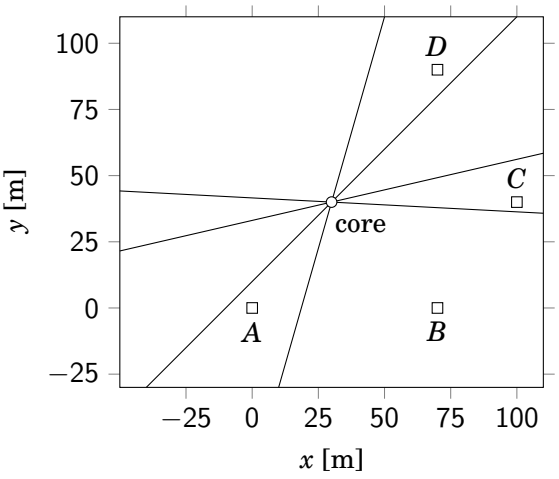

Figure 6.3: Four radical axes for the four triples of detectors which can be chosen out of A, B, C and D.

6.3 Sensitivity for the lateral density function

In the foregoing example the power m has fallen out the equations for the circles because the expected density ratios were derived from the distances. In reality we just have an observed density w in each detector. For instance, the equation for the ratio between signal w_A and w_C becomes

$$w_A^{2/m}\left(x^2+y^2\right) = w_C^{2/m}\left((x-100)^2+(y-40)^2\right)\ . \tag{6.16}$$

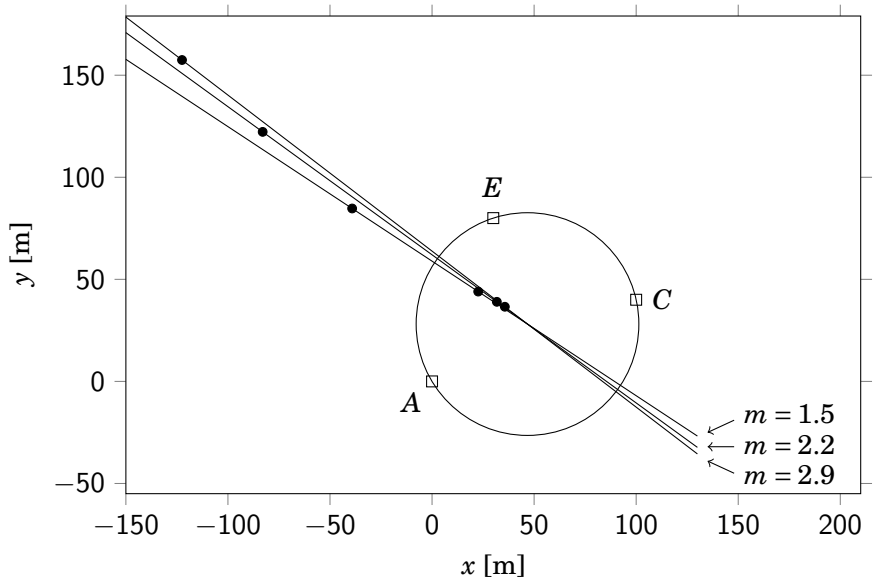

Figure 6.4: Possible core positions (black dots) and radical axes for three values of m, on the basis of signals in detectors A, C and E. The solid circle is the circumscribed circle of the triangle ACE.

The solution of Equation 6.16 depends on m. For each triple of detectors the position of the intersections of the DRC's depends on m. As a consequence the radical axis for each triple of detectors also depends on m. For the triple ACE the intersections and radical axis are shown for three values of m in Figure 6.4. On each radical axis shown in Figure 6.4 there are two possible core positions. The smaller m the closer the possible core positions are to the circle circumscribing triangle ACE. For a core outside the circumscribed circle of triangle ACE the distances between the detectors and the core are relatively large.

The insensitivity of radical axes for the value of m does not imply insensitivity of radical axes for variations of m as a function of distance to the core. For a realistic lateral density, such as the NKG function, m varies from values below 1 for small distances through values around 3 for large distances. The application of a NKG type of lateral density function leads to small differences with respect to the power law density. To illustrate it we consider the detectors A, C and E of the foregoing example. For the lateral density function the Equation 6.2 is used with $a = -0.5$, $b = -3.0$ and $r_0 = 30\,\mathrm{m}$. The equations for the ratios of the densities are more complicated. For the ratio between the expected densities at station A and C the equation reads

$$\rho_C \left(r_A^{-0.5} (30 + r_A)^{-3.0} \right) = \rho_A \left(r_C^{-0.5} (30 + r_C)^{-3.0} \right) , \tag{6.17}$$

where $\sqrt{(x - x_A)^2 + (y - y_A)^2}$ and $\sqrt{(x - x_C)^2 + (y - y_C)^2}$ should be read for r_A and r_C respectively. For the two other ratios the equations are similar. The equations are solved numerically. The result is shown in Figure 6.5.

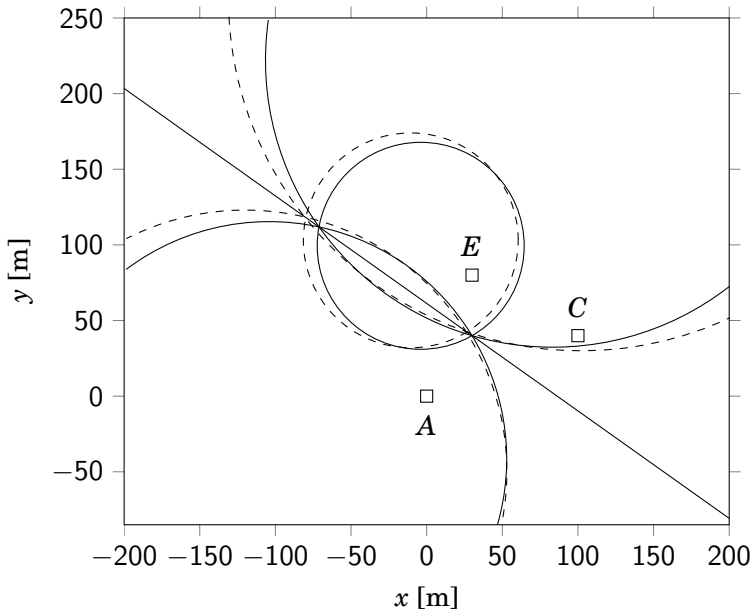

Figure 6.5: The three DRC's and the radical axis reconstructed from the densities in A, C and E assuming a power law density (solid) and assuming a NKG density (dashed).

In Figure 6.5 the analytical solution for the power law density is shown as well for comparison. For the NKG density the numerical solutions for the DRC's are not perfect circles. Of importance for the method is that the radical axis for the NKG density and the radical axis for the power law density practically coincide. For the imposed core at $(30,40)$ the distances to the detectors A, C and E are all larger than the 30 m we took for r_0. For these distances the NKG density is approximately a power law. However, if one detector is close to the core while another detector is more distant from the core the ratio of their densities will deviate from the power law. To see the consequences we move the imposed core to $(30,65)$. The result is shown in Figure 6.6.

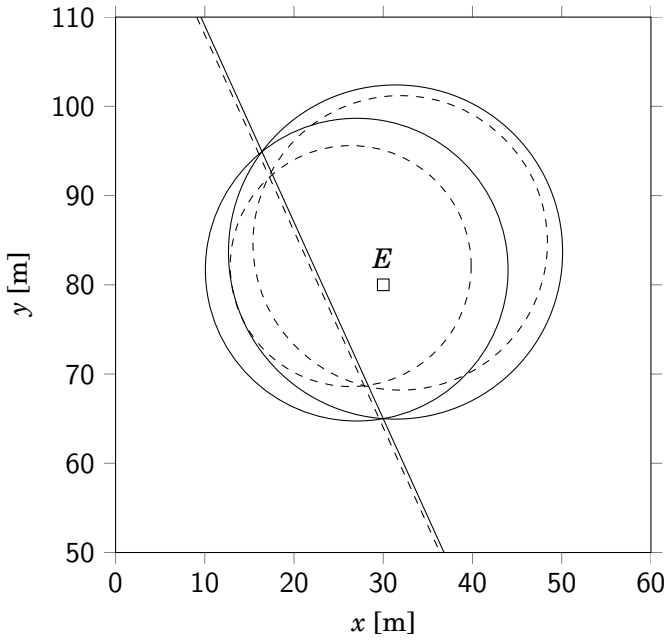

Figure 6.6: The two smallest DRC's and radical axis reconstructed from the densities in A, C and E assuming a power law density (solid) and assuming a NKG density (dashed).

Also here the radical axis for the NKG density is almost identical to the radical axis for the power law density. Figure 6.4 shows that the radical axis is not very sensitive for the value of m, while Figure 6.5 shows that the radical axis is rather immune for the applied density function. This allows us to use the power law with a single value for m. For the core estimations $m = 2.3$ is found to work best.

6.4 Core estimation from real signals

In general the observed signals will suffer from statistical fluctuations of physical nature (Landau distribution of energy losses and Poisson distribution of number of particles striking at a detector) and instrumental nature (measurement uncertainties). As a consequence the radical axis will no longer intersect in a single point. For many stations, and thus many radical axis,

there will be a cloud of intersection points. The idea behind the radical axis method is that the mean of the cloud can serve as an estimator for the core position. In Figure 6.7 a four station example is given of the radical axes for densities different from the expected ones.

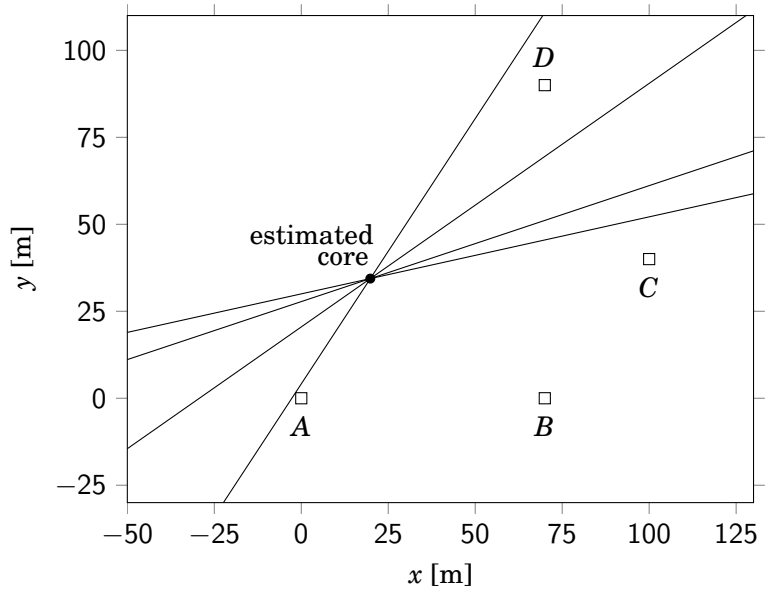

Figure 6.7: Four radical axes for realistic densities in detectors A, B, C and D.

The four radical axis of the quadruple $ABCD$ intersect in a single point. The situation changes with more than four detectors.

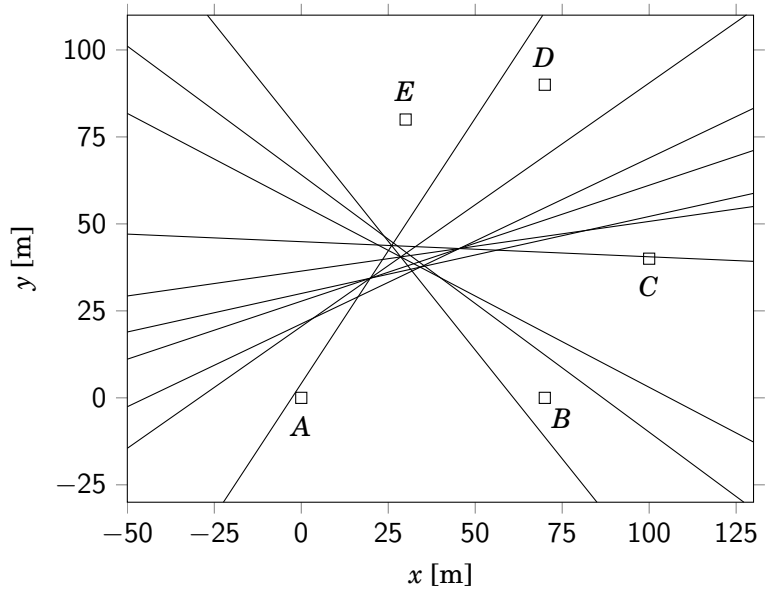

Figure 6.8: The radical axes for real signals in detectors A, B, C, D and E.

For 5 detectors we have 10 radical axes. Therefore $\binom{10}{2} = 45$ intersections are to be expected. For 5 detectors we also have $\binom{5}{4} = 5$ quadruples of detectors and thus 5 points of concurrency. So, 30 of the 45 intersections are grouped in 5 points of concurrency. For real signals in the 5 detectors A through E the 10 radical axes are shown in Figure 6.8. The pattern of intersections is shown in Figure 6.9. For the determination of the mean position of the intersections a sixfold intersection is counted as 6 single intersections. Alternatively, we just determine the 45 intersections of the 10 radical axes. The mean of it, shown as an open circle in Figure 6.9, is close to the imposed core.

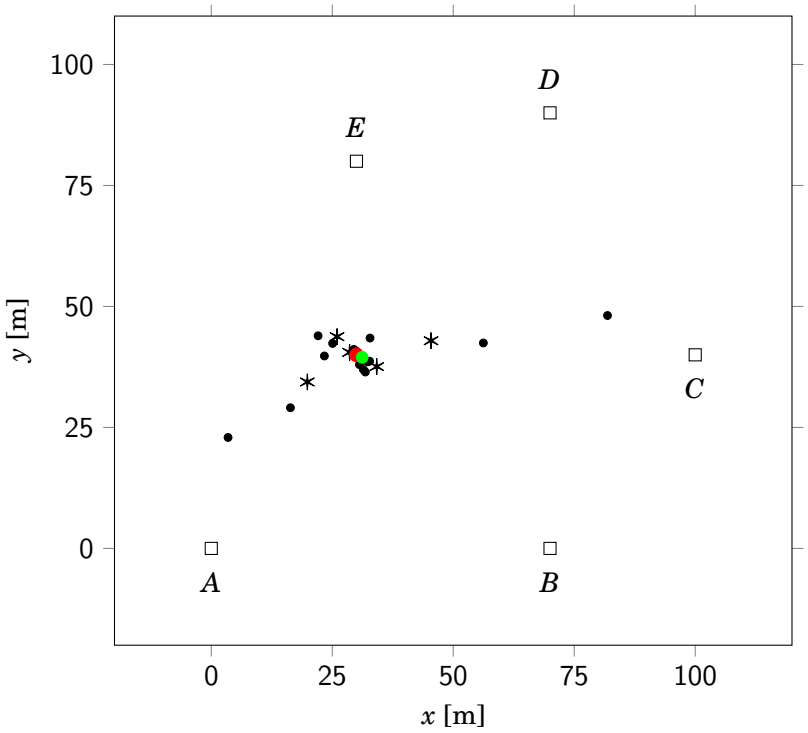

Figure 6.9: Intersections of 10 radical axes. The five points of concurrency are shown as an asterix, the other intersections as a dot. The mean of the intersections (green) is close to the imposed core (red).

6.5 Analysis for vertical showers

In this section the equations for the radical axes will be derived for vertical showers. That is, for the situation where the lateral density is concentrical around the core. For the analysis we consider three detectors 0, 1 and 2 at horizontal positions (x_0, y_0), (x_1, y_1) and (x_2, y_2). The detected signals in the three detectors are w_0, w_1 and w_2 respectively. For a core at position (x, y) the density at detector i is given by

$$w_i^{-\frac{2}{m}} \propto \left((x - x_i)^2 + (y - y_i)^2\right) , \tag{6.18}$$

where $i = 0,1,2$. From this we obtain the following two independent equations

$$p\left((x-x_0)^2+(y-y_0)^2\right) = (x-x_1)^2+(y-y_1)^2 \tag{6.19}$$

and

$$q\left((x-x_0)^2+(y-y_0)^2\right) = (x-x_2)^2+(y-y_2)^2 \ , \tag{6.20}$$

where

$$p = \left(\frac{w_0}{w_1}\right)^{\frac{2}{m}} \tag{6.21}$$

and

$$q = \left(\frac{w_0}{w_2}\right)^{\frac{2}{m}} \ . \tag{6.22}$$

The system of equations (6.19) and (6.20) can be reduced to

$$(x-a)^2+(y-b)^2 = r^2 \tag{6.23}$$

and

$$(x-c)^2+(y-d)^2 = s^2 \ , \tag{6.24}$$

where

$$a = \frac{x_1 - px_0}{1-p} \ , \quad b = \frac{y_1 - py_0}{1-p} \ , \tag{6.25}$$

$$c = \frac{x_2 - qx_0}{1-q} \ , \quad d = \frac{y_2 - qy_0}{1-q} \ , \tag{6.26}$$

$$r = \frac{\sqrt{p}}{1-p}\sqrt{(x_1-x_0)^2+(y_1-y_0)^2} \tag{6.27}$$

and

$$s = \frac{\sqrt{q}}{1-q}\sqrt{(x_2-x_0)^2+(y_2-y_0)^2} \tag{6.28}$$

Equations 6.23 and 6.24 represent two DRC's with centers (a,b) and (c,d) and radii r and s. The situation is illustrated in Figure 6.10. The line segment connecting the centers of the DRC's has length g and the projection of it onto the $x-$axis and $y-$axis are e and f respectively. The line through the intersections of the DRC's is the radical axis. The distance of both intersections with respect to the line through the centers of the DRC's is h. The radical axis divides the distance between the DRC centers in two parts with length k and $g-k$. From the identities

$$h^2 = r^2 - k^2 \tag{6.29}$$

and

$$h^2 = s^2 - (g-k)^2 \tag{6.30}$$

we obtain

$$k = \frac{g^2 + r^2 - s^2}{2g} \,. \tag{6.31}$$

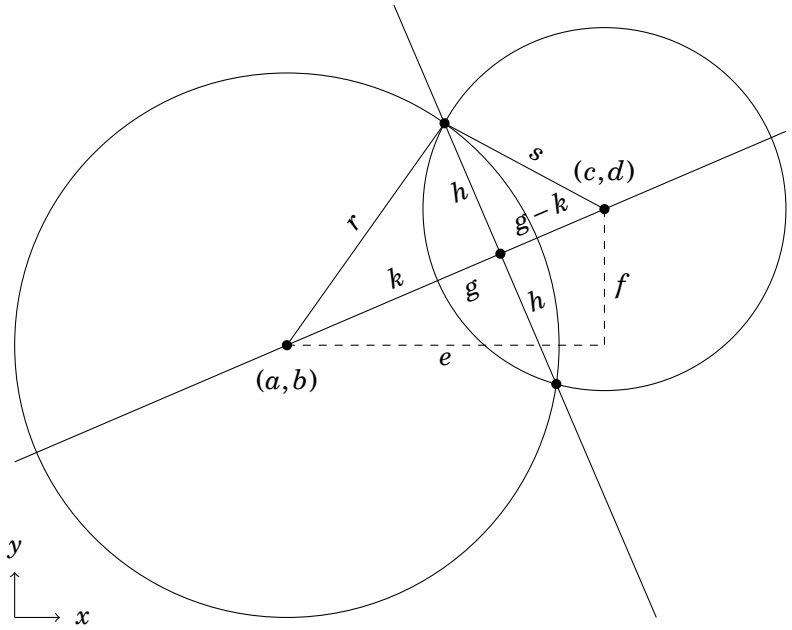

Figure 6.10: The intersection of two circles

An equation for the radical axis is obtained either from the geometry of Figure 6.10 or algebraicaly from the substraction of Equation 6.23 from Equation 6.24:

$$y = b - \frac{e}{f}(x - a) + \frac{g^2 + r^2 - s^2}{2f} \,, \tag{6.32}$$

where

$$e = c - a \,, \tag{6.33}$$

$$f = d - b \,, \tag{6.34}$$

and

$$g = \sqrt{e^2 + f^2} \,. \tag{6.35}$$

The coordinates of the intersections of the two circles (the possible cores) is obtained from the substitution of Equation 6.32 into Equation 6.23 or Equation 6.24:

$$x = a + \frac{ek \pm f\sqrt{r^2 - k^2}}{g} \tag{6.36}$$

and

$$y = b + \frac{fk \mp e\sqrt{r^2 - k^2}}{g} \ . \tag{6.37}$$

A plus sign in Equation 6.36 corresponds to a minus sign in Equation 6.37 and vice versa. Although the intersection of two circles is a standard mathematical exercise there are several ways to express the solutions. The present formulation is identical to a clear formulation found on the web [95]. The equation for the radical axis can also be written in the present formulation as

$$y = -\frac{e}{f}x + \frac{ae + bf + gk}{f} \ . \tag{6.38}$$

The DRC's do not intersect if $r^2 - k^2 < 0$. For this situation we have no predictions for the cores [96]. However, Equation 6.38 for the radical axis is independent of h. The radical axis therefore always exists. We therefore can still obtain information about the line on which a possible core is positioned.

For n detectors hit there are $m = \binom{n}{3}$ different triangles each delivering a radical axis. This results in $\binom{m}{2}$ intersections. For n detectors hit there are $\binom{n}{4}$ different quadruples. As a consequence $6 \cdot \binom{n}{4}$ of the m intersections are grouped in $\binom{n}{4}$ points of concurrency. When two radical axes are almost collinear the intersection may be far away. Such outliers are removed by discarding the distant ones. From the reduced set of intersections the mean is regarded as an estimator for the core position.

6.6 Inclined showers

In this section the analyses will be performed for inclined showers. The azimuthal angle ϕ and zenith angle θ are assumed to be determined from the arrival times. As before we start considering three detectors 0, 1 and 2 at horizontal positions (x_0, y_0), (x_1, y_1) and (x_2, y_2). The detected signals in the three detectors are w_0, w_1 and w_2 respectively. Also here the power law approximation will be taken for the lateral density. The projection of the inclined shower on a horizontal plane of observation reduces the density with a factor $\cos\theta$. On the other hand the energy loss of a particle in a scintillator is increased with a factor $\sec\theta$. Both effects compensate each other. What remains is the stretching of iso-density contours to ellipses. For the power law approximation we then have

$$w(r, \alpha; \theta; \phi) \propto u^{-m} \ , \tag{6.39}$$

where u is given by [60]

$$u = r\sqrt{1 - \cos^2(\alpha - \phi)\sin^2\theta} \ . \tag{6.40}$$

The expected signal at a given position (r,α) with respect to the core is

$$w^{-\frac{2}{m}} \propto u^2 = r^2\left(1-\cos^2(\alpha-\phi)\sin^2\theta\right) . \tag{6.41}$$

The situation is conveniently analyzed in a frame $(\hat{x},\hat{y})$ rotated by ϕ around the core with respect to the original frame (x,y). In the rotated frame $\hat{\phi}=0$, $\hat{\alpha}=\alpha-\phi$ and $\hat{r}=r$. The rotated frame is related to the original frame by

$$\begin{pmatrix}\hat{x}\\ \hat{y}\end{pmatrix} = \begin{pmatrix}\cos\phi & \sin\phi\\ -\sin\phi & \cos\phi\end{pmatrix}\begin{pmatrix}x\\ y\end{pmatrix}. \tag{6.42}$$

For a detector at position $(\hat{r}_i,\hat{\alpha}_i)$ this is

$$w_i^{-\frac{2}{m}} \propto \hat{u}^2 = \hat{r}_i^2\left(1-\cos^2\hat{\alpha}_i\sin^2\theta\right) . \tag{6.43}$$

For a core at position $(\hat{x},\hat{y})$ the expected signal at detector i then is given by

$$w_i^{-\frac{2}{m}} \propto \left((\hat{x}-\hat{x}_i)^2+(\hat{y}-\hat{y}_i)^2\right)-(\hat{x}-\hat{x}_i)^2\sin^2\theta , \tag{6.44}$$

or

$$w_i^{-\frac{2}{m}} \propto \left((\hat{x}-\hat{x}_i)^2\cos^2\theta+(\hat{y}-\hat{y}_i)^2\right) , \tag{6.45}$$

where $i=0,1,2$. From this we obtain the following two independent equations

$$p\left((\hat{x}-\hat{x}_0)^2\cos^2\theta+(\hat{y}-\hat{y}_0)^2\right) = (\hat{x}-\hat{x}_1)^2\cos^2\theta+(\hat{y}-\hat{y}_1)^2 \tag{6.46}$$

and

$$q\left((\hat{x}-\hat{x}_0)^2\cos^2\theta+(\hat{y}-\hat{y}_0)^2\right) = (\hat{x}-\hat{x}_2)^2\cos^2\theta+(\hat{y}-\hat{y}_2)^2 , \tag{6.47}$$

where

$$p=\left(\frac{w_0}{w_1}\right)^{\frac{2}{m}} \tag{6.48}$$

and

$$q=\left(\frac{w_0}{w_2}\right)^{\frac{2}{m}} . \tag{6.49}$$

The system of equations (6.46) and (6.47) differs from the system of equations (6.19) and (6.20) in that $x\to\hat{x}\cos\theta$ and $y\to\hat{y}$. That is, a rotation over ϕ and a stretching of circles to ellipses by a factor $\sec\theta$ in the direction of the azimuthal angle. We can therefore proceed in a similar way as for vertical showers. The system of equations (6.46) and (6.47) can be reduced to

$$(\hat{x}-\hat{a})^2\cos^2\theta+(\hat{y}-\hat{b})^2=\hat{r}^2 \tag{6.50}$$

and

$$(\hat{x}-\hat{c})^2\cos^2\theta+(\hat{y}-\hat{d})^2=\hat{s}^2\ , \tag{6.51}$$

where

$$\hat{a}=\frac{\hat{x}_1-p\hat{x}_0}{1-p}\ ,\quad \hat{b}=\frac{\hat{y}_1-p\hat{y}_0}{1-p}\ , \tag{6.52}$$

$$\hat{c}=\frac{\hat{x}_2-q\hat{x}_0}{1-q}\ ,\quad \hat{d}=\frac{\hat{y}_2-q\hat{y}_0}{1-q}\ , \tag{6.53}$$

$$\hat{r}=\frac{\sqrt{p}}{1-p}\sqrt{(\hat{x}_1-\hat{x}_0)^2\cos^2\theta+(\hat{y}_1-\hat{y}_0)^2} \tag{6.54}$$

and

$$\hat{s}=\frac{\sqrt{q}}{1-q}\sqrt{(\hat{x}_2-\hat{x}_0)^2\cos^2\theta+(\hat{y}_2-\hat{y}_0)^2}\ . \tag{6.55}$$

Equations 6.50 and 6.51 represent two ellipses with centers (a,b) and (c,d). An equation for the radical axis is obtained algebraically from the substraction of Equation 6.50 from Equation 6.51:

$$\hat{y}=\hat{b}-\frac{\hat{e}}{\hat{f}}(\hat{x}-\hat{a})\cos^2\theta+\frac{\hat{g}^2+\hat{r}^2-\hat{s}^2}{2\hat{f}}\ , \tag{6.56}$$

where

$$\hat{e}=\hat{c}-\hat{a}\ , \tag{6.57}$$

$$\hat{f}=\hat{d}-\hat{b}\ , \tag{6.58}$$

and

$$\hat{g}=\sqrt{\hat{e}^2\cos^2\theta+\hat{f}^2}\ . \tag{6.59}$$

The coordinates of the intersections of the two ellipses (the possible cores) is obtained algebraically from the substitution of Equation 6.56 into Equation 6.50 or Equation 6.51:

$$\hat{x}=\hat{a}+\frac{\hat{e}\cos\theta\hat{k}\pm\hat{f}\sqrt{\hat{r}^2-\hat{k}^2}}{\hat{g}\cos\theta} \tag{6.60}$$

and

$$\hat{y}=\hat{b}+\frac{\hat{f}\hat{k}\mp\hat{e}\cos\theta\sqrt{\hat{r}^2-\hat{k}^2}}{\hat{g}}\ , \tag{6.61}$$

where

$$\hat{k}=\frac{\hat{g}^2+\hat{r}^2-\hat{s}^2}{2\hat{g}}\ . \tag{6.62}$$

A plus sign in Equation 6.60 corresponds to a minus sign in Equation 6.61 and vice versa. The equation for the line through the intersections of the two ellipses can be written in the present formulation as

$$\hat{y}=-\frac{\hat{e}\cos^2\theta}{\hat{f}}\hat{x}+\frac{\hat{a}\hat{e}\cos^2\theta+\hat{b}\hat{f}+\hat{g}\hat{k}}{\hat{f}}\ . \tag{6.63}$$

In the (x, y) frame this is

$$y = Ax + B \ , \tag{6.64}$$

where

$$A = \frac{\hat{f}\sin\phi - \hat{e}\cos^2\theta\cos\phi}{\hat{f}\cos\phi - \hat{e}\cos^2\theta\sin\phi} \tag{6.65}$$

and

$$B = \frac{\hat{a}\hat{e}\cos^2\theta + \hat{b}\hat{f} + \hat{g}\hat{k}}{\hat{f}\cos\phi - \hat{e}\cos^2\theta\sin\phi} \ . \tag{6.66}$$

6.7 Implementation in SAPPHiRE

The present implementation in SAPPHiRE is specifically intended for the SPA site. The core is reconstructed on the basis of stations signals. A station signal is the mean of the detector signals. When a shower hits a number of stations of the SPA site there is a probability that the core is somewhere 'inside' the configuration of stations hit. For this situation a prediction for the core position is the barycenter: the mean of the station positions weighted with the station signals. The radical axis method deliver a prediction for the core position, either 'inside' or 'outside' the configuration of stations. In SAPPHIRE initially the core is estimated with both the barycenter method and the radical axes method. In case of the radical axes method an intersection can be extremely far away if two radical axes happen to be almost collinear. The disturbing effect of such outliers are avoided by discarding the intersections outside a 1200 m $\times$ 1200 m square around the center of the SPA site. Both the barycenter and the radical axes prediction are used as the initial value for further optimization. Afterwards one of the two survives on the basis of the χ^2 values.

An estimated core position is in general not the optimal position. A better core position is obtained by calculating χ^2 values for positions on a grid around a predicted core position. For each grid point the shower size is obtained by regression since the lateral density function scales linearly with shower size. The expected signal can then be written as

$$\rho(r) = N\nu(r) \ , \tag{6.67}$$

where N is the shower size. Equation 6.1 then reads

$$\chi^2 = \sum_{i=1}^{n} \frac{(w_i - Nv_i)^2}{Nv_i} \tag{6.68}$$

This can be elaborated to

$$\chi^2 = \sum_{i=1}^{n} \left(Nv_i - 2w_i + \frac{w_i^2}{Nv_i} \right) \tag{6.69}$$

The value of χ^2 is optimal if $\partial\chi^2/\partial N = 0$. The latter condition implies

$$N = \sqrt{\frac{\sum(w_i^2/v_i)}{\sum v_i}} \ , \tag{6.70}$$

where the summations runs over the n detectors. Substitution of the expression for N in the expression for χ^2 gives

$$\chi^2 = 2\sqrt{\frac{\sum(w_i^2/v_i)}{\sum v_i}} \sum v_i - 2\sum w_i \ . \tag{6.71}$$

Again, i runs from 1 through n. In conclusion, one can obtain a better value for the shower size N and a value for χ^2 by a few summations.

For the implementation in SAPPHiRE a 9 × 9 grid with grid spacing 20 m is taken around the barycenter prediction. By inspection the grid position with the smallest value for χ^2 is determined. Then a 9 × 9 grid with grid spacing 5 m is taken around the position found in the previous grid. Again, the position on the fine grid with the smallest value for χ^2 is determined by inspection. Also for the radical axes prediction a 9 × 9 grid is taken, with a large grid spacing 50 m because of the larger area 'outside' the configuration of stations. The grid position with the smallest value for χ^2 is determined by inspection. Also here an additional 9 × 9 grid, now with grid spacing 10 m, is taken around the position found in the previous grid and also here the position on the fine grid with the smallest value for χ^2 is determined by inspection. From the two resulting candidates, one originating from the barycenter and one from the radical axes prediction, the position with the smallest χ^2 value is taken. Finally, a 9 × 9 grid with grid spacing 4 m is taken around the 'best out of two choice' and the grid position with the smallest value for χ^2 is determined by inspection. The latter is considered as the 'best' result. The corresponding prediction for $N_{e+\mu}$ is regarded as the 'best' estimation for the shower size. The above procedure consumes about 40 ms computer time (on a 1.8 GHz Intel Core i7 processor) for the reconstruction of the core position and the shower size for a single shower.

In summary, the reconstruction of the core and size of a shower consists in a prediction by means of the barycenter and the radical axes method and the subsequent inspection of χ^2 values on a grid of limited size. The grid sizes and grid spacings are a result of trying out several combinations. Larger grids or smaller grid spacings do not lead a better performance for the SPA configuration of stations. Other configurations may require other grid sizes and grid spacings.

6.8 Performance

The performance of the reconstruction is investigated by means of a set of simulated showers with different energies and with different zenith angles: 0°, 15°, 30° and 45°. Each shower was randomly thrown 10 000 times on an area of $4\,\mathrm{km}^2$ around the stations 501 through 506, 508 and 509 of the SPA site. For instance, the simulated 10^{17} eV vertical shower has $N_{e+\mu} = 2.03 \cdot 10^7$. Only on 154 occasions the vertical shower hit all the eight stations 501 through 506, 508 and 509; an eightfold coincidence. For these cases the mean distance between the reconstructed and generated core, is 15.7 m. The distribution of reconstructed shower sizes is shown in Figure 6.11.

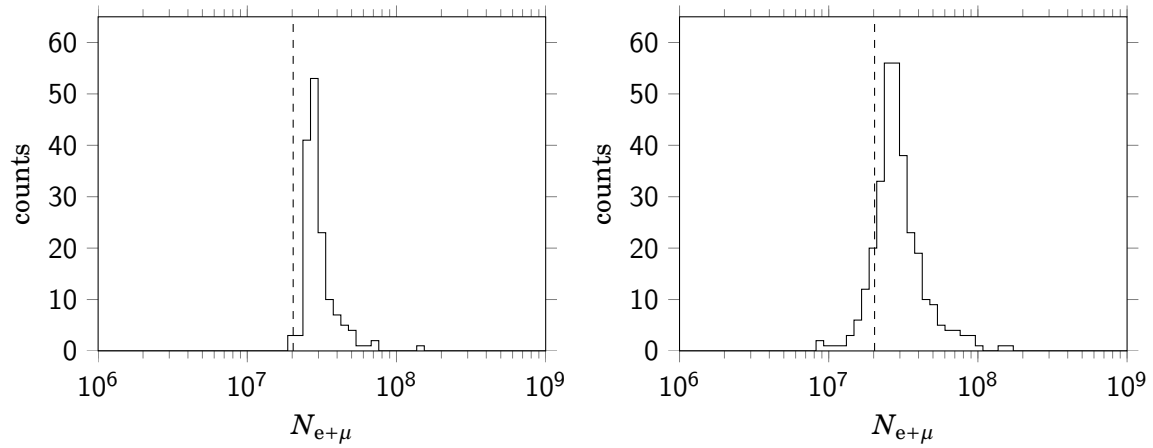

Figure 6.11: The distribution of reconstructed shower sizes for a simulated 10^{17} eV vertical shower which caused eightfold (left) and sevenfold (right) coincidences in the eight stations considered. The vertical dashed line represents the simulated shower size.

The mean and spread of the distribution is $\mu = 3.2 \cdot 10^7$ and $\sigma = 1.3 \cdot 10^7$. For the same shower sevenfold coincidences occurred on 312 occasions. The distribution of reconstructed shower sizes is also shown in Figure 6.11. Now the mean and spread of the distribution is $\mu = 3.2 \cdot 10^7$ and $\sigma = 1.7 \cdot 10^7$, and the mean distance between the reconstructed and the generated core is 31.1 m. The average reconstructed shower size is comparable to the situation for eightfold coincidences. In both cases the shower size is on average overestimated by 60 %. For the sevenfold coincidences the spread is larger since the reconstructed cores are at larger distances from the center of the configuration of stations.

Another simulated shower is a 10^{17} eV shower with zenith angle 15° and $N_{e+\mu} = 1.63 \cdot 10^7$. For each coincidence size, 4 through 8, the distribution of reconstructed shower sizes and the mean core deviations are determined. The errors below and above the mean values are separately determined to express the asymmetry of the distributions. The results are shown in Figure 6.12.

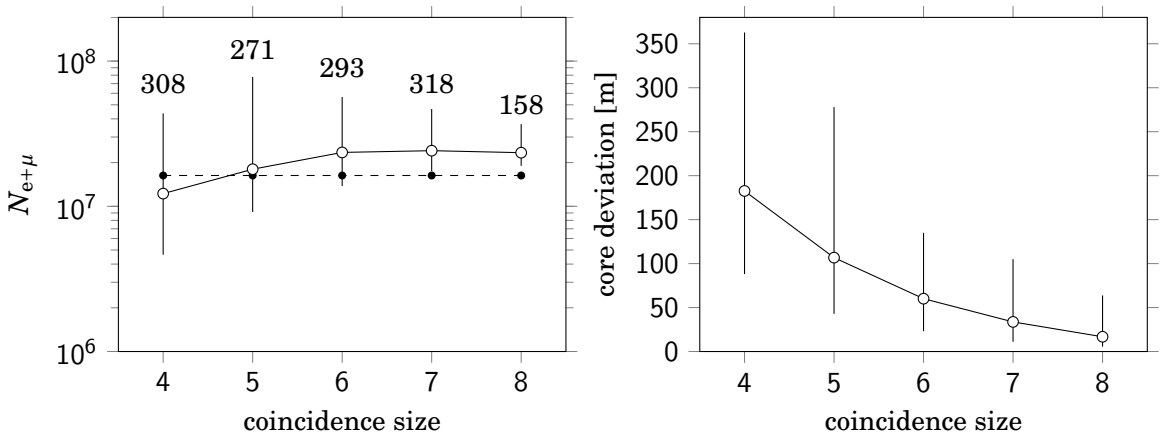

Figure 6.12: Left panel: Reconstructed shower sizes for fourfold through eightfold coincidences caused by a 10^{17} eV shower with zenith angle 15°. The black dots, connected by a horizontal dashed line, represent the simulated shower size. The number of entries are shown above the error bars. Right panel: For the same entries the distance between the reconstructed and simulated core positions.

As expected, the spread in the reconstructed shower sizes and the mean core deviation decrease for increasing coincidence size. For eightfold coincidences the core position can be accurately reconstructed because 10^{17} eV showers causing eightfold coincidences are close to the center of the configuration of stations. For 10^{18} eV showers n-fold coincidences can be caused by more distant cores. Fourfold and fivefold coincidences caused by a distant 10^{18} eV shower can be mistaken for a nearby shower with less energy. For this reason the reconstructed shower size tends to smaller values for smaller coincidence sizes, see left panel of Figure 6.13. As a consequence the core reconstructions becomes less accurate, see right panel of Figure 6.13.

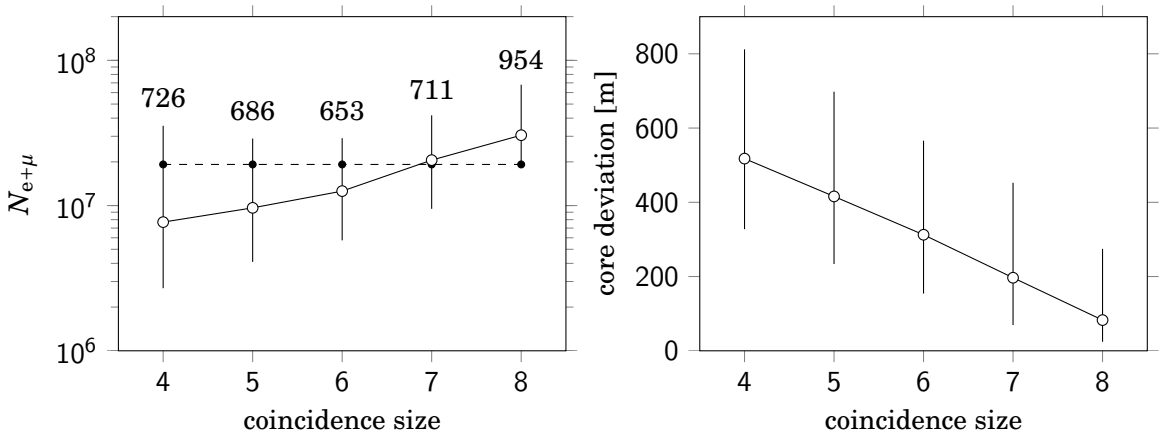

Figure 6.13: Left panel: Reconstructed shower sizes for fourfold through eightfold coincidences caused by a 10^{18} eV shower with zenith angle 45°. The black dots, connected by a horizontal dashed line, represent the simulated shower size. The number of entries are shown above the error bars. Right panel: For the same entries the distance between the reconstructed and simulated core positions.

Next the distribution of reconstructed shower sizes is investigated for different zenith angles. For 10^{15} eV showers the reconstructions are almost absent since they are in general not large enough to cause fourfold coincidences. We therefore start with the reconstructions for 10^{16} eV showers with zenith angles 0°, 15°, 30° and 45°. The results are shown in Figure 6.14 for fourfold and fivefold coincidences.

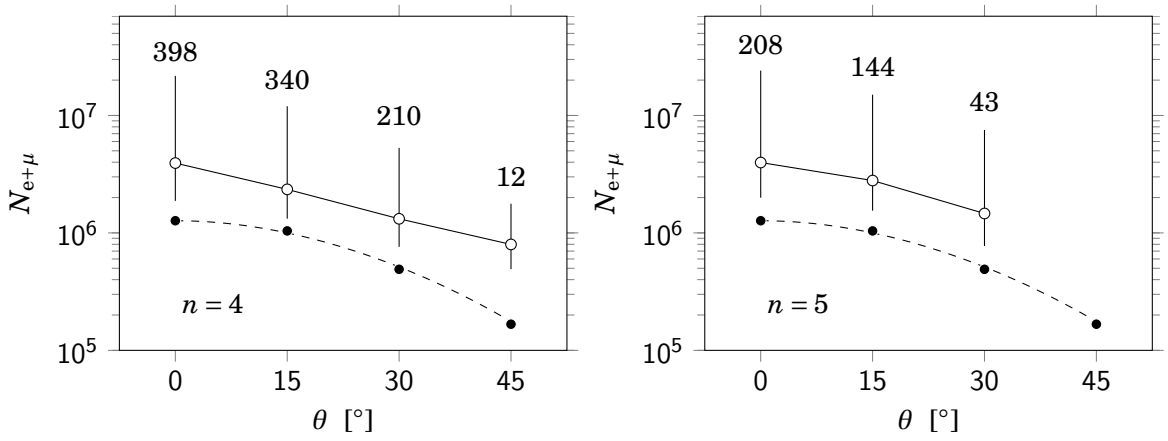

Figure 6.14: Reconstructed shower sizes for 10^{16} eV showers with zenith angles 0°, 15°, 30° and 45° which caused fourfold (left) and fivefold (right) coincidences in the eight stations considered. In the right panel the result for 45° is not shown because of absence of entries. The number of entries are shown above the error bars. The black dots, connected by a dashed curve, represent the simulated shower sizes.

For the few sixfold coincidences caused by 10^{16} eV showers with zenith angle 0° and 15° the results are comparable with the ones for fivefold coincidences. Large coincidence sizes can occur for 10^{17} eV showers if the zenith angle is not too large. For this energy the reconstruction results are shown in Figure 6.15 for fivefold through eightfold coincidences. The reconstructed shower sizes follow the zenith angle dependence. Nevertheless, a structural overestimation is present. The causes are not clear. The difference between the real and simulated energy losses for low energy electrons might be one of the causes.

The accuracy of the reconstruction might depend on the number of stations that are on duty. To this end station 510 is included in the simulations. Showers which cause eightfold coincidences in the situation without station 510 will almost certainly cause ninefold coincidences in the situation with station 510 since station 510 is very close to station 501. The reconstructions for both situations are conducted with a 10^{17} eV shower with zenith angle 15° thrown 10 000 times. The simulated shower size is $1.63 \cdot 10^7$ ground particles. For the situation without station 510 there are 158 eightfold coincidences. For the situation with station 510 there are 162 ninefold coincidences. For both cases the distribution of reconstructed shower sizes is shown in Figure 6.16.

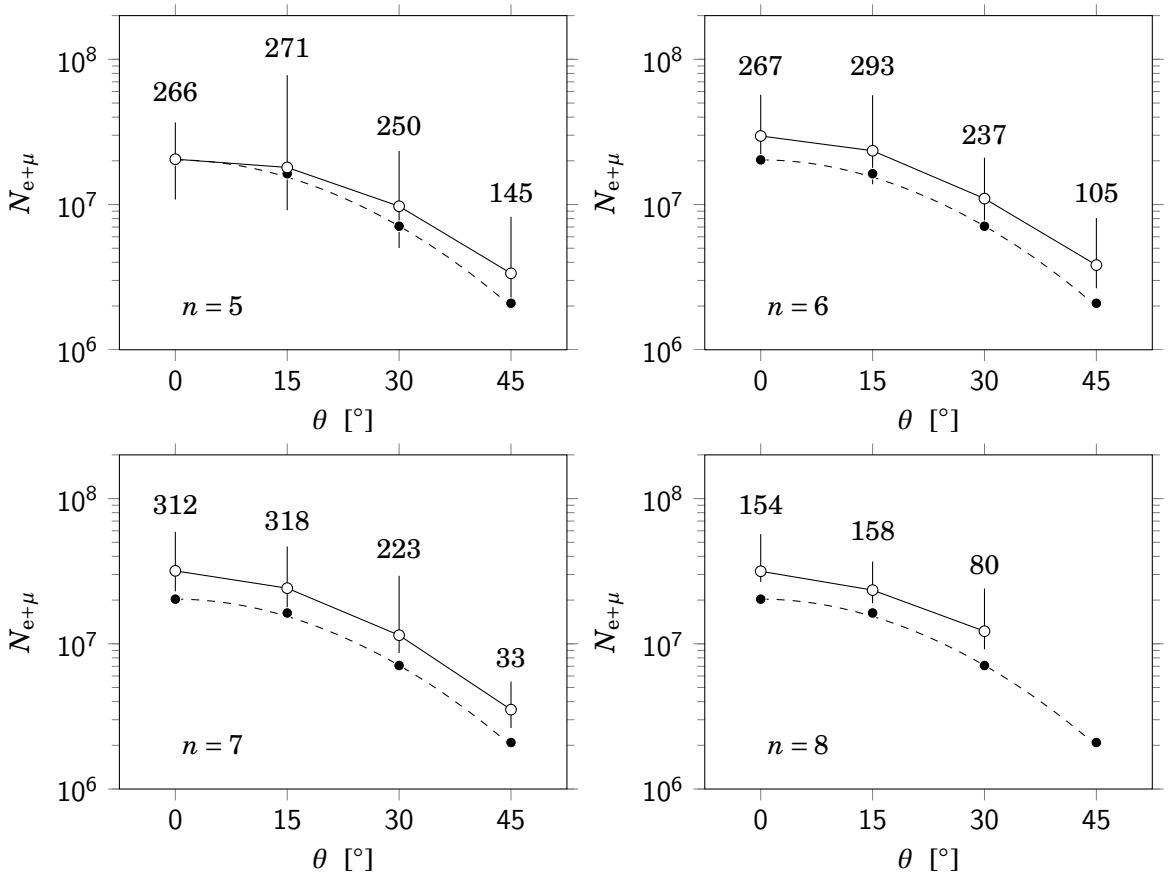

Figure 6.15: Reconstructed shower sizes for 10^{17} eV showers with zenith angles 0°, 15°, 30° and 45° which caused fourfold (upper left) through eightfold (lower right) coincidences in the eight stations considered. The black dots, connected by a dashed curve, represent the simulated shower sizes.

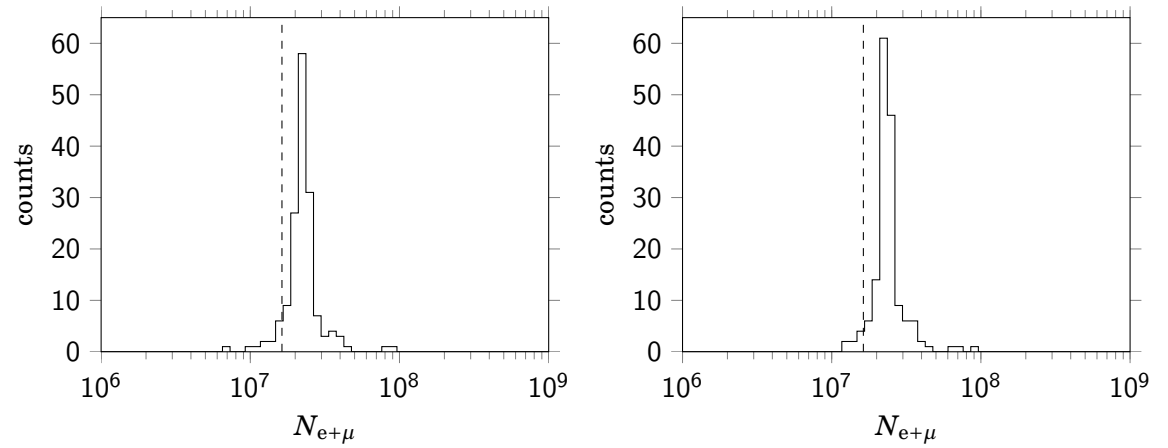

Figure 6.16: The distribution of reconstructed shower sizes for simulated 10^{17} eV shower with zenith angle 15° which caused eightfold coincidences in the eight stations considered (left) and which caused ninefold coincidences in nine stations considered, thus with station 510 included. The vertical line represents the simulated shower size.

For the situation without station 510 the reconstructed shower size has a mean of $2.34 \cdot 10^7$ and a standard deviation of $8.5 \cdot 10^6$. For the situation with station 510 the reconstructed shower size has a mean of $2.47 \cdot 10^7$ and a standard deviation of $8.7 \cdot 10^6$. In both situations a structural overestimation is present. The distributions are comparable. This implies that a 'double' station has not a large effect on the reconstruction in comparison with a single station. For shower reconstructions it is best to take a different location for each additional station.

In the shower size distributions shown there are a few outliers. One might consider to inspect the χ^2 values of the reconstructions. If there turns out to be a clear relation between 'bad' reconstructions and large χ^2 values, one might consider to use the χ^2 value as a criterium for rejection. The consequences for the acceptance should then be investigated. The overall conclusion is that further research is required for possible improvement of the algorithm and for the determination of the accuracy of the reconstructions for different energies, different zenith angles, different constellations of station and different coincidence sizes.

6.9 Energy reconstruction

With the shower size is meant the total number of electrons and muons: $N_{e+\mu}$. Once the shower size is estimated, the energy of the shower can also be estimated. This requires the relation between the energy and shower size for each zenith angle. The relation is derived from the inspection of simulated showers, 27 688 at the time of investigation.

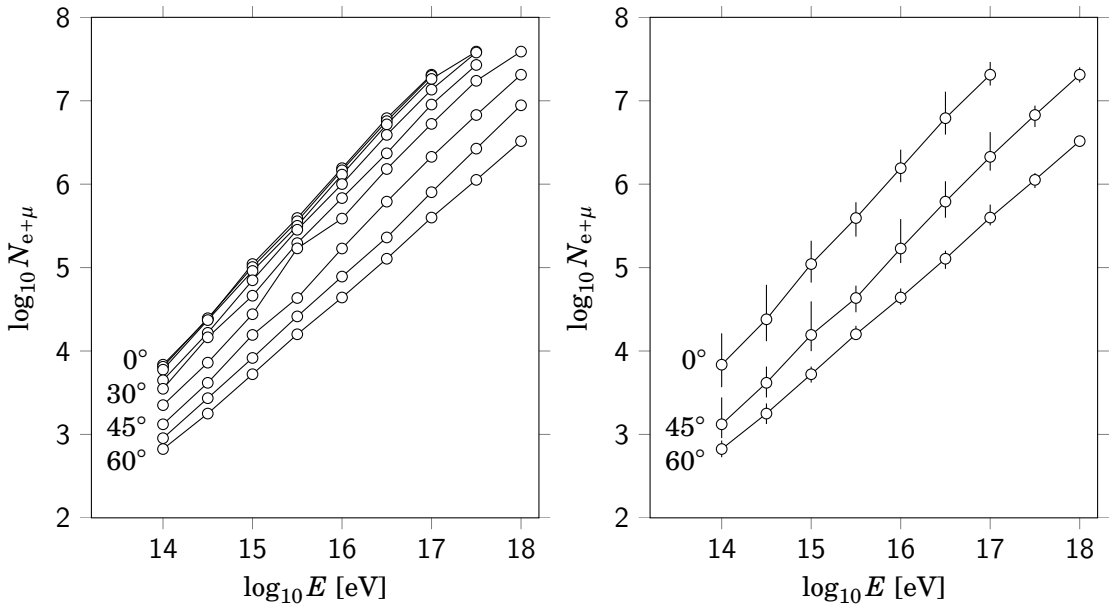

Figure 6.17: The shower size against energy for zenith angles 0° through 60° in steps of 7.5° (left). The same plot with error bars restricted to 0°, 45° and 60° to avoid overlap.

For each energy there is a distribution of shower sizes because of variations in the altitude of first interaction and in the further evolution. The energy is reconstructed on the basis of the mean shower size. In the left panel of Figure 6.17 the mean shower size is plotted against energy. In the right panel the error bars are plotted as well for a few zenith angles to given an impression of the uncertainty. The curves are fitted with a linear function:

$$\log_{10} N_{e+\mu} = a \cdot \log_{10} E + b \ , \tag{6.72}$$

where E is in eV.

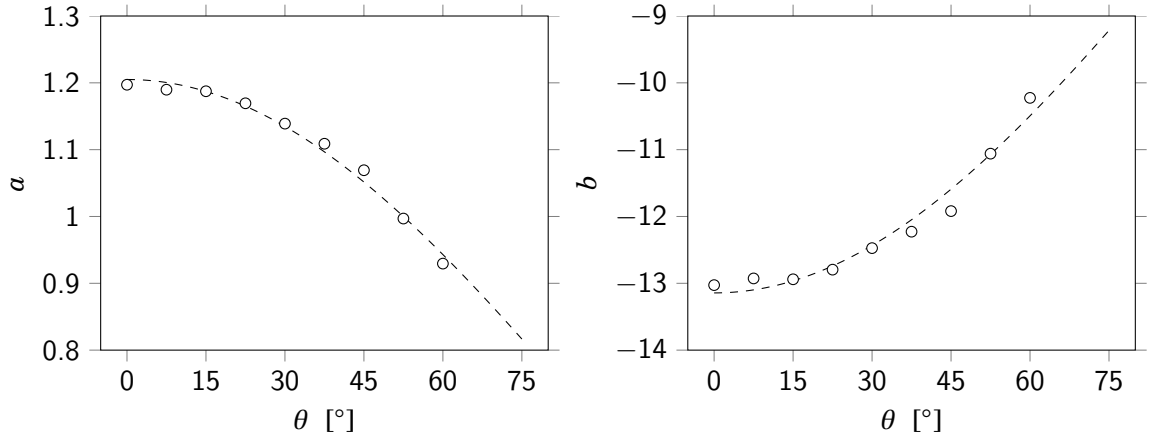

Figure 6.18: The coefficients a (left) and b (right) versus zenith angle and the fit curves (dashed)

For each zenith angle the coefficients a and b are determined. The coefficients, plotted against zenith angle in Figure 6.18, are fitted with $w + v\cos\theta$. For coefficient a: $w = 0.681$ and $v = 0.524$, and for coefficient b: $w = -7.844$ and $v = -5.300$. The values of a are highly correlated to the values of b, the correlation coefficient being 0.997. The shower size versus energy can therefore be parameterized as

$$\log_{10} N_{e+\mu} = (0.681 + 0.524\cos\theta) \cdot \log_{10} E - (7.844 + 5.300\cos\theta) \ , \tag{6.73}$$

By means of this relation the diagrams in the left panel of Figure 6.12 and the lower left panel of Figure 6.15 are transformed to the diagrams shown in the left panel and the right panel of Figure 6.19.

The left panel of Figure 6.20 shows the reconstructed energy distribution for simulated showers with energy 10^{17} eV and zenith angle 0°, 15°, 30° and 45° that have caused coincidence sizes 6 through 8. For the energy distribution: $\mu = 1.40 \cdot 10^{17}$ and $\sigma = 7.4 \cdot 10^{16}$. The right panel of Figure 6.20 shows the reconstructed energy distribution for simulated showers with energy 10^{18} eV and zenith angle 45° that have caused coincidence sizes 6 through 8. For the energy

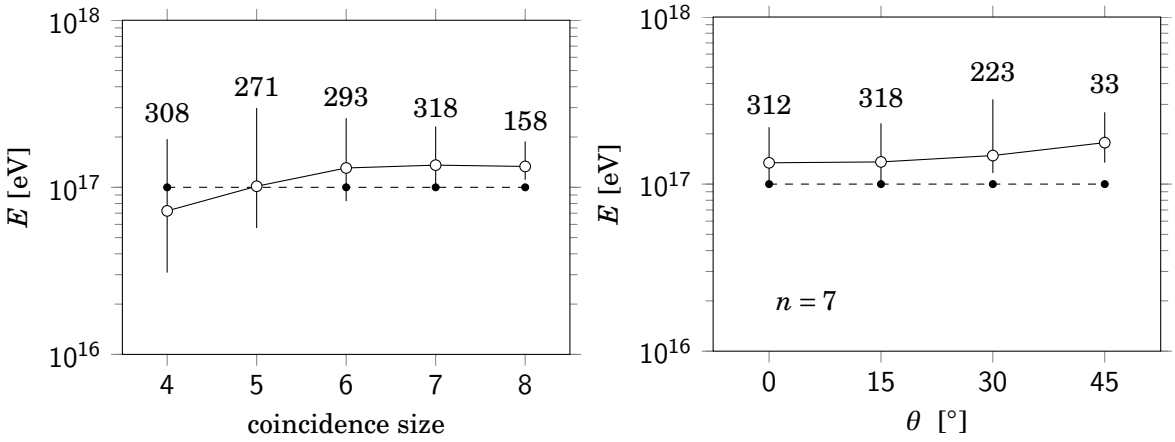

Figure 6.19: Left panel: Reconstructed shower energies for fourfold through eightfold coincidences caused by a 10^{17} eV shower with zenith angle 15°. The number of entries are shown above the error bars. Right panel: Reconstructed shower energies for 10^{17} eV showers with zenith angles 0°, 15°, 30° and 45° which caused sevenfold coincidences in the eight stations considered. In both panels the black dots, connected by a horizontal dashed line, represent the simulated shower energies.

distribution: $\mu = 1.02 \cdot 10^{18}$ and $\sigma = 8.5 \cdot 10^{17}$. The tail to the left in the distribution of the right panel in Figure 6.20 is, as mentioned before, due to far away cores ascribed to nearby cores.

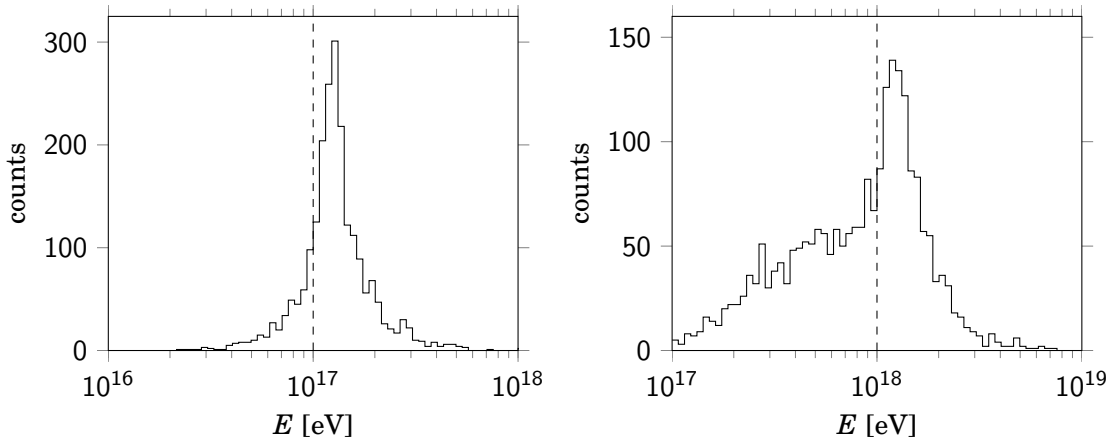

Figure 6.20: Left panel: Distribution of 2184 reconstructed energies for simulated showers with energy 10^{17} eV and zenith angle 0°, 15°, 30° and 45° that have caused coincidence sizes 6 through 8. Right panel: Distribution of 2318 reconstructed energies for simulated showers with energy 10^{18} eV and zenith angle 45° that have caused coincidence sizes 6 through 8. In both panels the vertical dashed line is the imposed energy.

6.10 Summary

For the reconstruction of the shower core a method has been developed on the basis of radical axes. To my best knowledge such a method is not present in the literature. The method delivers in a reasonable amount of time an estimation for the core position. The core prediction is further improved by inspecting an array of possible core positions around the estimated position. The present implementation of the radical axis method is based on vertical showers. Differences caused by the inclination of a shower are assumed to be abolished because of the subsequent inspection of an array of possible core positions. Nevertheless, it seems worthwhile to investigate if better accuracies may be achieved by generalizing the radicals axis method to inclined showers as described in the text.

Although the radical axis method works satisfactorily, the reconstructions on the basis of a small number of stations are unavoidably inaccurate. Firstly because the reconstruction is more sensitive for deviations between observed and expected densities if the number of stations is small. Secondly because a shower with the core at a large distance from the stations can be mistaken for a shower with less energy with the core close to the stations. This is not a shortcoming of the radical axis method. For any method the inaccuracies will increase for decreasing coincidence size. For the reconstruction of individual showers it therefore is recommended to restrict to at least sixfold coincidences.

7

Shower data analysis

7.1 Event characteristics

When almost simultaneous signals in two detectors of a station are large enough, the station is triggered and the traces of this event are recorded. From the traces the pulse heights and pulse integrals are determined. From the pulse integrals and the MIP (Minimum Ionizing Particle) peak, the signals are expressed as a number of MIPs. This can roughly be interpreted as the number of particles that have passed the scintillator plate of a detector. In Figure 7.1 a pulse height diagram and a pulse integral diagram for detector 0 of station 501 are shown. The peaks do follow Gaussian distributions, appearing as a parabolas because of the logarithmic scale, with $\sigma = 0.3\mu$ as derived in Chapter 4.

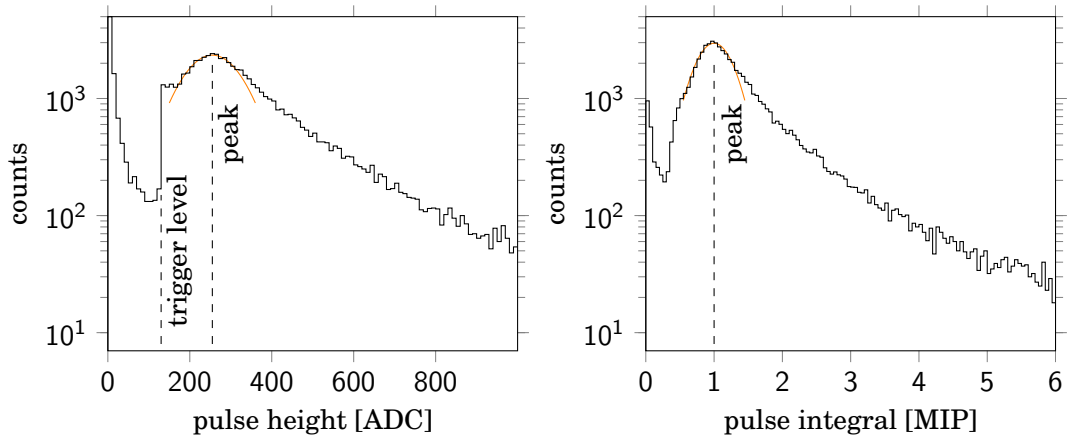

Figure 7.1: Pulse height (left) and pulse integral (right) distributions for detector 0 of station 501. Data taken between 2015-08-28, 00:00:00 and 2015-08-30, 00:00:00. The orange curves are Gaussian functions with $\sigma = 0.3\mu$.

The 'peak' at the most left part of the pulse height diagram is caused by the gamma's. The peak to the right of the 'two high' trigger level is caused by the charged particles, by far mostly electrons and muons. Once the events of a station are registered one can afterwards determine the number of events where 0, 1, 2, 3 or 4 detectors have a pulse height exceeding a chosen threshold value. In Figure 7.2 these five numbers are plotted against the threshold value in ADC.

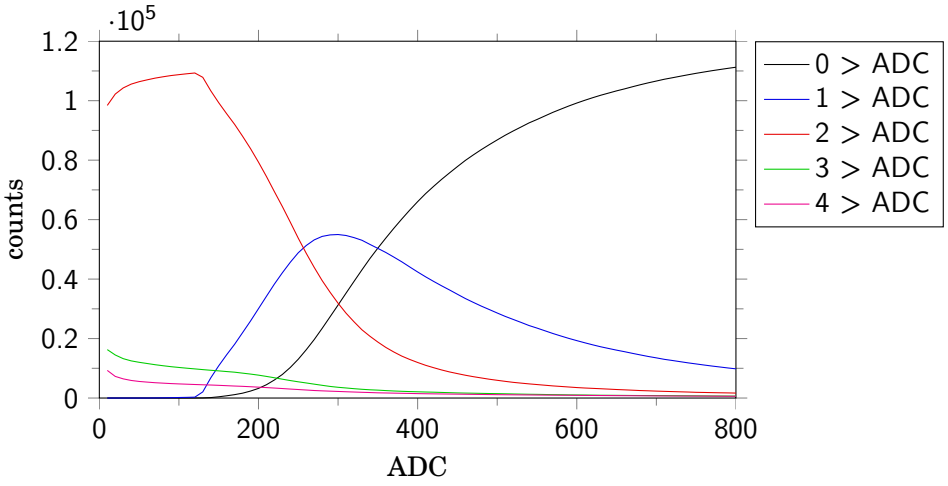

Figure 7.2: Numbers of events where the pulse height in 0, 1, 2, 3 or 4 detectors of station 501 has exceeded a given value in ADC. Data taken from 2013-08-28, 00:00:00 through 2013-08,-30 0:00:00.

We see the curve for 2 detector having a pulse height larger than a given value drops downwards, in favor of the curve for 1 detector, around 125 ADC. A similar diagram can be made for the pulse integrals in MIP, see Figure 7.3.

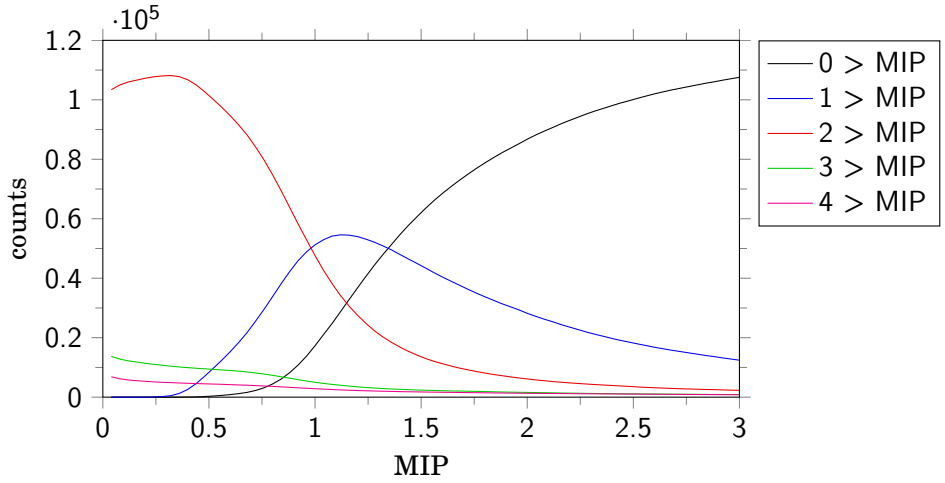

Figure 7.3: Numbers of events where the pulse integral in 0, 1, 2, 3 or 4 detectors of station 501 has exceeded a given value in MIP. Data taken from 2013-08-28, 00:00:00 through 2013-08-30, 00:00:00.

Both diagrams show a great similarity. For increasing threshold the red curves drop downwards, in favor of the blue curves, around 125 ADC and 0.3 MIP respectively. In both diagrams the blue curve intersects the red curve at a threshold value close to the peak value of the pulse height distribution and pulse integral distribution respectively. For larger thresholds also the blue curve drops down in favor of the black curve. In both diagrams the threshold value for which the blue curve reaches its maximum is about 15 % larger than the peak value of the pulse height and pulse integral distributions. The threshold value where the blue curves obtain their maximum being in the neighborhood of the threshold value where the red and black curves intersect, implies that the slopes of red and black curves at the point of intersection are almost equal (except for the opposite sign).

If 0.3 MIP is taken as the offline threshold, most events have 2 plates passing the threshold, while the numbers for 3 plates and 4 plates passing the threshold are small. Increasing the threshold changes the counts. If the threshold in MIP is taken as an offline trigger condition, we can determine the counts with two, three and four plates 'hit', where 'hit' means 'passed the threshold'. In Figure 7.4 the fractions of two, three and fourfold hits are plotted against the threshold value. At 3.5 MIP threshold there are as many threefold hits as fourfold hits.

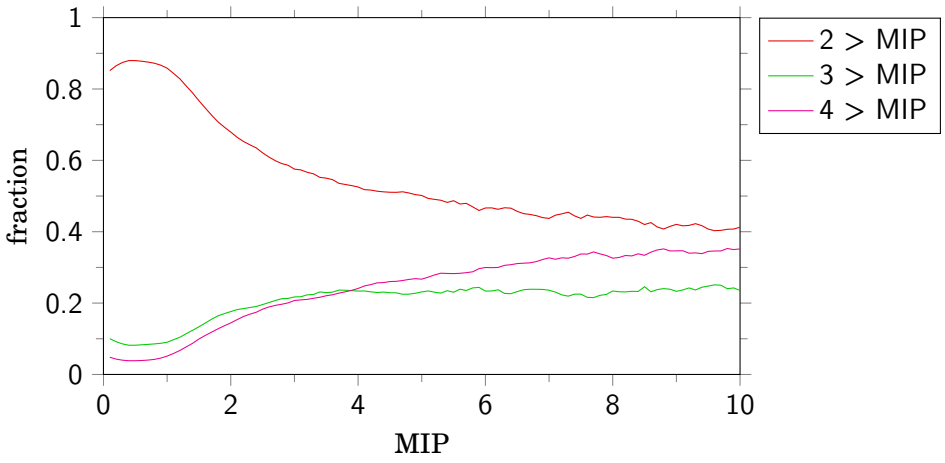

Figure 7.4: Fractions of 2, 3 and 4 plates of station 501 having passed a threshold value in MIP. Data taken from 2013-08-28, 00:00:00 through 2013-08-30, 0:00:00.

Since the three fractions add up to unity, one can also plot them in a ternary diagram, see Figure 7.5. As can be expected for low thresholds (and thus in general for low densities) the fractions start in the neighborhood of the lower right corner. It can also be expected that for very high thresholds (and thus very high densities) the fractions end in the lower left corner. In between the fractions follow approximately the dashed curve in Figure 7.5.

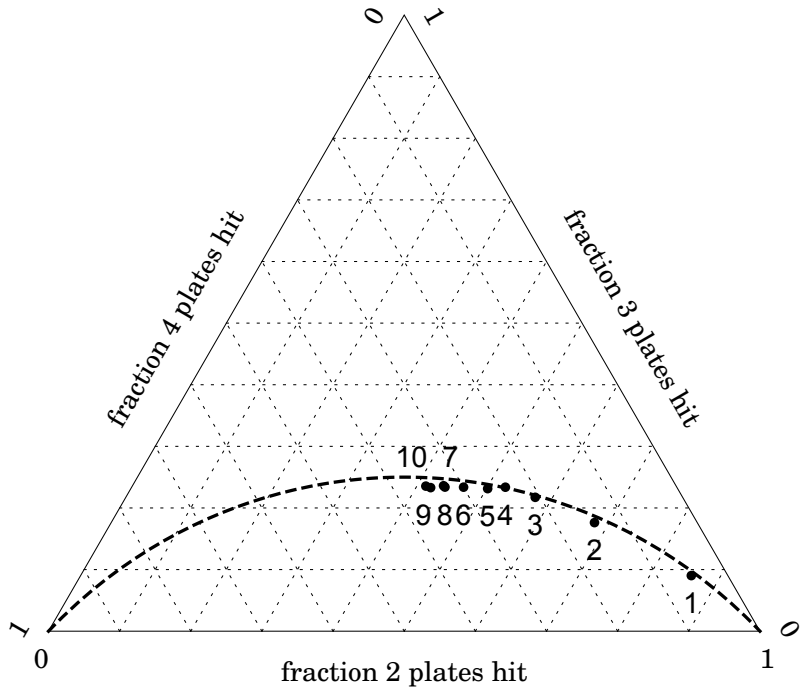

Figure 7.5: Fractions of 2, 3 and 4 plates of station 501 having passed a threshold value of 1, 2, 3, 4, 5, 6, 7, 8, 9 and 10 MIP. Data taken from 2013-08-28 00:00:00 through 2013-08-30 00:00:00. The fractions are close to an ellipse (dashed).

7.2 Coincidence characteristics

Here we will consider ternary diagrams for SPA stations that have participated in coincidences. Coincidences of k events (thus k triggered stations) will be denoted as $n = k$ coincidences. Events will be denoted as $n = 1$ coincidences. As an example, for the period 2013-08-15, 00:00:00 and 2013-09-12, 00:00:00 the fraction of two plates of station 501 passing a threshold of 0.3 MIP for $n = 2$ coincidences is 0.577. For three and four plates these fractions are 0.251 and 0.172 respectively. It turns out that larger thresholds, 0.4 or 0.5 MIP say, do not change the fractions significantly. Passing a threshold of 0.3 MIP is therefore denoted as being 'hit'. For different coincidence sizes the fractions are plotted in a ternary diagram, see Figure 7.6.

The dashed curve in Figure 7.6 can be partly understood by means of a simplistic model where the lateral density is considered identical for all four detectors of a station. The number of particles in a small area is Poisson distributed. The Poisson distribution is present in the lateral distribution of simulated showers. Dividing the area at distance r from the core between $r - 0.5$ and $r + 0.5$ m in tiles of surface $0.5\,\mathrm{m}^2$ and inspecting the number of particles in these tiles approximately results in a Poisson distribution, see Figure 7.7. The Poisson distribution is also verified experimentally, see figure 5.8 of [82].

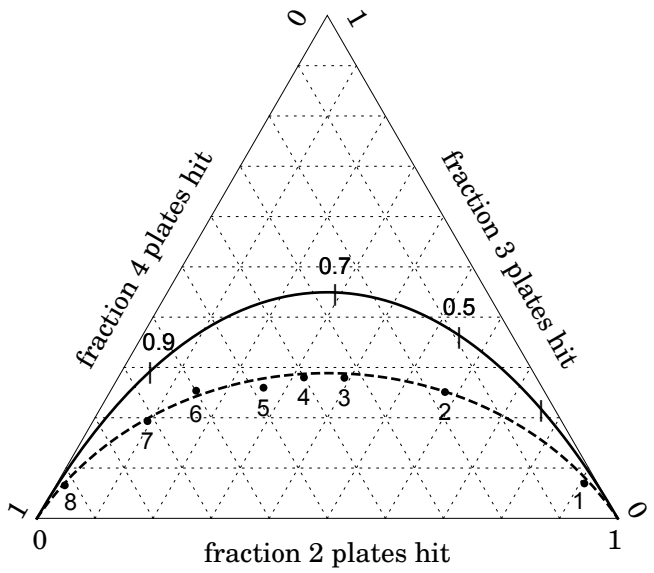

Figure 7.6: Ternary plot of the fractions of 2, 3 and 4 plates hit in station 501 events who participated in $n = 1$ through $n = 8$ coincidences. Data taken from 2013-08-15 00:00:00 through 2013-09-12 00:00:00. The fractions are close to an ellipse (dashed); the solid curve is a crude prediction, see text.

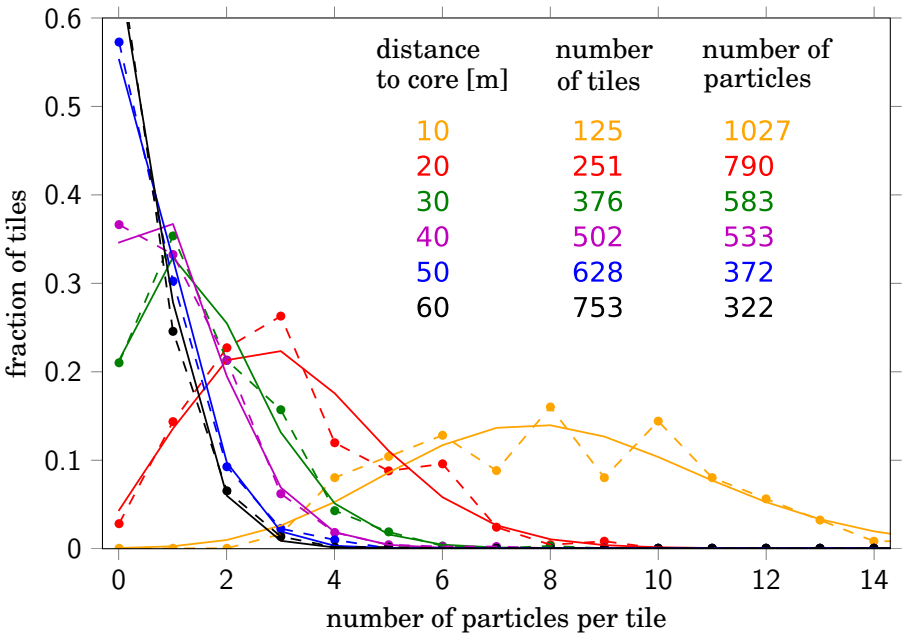

Figure 7.7: For a 1 PeV vertical proton shower the distribution of the number of charged particles at sea level in tiles with surface 0.5 m^2 at several distances to the core (dashed) and the corresponding Poisson distribution (solid).

If the lateral density at detector level is ρ particles per m^2, then 0.5ρ is the average number of particles on a detector plate of $0.5\,m^2$. For this density the probability that k particles will hit a detector is Poisson distributed:

$$P(k) = \frac{1}{k!}(0.5\rho)^k e^{-0.5\rho} \; . \tag{7.1}$$

The probability p for a plate to be hit, the detection probability, is

$$p = 1 - P(0) = 1 - e^{-0.5\rho} \; . \tag{7.2}$$

All four plates in a station are assumed to have equal probability p to be hit when a shower strikes a station. Then the probability for precisely m plates out of 4 to be hit is given by a binomial distribution:

$$P(m) = \binom{4}{m} p^m (1-p)^{4-m} \; , \tag{7.3}$$

where $p = 1 - e^{-0.5\rho}$. For the probability for a station to be triggered we restrict ourselves to the 'two-high' threshold criterion and neglect the Landau distribution of the energy loss as well as further normal distributions in the process that leads to a signal. The trigger probability then is

$$P_{\text{trigger}} = 6p^2(1-p)^2 + 4p^3(1-p) + p^4 \; , \tag{7.4}$$

with $p = 1 - e^{-0.5\rho}$. In Figure 7.8 the detection probability and the trigger probability according to the simplistic model are plotted against the density.

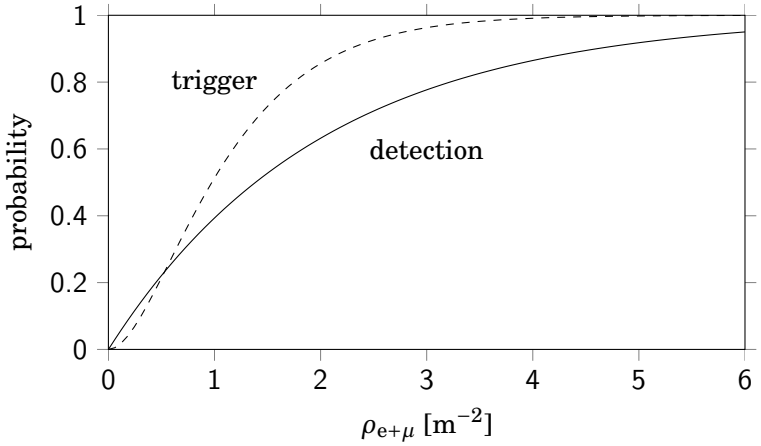

Figure 7.8: The detection probability, which is the probability a detector to be hit (solid), and the trigger probability (dashed) versus the density of electrons and muons.

For densities above 1 m^{-2} the probability for a station to be triggered is larger than 0.5. For smaller densities the trigger probability rapidly decreases. The expected fraction $f(2)$ of pre-

cisely two plates hit is

$$f(2) = \frac{6p^2(1-p)^2}{P_{\text{trigger}}} = \frac{6(1-p)^2}{6-8p+3p^2} \ . \tag{7.5}$$

The equations for the expected fractions $f(3)$ and $f(4)$ for three and four plates hit are:

$$f(3) = \frac{4p(1-p)}{6-8p+3p^2} \qquad f(4) = \frac{p^2}{6-8p+3p^2} \ . \tag{7.6}$$

Taking the lower left corner as the origin $(0,0)$ a point corresponding to the fractions $f(2)$, $f(3)$ and $f(4)$ has the coordinates

$$x = f(2) + \frac{1}{2}f(3) = \frac{6-10p+4p^2}{6-8p+3p^2} \tag{7.7}$$

and

$$y = \frac{1}{2}\sqrt{3}f(3) = \frac{2\sqrt{3}p(1-p)}{6-8p+3p^2} \ . \tag{7.8}$$

After elimination of p the equation for an ellipse is obtained:

$$\left(\frac{x-\frac{1}{2}}{\frac{1}{2}\sqrt{3}}\right)^2 + \left(\frac{y+\sqrt{3}}{\frac{3}{2}\sqrt{2}}\right)^2 = 1 \ . \tag{7.9}$$

The part of the ellipse inside the ternary diagram is drawn as a solid curve in Figure 7.6. The positions on the solid curve are marked for $p = 0.3, 0.5, 0.7, 0.9$ and labelled for $p = 0.5, 0.7, 0.9$. The values 0.3, 0.5, 0.7 and 0.9 for p correspond to the values .7, 1.4, 2.4 and $4.6\,\text{m}^{-2}$ respectively for the density ρ.

The dashed curve can not be given a full quantitative explanation on the basis of a single 'hit' probability. For a twofold coincidence it will in general be the case that the two stations involved are in regions with different density and thus with different p. The average fraction will be at the barycenter of these two points, causing the curve to be shrunk downwards. Even for a single event the density and thus the probability is in general larger in the two detectors that caused the trigger and smaller in the other detectors. This also causes the curve to shrink downwards. As a result the actual fractions are positioned close to a circle with equation

$$\left(x-\frac{1}{2}\right)^2 + (y+q)^2 = q^2 + \frac{1}{4} \ , \tag{7.10}$$

where $q \approx 0.37$. This is also the case for other stations and other station configurations. For the 501 station the fractions are plotted for a period of time when only station 501 through 506 were present, see Figure 7.9. In Figure 7.10 the ternary plot is shown for station 503. Although the fractions depend on the coincidence size, the positions of the fraction all are for each station close to the same dashed curve. The dashed curves are therefore characteristic.

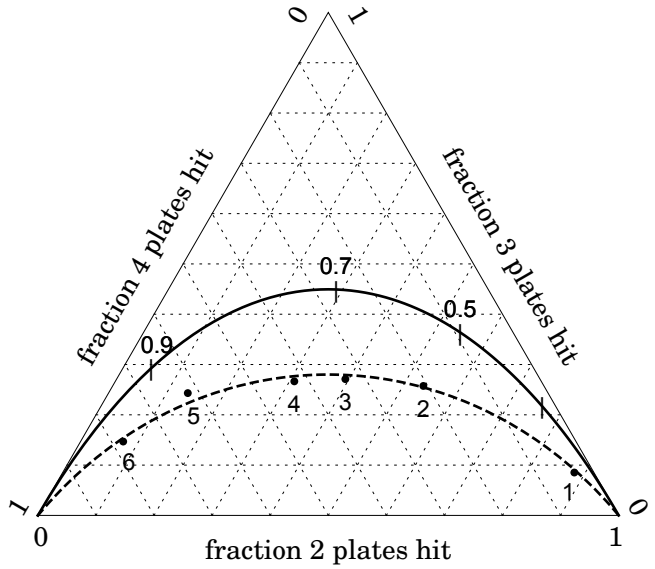

Figure 7.9: Ternary plot of the fractions of participating events with 2, 3 and 4 plates hit in station 501 for coincidence size $n = 1$ through $n = 6$. Data taken from 2012-02-01, 00:00:00 through 2012-03-01, 00:00:00. The fractions are close to an ellipse (dashed); the solid curve is a crude prediction.

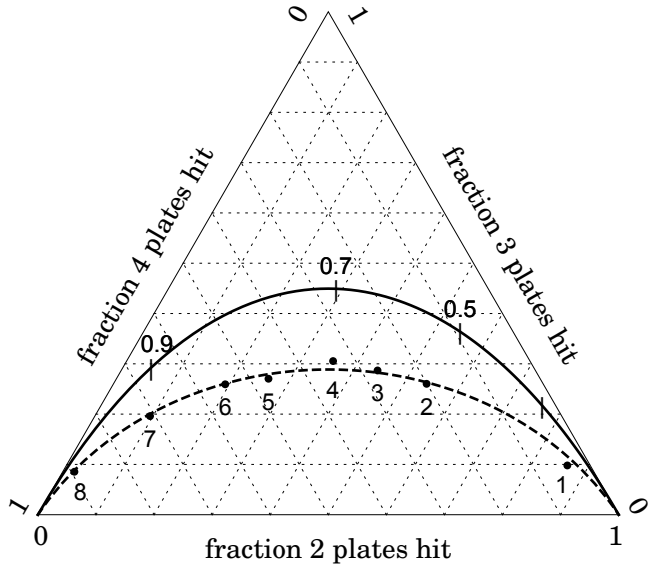

Figure 7.10: Ternary plot of the fractions of participating events with 2, 3 and 4 plates hit in station 503 for coincidence size $n = 1$ through $n = 8$. Data taken from 2013-08-15, 00:00:00 through 2013-09-12, 00:00:00. The fractions are close to an ellipse (dashed); the solid curve is a crude prediction.

7.3 Zenith and azimuth distributions

For the distribution of the reconstructed azimuthal angles data is taken for two time intervals. In the first time interval only stations 501 through 506 were present at SPA. In the second time interval also stations 508 and 509 were present. The reconstructed azimuth distributions for both time intervals are shown in Figure 7.11. Obviously, the azimuthal distribution is sensitive to the layout of the detector stations.

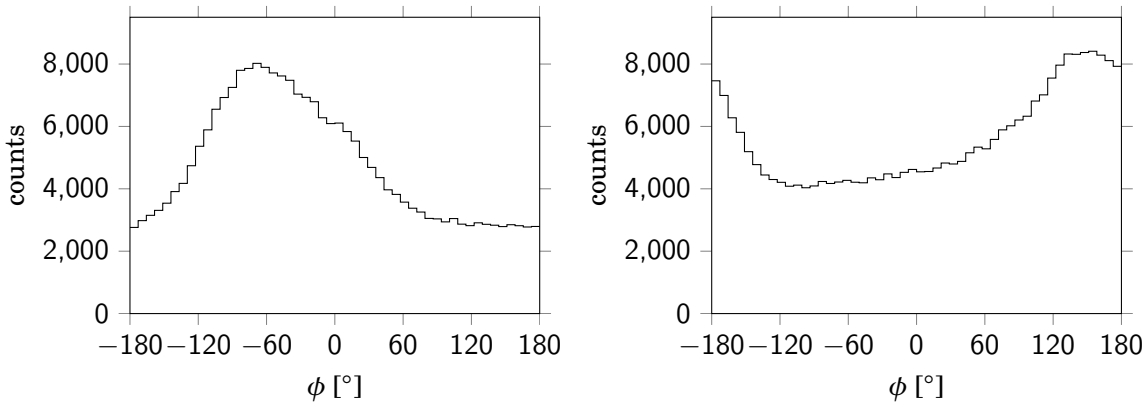

Figure 7.11: Azimuth distribution for showers on SPA cluster for the time interval 2009-02-01 through 2011-05-01 when only stations 501 through 506 were present (left) and for the time interval 2013-07-01 through 2015-02-01 were also stations 508 and 509 were present (right).

For a reconstructed zenith distribution data is taken from 2013-08-15, 00:00:00 through 2013-09-12, 00:00:00. The zenith distribution and the fractions of $n = 3$ through $n = 8$ coincidences that contributed to the zenith distribution are shown in Figure 7.12.

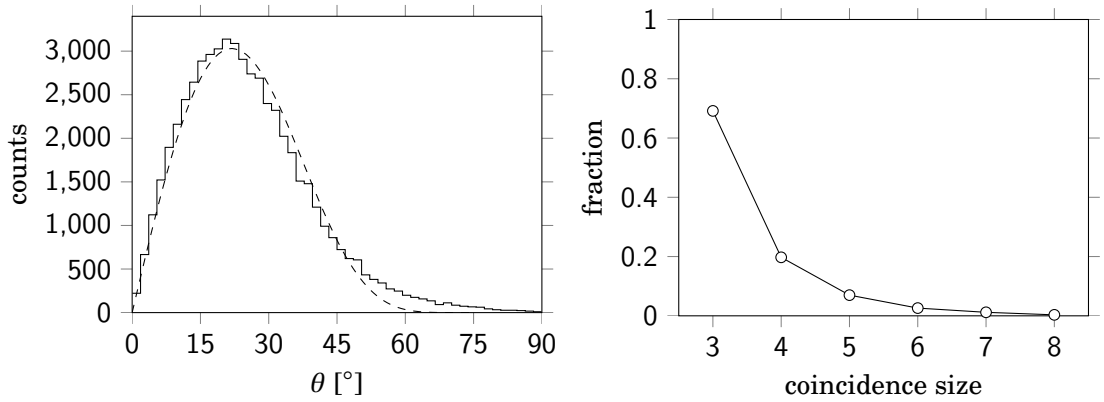

Figure 7.12: Left panel: zenith distribution. The dashed curve is a fit with a function given in the text. Right panel: fraction of $n = 3$ through $n = 8$ coincidences. Data taken from 2013-08-15, 00:00:00 through 2013-09-12, 00:00:00.

The zenith distribution is fitted with

$$dN_e(\theta) = N_e(0) e^{-C(\sec\theta - 1)} \sin\theta \, d\theta \, , \tag{7.11}$$

where the constant C is given by

$$C = \frac{X_0(\gamma - 1)}{2.3\lambda} \tag{7.12}$$

with X_0 the atmospheric depth at the altitude of the detector, $X_0 \approx 1030\,\mathrm{g\,cm^{-2}}$, with γ the cosmic ray energy spectrum index and with λ the attenuation length of the electromagnetic component of a shower [93, 97]. The fit resulted in the value 5.7 for C. For $\gamma = 2.75$ this corresponds to $\lambda \approx 138\,\mathrm{g\,cm^{-2}}$, while in the literature values between 175 and $196\,\mathrm{g\,cm^{-2}}$ are reported [97, 98]. The size of the electromagnetic part of a shower decreases approximately exponentially with atmospheric depth. A consequence of the attenuation is that the number of showers reaching the surface of the earth decreases exponentially with atmospheric depth. The corresponding characteristic lengths, the attenuation length λ (the length over which the shower size decreases to e^{-1} of its value) and the absorption length Λ (the length over which the number of showers extinct to e^{-1} of its value) are related to each other by $\Lambda = \lambda/(\gamma - 1)$ [98]. The zenith distribution can also be fitted to the equation:

$$dN_e(\theta) = N_e(0) \cos^k\theta \sin\theta \, d\theta \, . \tag{7.13}$$

The fit results in the value 7.3 for k. This value is comparable to values reported in the literature [99].

7.4 Arrival time statistics

In this section the distribution of the time lapses between the arrival times of successive showers is analyzed for the time interval 2013-08-15, 00:00:00 through 2013-09-12, 00:00:00. Also here showers are considered which have hit three or more stations. The distribution of the number of arrivals in a time interval Δt is expected to follow a Poisson distribution:

$$P(N_{\Delta t} = k) = \frac{1}{k!}(a\Delta t)^k e^{-a\Delta t} \, , \tag{7.14}$$

where a is the average rate. The probability that k successive arrivals take at least a time Δt is equal to the probability that there are less than k arrivals in time Δt. Alternatively, $P(T_k > \Delta t) = P(N_{\Delta t} < k)$. From this equality it can be derived that the intervals Δt between two arrivals with k arrivals in between follow the Erlang distribution

$$P_k(\Delta t) = \frac{1}{k!} a^{k+1} \Delta t^k e^{-a\Delta t} \, . \tag{7.15}$$

A fit of the distribution of time differences between a shower and the next shower with $P_0(\Delta t) = a \cdot e^{-a\Delta t}$ results in a rate of a =0.0233 s^{-1}. A fit of the distribution of time differences between a shower and the next to next shower with $P_1(\Delta t) = a^2 \Delta t e^{-a\Delta t}$ results in a rate of a =0.0233 s^{-1}. These two distributions are shown in Figure 7.13

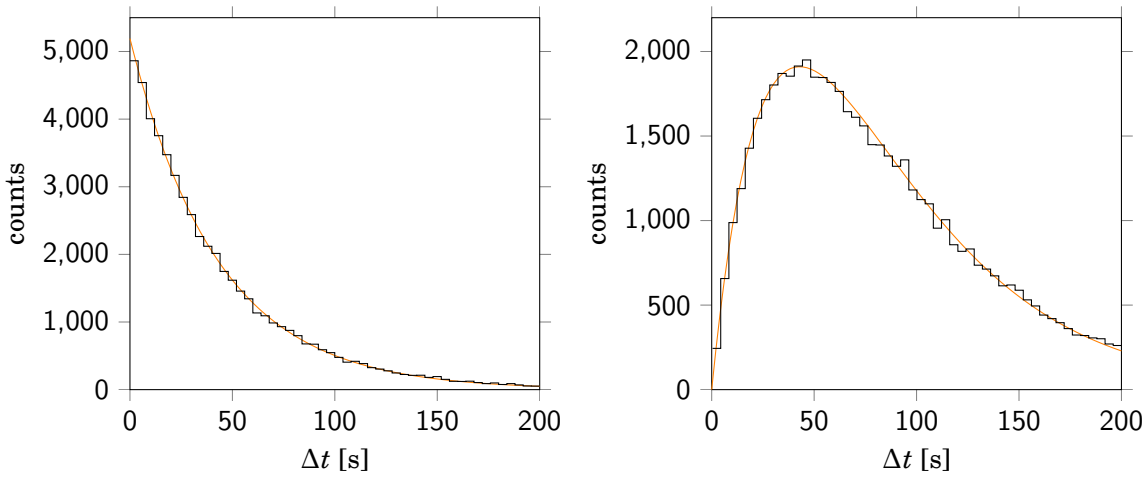

Figure 7.13: Arrival time difference distributions between a shower and the next shower (left) and between a shower and the next to next shower (right) for period 4. The orange curves are the fits with the Erlang distributions.

A fit of the distribution of time differences between a shower and the next to next to next shower with $P_2(\Delta t) = \frac{1}{2} a^3 \Delta t^2 e^{-a\Delta t}$ also resulted in a rate of a =0.0233 s^{-1}. This means that on average 84 showers an hour trigger at least three stations. The fact that the three fits deliver the same arrival rate confirm the Poisson nature of the arrival times.

7.5 Cosmic ray fluxes

For a dense array of detectors cosmic ray fluxes can be determined from observations of individual showers. For the sparse array at the SPA site showers which cause less than threefold coincidences can not be reconstructed. For fourfold and fivefold coincidences the reconstruction is inaccurate. Showers which cause fivefold or lower coincidences have an energy less than about 10^{16} eV. From these showers the cosmic ray fluxes can still be determined from the observed coincidence rates. This will be described below. At the end of this chapter the cosmic ray flux will be determined from individual showers with an energy larger than 10^{16} eV. For both methods the data is taken from the 28 days between 2013-08-15, 00:00:00 and 2013-09-12, 00:00:00. In this time interval, which is between the HiSPARC timestamps 1376524800 and 1378943995 seconds in the Unix era, the eight stations 501, 502, 503, 504, 505, 506, 508 and 509 were fully operational and well functioning without interruption.

When a simulated shower is at random thrown on the eight stations 501 through 506, 508 and 509, it will cause $n = k$ coincidences with $k \leq 8$. If no coincidences occur for a throw, we speak about a $n = 0$ coincidence. From the number of core positions which cause a k-fold coincidence the effective area for such a coincidence can be determined. In combination with frequencies of observed coincidences a cosmic ray spectrum can, to a certain extent, be synthesized. Theoretically

$$\nu_n = 2\pi \int_0^\infty \int_0^{\pi/2} f(E) A_n(E,\theta) \sin\theta \mathrm{d}\theta \mathrm{d}E \,, \tag{7.16}$$

where ν_n is the observed frequency of n stations hit, A_n is the effective area of core positions of showers with energy E and zenith angle θ hitting n stations and $f(E)$ is the cosmic ray flux of particles with energy E. Of course, the cosmic ray energy will not range from zero through infinity. The lower limit is where the showers will practically not reach sea level: $\approx 10^{13}$ eV. A theoretical upper limit is derived by Greisen, Zatsepin and Kuzmin (GKZ) [13, 14]. The GKZ limit, $\approx 10^{20}$ eV, is set by the interactions of cosmic ray protons with the microwave background radiation. The observed frequencies ν_n observed are tabulated in Table 7.1. The error in the observed frequencies, which is just the Poisson error, ranges from $3 \cdot 10^{-4}$ % for $n = 1$ coincidences through 7 % for $n = 8$ coincidences and is in practice negligible.

n	observed in 28 days	frequency [yr^{-1}]	frequency [s^{-1}]
1	$1.15 \cdot 10^7$	$1.50 \cdot 10^8$	4.75
2	188860	$2.46 \cdot 10^6$	$7.81 \cdot 10^{-2}$
3	39355	$5.13 \cdot 10^5$	$1.63 \cdot 10^{-2}$
4	11248	$1.47 \cdot 10^5$	$4.65 \cdot 10^{-3}$
5	4029	$5.25 \cdot 10^4$	$1.67 \cdot 10^{-3}$
6	1528	$1.99 \cdot 10^4$	$6.32 \cdot 10^{-4}$
7	667	$8.70 \cdot 10^3$	$2.76 \cdot 10^{-4}$
8	199	$2.59 \cdot 10^3$	$8.23 \cdot 10^{-5}$

Table 7.1: Observed rate (column 2), frequency per year (column 3),frequency per second (column 4) for coincidence sizes 1 through 8 (column 1). Data taken from 2013-08-15 00:00:00 through 2013-09-12 00:00:00.

With the ν_n known from the observed data and the A_n known from the simulations the $f(E)$ can, in principle, be reconstructed. In the simulations the generated shower energies and zenith angles are discrete. The discrete equivalent of Equation 7.16 is

$$\nu_n = \sum_j \sum_k \Delta F(\log_{10} E_j) A_n(E_j, \theta_k) g(\theta_k) \,, \tag{7.17}$$

where j and k are the indices of the discrete energies and the discrete zenith angles respectively. Here $g(\theta_k)$ represents the discrete distribution of zenith angles in steradians. The values

of $g(\theta_k$ will be derived further on. $F(E)$ is the integral flux of cosmic rays with energy larger than E: $F(E) = \int_E^\infty f(x)dx$. It is proportional to $E^{1-\gamma}$. The integral flux for the energy bin $10^{m-0.5} < E[\text{eV}] < 10^{m+0.5}$ is denoted as $\Delta F(m)$, where $m = \log_{10} E$. Thus $\Delta F(14)$, to give an example, is $F(10^{13.5}) - F(10^{14.5})$. For the effective area we consider the four energies 10^{14}, 10^{15}, 10^{16} and 10^{17} eV and the four zenith angles 15°, 30°, 45° and 60°. For each energy and each zenith angle the mean and FWHM of the distribution of the shower sizes is shown in Table 7.2.

	10^{14} eV	10^{15} eV	10^{16} eV	10^{17} eV
15°	$6.0 \cdot 10^3$ $(3 \cdot 10^3)$	$9.1 \cdot 10^4$ $(6 \cdot 10^4)$	$1.3 \cdot 10^6$ $(9 \cdot 10^5)$	$1.8 \cdot 10^7$ $(1 \cdot 10^7)$
30°	$3.5 \cdot 10^3$ $(2 \cdot 10^3)$	$4.6 \cdot 10^4$ $(2 \cdot 10^4)$	$6.8 \cdot 10^5$ $(3 \cdot 10^5)$	$9.0 \cdot 10^6$ $(5 \cdot 10^6)$
45°	$1.3 \cdot 10^3$ $(6 \cdot 10^2)$	$1.6 \cdot 10^4$ $(7 \cdot 10^3)$	$1.7 \cdot 10^5$ $(7 \cdot 10^4)$	$2.1 \cdot 10^6$ $(1 \cdot 10^6)$
60°	$6.7 \cdot 10^2$ $(3 \cdot 10^2)$	$5.3 \cdot 10^3$ $(3 \cdot 10^3)$	$4.4 \cdot 10^4$ $(2 \cdot 10^4)$	$4.0 \cdot 10^5$ $(1 \cdot 10^5)$

Table 7.2: Average $N_{e+\mu}$ for various energies and zenith angles at sea level for proton initiated showers. The FWHM is in brackets; the upper FWHM boundary is in the neighborhood of the mean.

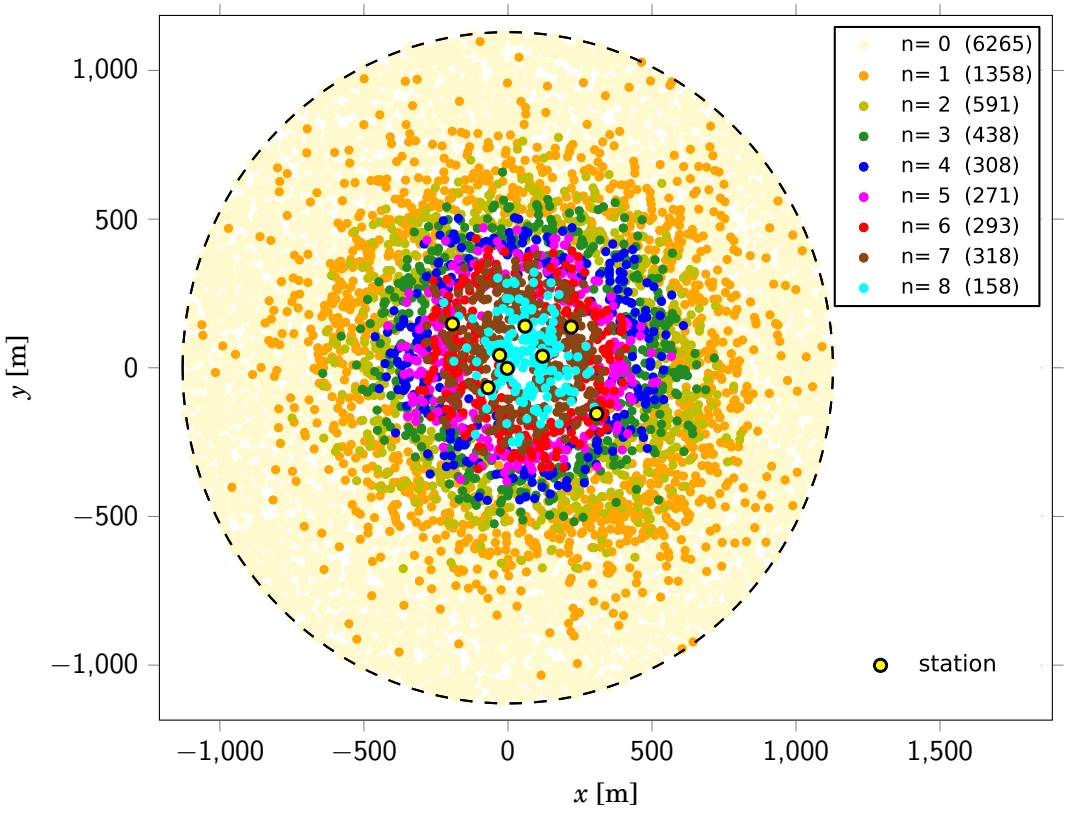

Figure 7.14: A 100 PeV proton shower with $\theta = 15°$ randomly thrown 10 000 times within a circle with area $4 \cdot 10^6$ m^2. The 10 000 core positions are colored depending on the number of stations hit, see legend.

For each of the four energies and each of the four zenith angles one shower is selected out of the simulated showers with the shower size within 5 % from the mean value. Each of the 16 selected showers is artificially thrown on 10 000 random positions at the SPA stations 501 through 506, 508 and 509. For 10^{14} and 10^{15} eV the throws are within a circle with area $1 \cdot 10^6\,\mathrm{m}^2$, corresponding to an effective area of $100\,\mathrm{m}^2$ per throw. For 10^{16} and 10^{17} eV the throws are within a circle with area $4 \cdot 10^6\,\mathrm{m}$, corresponding to an effective area of $400\,\mathrm{m}^2$ per throw. For 10^{16} eV additional throws are made in a circle with area $10^6\,\mathrm{m}^2$ in order to reduce the Poisson error. The result for a 10^{17} eV proton shower with $\theta = 15°$ is shown in Figure 7.14. From Figure 7.14 it can be read off that 438 out of 10 000 throws have caused a threefold coincidence: $A_3(10^{17}, 15°) = 175\,200\,\mathrm{m}^2$. The complete simulation result is shown in Table 7.3.

p	$n=1$	$n=2$	$n=3$	$n=4$	$n=5$	$n=6$	$n=7$	$n=8$
17,15	5432 (147)	2364 (97)	1752 (120)	1232 (84)	1084 (66)	1172 (68)	1272 (71)	632 (50)
17,30	5096 (143)	2176 (93)	1408 (75)	1072 (65)	956 (62)	972 (62)	968 (62)	252 (32)
17,45	3976 (126)	1564 (79)	988 (63)	656 (51)	580 (48)	420 (41)	132 (23)	16 (8)
17,60	2584 (102)	484 (44)	140 (24)	24 (10)	0	0	0	0
16,15	2420 (98)	948 (62)	608 (49)	432 (42)	272 (33)	80 (18)	4 (4)	0
16,30	2072 (91)	696 (26)	424 (21)	204 (14)	56 (8)	8 (3)	0	0
16,45	1360 (37)	320 (18)	76 (9)	12 (3)	0	0	0	0
16,60	87 (9)	1 (1)	0	0	0	0	0	0
15,15	954 (31)	139 (12)	12 (3)	0	0	0	0	0
15,30	624 (25)	54 (7)	2 (1)	0	0	0	0	0
15,45	144 (12)	3 (2)	0	0	0	0	0	0
15,60	1 (1)	0	0	0	0	0	0	0
14,15	69 (8)	0	0	0	0	0	0	0
14,30	18 (4)	0	0	0	0	0	0	0
14,45	1 (1)	0	0	0	0	0	0	0
14,60	0	0	0	0	0	0	0	0

Table 7.3: Effective area in units of 100 m^2 for proton initiated showers of different energies and different zenith angles. The Poisson error is in brackets. The first and second number of the row entries are $\log_{10} E_0$[eV] respectively θ in degrees. The column entries are the coincidence sizes.

7.6 Distribution correction

For each energy and zenith there is a distribution of shower sizes. The distributions of $N_{e+\mu}$ for p and Fe initiated showers with 10^{16} eV energy and zenith angle 15° are shown in Figure 7.15.

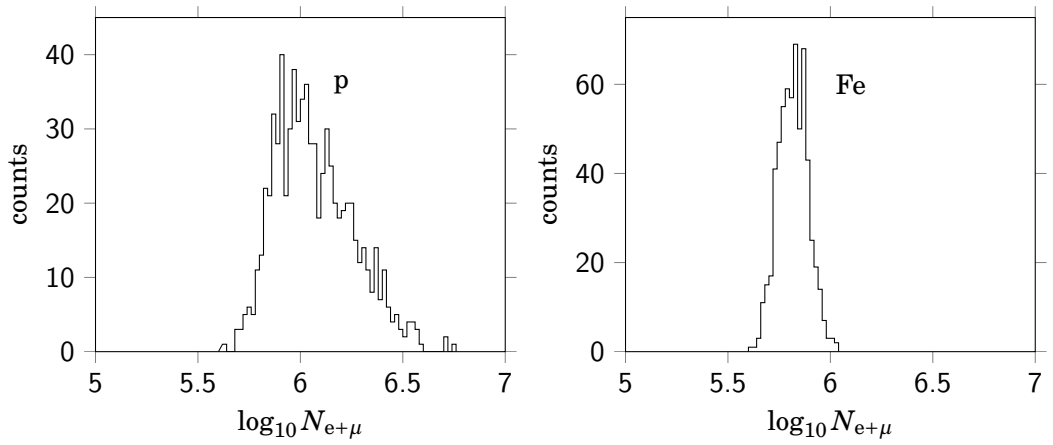

Figure 7.15: Distribution of the number of electrons and muons at observation level for a 10^{16} eV shower with zenith angle 15° initiated by a proton (left) and by an iron nucleus (right).

The spread in a shower size distribution will lead to a spread in the effective area. The spread in the effective area is obtained by application of a relation between shower size and the effective area. It is found that the square root of the effective area is approximately linear with the logarithm of the shower size. In Figure 7.16 the square root of the effective area for showers with zenith angle 15° and 30° is plotted against $\log_{10} N_{e+\mu}$ for $n = 1$ through $n = 4$ coincidences.

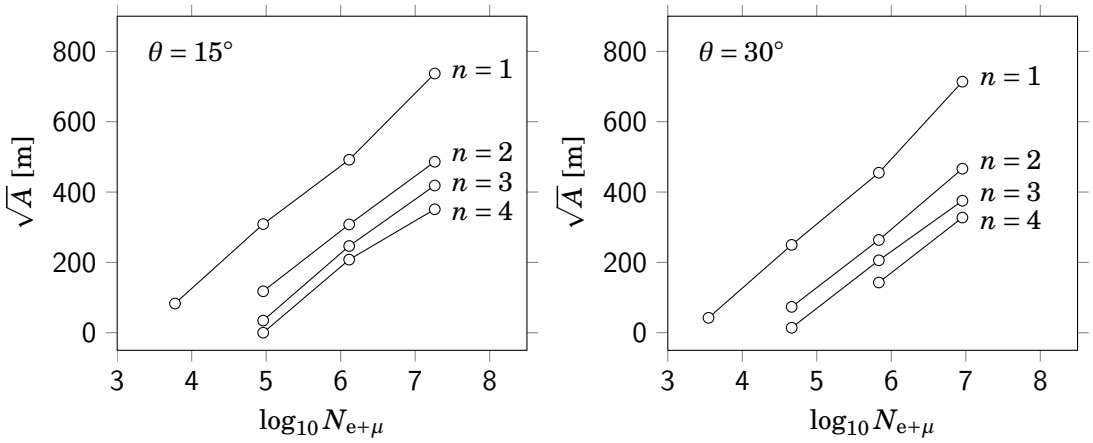

Figure 7.16: The square root of the effective area versus shower size for events, twofold, threefold and fourfold coincidences, for zenith angle 15° (left) and 30° (right).

The diagrams in Figure 7.16 suggest a linear relation:

$$\sqrt{A} = v \cdot \log_{10}(N_{e+\mu}) + w \ . \tag{7.18}$$

For instance, for $n = 1$ and $\theta = 15°$ the fit yields $v = 185$ and $w = -616$. For other coincidence sizes and other zenith angles the slopes are comparable. To each distribution of $N_{e+\mu}$ the corresponding linear relation is applied. It results in corrected values for the mean effective area, see Table 7.4. The spread in each distribution of $N_{e+\mu}$ contributes to the uncertainty. Together with the Poisson error it determines the total uncertainty, which is between brackets in Table 7.4.

p	$n=1$	$n=2$	$n=3$	$n=4$	$n=5$	$n=6$	$n=7$	$n=8$
17,15	5185 (460)	2337 (270)	1768 (260)	1207 (160)	1058 (170)	1135 (260)	1226 (350)	610 (170)
17,30	4767 (510)	2090 (300)	1386 (230)	1038 (210)	919 (240)	930 (290)	925 (320)	242 (100)
17,45	3852 (600)	1452 (280)	940 (260)	620 (210)	546 (220)	395 (160)	125 (110)	20 (30)
17,60	2540 (500)	475 (110)	140 (65)	25 (25)	0	0	0	0
16,15	2565 (380)	893 (200)	522 (160)	415 (110)	260 (95)	81 (80)	22 (50)	0
16,30	2198 (420)	690 (200)	377 (140)	189 (100)	58 (80)	17 (35)	0	0
16,45	1281 (360)	350 (140)	89 (65)	20 (50)	8 (35)	2 (20)	0	0
16,60	100 (30)	4 (10)	0	0	0	0	0	0
15,15	842 (270)	131 (95)	23 (40)	1 (5)	0	0	0	0
15,30	581 (240)	50 (60)	10 (25)	0	0	0	0	0
15,45	134 (150)	9 (30)	0	0	0	0	0	0
15,60	1 (2)	0	0	0	0	0	0	0
14,15	66 (95)	1 (4)	0	0	0	0	0	0
14,30	25 (55)	0	0	0	0	0	0	0
14,45	2 (2)	0	0	0	0	0	0	0
14,60	0	0	0	0	0	0	0	0

Table 7.4: Effective area in 100 m^2 for proton initiated showers of different energies and different zenith angles. The uncertainty is in brackets. The first and second number of the row entries are $\log_{10} E_0$ [eV] respectively θ in degrees. The column entries are the coincidence sizes.

For the calculation of the discrete zenith angle distribution the discrete zenith angles $\theta_1 = 15°$, $\theta_2 = 30°$, $\theta_3 = 45°$ and $\theta_4 = 60°$ represent the zenith angle intervals $0° < \theta < 22.5°$, $22.5° < \theta < 37.5°$, $37.5° < \theta < 52.5°$ and $52.5° < \theta < 67.5°$ respectively. For instance, for $g(\theta_1)$ it follows

$$g(\theta_1) = 2\pi \int_0^{\pi/8} \sin\theta \mathrm{d}\theta \approx 0.48 \; . \tag{7.19}$$

In a similar way it follows for the other angles $g(\theta_2) = 0.82$, $g(\theta_3) = 1.16$ and $g(\theta_4) = 1.42$. For the remaining 2.4 sr for $\theta > 67.5°$ it is assumed the inclined showers will not lead to events or

coincidences. For the events, $n = 1$, the following equation is obtained:

$$\begin{aligned}\nu_1 = \Delta F(14)(0.48\cdot 6600 + 0.82\cdot 2500 + 1.16\cdot 200 + 1.42\cdot 0) + \\ \Delta F(15)(0.48\cdot 84200 + 0.82\cdot 58100 + 1.16\cdot 13400 + 1.42\cdot 100) + \\ \Delta F(16)(0.48\cdot 256500 + 0.82\cdot 219800 + 1.16\cdot 128100 + 1.42\cdot 10000) + \\ \Delta F(17)(0.48\cdot 518500 + 0.82\cdot 476700 + 1.16\cdot 385200 + 1.42\cdot 254000)\ . \end{aligned} \tag{7.20}$$

With the substitution of the observed value ν_1 =4.75 s^{-1}, see the fourth column of Table 7.1, the latter reads

$$4.75 = 5.45\cdot 10^3\Delta F(14) + 1.04\cdot 10^5\Delta F(15) + 4.67\cdot 10^5\Delta F(16) + 1.45\cdot 10^6\Delta F(17)\ . \tag{7.21}$$

In a similar way we obtain for $n = 2$ through $n = 8$

$$7.81\cdot 10^{-2} = 48\Delta F(14) + 1.14\cdot 10^4\Delta F(15) + 1.41\cdot 10^5\Delta F(16) + 5.19\cdot 10^5\Delta F(17)\ . \tag{7.22}$$

$$1.63\cdot 10^{-2} = 1.92\cdot 10^3\Delta F(15) + 6.63\cdot 10^4\Delta F(16) + 3.27\cdot 10^5\Delta F(17)\ . \tag{7.23}$$

$$4.65\cdot 10^{-3} = 48\Delta F(15) + 3.77\cdot 10^4\Delta F(16) + 2.19\cdot 10^5\Delta F(17)\ . \tag{7.24}$$

$$1.67\cdot 10^{-3} = 1.82\cdot 10^4\Delta F(16) + 1.89\cdot 10^5\Delta F(17)\ . \tag{7.25}$$

$$6.32\cdot 10^{-4} = 5.51\cdot 10^3\Delta F(16) + 1.77\cdot 10^5\Delta F(17)\ . \tag{7.26}$$

$$2.76\cdot 10^{-4} = 1.06\cdot 10^3\Delta F(16) + 1.49\cdot 10^5\Delta F(17)\ . \tag{7.27}$$

$$8.23\cdot 10^{-5} = 5.14\cdot 10^4\Delta F(17)\ . \tag{7.28}$$

This is an overdetermined system of 8 equations for the four unknowns $\Delta F(14)$ through $\Delta F(17)$, where ΔF is in $\mathrm{m}^{-2}\,\mathrm{sr}^{-1}\,\mathrm{s}^{-1}$. Minimization of

$$\sum_{n=1}^{8}\left(\nu_n - \sum_j\sum_k \Delta F(\log_{10}E_j)A_n(E_j,\theta_k)g(\theta_k)\right)^2 \tag{7.29}$$

results in the following solution: $\Delta F(14) = 7.1\cdot 10^{-4}$, $\Delta F(15) = 3.9\cdot 10^{-6}$, $\Delta F(16) = 8.4\cdot 10^{-8}$ and $\Delta F(17) = 1.4\cdot 10^{-9}$. The relative errors are 70 %, 50 %, 35 % and 20 % respectively. The final thing to do is to relate the discrete quantities $\Delta F(14)$, $\Delta F(15)$, $\Delta F(16)$ and $\Delta F(17)$ to the energy dependent cosmic ray flux. For instance, $\Delta F(14)$ is the integral flux in the energy range $10^{4.5}$ through $10^{5.5}$ GeV. The flux therefore is given by

$$f(10^{14}) = \frac{\Delta F(14)}{10^{5.5} - 10^{4.5}}\ . \tag{7.30}$$

Substitution of the value for $\Delta F(14)$ gives $f(10^{14}) = 2.5 \cdot 10^{-9}\,\mathrm{m}^{-2}\,\mathrm{sr}^{-1}\,\mathrm{s}^{-1}\,\mathrm{GeV}^{-1}$. The other fluxes are: $f(10^{15}) = 1.4 \cdot 10^{-12}$, $f(10^{16}16) = 3.0 \cdot 10^{-15}$ and $f(10^{17}) = 4.9 \cdot 10^{-18}\,\mathrm{m}^{-2}\,\mathrm{sr}^{-1}\,\mathrm{s}^{-1}\,\mathrm{GeV}^{-1}$. Because of the non-linear relation between the flux and the energy a bin center correction is applied:

$$f_{\mathrm{corr}}(E) = f_{\mathrm{bin}} \frac{f(E)}{< f(E) >} \,, \tag{7.31}$$

where $f(E) = E^{-\gamma}$ and where the bin average is given by

$$< f(E) >= \frac{1}{E_{\mathrm{max}} - E_{\mathrm{min}}} \int_{E_{\mathrm{min}}}^{E_{\mathrm{max}}} f(E)\,\mathrm{d}E = \frac{E_{\mathrm{min}}^{1-\gamma} - E_{\mathrm{max}}^{1-\gamma}}{(\gamma - 1)(E_{\mathrm{max}} - E_{\mathrm{min}})} \,, \tag{7.32}$$

with E_{min} and E_{max} the bin edges. After the bin center correction the fluxes are $f(10^{14}) = 1.7 \cdot 10^{-9}$, $f(10^{15}) = 9.4 \cdot 10^{-13}$, $f(10^{16}) = 1.7 \cdot 10^{-15}$ and $f(10^{17}) = 2.8 \cdot 10^{-18}\,\mathrm{m}^{-2}\,\mathrm{sr}^{-1}\,\mathrm{s}^{-1}\,\mathrm{GeV}^{-1}$. The relative errors are the same as for the integral fluxes. They fall within the marker size when plotted in a cosmic ray energy flux diagram. The value of γ between two energy decades follows from

$$\gamma = \log_{10} f(E) - \log_{10} f(10 \cdot E) \,. \tag{7.33}$$

From the fluxes at the energies 10^{15} eV and 10^{16} eV the value $\gamma = 2.7 \pm 0.4$ is obtained. For the fluxes at the energies 10^{16} eV and 10^{17} eV this is $\gamma = 2.8 \pm 0.2$. It slightly indicates an agreement with the actual cosmic ray spectrum where the 'knee' is at about $10^{15.6}$ eV.

7.7 Iron spectrum

The previous analysis was entirely based on proton initiated showers. In reality cosmic rays consist also of heavier elements. The first interaction will on average occur at a larger altitude. As a consequence less particles will survive to the Earth's surface. In the right panel of Figure 7.15 the shower size distribution for an iron initiated shower with the same energy and zenith angle as taken for the proton initiated shower in the left panel. Less particles lead to a smaller effective area and therefore to larger estimations for the cosmic ray fluxes. Ignoring heavier elements causes underestimated cosmic ray fluxes. In order to get an idea of the influence of heavier primary nuclei we conduct the same analysis for iron primaries as we did in the previous section for proton primaries. To this end we throw with 13 iron initiated showers, one for each energy and zenith angle as shown in the Table 7.5.

The selection of showers and the throwing procedure is similar as for the proton. The results are shown in Table 7.6. The estimated uncertainties are comparable to the ones for proton initiated showers. The asymmetric distribution of shower sizes of proton initiated showers, see Figure 7.15, was the reason for the transition of Table 7.3 to Table 7.4. However, the fluxes from the effective areas as given in Table 7.3 are practically the same fluxes as for Table 7.4.

	10^{14} eV	10^{15} eV	10^{16} eV	10^{17} eV
15°	$3.1\cdot10^3$ $(9\cdot10^2)$	$4.1\cdot10^4$ $(2\cdot10^4)$	$6.7\cdot10^5$ $(3\cdot10^5)$	$9.9\cdot10^6$ $(3\cdot10^6)$
30°	$2.3\cdot10^3$ $(6\cdot10^2)$	$2.6\cdot10^4$ $(9\cdot10^3)$	$3.7\cdot10^5$ $(2\cdot10^5)$	$5.3\cdot10^6$ $(1\cdot10^6)$
45°	$1.6\cdot10^3$ $(3\cdot10^2)$	$1.3\cdot10^4$ $(3\cdot10^3)$	$1.4\cdot10^5$ $(4\cdot10^4)$	$1.6\cdot10^6$ $(4\cdot10^5)$
60°	-	-	-	$5.1\cdot10^5$ $(5\cdot10^4)$

Table 7.5: Average $N_{e+\mu}$ for various energies and zenith angles at sea level for iron initiated showers; the FWHM is in brackets. The mean is close to the center of the FWHM range.

Even the errors caused by the width of the shower size distribution are small, smaller than the marker size. This is even more so for iron initiated showers since the shower size distribution is smaller and more symmetrical than for proton initiated showers, see Figure 7.15. Uncertainties are therefore left out of Table 7.6.

Fe	$n=1$	$n=2$	$n=3$	$n=4$	$n=5$	$n=6$	$n=7$	$n=8$
17,15	5720	2588	1752	1220	1060	1092	1008	496
17,30	5628	2476	1572	1268	1164	828	712	340
17,45	4668	1984	1072	828	540	312	88	4
17,60	3228	841	230	67	8	2	0	0
16,15	2240	804	508	260	124	12	0	0
16,30	1960	624	308	116	44	0	0	0
16,45	1204	184	28	0	0	0	0	0
16,60	87	1	0	0	0	0	0	0
15,15	550	42	1	0	0	0	0	0
15,30	249	2	0	0	0	0	0	0
15,45	45	0	0	0	0	0	0	0
15,60	1	0	0	0	0	0	0	0
14,15	3	0	0	0	0	0	0	0
14,30	1	0	0	0	0	0	0	0
14,45	0	0	0	0	0	0	0	0
14,60	0	0	0	0	0	0	0	0

Table 7.6: Effective area in 100 m^2 for iron initiated showers of different energies and different zenith angles. The first and second number of the row entries are $\log_{10} E_0\,[\mathrm{eV}]$ respectively θ in degrees. For the row entries (14,60), (15,60) and (16,60) estimated values are used).

Proceeding directly from Table 7.6 in a similar manner as for the proton initiated showers we obtain the following system of equations:

$$4.75 = 2.26\cdot10^2\Delta F(14) + 5.22\cdot10^4\Delta F(15) + 4.20\cdot10^5\Delta F(16) + 1.74\cdot10^6\Delta F(17)\,. \qquad (7.34)$$

$$7.81 \cdot 10^{-2} = 2.18 \cdot 10^{3} \Delta F(15) + 1.11 \cdot 10^{5} \Delta F(16) + 6.77 \cdot 10^{5} \Delta F(17) \,. \tag{7.35}$$

$$1.63 \cdot 10^{-2} = 48 \Delta F(15) + 5.29 \cdot 10^{4} \Delta F(16) + 3.70 \cdot 10^{5} \Delta F(17) \,. \tag{7.36}$$

$$4.65 \cdot 10^{-3} = 2.20 \cdot 10^{4} \Delta F(16) + 2.68 \cdot 10^{5} \Delta F(17) \,. \tag{7.37}$$

$$1.67 \cdot 10^{-3} = 9.56 \cdot 10^{3} \Delta F(16) + 2.10 \cdot 10^{5} \Delta F(17) \,. \tag{7.38}$$

$$6.32 \cdot 10^{-4} = 5.76 \cdot 10^{2} \Delta F(16) + 1.57 \cdot 10^{5} \Delta F(17) \,. \tag{7.39}$$

$$2.76 \cdot 10^{-4} = 1.17 \cdot 10^{5} \Delta F(17) \,. \tag{7.40}$$

$$8.23 \cdot 10^{-5} = 5.22 \cdot 10^{4} \Delta F(17) \,. \tag{7.41}$$

The optimal solution is: $\Delta F(14) = 1.4 \cdot 10^{-2}$, $\Delta F(15) = 2.7 \cdot 10^{-5}$, $\Delta F(16) = 1.8 \cdot 10^{-7}$ and $\Delta F(17) = 1.9 \cdot 10^{-9}$. It gives the following fluxes: $f(10^{14}) = 4.9 \cdot 10^{-8}$, $f(10^{15}) = 9.5 \cdot 10^{-12}$, $f(10^{16}) = 6.3 \cdot 10^{-15}$ and $f(10^{17}) = 6.7 \cdot 10^{-18}\,\mathrm{m^{-2}\,sr^{-1}\,s^{-1}\,GeV^{-1}}$. After the bin center correction the corrected fluxes are $f(10^{14}) = 3.3 \cdot 10^{-8}$, $f(10^{15}) = 6.4 \cdot 10^{-12}$, $f(10^{16}) = 3.6 \cdot 10^{-15}$ and $f(10^{17}) = 3.8 \cdot 10^{-18}\,\mathrm{m^{-2}\,sr^{-1}\,s^{-1}\,GeV^{-1}}$.

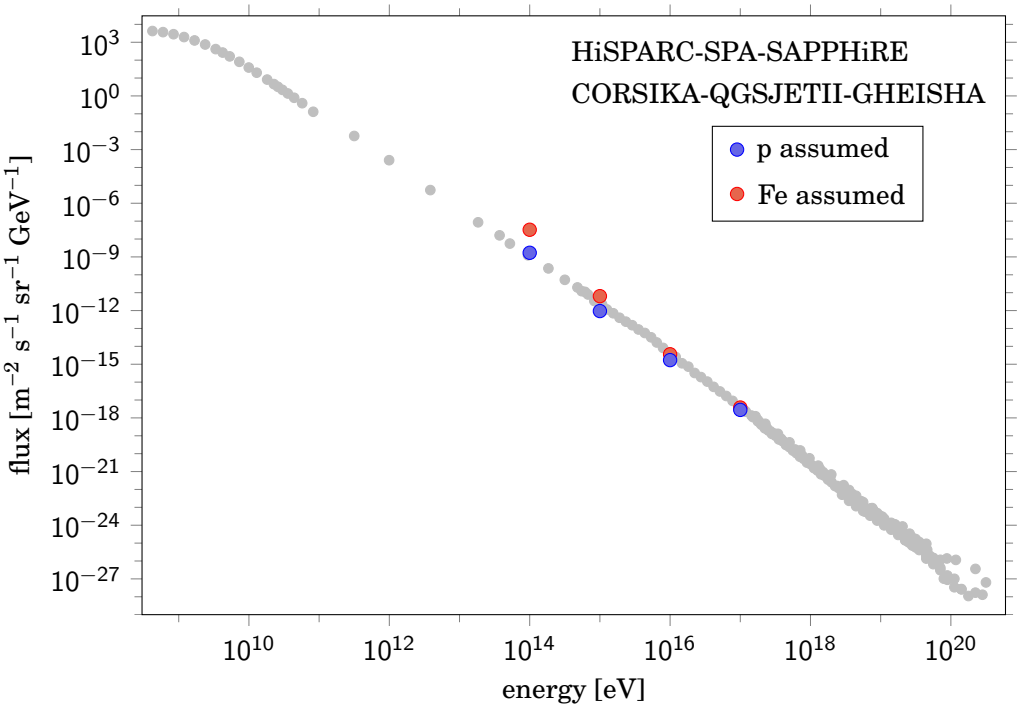

Figure 7.17: Cosmic ray energy spectrum. Gray are the fluxes as shown in Figure 1.1. Colored are the fluxes, blue for proton assumed and red for iron assumed cosmic rays, derived from rates of coincidence sizes observed at the Science Park Amsterdam site of HiSPARC.

In fig. 7.17 the fluxes are plotted for both the situation where all cosmic rays are assumed to be protons and the situation where all cosmic rays are assumed to be iron nuclei. Taking

Figure 7.17 literally, it implies the 10^{14} eV showers to be mainly proton initiated showers. For 10^{15} eV showers it indicates an increasing contribution of showers initiated by heavier elements, in agreement with existing galactic models for the explanation of the the cosmic ray spectrum. For larger energies we can not draw any conclusions because of the vanishing difference between the fluxes for proton initiated showers and iron initiated showers.

7.8 Individual showers

In the foregoing sections the cosmic ray fluxes were estimated solely on the basis of observed frequencies of coincidence sizes and Monte Carlo values for the effective areas. Instead one can also reconstruct the energy of individual showers and collect the result in energy bins. Since reconstructions of showers is inaccurate for small coincidence sizes, we will confine ourselves to $n > 5$ coincidences. It can be readily assumed that they are caused by showers with energy larger than $10^{15.75}$ eV. For the reconstruction of individual showers we consider again the period of 28 days between 2013-08-15, 00:00:00 through 2013-09-12, 00:00:00. From the 2394 showers (see Table 7.1) the reconstruction was successful in 2332 cases. The reconstructed core positions are shown in Figure 7.18.

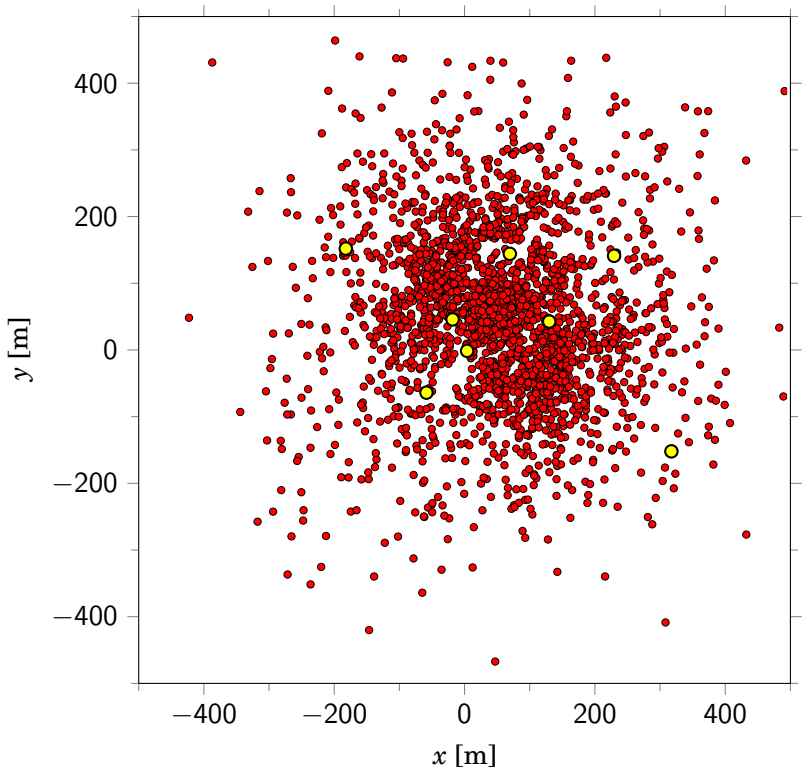

Figure 7.18: The reconstructed core positions (red) for the 2332 showers as described in the text. The yellow dots are the stations.

n	reconstr	$<10^{15.75}$ eV	10^{16} eV	$10^{16.5}$ eV	10^{17} eV	$10^{17.5}$ eV	10^{18} eV	$>10^{18.25}$ eV
6	1491	0	134	770	467	105	13	2
7	647	0	13	216	295	99	22	2
8	194	0	0	11	84	67	22	10
>5	2332	0	147	997	846	271	57	14

Table 7.7: Number of reconstructed energies for six-, seven- and eightfold coincidences. Data taken between 2013-08-15, 00:00:00 and 2013-09-12, 00:00:00. The entry 10^{17} eV, for instance, stands for the energy bin between $10^{16.75}$ and $10^{17.25}$ eV.

The reconstructed showers energies are tabulated in Table 7.7. The distributions of the reconstructed energies for different coincidence sizes are shown in Figure 7.19.

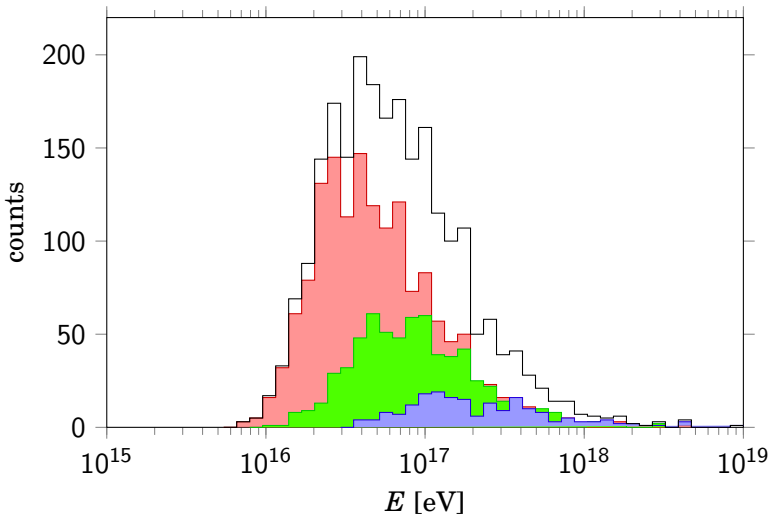

Figure 7.19: The distribution of the reconstructed energies broken down to coincidence sizes 6 (red), 7 (green) and 8 (blue), and the total distribution (black) for the 2332 showers as described in the text.

Without the summation over the energies Equation 7.17 reads

$$\nu_{nj} = \sum_k \Delta F(\log_{10} E_j) A_n(E_j, \theta_k) g(\theta_k) \,, \tag{7.42}$$

where ν_{nj} is the frequency of showers with energy E_j and coincidence size n. For reconstructed energies the summation over the coincidence sizes is considered:

$$\nu_j = \sum_n \sum_k \Delta F(\log_{10} E_j) A_n(E_j, \theta_k) g(\theta_k) \,. \tag{7.43}$$

Here ν_j is the frequency of showers with energy E_j. The frequencies per second are the numbers in the last row of Table 7.7 divided by the number of seconds contained in 28 days. The discrete integral fluxes now follow directly from

$$\Delta F(\log_{10} E_j) = \frac{\nu_j}{\sum_k \sum_n A_n(E_j,\theta_k) g(\theta_k)} \ . \tag{7.44}$$

The denominator of the latter equation are the Monte Carlo values obtained from randomly thrown simulated showers. For this we will confine to the situation where the cosmic rays are assumed to be protons. For the energies 10^{16} and 10^{17} eV the values are used as already obtained, see Table 7.3. For the energies $10^{16.5}$ and $10^{17.5}$ eV additional throws are conducted. The results for the four discrete energies are shown in Table 7.8.

p	$n=6$	$n=7$	$n=8$	$\sum_n A_n(E_j,\theta_k)$	$g(\theta_k)$	$\sum_n A_n(E_j,\theta_k) g(\theta_k)$
17.5,15	1608	2088	2452	6148	0.48	2951
17.5,30	1584	1904	1876	5364	0.82	4398
17.5,45	1266	1216	632	3114	1.16	3612
17.5,60	98	14	2	114	1.42	162
17.0,15	1172	1272	632	3076	0.48	1476
17.0,30	972	968	252	2192	0.82	1797
17.0,45	420	132	16	568	1.16	659
17.0,60	0	0	0	0	1.42	0
16.5,15	584	232	24	840	0.48	403
16.5,30	333	84	9	426	0.82	349
16.5,45	9	0	0	9	1.16	10
16.5,60	0	0	0	0	1.42	
16.0,15	80	4	0	84	0.48	40
16.0,30	8	0	0	8	0.82	7
16.0,45	0	0	0	0	1.16	0
16.0,60	0	0	0	0	1.42	0

Table 7.8: Effective area in 100 m^2 for showers of different energies and different zenith angles. The first and second number of the row entries are $\log_{10} E_0$ [eV] respectively θ in degrees.

As before we apply the distribution correction. The corrected effective areas are shown in Table 7.9.

p	$n=6$	$n=7$	$n=8$	$\sum_n A_n(E_j,\theta_k)$	$g(\theta_k)$	$\sum_n A_n(E_j,\theta_k)g(\theta_k)$
17.5,15	1610	2080	2400	6090	0.48	2923
17.5,30	1560	1890	1890	5340	0.82	4379
17.5,45	1230	1170	622	3022	1.16	3505
17.5,60	100	22	6	128	1.42	182
17.0,15	1135	1226	610	2971	0.48	1426
17.0,30	930	925	242	2097	0.82	1720
17.0,45	395	125	20	540	1.16	626
17.0,60	0	0	0	0	1.42	0
16.5,15	568	213	22	803	0.48	385
16.5,30	264	77	9	350	0.82	287
16.5,45	24	4	0	28	1.16	32
16.5,60	0	0	0	0	1.42	0
16.0,15	81	22	0	103	0.48	49
16.0,30	17	0	0	17	0.82	14
16.0,45	2	0	0	2	1.16	2
16.0,60	0	0	0	0	1.42	0

Table 7.9: Effective area in 100 m^2 for showers of different energies and different zenith angles. The first and second number of the row entries are $\log_{10} E_0(\mathrm{eV})$ respectively θ in degrees. The column entries are the coincidence sizes.

Summing over the discrete zenith angles we obtain, for instance, for the energy bin $10^{16.5}$ eV:

$$\Delta F(16.5) = \frac{4.12 \cdot 10^{-4}}{38500 + 28700 + 3200 + 0} = 5.85 \cdot 10^{-9} \; . \tag{7.45}$$

In a similar way we obtain for the other energy bins $\Delta F(16) = 9.35 \cdot 10^{-9}$, $\Delta F(17) = 9.27 \cdot 10^{-10}$ and $\Delta F(17.5) = 1.02 \cdot 10^{-10}\,\mathrm{m^{-2}\,s^{-1}\,sr^{-1}}$. The corresponding fluxes are $f(10^{16}) = 7.69 \cdot 10^{-16}$, $f(10^{16.5}) = 1.52 \cdot 10^{-16}$, $f(10^{17}) = 7.62 \cdot 10^{-18}$ and $f(10^{17.5}) = 2.65 \cdot 10^{-19}\,\mathrm{m^{-2}\,s^{-1}\,sr^{-1}\,GeV^{-1}}$ respectively. After the bin center correction these values are $f(10^{16}) = 6.6 \cdot 10^{-16}$, $f(10^{16.5}) = 1.3 \cdot 10^{-16}$, $f(10^{17}) = 6.5 \cdot 10^{-18}$ and $f(10^{17.5}) = 2.3 \cdot 10^{-19}\,\mathrm{m^{-2}\,s^{-1}\,sr^{-1}\,GeV^{-1}}$ respectively. The relative errors are 50 %, 25 % 15 % and 10 % respectively. If a structural overestimation (or underestimation) of 40 % is also taken into account the errors are 65 %, 50 % 45 % and 40 % respectively. Also here the errors are smaller than the marker size. The flux for 10^{16} eV is too small. This is probably due to the spread of the distribution of the reconstructed energies. If a shower in a certain energy bin is reconstructed, there is a probability for the reconstructed

energy to arrive in a bin with larger or smaller energy. Since the flux in an energy bin is larger than the flux in the next bin, the effect is a relatively large underestimation of the flux in the lowest energy bin and a relatively small overestimation in the following bins. For this reason the flux of the lowest energy is discarded. In Figure 7.20 the remaining three fluxes are added to the fluxes shown in Figure 7.17.

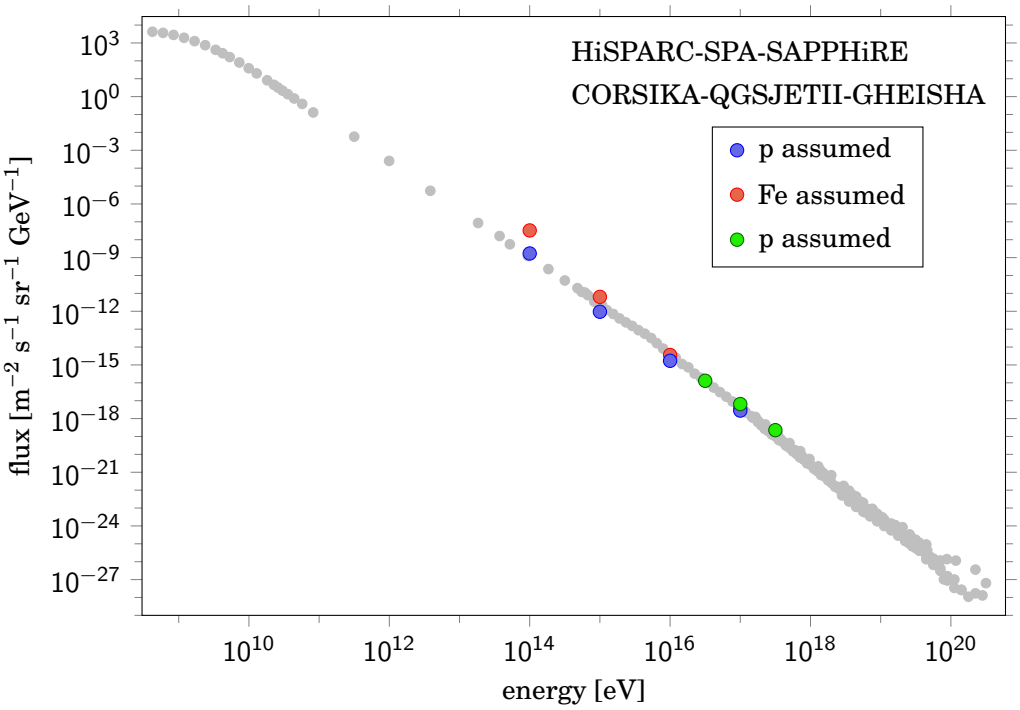

Figure 7.20: Cosmic ray energy spectrum. Gray are the fluxes as shown in Figure 1.1. Colored are the fluxes derived from coincidence rates (blue, red, see Figure 7.17) and derived from the reconstruction of individual showers (green) as observed at the Science Park Amsterdam site of HiSPARC.

Cosmic ray fluxes have been reconstructed from the HiSPARC data in two ways: by means of observed coincidence rates and by means of binning reconstructed energies of individual showers. Since the results of both methods are in agreement with the known energy spectrum, it can be concluded that the cosmic ray fluxes as reconstructed from the HiSPARC data are close to the ones obtained at other observatories.

8

Jet kinematics

8.1 Introduction

8.2 Jet momenta

Since cosmic rays are mainly protons we are interested in p-p collisions and consider jet kinematics in the CM and FT frame. We start considering two colliding protons in the center of mass (CM) frame. Before the collision each proton has energy $E_{\mathrm{CM}} = \gamma mc^2$, where m is the proton mass and where $\gamma = (1 - v^2/c^2)^{-1/2}$ with v the proton speed in the CM frame. In the FT frame the energy of the proton at rest is $E = mc^2$. The energy of the moving proton is $E_{\mathrm{FT}} = \gamma' mc^2 \approx 2\gamma^2 mc^2$. In four vector notation and with the $c = 1$ convention: $p_{\mathrm{CM}} = (E_{\mathrm{CM}}, 0, 0, p_z)$ respectively $p_{\mathrm{CM}} = (E_{\mathrm{CM}}, 0, 0, -p_z)$, where $p_{\mathrm{CM}}^2 = E_{\mathrm{CM}}^2 - p_z^2 = m^2$. For the Mandelstam variable s there holds:

$$s = \begin{pmatrix} E_{\mathrm{CM}} + E_{\mathrm{CM}} \\ 0 \\ 0 \\ p_z + -p_z \end{pmatrix}^2 = \begin{pmatrix} 2E_{\mathrm{CM}} \\ 0 \\ 0 \\ 0 \end{pmatrix}^2 = 4E_{\mathrm{CM}}^2 = 4\gamma^2 m^2 \ . \tag{8.1}$$

As is obvious, the total center of mass energy is $\sqrt{s} = 2E_{\mathrm{CM}}$. In the FT frame we have for the two momenta: $p_{\mathrm{FT}} = (E_{\mathrm{FT}}, 0, 0, p'_z)$ respectively $p_0 = (E_0, 0, 0, 0)$, where $p_{\mathrm{FT}}^2 = E_{\mathrm{FT}}^2 - p'^2_z = m^2$

and $p_0^2 = E_0^2 = m^2$. For s:

$$s = \begin{pmatrix} E_{\mathrm{FT}} + E_0 \\ 0 \\ 0 \\ p'_z + 0 \end{pmatrix}^2 = \begin{pmatrix} E_{\mathrm{FT}} + m \\ 0 \\ 0 \\ p'_z \end{pmatrix}^2 = E_{\mathrm{FT}}^2 + 2mE_{\mathrm{FT}} + m^2 - p'^2_z = 2mE_{\mathrm{FT}} + 2m^2 \approx 2mE_{\mathrm{FT}} \,. \quad (8.2)$$

The comparison of Equations 8.1 and 8.2 also leads to $E_{\mathrm{FT}} = 2\gamma^2 m$. Since the proton mass is about 0.938 GeV it follows from Equation 8.2 that cosmic protons with energy 10^{14} and 10^{15} eV correspond to $\sqrt{s} = 440\,\mathrm{GeV}$ and $\sqrt{s} = 1400\,\mathrm{GeV}$ respectively.

Now we focus our attention on the situation for the jets after the collision in both frames. In the CM frame the two jets move off in almost opposite directions and opposite momenta, see left side of Figure 8.1.

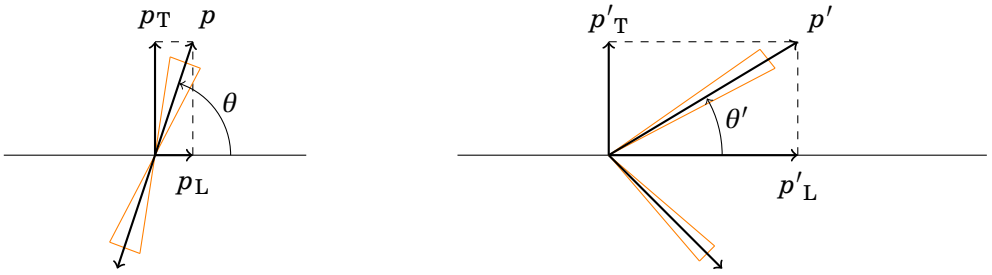

Figure 8.1: Jet momenta in the CM frame (left) and the FT frame (right).

In the CM frame p, p_{T} and p_{L} respectively are the jet momentum, the transverse jet momentum and the jet momentum along the beam axis. For relativistic jet energy E the mass can be ignored and $E = |p| = \sqrt{p_{\mathrm{T}}^2 + p_{\mathrm{L}}^2}$. The pseudorapidity is defined as

$$\eta = -\ln\left(\tan\frac{\theta}{2}\right) . \quad (8.3)$$

from the latter it follows

$$e^{2\eta} = \frac{1}{\tan^2(\theta/2)} = \frac{\cos^2(\theta/2)}{\sin^2(\theta/2)} = \frac{1+\cos\theta}{1-\cos\theta} . \quad (8.4)$$

Since $p_{\mathrm{L}} = |p|\cos\theta$ for the jet in the CM frame, the latter can also be written as

$$e^{2\eta} = \frac{\sqrt{p_{\mathrm{T}}^2 + p_{\mathrm{L}}^2} + p_{\mathrm{L}}}{\sqrt{p_{\mathrm{T}}^2 + p_{\mathrm{L}}^2} - p_{\mathrm{L}}} . \quad (8.5)$$

which is equivalent to

$$\eta = \frac{1}{2}\ln\left(\frac{\sqrt{p_{\mathrm{T}}^2 + p_{\mathrm{L}}^2} + p_{\mathrm{L}}}{\sqrt{p_{\mathrm{T}}^2 + p_{\mathrm{L}}^2} - p_{\mathrm{L}}}\right) . \tag{8.6}$$

From Equation 8.5 it follows that $E = p_{\mathrm{T}}\cosh\eta$ and $p_{\mathrm{L}} = p_{\mathrm{T}}\sinh\eta$. The jet four momentum in the CM frame therefore can be written as

$$\vec{p}_{\mathrm{jet}} = p_{\mathrm{T}}\left(\cosh\eta, \cos\phi, \sin\phi, \sinh\eta\right) , \tag{8.7}$$

where ϕ is the azimuthal angle. Multiplying both the numerator and denominator of Equation 8.5 with $\sqrt{p_{\mathrm{T}}^2 + p_{\mathrm{L}}^2} + p_{\mathrm{L}}$ and taking the square root we obtain

$$e^{\eta} = \frac{p_{\mathrm{L}} + \sqrt{p_{\mathrm{T}}^2 + p_{\mathrm{L}}^2}}{p_{\mathrm{T}}} . \tag{8.8}$$

The rapidity is defined as

$$y = \frac{1}{2}\ln\left(\frac{E + p_{\mathrm{L}}}{E - p_{\mathrm{L}}}\right) . \tag{8.9}$$

For relativistic energies, where the mass can be ignored, the rapidity is practically equal to the pseudorapidity.

For a cosmic ray, a proton in our case, the incoming particle collides with a fixed target, a proton or neutron of an nitrogen or oxygen nucleus. We will restrict ourselves to the proton of an air nucleus. Since nucleons in nuclei are almost free in high energy collisions, it will be considered as a p-p collision with one proton as the fixed target. The transverse part of the jet momentum is the same as in the CM frame, while the total jet momentum is more close to the beam axis, see left side of Figure 8.1. The quantities in the FT frame will be denoted with a prime. The kinematic relations in the FT frame are obtained from the foregoing CM relations by replacing the quantities by their primed equivalents. For instance

$$e^{\eta'} = \frac{p'_{\mathrm{L}} + \sqrt{p'^2_{\mathrm{T}} + p'^2_{\mathrm{L}}}}{p'_{\mathrm{T}}} . \tag{8.10}$$

In the FT frame p', p'_{T} and p'_{L} respectively are the jet momentum, the transverse jet momentum and the jet momentum along the beam axis. Their values are related to their values in the CM frame by means of a Lorentz transformation. In the relativistic regime the relations are:

$$E' \approx p'_{\mathrm{L}} \approx \gamma E + \gamma p_{\mathrm{L}} \approx \gamma\left(p_{\mathrm{L}} + \sqrt{p_{\mathrm{T}}^2 + p_{\mathrm{L}}^2}\right) \tag{8.11}$$

and

$$p'_{\mathrm{T}} = p_{\mathrm{T}} . \tag{8.12}$$

From Equations 8.8 and 8.11 it follows for the jet energy in the FT frame:

$$E' = p'_{\mathrm{L}} = \gamma p_{\mathrm{T}} e^{\eta} \ . \tag{8.13}$$

Substitution of the latter into Equation 8.10 gives

$$e^{\eta'} = \gamma e^{\eta} + \sqrt{1 + \gamma^2 e^{2\eta}} \ . \tag{8.14}$$

Since $\gamma^2 e^{2\eta} >> 1$ in the relativistic regime, the latter is reduced to

$$e^{\eta'} = 2\gamma e^{\eta} \ . \tag{8.15}$$

Hence

$$\eta' = \eta + \ln(2\gamma) \ . \tag{8.16}$$

This leads to the exact relation that pseudorapidity differences are invariant under collinear Lorentz boosts:

$$\Delta\eta' = \Delta\eta \ . \tag{8.17}$$

8.3 Jet properties

In this section several jet properties of p-p collisions will be investigated by means of PYTHIA. The amount of transverse momentum, $\hat{p}_{\mathrm{T}}$, is steered in PYTHIA with the phase space cuts $\hat{p}_{\mathrm{T}}^{\mathrm{min}}$ and $\hat{p}_{\mathrm{T}}^{\mathrm{max}}$. After the collision a jet finder, SLOWJET in our case, clusters the particle momentums in a cone with radius R. The jet clustering is conducted with the anti-k_t algorithm [100]. The cone radius is defined as

$$R = \sqrt{\Delta\phi^2 + \Delta\eta^2} \ , \tag{8.18}$$

where ϕ is the azimuthal angle and where η is the pseudorapidity. The desired jet radius is given as a parameter to the jet finder. Jet properties as the multiplicity (number of particles in a jet) and the transverse jet momentum depend on the jet radius. Also the number of jets obtained by the jet finder depends on the radius. For decreasing radii the number of jets tends to the number of particles. For increasing jet radii the number of jets decreases to about 6 for a radius of 1. For our purpose only the jets with the largest and next to largest transverse momentum are of interest. They are called the leading jet (L) and the next to leading jet (NL).

To investigate some jet properties the jet radius was taken from 0.01 through 1 in steps of 0.01. For each step the average of a quantity is taken over 1000 events. In Figure 8.2 the average multiplicity and the average transverse momentum of the leading jet and next to leading jet for $p-p$ collisions with $\sqrt{s} = 440\,\mathrm{GeV}$ are shown for two different $\hat{p}_{\mathrm{T}}^{\mathrm{min}}$.

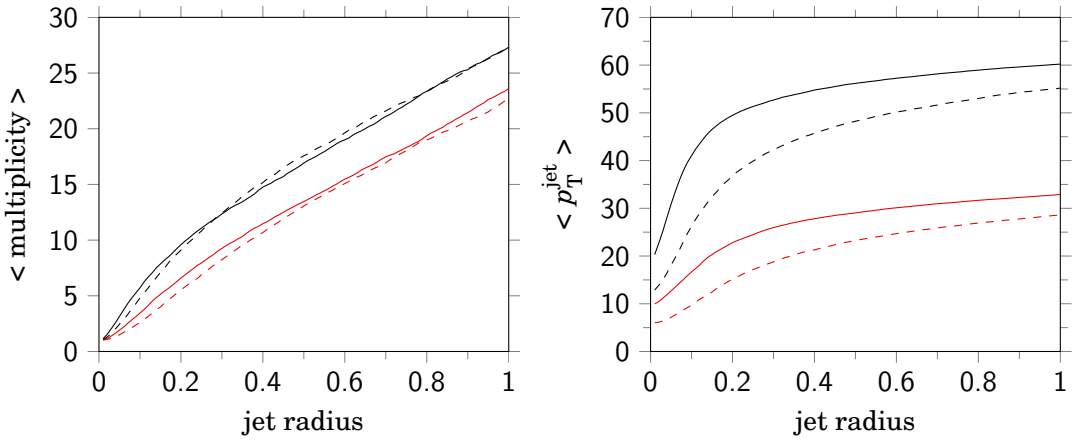

Figure 8.2: Average multiplicity (left) and average p_T^{jet} (right) versus jet radius for the leading jet (solid) and next to leading jet (dashed). Both for $\sqrt{s}$=440 GeV and $\hat{p}_T^{min}$=50 GeV/c (black) and $\hat{p}_T^{min}$=25 GeV/c (red).

We see the leading jet and next to leading jet have a comparable multiplicity and a comparable transverse momentum. The agreement is better for larger $\hat{p}_T^{min}$. A similar picture is obtained for a Pythia simulation with $\sqrt{s}$ = 1400 GeV, see Figure 8.3.

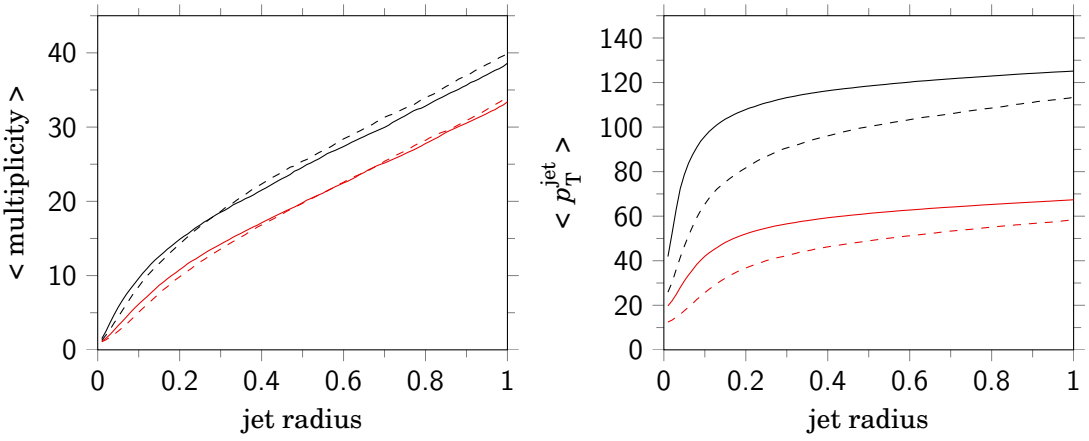

Figure 8.3: Average multiplicity (left) and average p_T^{jet} (right) versus jet radius for the leading jet (solid) and next to leading jet (dashed). Both for $\sqrt{s}$=1400 GeV and $\hat{p}_T^{min}$=100 GeV/c (black) and $\hat{p}_T^{min}$=50 GeV/c (red).

We also see that the transverse jet momentum is quite insensitive to the jet radius for jet radii larger than 0.2 if $\hat{p}_T^{min}$ = 50 GeV/c or larger. Alternatively, most of the transverse momentum inside a jet is carried by the particles inside a radius 0.2. For smaller $\hat{p}_T^{min}$ this is the case for larger jet radius. The value $R = 0.7$ seems to be a convention since it is applied in many jet analyses. Everywhere hereafter this convention will be applied.

In Figure 8.4 the rapidity distributions of the leading jet and the next to leading jet in a $\sqrt{s} =$ 440 GeV p-p collision are shown for $p_{\mathrm{T}}^{\mathrm{min}} = 50\,\mathrm{GeV/c}$ and $p_{\mathrm{T}}^{\mathrm{min}} = 25\,\mathrm{GeV/c}$ respectively.

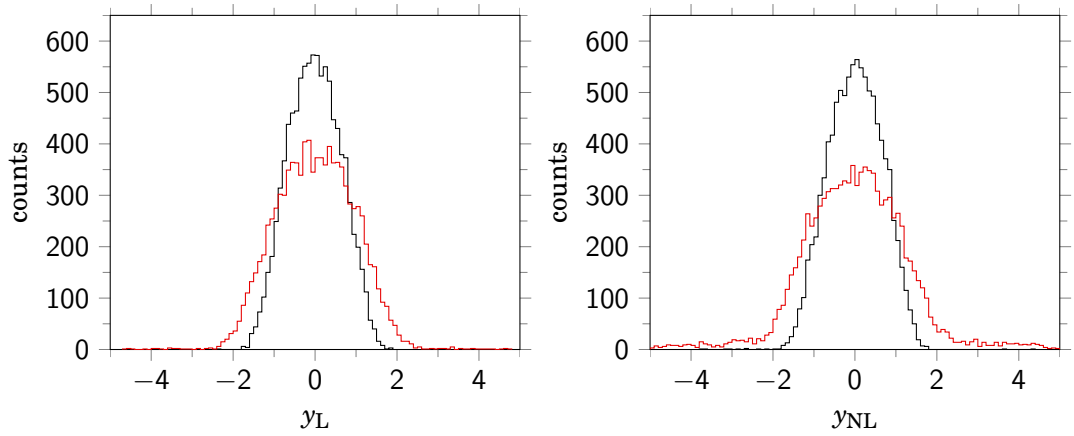

Figure 8.4: The rapidity distribution of the leading jet (left) and the next to leading jet (right). Both for p-p collisions with $\sqrt{s} = 440$ GeV and $\hat{p}_{\mathrm{T}}^{\mathrm{min}} = 50$ GeV/c (black) and $\hat{p}_{\mathrm{T}}^{\mathrm{min}} = 25$ GeV/c (red); jet radius 0.7.

In Figure 8.5 the rapidity distributions of the leading jet and the next to leading jet in a $\sqrt{s} =$ 1400 GeV p-p collision are shown for $p_{\mathrm{T}}^{\mathrm{min}} = 100\,\mathrm{GeV/c}$ and $p_{\mathrm{T}}^{\mathrm{min}} = 50\,\mathrm{GeV/c}$ respectively.

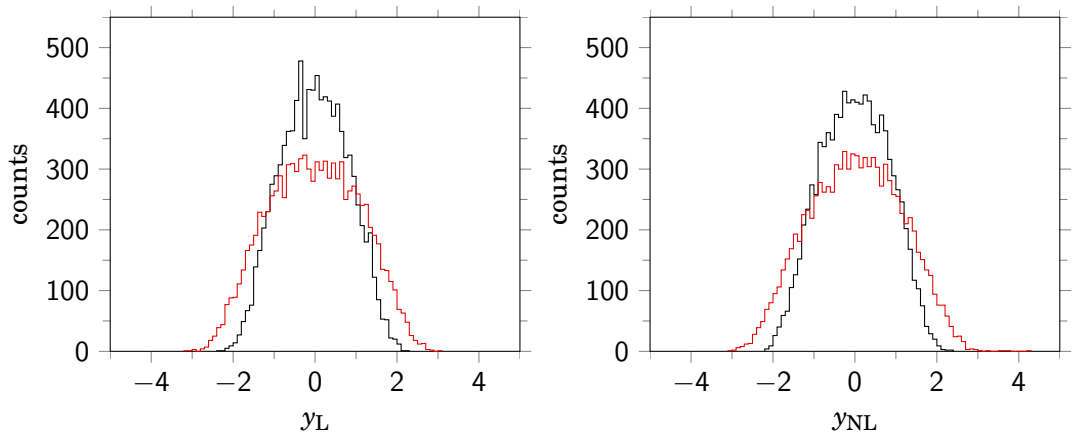

Figure 8.5: The rapidity distribution of the leading jet (left) and the next to leading jet (right). Both for p-p collisions with $\sqrt{s} = 1400$ GeV and $\hat{p}_{\mathrm{T}}^{\mathrm{min}} = 100$ GeV/c (black) and $\hat{p}_{\mathrm{T}}^{\mathrm{min}} = 50$ GeV/c (red); jet radius 0.7.

From the comparison of the rapidity distributions for the two different $\sqrt{s}$ values and identical $\hat{p}_{\mathrm{T}}^{\mathrm{min}}$ we see that the rapidity distribution widens for increasing $\sqrt{s}$. The diagrams in Figures 8.6 and 8.7 illustrate that the leading jet and next to leading jet are mostly back to back. That is, they are mostly back to back as far as the azimuthal angle is concerned and less back to back when the angle θ is considered. The sum of the θ's of the leading jet and next to leading jet should be π for complete back to back. Although the sum is on average equal to π there is a large spread. The spread in the sum of the θ's is larger than the spread in the

azimuthal difference. For both the distributions the width increases for decreasing $\widehat{p}_{\mathrm{T}}^{\mathrm{min}}$. For the distribution of the sum of the θ's the width increases for increasing $\sqrt{s}$.

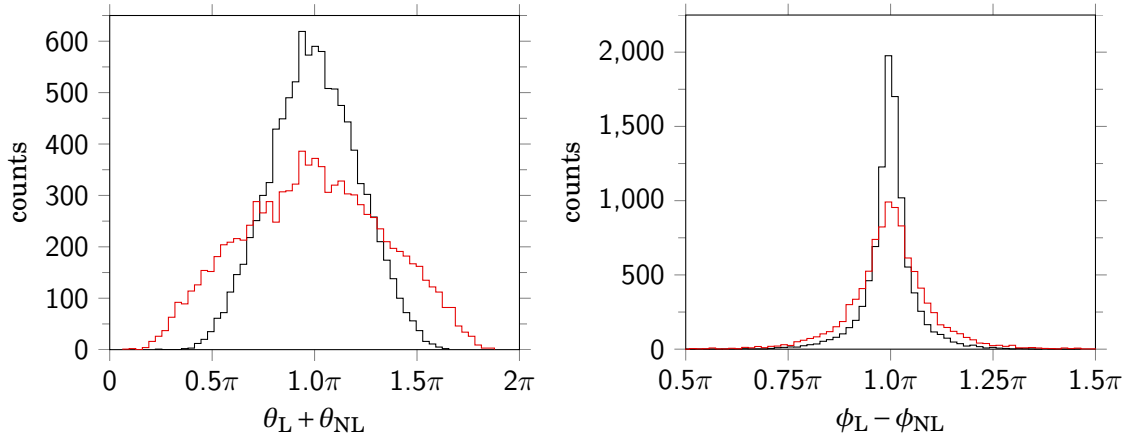

Figure 8.6: The distribution of the sum of the θ of the leading jet and the next to leading jet (left) and of the difference between the ϕ of the leading jet and the next to leading jet (left). For p-p collisions with $\sqrt{s}$ = 440 GeV and $\widehat{p}_{\mathrm{T}}^{\mathrm{min}}$= 50 GeV/c (black) and $\widehat{p}_{\mathrm{T}}^{\mathrm{min}}$= 25 GeV/c (red); jet radius 0.7.

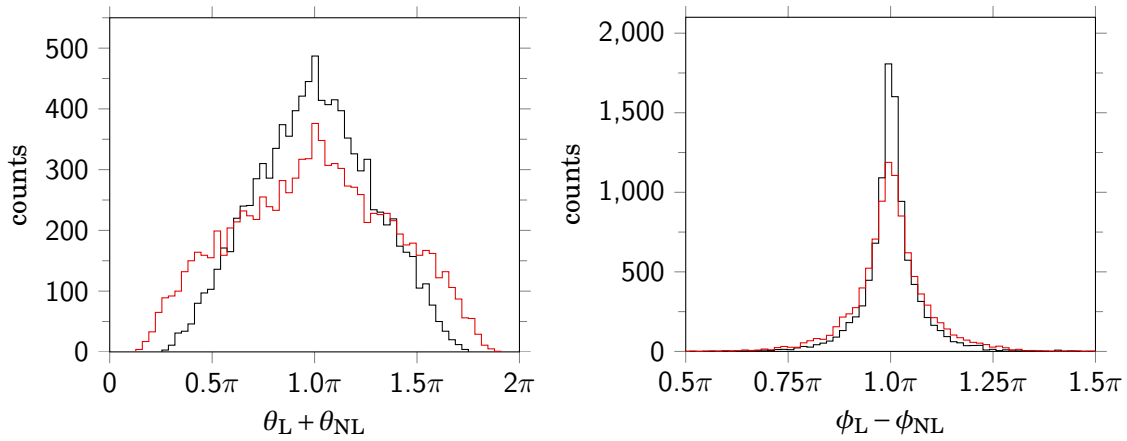

Figure 8.7: The distribution of the sum of the θ of the leading jet and the next to leading jet (left) and of the difference between the ϕ of the leading jet and the next to leading jet (left). For p-p collisions with $\sqrt{s}$ = 1400 GeV and $\widehat{p}_{\mathrm{T}}^{\mathrm{min}}$= 100 GeV/c (black) and $\widehat{p}_{\mathrm{T}}^{\mathrm{min}}$= 50 GeV/c (red); jet radius 0.7.

8.4 Jet footprints

In p − p and p−air scattering the bulk of particles will be in the forward direction. The jet will give rise to a sub shower. The core of the sub shower will be called the 'jet core'. The distance d of the jet core with respect to the core of the main shower will be called the 'jet distance' or

'sub core distance'. The extremely small angle θ' in the FT frame determines the jet distance:

$$d = \Delta h \tan\theta' \,, \tag{8.19}$$

where Δh is the difference between the altitude of the first collision and the altitude of the observation level. Since

$$\tan\theta' = \frac{p'_{\mathrm{T}}}{p'_{\mathrm{L}}} = \frac{1}{\gamma e^{\eta}} \tag{8.20}$$

the distance d is given by

$$d = \frac{\Delta h}{\gamma e^{\eta}} \tag{8.21}$$

or, equivalently,

$$d = \frac{\Delta h\, p_{\mathrm{T}}}{E'} = \frac{\Delta h \tan(\theta/2)}{\gamma} \,. \tag{8.22}$$

For a di-jet there are two angles θ_1 and θ_2 and two angles ϕ_1 and ϕ_2. For completely opposite momenta $\phi_2 = \phi_1 \pm \pi$, $\theta_2 = \pi - \theta_1$, $\tan(\theta/2) = \tan^{-1}(\theta_1/2)$, $\eta_2 = -\eta_1$ and $d_1 d_2 = (\Delta h)^2 \gamma^{-2}$.

For instance $\sqrt{s} = 1400\,\mathrm{GeV}$ corresponds to a proton energy of 1 PeV in the FT frame and the values of γ is about 745. In case $\eta = 0$ and $h = 20\,\mathrm{km}$ the jet distance is about 27 m. If in addition p_{T} is taken equal to 60 GeV/c the corresponding jet energy is 45 TeV, thus 4.5 % of the shower energy. For non zero η the distances are e^{η} times smaller and the energies are e^{η} times larger. For energies before and after the knee the flux of cosmic rays approximately goes as $f \approx 7 \cdot 10^{19} \cdot E^{-2.7}$ and $f \approx 2.6 \cdot 10^{24} \cdot E^{-3.0}$ respectively, where E is in eV and f is in $\mathrm{m^{-2}\,sr^{-1}\,s^{-1}\,eV^{-1}}$. For relevant cosmic proton energies a small overview is given of the relation between the energy in the FT frame, the $\sqrt{s}$ value, the value for the relativistic factor γ and, approximately, the cosmic ray flux in Table 8.1

E [eV]	$10^{13.5}$	10^{14}	$10^{14.5}$	10^{15}	$10^{15.5}$	10^{16}
$\sqrt{s}$ [GeV]	250	440	770	1400	2500	4400
γ	135	235	410	745	1330	2350
flux [$\mathrm{m^{-2}\,sr^{-1}\,s^{-1}}$]	$1.0 \cdot 10^{-3}$	$1.5 \cdot 10^{-4}$	$2.1 \cdot 10^{-5}$	$3.0 \cdot 10^{-6}$	$3.7 \cdot 10^{-7}$	$3.7 \cdot 10^{-8}$

Table 8.1: Energies in the FT frame and the corresponding values for $\sqrt{s}$ and γ.

At observation level a sub core is a more or less circular spot. The density is large at the center of the spot and decreases with distance from this center. For an estimate of the size of the spot caused by a jet we consider a jet cone with radius R. The larger R the larger the variation of the azimuth angle $\Delta\phi$ and the variation of the pseudorapidity $\Delta\eta$, see Equation 8.18. For a circular spot $\Delta\phi = \Delta\eta = R/\sqrt{2}$. A spread of the azimuthal angle then implies an axial spread of

the subcore over a range $d\Delta\phi$ given by

$$d \cdot \Delta\phi = \frac{d \cdot R}{\sqrt{2}} \ . \tag{8.23}$$

From $\eta' \approx -\ln(\theta'/2)$ it follows $|\Delta\theta'| \approx \theta' \Delta\eta' \approx \Delta\eta'/(\gamma e^{\eta}) = \Delta\eta/(\gamma e^{\eta})$. A spread of the pseudorapidity therefore leads to a radial spread of the subcore over a range Δd given by

$$\Delta d = \Delta h |\Delta\theta'| = \frac{\Delta h \cdot \Delta\eta}{\gamma e^{\eta}} = \frac{d \cdot R}{\sqrt{2}} \ . \tag{8.24}$$

For the radius r of the spot at observation level we therefore have

$$r = \frac{d \cdot R}{\sqrt{2}} \ . \tag{8.25}$$

Assuming that most of the density of a jet is inside $R = 0.1$, we approximately obtain $r \approx 0.07d$. In Chapter 10 it will be used as a guide for the size of a cluster of detectors for the detection of wide spread sub cores.

8.5 Cross sections

The interaction of a primary particle with a nucleus in an atom of the air has much in common with p-p interactions. The latter can be investigated by means of a Monte Carlo (MC) model as PYTHIA. The interactions can be divided in elastic and inelastic interactions. The inelastic processes in the soft QCD domain are divided in non-diffractive (ND)and diffractive processes. The ND processes are sometimes also called minimum bias (MB) processes. Three diffractive processes are distinguished: central diffractive (CD), double diffractive (DD) and single diffractive (SD). If desired the latter process can be divided in the two sides of the single diffraction: left (SD_L) or right (SD_R), both with the same cross section. For instance, for p-p collisions with $\sqrt{s} = 1400\,\text{GeV}$ the inelastic cross section is about 55 mb of which 68 % is ND, 18 % is SD, 13 % is DD and 1 % is CD. The diffractive processes are in the forward direction. In hard interactions with a large virtuality the inelastic processes are described by perturbative QCD. In these processes multiples of particles are produced with a large component in the transverse direction, sometimes almost collinear: jets. The cross section for hard QCD processes is a small fraction of the total inelastic cross section. For brevity, if 6 GeV/c and 18 GeV/c is taken for $\widehat{p}_{\text{T}}^{\,\text{min}}$ and $\widehat{p}_{\text{T}}^{\,\text{max}}$ respectively, the phase space will be referred to by its center $\widehat{p}_{\text{T}} = 12\,\text{GeV/c}$. The larger $\sqrt{s}$ the larger the hard QCD cross section, σ_{QCD}, whereas the larger $\widehat{p}_{\text{T}}$ the smaller σ_{QCD}, see Figure 8.8. To obtain jet rates we have to consider the probability for a jet to occur in a shower. That is, we have to consider the cross sections for hadronic collisions with large jet transverse momentum. Since we will frequently use them the cross section values are tabulated in Table 8.2 with different $\sqrt{s}$ and $\widehat{p}_{\text{T}}$ as the entries.

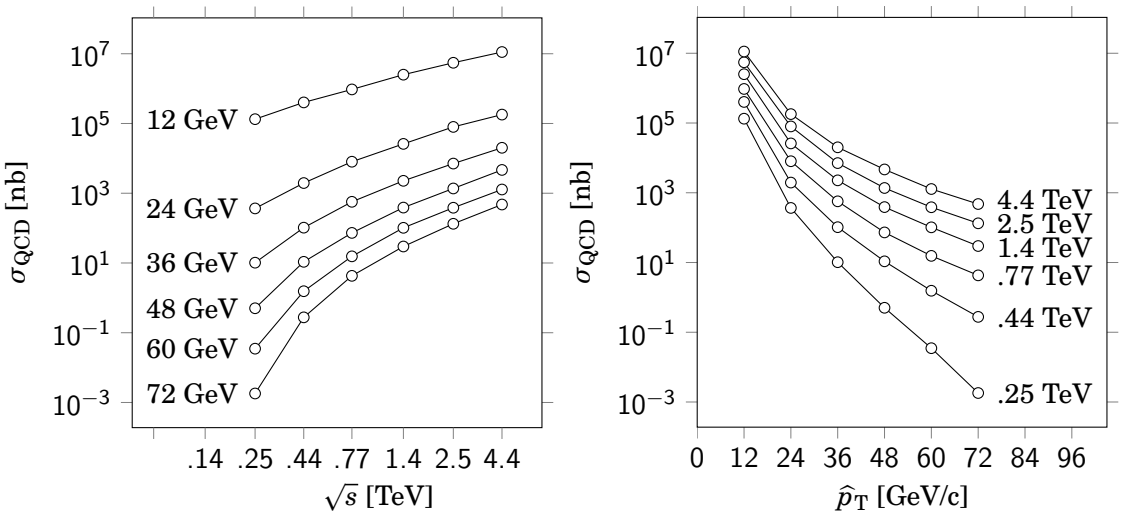

Figure 8.8: Inelastic cross section versus $\sqrt{s}$ for six values of $\widehat{p}_{\mathrm{T}}$ (left) and versus $\widehat{p}_{\mathrm{T}}$ for six values of $\sqrt{s}$ (right). The markers are connected with solid line segments to guide the eye.

$\sqrt{s}$ \ $\widehat{p}_{\mathrm{T}}$	12 GeV/c	24 GeV/c	36 GeV/c	48 GeV/c	60 GeV/c	72 GeV/c	84 GeV/c
250 GeV	$1.33 \cdot 10^5$	$3.67 \cdot 10^2$	$1.02 \cdot 10^1$	$5.03 \cdot 10^{-1}$	$3.49 \cdot 10^{-2}$	$1.81 \cdot 10^{-3}$	$7.82 \cdot 10^{-5}$
440 GeV	$4.02 \cdot 10^5$	$1.96 \cdot 10^3$	$1.03 \cdot 10^2$	$1.08 \cdot 10^1$	1.55	$2.76 \cdot 10^{-1}$	$4.88 \cdot 10^{-2}$
770 GeV	$9.48 \cdot 10^5$	$8.01 \cdot 10^3$	$5.68 \cdot 10^2$	$7.29 \cdot 10^1$	$1.55 \cdot 10^1$	4.28	1.26
1400 GeV	$2.51 \cdot 10^6$	$2.60 \cdot 10^4$	$2.27 \cdot 10^3$	$3.88 \cdot 10^2$	$1.02 \cdot 10^2$	$2.97 \cdot 10^1$	$1.05 \cdot 10^1$
2500 GeV	$5.51 \cdot 10^6$	$7.98 \cdot 10^4$	$7.09 \cdot 10^3$	$1.37 \cdot 10^3$	$3.84 \cdot 10^2$	$1.33 \cdot 10^2$	$5.19 \cdot 10^1$
4400 GeV	$1.12 \cdot 10^7$	$1.80 \cdot 10^5$	$2.01 \cdot 10^4$	$4.66 \cdot 10^3$	$1.28 \cdot 10^3$	$4.75 \cdot 10^2$	$1.84 \cdot 10^2$
7700 GeV	$2.14 \cdot 10^7$	$4.29 \cdot 10^5$	$5.39 \cdot 10^4$	$1.22 \cdot 10^4$	$3.72 \cdot 10^3$	$1.51 \cdot 10^3$	$6.97 \cdot 10^2$

Table 8.2: Cross sections in nb for inelastic p-p collisions with large $\widehat{p}_{\mathrm{T}}$. The $\sqrt{s}$ values correspond to energies $10^{13.5}$, 10^{14}, ..., $10^{16.5}$ eV in the FT frame.

The inelastic p-p cross section is up to $\sqrt{s} = 7\,\mathrm{TeV}$ and even $\sqrt{s} = 13\,\mathrm{TeV}$ obtained from collider experiments [101–104]. For $\sqrt{s} > 10\,\mathrm{GeV}$ it is approximately given by

$$\sigma_{\mathrm{p\text{-}p}}^{\mathrm{inel}}[\mathrm{mb}] \approx 39.3 - 25.95 \ln\sqrt{s} + 18.11 \left(\ln\sqrt{s}\right)^{1.22} , \tag{8.26}$$

where $\sqrt{s}$ is in GeV. The probability for a jet to occur in a p-p collision is the ratio of σ_{QCD} and $\sigma_{\mathrm{p-p}}^{\mathrm{inel}}$. For instance, for $\sqrt{s} = 1400\,\mathrm{GeV}$ and $\widehat{p}_{\mathrm{T}} = 36\,\mathrm{GeV/c}$ the QCD cross section is $2.27 \cdot 10^3$ nb

for p-p collisions, see Table 8.2. Since the inelastic cross section for p-p collisions at this energy is about 55 mb, the probability for a jet for the p-p collision under the given conditions is $4.1 \cdot 10^{-5}$. Since 1400 GeV corresponds to $1 \cdot 10^{15}$ eV in the FT frame, this implies the probability for a jet generated in the first interaction of a 10^{15} eV shower to be $4.1 \cdot 10^{-5}$ per shower. That is, if the first interaction would be a p-p collision. In reality it will be a p-air collision. For p-air collisions the cross section is larger since there are more nucleons available for interaction in an air nucleus. The cross section is almost linear with the logarithm of the energy [105, 106]. It is approximately given by

$$\sigma^{\text{inel.}}_{\text{p-air}}[\text{mb}] \approx -210 + 40 \log_{10}(E[\text{eV}]) \,, \tag{8.27}$$

The relation between the ratio of inelastic p-air and p-p cross sections and the mass number of air is often expressed as [107]

$$\sigma^{\text{inel.}}_{\text{p-air}} = A^{\alpha} \sigma^{\text{inel.}}_{\text{p-p}} \,, \tag{8.28}$$

where A is the mass number of air, $A \approx 14.5$ and where $\alpha = 2/3$. It can be obtained from geometrical considerations by taking the mass number of a nucleus proportional to a spherical volume, $A \propto r^3$, and the cross section proportional to area of the circle, $\sigma \propto r^2$. In reality α is a little larger. That is, it decreases from about 0.78 at $\sqrt{s} = 0.14\,\text{TeV}$ to 0.67 at $\sqrt{s} = 14\,\text{TeV}$. A plot of the inelastic p-air cross section against primary energy and a plot of inelastic p-p cross section against center of mass energy are shown in Figure 8.9.

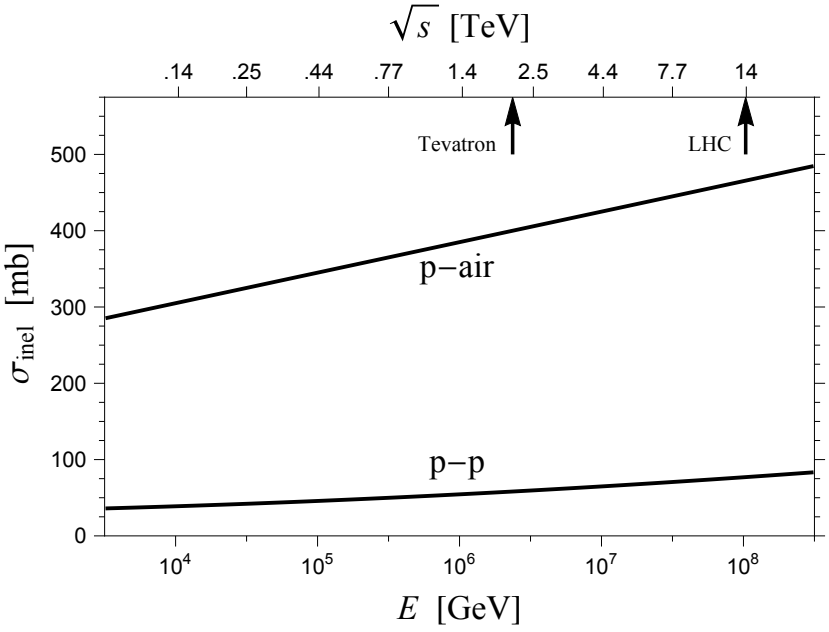

Figure 8.9: Inelastic p-air cross section against primary energy and inelastic p-p cross section against center of mass energy.

The relation between the jet cross section for p-air collisions and for p-p collisions also is expressed via a power of the mass number:

$$(\mathrm{d}\sigma/\mathrm{d}p_\mathrm{T})^{\mathrm{jet}}_{\mathrm{p-air}} \approx A^{\alpha}(\mathrm{d}\sigma/\mathrm{d}p_\mathrm{T})^{\mathrm{jet}}_{\mathrm{p-p}} \,. \tag{8.29}$$

If a proton collides with the first nucleon it meets in a nucleus a jet can occur. If not, there is a probability that the leading particle after the former collision will cause a jet. The probability for a jet to occur is, roughly speaking, proportional with the size of the nucleus, thus with $A^{1/3}$. The jet cross section is therefore enhanced with respect to the usual inelastic cross section in that $\alpha \approx 1$. In reality α deviates from 1 dependent on the transverse momentum, the Cronin effect [108–110]. For energy $\sqrt{s} = 500\,\mathrm{GeV}$ and transverse momentum, $p_\mathrm{T} \approx 20\,\mathrm{GeV/c}$, it is found from jet observations in cosmic showers that α is 1.56 [111]. The α found for p-air is close to the α values found for p-Al and p-Pb in collision experiments [112–114]. For larger transverse momenta α seems to flatten or even decrease for increasing transverse momenta. For smaller transverse momenta α decreases to 2/3 for $p_\mathrm{T}^{\mathrm{jet}} \to 0$. After correction for the underlying event α still takes on values between 1 and 1.26 for $p_\mathrm{T}^{\mathrm{jet}}$ in the neighborhood of 10 GeV/c [115]. For larger transverse momenta α diminishes to 1. For the calculation of jet probabilities in the present analysis α will be taken equal to 1. Since $14.5^{0.26} \approx 2$ we have to keep in mind that the resulting rates for jet observations may be 50 % too small.

The value 1 for α implies a 14.5 times larger jet cross section for p-air than for p-p. For instance, for a $10^{15}\,\mathrm{eV}$ shower and $\widehat{p}_\mathrm{T} = 24\,\mathrm{GeV/c}$ we obtain $\Delta\sigma^{\mathrm{jet}}_{\mathrm{p\text{-}air}} \approx 0.38\,\mathrm{mb}$ while the total inelastic cross section is 390 mb. The corresponding probability for such a jet is $1.0 \cdot 10^{-3}$ per shower. For different cosmic ray energies and different $\widehat{p}_\mathrm{T}$ the jet probabilities are calculated in the same way. The results are shown in Table 8.3.

$\sqrt{s}$ \ $\widehat{p}_\mathrm{T}$	12 GeV/c	24 GeV/c	36 GeV/c	48 GeV/c	60 GeV/c	72 GeV/c	84 GeV/c
250 GeV	$5.8 \cdot 10^{-3}$	$1.6 \cdot 10^{-5}$	$4.5 \cdot 10^{-7}$	$2.2 \cdot 10^{-8}$	$1.5 \cdot 10^{-9}$	$8.0 \cdot 10^{-11}$	$3.4 \cdot 10^{-12}$
440 GeV	$1.7 \cdot 10^{-2}$	$8.1 \cdot 10^{-5}$	$4.3 \cdot 10^{-6}$	$4.5 \cdot 10^{-7}$	$6.4 \cdot 10^{-8}$	$1.1 \cdot 10^{-8}$	$2.0 \cdot 10^{-9}$
770 GeV	$3.7 \cdot 10^{-2}$	$3.1 \cdot 10^{-4}$	$2.2 \cdot 10^{-5}$	$2.9 \cdot 10^{-6}$	$6.1 \cdot 10^{-7}$	$1.7 \cdot 10^{-7}$	$4.9 \cdot 10^{-8}$
1400 GeV	$9.3 \cdot 10^{-2}$	$1.0 \cdot 10^{-3}$	$8.4 \cdot 10^{-5}$	$1.3 \cdot 10^{-5}$	$3.8 \cdot 10^{-6}$	$1.1 \cdot 10^{-6}$	$3.9 \cdot 10^{-7}$
2500 GeV	$1.9 \cdot 10^{-1}$	$2.8 \cdot 10^{-3}$	$2.5 \cdot 10^{-4}$	$4.8 \cdot 10^{-5}$	$1.4 \cdot 10^{-5}$	$4.7 \cdot 10^{-6}$	$1.8 \cdot 10^{-6}$
4400 GeV	$3.8 \cdot 10^{-1}$	$6.1 \cdot 10^{-3}$	$6.8 \cdot 10^{-4}$	$1.6 \cdot 10^{-4}$	$4.3 \cdot 10^{-5}$	$1.6 \cdot 10^{-5}$	$6.2 \cdot 10^{-6}$
7700 GeV	$6.9 \cdot 10^{-1}$	$1.4 \cdot 10^{-2}$	$1.7 \cdot 10^{-3}$	$3.9 \cdot 10^{-4}$	$1.2 \cdot 10^{-4}$	$4.9 \cdot 10^{-5}$	$2.2 \cdot 10^{-5}$

Table 8.3: Jet probability in first interaction.

9

Simulating jets in cosmic air showers

9.1 Simulation

This chapter concerns the simulation of jets in showers and the inspection of the fluctuations in the simulated signals of a large array of detectors. The way to distinguish the jet fluctuations from background fluctuations in the density is described. The simulation of jets is conducted for observation level at 4, 2 and 0 km altitude. Jets are actually observed with a large array at 4 km altitude by the ARGO-YBJ experiment at a rate of 10^2 per month [116, 117]. These observed jet rates are compared with the simulated jet rate at 4 km altitude. For the Netherlands the simulation for 0 km altitude gives an estimate of the expected rate.

For the simulation of jets in cosmic air showers we will use the output of large p_T events generated with PYTHIA as input for CORSIKA. This can be done by means of the STACKIN option which requires a list of secondary particles for the first collision. The conversion of the final state particles of the PYTHIA events to the secondary particles for the CORSIKA/STACKIN input is summarized in Table 9.1.

particle	C-id.	P-id.	particle	C-id.	P-id.	particle	C-id.	P-id.
γ	1	22	π^0	7	111	K^-	12	-321
e^+	2	-11	π^+	8	211	n	13	2112
e^-	3	11	π^-	9	-211	p	14	2212
μ^+	5	-13	K^0_L	10	130	$\overline{p}$	15	-2212
μ^-	6	13	K^+	11	321	$\overline{n}$	16	-2112

Table 9.1: CORSIKA and PYTHIA identifiers for shower particles.

With PYTHIA the p-p collisions are simulated for a given energy and a given cut by means of $\widehat{p}_{\mathrm{T}}^{\,\mathrm{min}}$ and $\widehat{p}_{\mathrm{T}}^{\,\mathrm{max}}$. The simulations are performed in the CM frame to obtain the transverse momentum, η and ϕ of the leading jet and the next to leading jet with the jet finder. The secondary particles are given a Lorentz boost to obtain the FT values of the energy and momenta of the particles as required for the CORSIKA/STACKIN input. A C++ code steers PYTHIA and generates the files to steer CORSIKA, the input files for CORSIKA and a separate text file with the information obtained by the jet finder. The CORSIKA runs deliver 'DATnnnnnn' files with information about the lateral distribution. These files are converted to files in HDF5 format by means of the store-corsika-data module of the Python package SAPPHiRE. A Python script reads the lateral positions of the electrons and muons from the HDF5 files, throws them on an array of detectors and inspects the resulting detector signals for jet cores. The results of the inspection are stored in a text file. Both the text file with the jet finder results and the text file with the results of the Monte Carlo form the input for a Mathematica code which compares the simulated sub cores with the simulated jets.

For the analysis of the simulated data we follow to a certain extent a similar approach as performed for data by the ARGO-YBJ experiment [116, 117]. The size of their 'BigPads' is $1.4\times 1.25\,\mathrm{m}$ in an area of $1.5\times 1.3\,\mathrm{m}$. For the present investigation the particles are thrown on two kinds of regular arrays of joint detector plates. One kind of array consists of 53×53 detector plates with size $\sqrt{2}\times\sqrt{2}$ m, while the other kind of array consists of 75×75 detector plates with size 1×1 m. In both cases the total observational area is $5.6\cdot 10^3\,\mathrm{m}^2$, comparable with the observational area of the ARGO-YBJ experiment. The number of detector plates is 2809 and 5625 respectively. In addition we will consider for each kind of array the situation where the neighbors of a plate are alternately removed, see Figure 9.1. The latter chessboard constellation requires half the number of square plates.

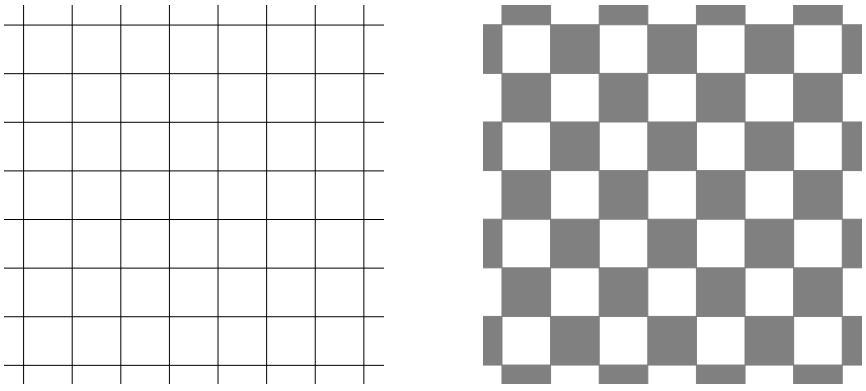

Figure 9.1: Detector plates in a filled array constellation (left) and an alternate array constellation (right). The black squares represent the absence of a detector plate.

For the simulations we use $10^{13.5}$, 10^{14}, $10^{14.5}$, 10^{15}, $10^{15.5}$ and, for as far necessary, 10^{16} eV

vertical showers. For the jets we take the distributions as generated by different slices of $\widehat{p}_T$ with edges 6, 18, 30, 42, 54, 66 and 78 GeV/c. The slices are briefly denoted by their bin centers: 12, 24, 36, 48, 60 and 72 GeV/c. For each $\widehat{p}_T$ bin the transverse momentum and pseudorapidity of the leading and next to leading jet is obtained from the jet finder. For 100 showers per bin this gives 200 transverse jet momenta and 200 jet pseudorapidities. As an illustration the generated distributions of p_T^{jet} and η^{jet} in 10^{15} eV showers are shown in Figure 9.2. For a constant energy the distribution of the pseudorapidity of jets narrows for increasing transverse momentum, see Figure 9.2.

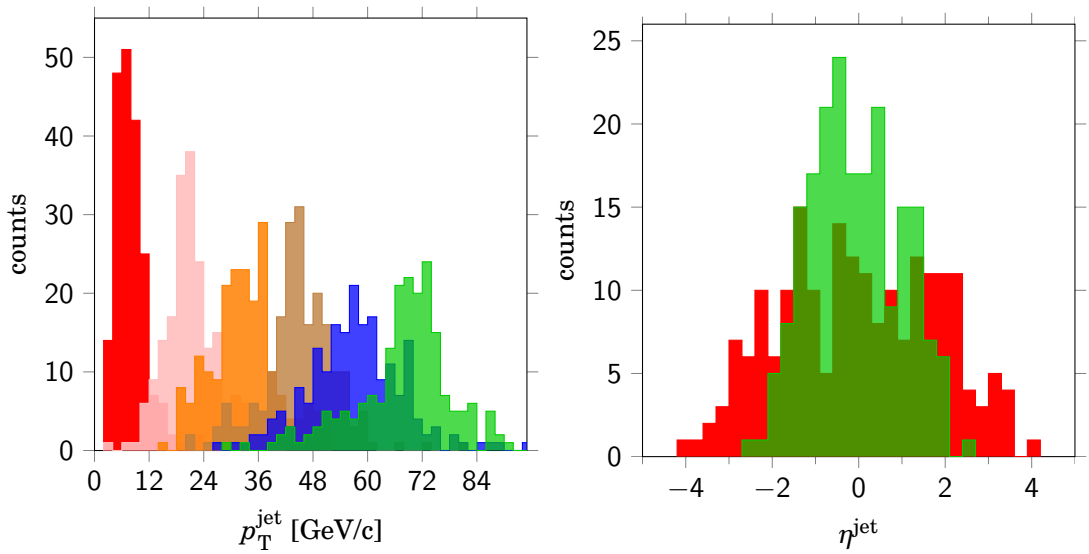

Figure 9.2: Left panel: distribution of transverse jet momentum for $\sqrt{s}$= 1400 GeV and for $\widehat{p}_T$ bin centers 12, 24, 36, 48, 60 and 72 GeV/c (red, pink, orange, brown, blue and green). Right panel: distribution of jet pseudorapidity for $\sqrt{s}$= 1400 GeV and for $\widehat{p}_T$ bin centers 12 and 72 GeV/c (red and green).

9.2 Altitude of first interaction

The STACKIN option for CORSIKA requires a specified altitude of first interaction in the input file of a shower. Different altitudes in the sample of showers are achieved by specifying a different altitude for each shower. The distribution of altitudes is determined by the cross section for p-air collisions. The distribution of altitudes and of atmospheric depths of first interaction are shown in Figure 9.3. The shape of the distributions can be understood as follows. The distribution of atmospheric depth of first interaction is given by the zero order Erlang distribution: $f(X) = \frac{1}{\lambda} e^{-X/\lambda}$, where λ is the interaction length. For a p-air cross section of 390 mb, valid for a 10^{15} PeV shower, the interaction length is about 61 g cm^{-2}. The theoretical distribution $f(X) \approx \frac{1}{61} e^{-X/61}$ is shown as a red curve in the right panel of Figure 9.3.
The distribution of the altitude of first interaction follows from $f(h) = |\frac{dX}{dh}| f(X)$. The U.S. 1976

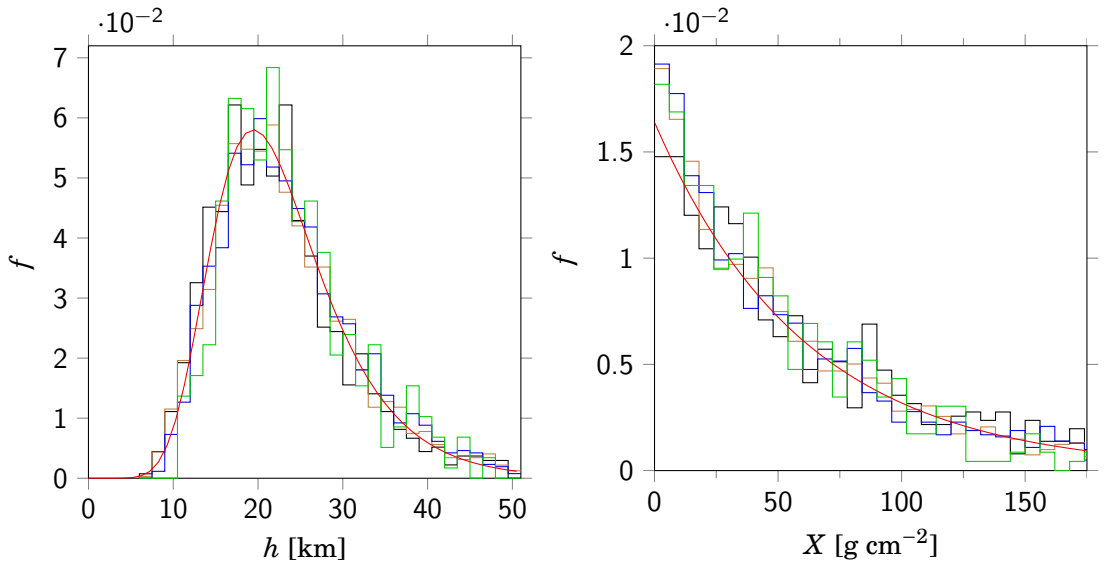

Figure 9.3: Normalized distribution of altitude (left) and atmospheric depth (right) of first interaction for showers with energy 10^{14} (black), 10^{15} (brown), 10^{16} (blue) and 10^{17} eV (green). In each panel the red curve is a fit for the 10^{15} eV distribution, see the text.

Standard Atmosphere, which is the default in CORSIKA, is for altitudes between 11 and 25 km approximately given by [118]:

$$X = 1308 \cdot e^{-h/6.34} \,, \tag{9.1}$$

with h in km. If this relation is taken for the altitudes of first interaction the distribution of height of first interaction reads

$$f(h) = \frac{1308}{6.34\lambda} e^{\left(-\frac{h}{6.34} - \frac{1308}{\lambda} e^{-h/6.34}\right)} \,. \tag{9.2}$$

The latter is shown as a red curve in the left panel of Figure 9.3 for $\lambda = 61\,\mathrm{g\,cm^{-2}}$. The distribution Equation 9.2 can be written in the form of a Gumbel distribution:

$$f(x) = \frac{1}{\beta} e^{-(x-\mu)/\beta - e^{-(x-\mu)/\beta}} \,. \tag{9.3}$$

Fits of the distributions shown in Figure 9.3 deliver $\lambda \approx 67, 61, 58, 54\,\mathrm{g\,cm^{-2}}$ for shower energies 10^{14}, 10^{15}, 10^{16} and 10^{17} eV. The corresponding cross sections $3.6 \cdot 10^2$, $3.9 \cdot 10^2$, $4.2 \cdot 10^2$ and $4.5 \cdot 10^2$ mb are in agreement with p-air cross sections in the literature [106].

To simulate variable heights of first interaction we take the cumulative h distribution by integrating Equation 9.2

$$F(h) = e^{\left(-\frac{1308}{\lambda} e^{-h/6.34}\right)} \tag{9.4}$$

and invert it to

$$h = -6.34 \ln\left(-\frac{\lambda}{1308} \ln F\right) . \tag{9.5}$$

Now one can either draw a random number between 0 and 1 for F or one can divide the interval $(0,1)$ in a number of equidistant values for F. For samples of 100 different showers per energy the latter approach is preferred. That is, the values 0.005 through 0.995 in steps of 0.01 for F then deliver values for h according to Equation 9.2. The values for h obtained this way are used in the STACKIN input files.

9.3 Lateral density from array signals

On the basis of the simulated signals of the array detectors the combined lateral density of electrons and muons is foreach shower fitted with a fit function. A NKG type of fit function is less suited since the densities observed with the array detectors are limited in number and in distance to the core. For this reason the following close-to-core approximation of the lateral density is applied by the ARGO-YBJ experiment [116]

$$\rho(r) \approx p_1 \cdot r^{p_2} , \tag{9.6}$$

where p_1 and p_2 are the fit parameters. The density approximately follows a power law for distances smaller than 10 m. In Figure 9.4 a fit with this function shows that it is not accurate when larger distances are considered.

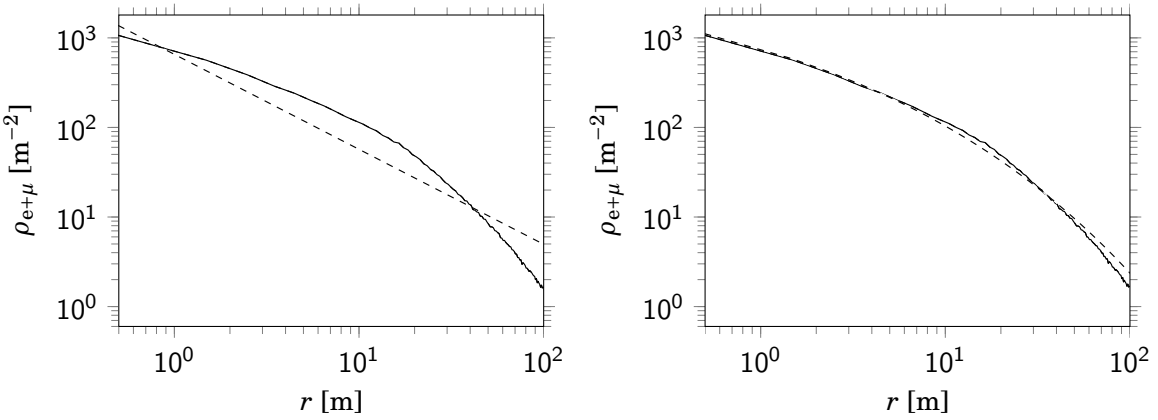

Figure 9.4: Fit curve (dashed) of lateral density (solid) by means of Equation 9.6 (left) and Equation 9.7 (right).

We therefore will apply a different fit function:

$$\rho_{\text{fit}}(r) \approx a \cdot e^{(r/r_0)^{0.28}} , \tag{9.7}$$

with a and r_0 as fit parameters. In the right panel of Figure 9.4 a fit with this function illustrates its improved accuracy.

It is instructive to see how things look when all the signals of the array detectors are scattered against distance to the main core, see Figure 9.5.

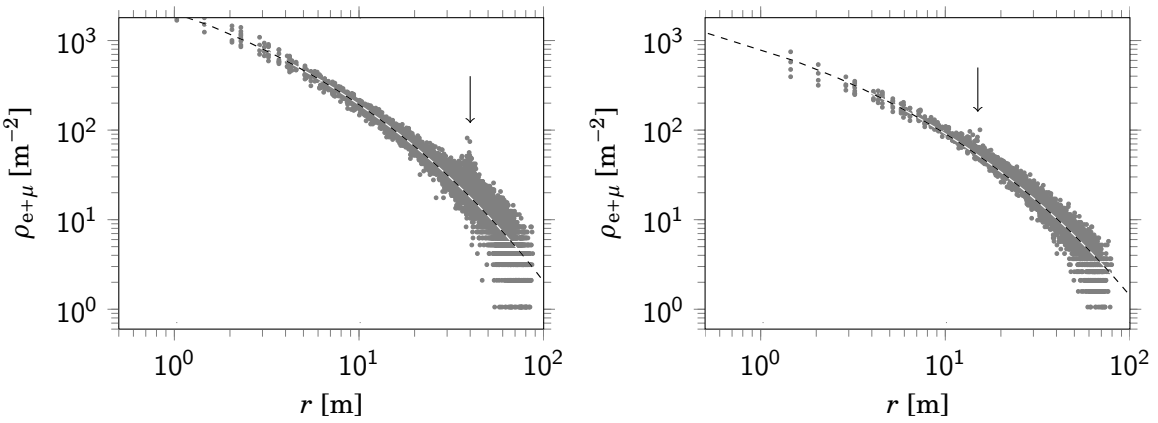

Figure 9.5: Detector densities for a $\sqrt{2} \times \sqrt{2}$ filled array as caused by two different 1 PeV showers with p_T^{jet}=100 GeV/c. For one shower the observation level is at 4 km (left) and for the other shower the observation the observation level is at 2 km (right). The dashed curve is the fit by means of Equation 9.7. The arrows indicate the jet fluctuations.

We see in the left panel clearly the footprint of a jet at a distance of about 40 m. In the right panel a footprint of a jet for another shower can be seen at a distance of about 15 m.

9.4 Fluctuations in a shower

The ground particles resulting from the CORSIKA simulations are inspected for density fluctuations. To distinguish strong jet fluctuations from statistical fluctuations we need a measure. For this the ratio N_{obs}/N_{fit} is considered, where N_{obs} is the observed number of particles on a plate and where N_{fit} is the number of particles on a plate as expected on the basis of ρ_{fit}. Since N_{obs} can not take on values below zero, the distribution of the ratio is rather log normal distributed. This means that the logarithm of the ratio approximately follows a Gaussian distribution. Therefore the distribution of

$$f = \log_{10}(N_{obs}(r)) - \log_{10}(N_{fit}(r)) \ . \tag{9.8}$$

is usually considered. The distribution of f is approximately Gaussian, with μ close to zero. Figure 9.6 shows the distributions of f and the Gaussian fit curves for two different 1 PeV showers thrown on an array of $\sqrt{2} \times \sqrt{2}$ m detectors.

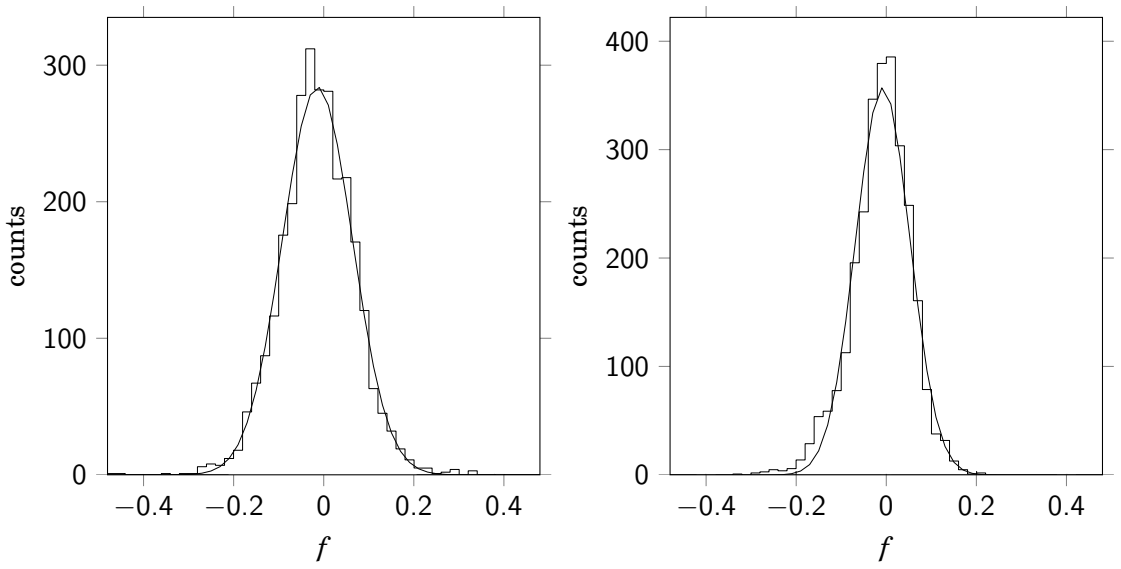

Figure 9.6: Distribution of f and the Gaussian fit curves for two different 1 PeV showers. For the left panel σ is 0.078 and for the right panel it is 0.060.

The σ for each shower in Figure 9.6 is based on all the array signals. However, σ depends on the distance to the main core. From uncertainty analysis, with the Poisson variance for the uncertainty, it follows that

$$\sigma = \sqrt{\left[\frac{\partial f}{\partial N_{\text{obs}}}\sigma(N_{\text{obs}})\right]^2_{N_{\text{obs}}=N_{\text{fit}}}} = \frac{1}{\ln(10)\cdot\sqrt{N_{\text{fit}}}}\,. \tag{9.9}$$

The substitution of $N_{\text{fit}}(r)$, based on the density function ρ_{fit}, gives a semi-theoretical prediction for σ as a function of distance. Of course, not completely theoretical since the observed density is substituted. Since $N_{\text{fit}} = a\rho_{\text{fit}}$, with a the detector area, the semi-theoretical prediction is

$$\sigma(r) \approx \frac{1}{\ln(10)\cdot\sqrt{a\rho_{\text{fit}}(r)}}\,. \tag{9.10}$$

To investigate the dependence of σ on the distance to the main core the σ is determined for distributions of f binned for different radii. In Figure 9.7 the σ's as obtained by binned distributions are shown for a 1 PeV shower thrown at 25 arbitrary positions within an array at 4 km altitude. For comparison the $\sigma(r)$ according to the semi-theoretical equation are also shown.

We see the binning result for $\sigma(r)$ follows the semi-theoretical prediction. For the alternate arrays the plots are comparable. It therefore is inaccurate to consider a single value for σ on the basis of the whole array, or of a part of it. For the determination of $\sigma(r)$ the detectors with zero particles are discarded since the f values become $-\infty$. As a consequence the binning

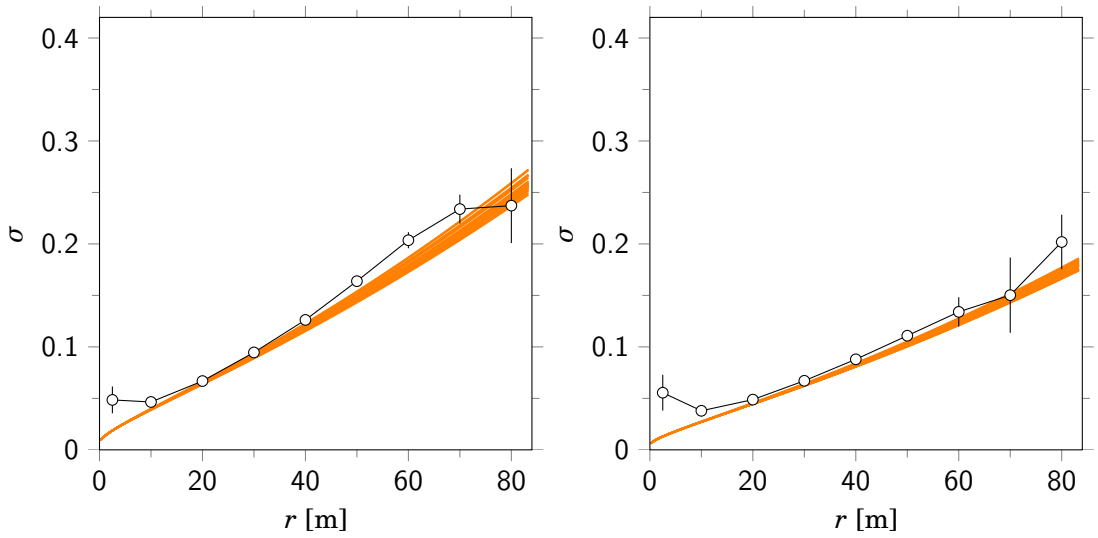

Figure 9.7: The σ of the distribution of f against distance from the main core for a 10^{15} eV shower thrown 25 times at a filled array of 1×1 detectors (left) and $\sqrt{2} \times \sqrt{2}$ detectors (right). In both cases the observation level is 4 km. In orange are shown the 25 curves according to the semi-theoretical prediction.

result for σ tends to too small values in the region where the number of particles per detector is smaller than 3. It flattens the $\sigma(r)$ curve as can be seen at the binning result for $r = 80\,\mathrm{m}$ in the left panel of Figure 9.7. The binning results are therefore not plotted for densities below 3 particles per detector. As another example we consider the σ for a $10^{14.5}$ eV shower at 4 km altitude, see Figure 9.8.

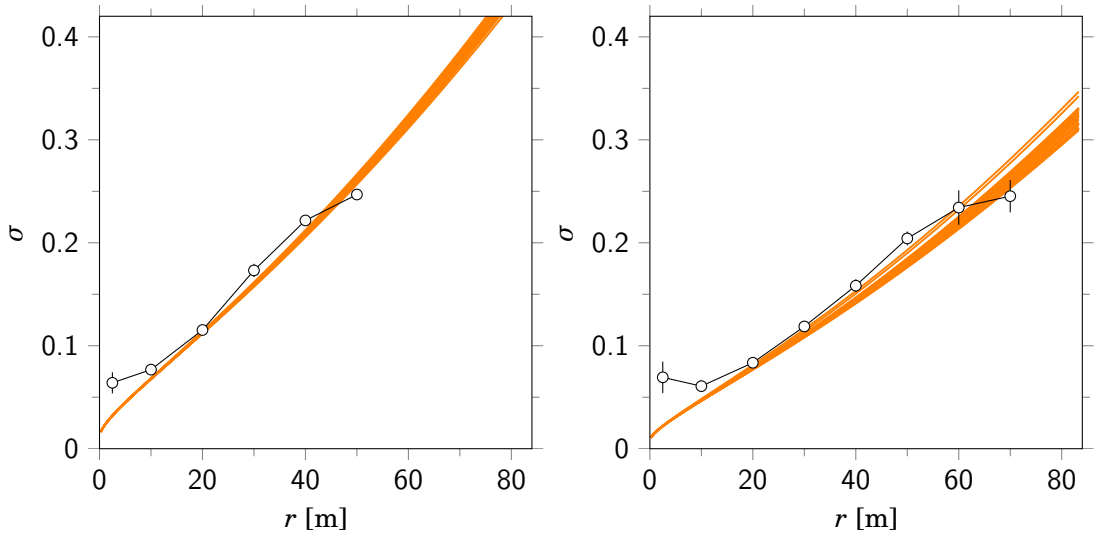

Figure 9.8: The σ of the distribution of f against distance from the main core for a $10^{14.5}$ eV shower thrown 25 times at a filled array of 1×1 detectors (left) and $\sqrt{2} \times \sqrt{2}$ detectors (right). In both cases the observation level is 4 km. In orange are shown the 25 curves according to the semi-theoretical prediction.

As a final example we consider the σ for a 10^{15} eV shower at 2 km altitude and a $10^{15.5}$ eV shower at 0 km altitude, see Figure 9.9.

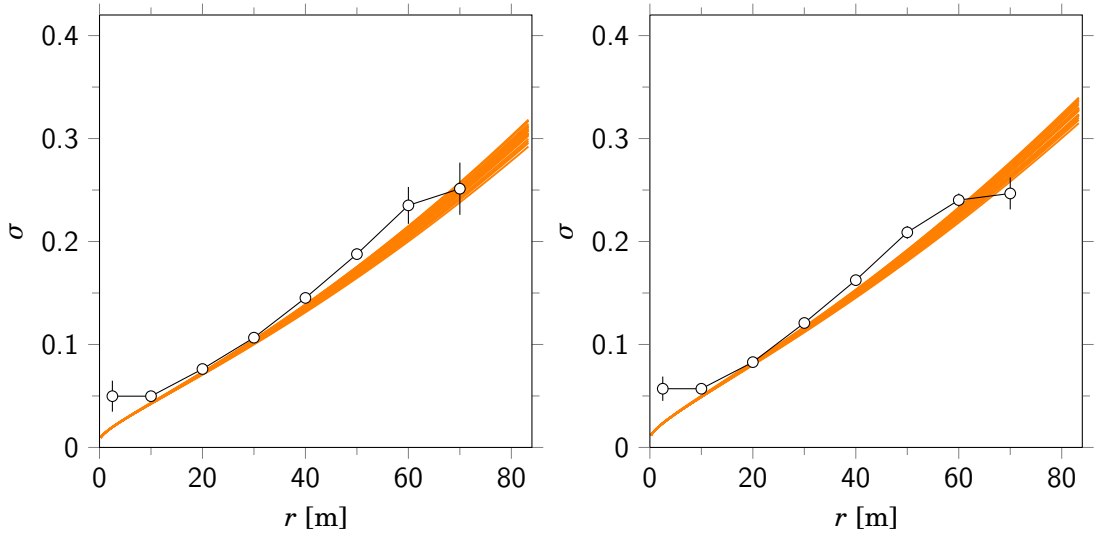

Figure 9.9: The σ of the distribution of f against distance from the main core for a 10^{15} eV shower thrown 25 times at a filled array of 1×1 detectors at 2 km altitude (left) and for a $10^{15.5}$ eV shower thrown 25 times at a filled array of 1×1 detectors at 0 km altitude (right). In orange are shown the 25 curves according to the semi-theoretical prediction.

Also for other energies the binning result follows the semi-theoretical prediction. The semi-theoretical prediction will therefore be applied. However, near the main core the binning result for σ is larger than the semi-theoretical prediction. This means that near the main core the fluctuations are larger than as expected from a Poisson distribution. The large fluctuations are sub cores caused by hadronic interactions at different stages of the development of the shower. The rate and geometric structure of hadronic sub cores near the main core have been measured [119, 121]. If we solely apply the semi-theoretical prediction to the near core distances, the small σ will act as a sink. That is, the algorithm will be attracted to find the best sub cores close to the main core. Since jet observations at altitude 4 km is dominated by 10^{14} and $10^{14.5}$ eV showers we do not expect many sub cores due to simulated jets close to the main core. Near the main core a minimum level for σ will be applied to avoid the sink effect.

The minimum level depends on the size of the shower. In Figure 9.10 the minimum level is plotted against the main core density for 500 different showers taken from different energies and different observation levels.

A fit with the function $\sigma_{\min} = c_1 \cdot M^{c_2}$, where M stands for the main core density, delivered for the parameters c_1 and c_2 the values 0.41 and -0.28 respectively for 1×1 array, and 0.50 and -0.38 for $\sqrt{2} \times \sqrt{2}$ array. For 1×1 arrays the minimum level given by $\sigma_{\min} = 0.41 \cdot M^{-0.28}$

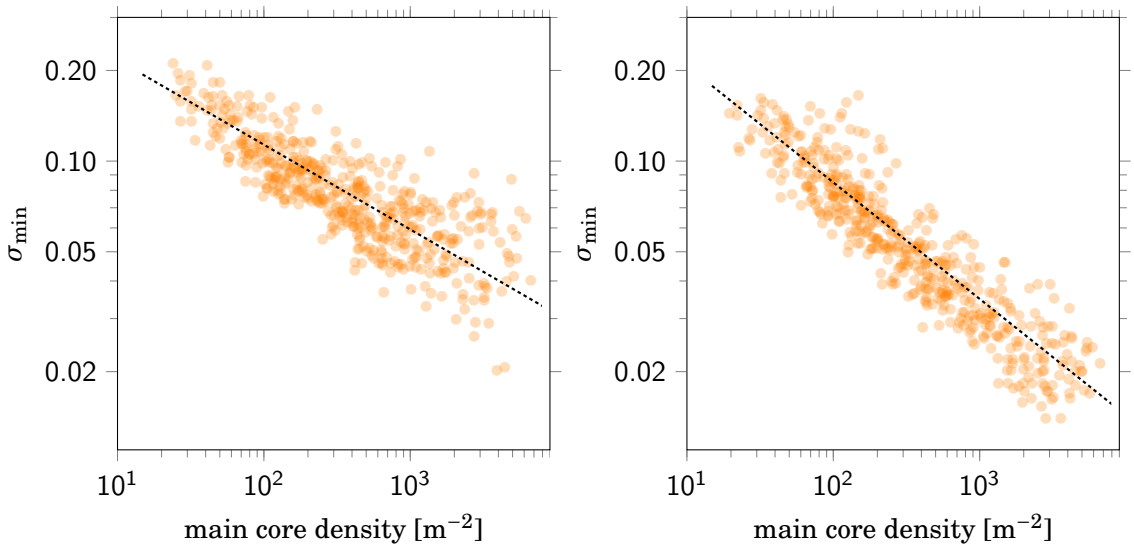

Figure 9.10: The minimum level for σ against main core density for 500 different showers taken from different energies and different observation levels for 1×1 filled array (left) and for $\sqrt{2} \times \sqrt{2}$ filled array (right). The dotted line is a fit with a power law function.

works satisfactorily. This is not the case for a minimum level $\sigma_{\min} = 0.50 \cdot M^{-0.38}$ for $\sqrt{2} \times \sqrt{2}$ arrays. The minimum level seems to be too low in that the $\sqrt{2} \times \sqrt{2}$ arrays become too sensitive for fluctuations. From the right panels in Figure 9.7 and Figure 9.8 we see $\sigma(r)$ has a negative slope for $\sqrt{2} \times \sqrt{2}$ arrays and that the spread is larger in comparison to the situation for 1×1 arrays. This may cause an underestimation of the minimum level for $\sqrt{2} \times \sqrt{2}$ arrays. For all types of arrays a single minimum level is applied:

$$\sigma(r) = \max\left(0.41 \cdot M^{-0.28}, \frac{1}{\ln(10) \cdot \sqrt{a \rho_{\text{fit}}(r)}}\right) \tag{9.11}$$

Afterwards we determine the threshold f value in units of $\sigma(r)$ for a fluctuation to be ascribed to a simulated jet. If the minimum level $0.41 \cdot M^{-.28}$ is slightly too large for $\sqrt{2} \times \sqrt{2}$ arrays it will lead to a lower threshold for f. In this way a too large minimum level will be compensated. The notation $\sigma(r)$ is to express its essential difference with a constant value. It turns out that the application of the latter expression for $\sigma(r)$ leads to comparable $f/\sigma(r)$ values in the different types of arrays. For showers without simulated jets the best $f/\sigma(r)$ values run to approximately 5.5. Larger values occur for low densities and in detectors close to the core, probably caused by hadronic fluctuations at a late stage of the shower. To avoid them some quality cuts are applied. Firstly, a minimum density of $100\,\text{m}^{-2}$ is required for the main core density. Secondly, the inspection region for f is restricted to distances to the core larger than 3, 4 and 5 m for altitudes of 4, 2 and 0 km respectively. The minimum density requirement for the main core is identical to the experimental quality cut applied in the ARGO-YBJ experiment [116].

9.5 Method

For each throw the density for all the detectors will be inspected. The position of the detector with the largest signal is considered as the main core. Then the value of f is evaluated for each detector plate for which $N_{obs} > 0$. The ratio $f/\sigma(r)$ is used as a selection criterium for the best fluctuation. The best cores selected on the basis of f/σ will in general correspond to a large density surplus. The algorithm will always find a best sub core.

To investigate to which extent jet cores can be observed each generated shower is thrown at 100 random positions within an array of detectors. Rotations of the distribution of particles will not be considered since consequences of rotations for the effective area are small. For each throw the signals of the array of detectors are inspected for the determination of the main core and the best sub core. The number of particles in a detector, as obtained by CORSIKA/STACKIN without thinning, is taken as the signal. We will not apply a conversion to a 'real' signal since we are looking here at the best sub cores with densities, of the order of 10^2 m^{-2} and larger. The variance of the number of particles for a pure Poisson distribution is $\sqrt{N}$. The variance caused by the measurement uncertainty is $0.3\sqrt{N}$, see Chapter 4. The combined variance, $1.044\sqrt{N}$, is practically equal to the Poisson variance for large numbers. The measurement uncertainty therefore is not taken into account in the simulation. In addition, the real signal also depends on the directions of individual particles. For the main core these will for a vertical shower be close to the vertical. The best sub cores are close to the main core, the distance is mostly of the order of 15 m. In Figure 9.11 the $\sec\theta$ distribution is shown for the angles of individual electrons and muons for the main core and for a detector at a distance of 15 m.

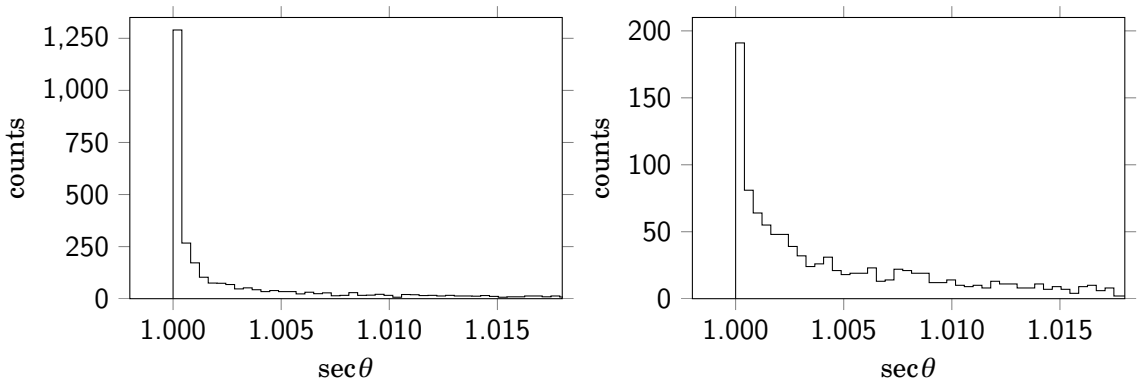

Figure 9.11: The $\sec\theta$ distribution of the zenith angle of individual electrons and muons in a $\sqrt{2}\times\sqrt{2}$ detector at the main core (left) and at a distance 15 m from the main core (right) for a vertical 1 PeV shower at sea level.

As the variation is small, less than 1 %, it can be left out of the simulation. Besides, a precise simulation of the real signal would require the inspection of the direction of all the particles

in all the detectors. For 4 different shower energies, 7 different transverse jet momenta and 3 different observation levels and 4 kinds of arrays we have 336 situations. With 100 showers for each situation and 100 throws for each shower we have 3.4 million throws. The number of particles in a detector ranges from 0, far away from the main core, to several thousands near the main core. All in all one arrives at something of the order of 10^{13} conversions to 'real' signals. This is very time consuming. Besides, it turns out that the main contribution to jet observations is at the edge where a few best sub cores are caused by relatively small transverse jet momenta in relatively low energy showers. The corresponding effective area is consequently uncertain. This uncertainty is far larger than the inaccuracy involved by the aforementioned simplifications. The present analysis is intended to obtain an estimate of the flux of jet observations at different observation levels and for different kinds of arrays. For this it suffices to take the particle number as the detector signal.

For each throw the simulated detector signals will be inspected for the best sub core on the basis of the $f/\sigma(r)$. The position and other properties of the sub core with the best f/σ ratio will be stored and afterwards compared with the position of the two largest simulated jets. A sub core is ascribed to a simulated jet if both the difference Δx and Δy between the sub core position and a jet position are smaller than $1.0 + 0.04d$. If the sub core position and the jet position can not be matched the sub core is ascribed to a non-matching fluctuation. A non-matching fluctuation may be accidental or induced by the jet. In general we will not make a distinction since in real data analysis one can not make the distinction either. Nevertheless, matching sub cores give information of the simulated jets which caused it. For this reason we will separately keep track of matching sub cores.

The method will be illustrated with an example of a 1 PeV shower with simulated jets generated with $\hat{p}_{\mathrm{T}}^{\min} > 100\,\mathrm{GeV/c}$. The observational array is with the $\sqrt{2}\times\sqrt{2}$ plates at an altitude of 4 km. The lateral distribution and the detector densities are shown in Figure 9.12. For the example the altitude of first interaction is 21.8 km. The jet finder returned p_{T} =121.6 GeV/c, $\eta = -1.13$ and $\phi = 0.94$ radian for the leading jet and p_{T} =94.1 GeV/c, $\eta = 0.55$ and $\phi = -1.94$ radian for the next to leading jet. The expected distances of the sub cores with respect to the main core are 74 m respectively 13.8 m. The inspection of the plate densities delivered a best sub core around 14 m and $\phi = -2.0$ radian. The predicted distance and angle for the next to leading jet is in good agreement with the 'observed' distance and angle for the best sub core. The algorithm therefore delivers an 'observed' jet. The density of the best sub core is $270\,\mathrm{m}^{-2}$ while $92\,\mathrm{m}^{-2}$ is expected. The f value of the sub core is 0.47. The semi-theoretical value of σ at a distance of 14 m is 0.047. That is, f is $10\sigma(r)$. This example also shows that the rapidity of a jet is as important as the transverse momentum of a jet.

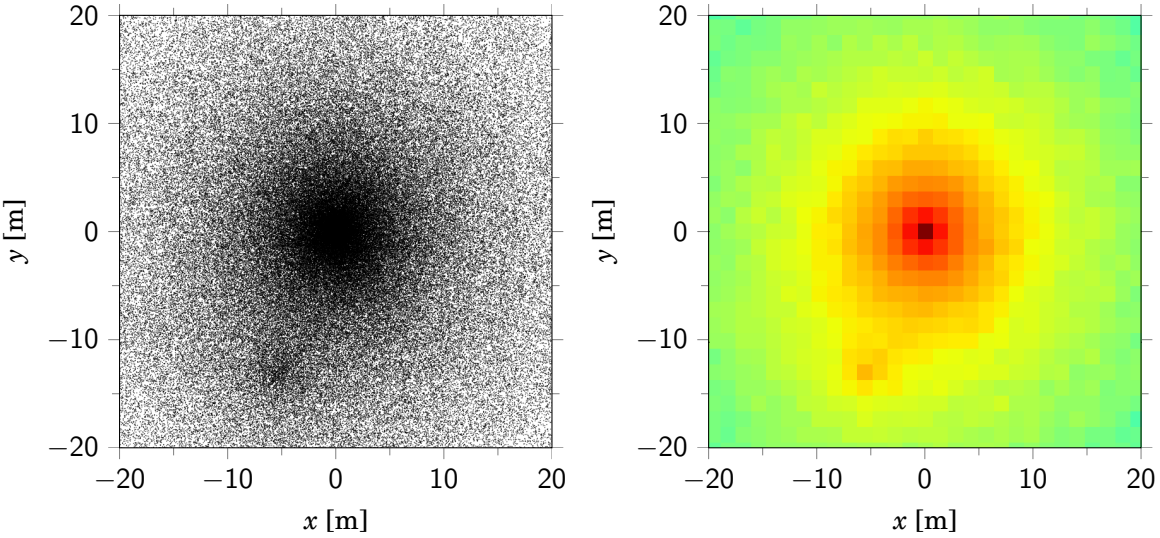

Figure 9.12: Lateral distribution of particles at observation level (left) and detector densities (right) for a shower with an obvious sub core.

9.6 Significance

Each throw delivers a distribution of f/σ of which the best value will be denoted a f^*. A sample of 10 000 throws then will deliver a distribution of f^* values. The showers without a simulated jet deliver a distribution of f^* values which acts as a background signal. In Figure 9.13 the background distribution of f^* is shown for 10^{14} eV showers.

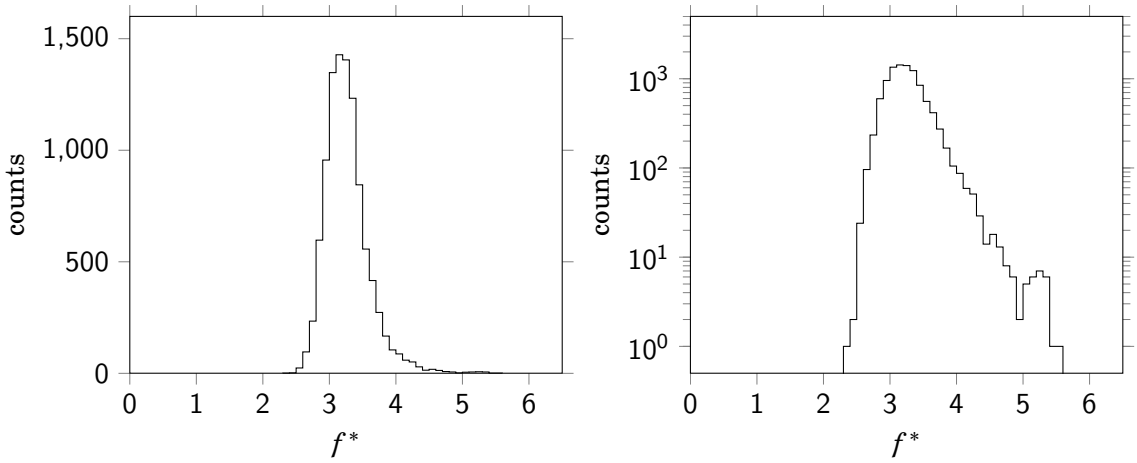

Figure 9.13: The background distribution of f^* for $10^{14.5}$ eV showers for a 1×1 array at 4 km altitude, plotted on a linear scale (left) and on a logarithmic scale (right). Both for a 1×1 array at 4 km altitude.

The distribution of f^* is asymmetric, it has a high end tail. As becomes clear from the plot on a logarithmic scale, the tail falls off exponentially. To determine the slope a domain is considered

in the region where the tail of the distribution is half the maximum and where it is 1 % of the maximum. The extension of the exponentially decreasing function is used as the background for the comparison with large f^* values caused by jets. To ascribe large f^* values to jets we require a 5σ significance. For a normal distribution 5σ corresponds to a probability of $2.87 \cdot 10^{-7}$. Similar to the situation for a normal distribution the f^* value is determined for which the area is a fraction $2.87 \cdot 10^{-7}$ of the total area of the background distribution. For $10^{14.5}$ eV showers for a 1×1 array at 4 km altitude the background distribution of f^* is shown in Figure 9.14. The determination of the 5σ threshold at $f^* = 7.0$ is illustrated in Figure 9.14.

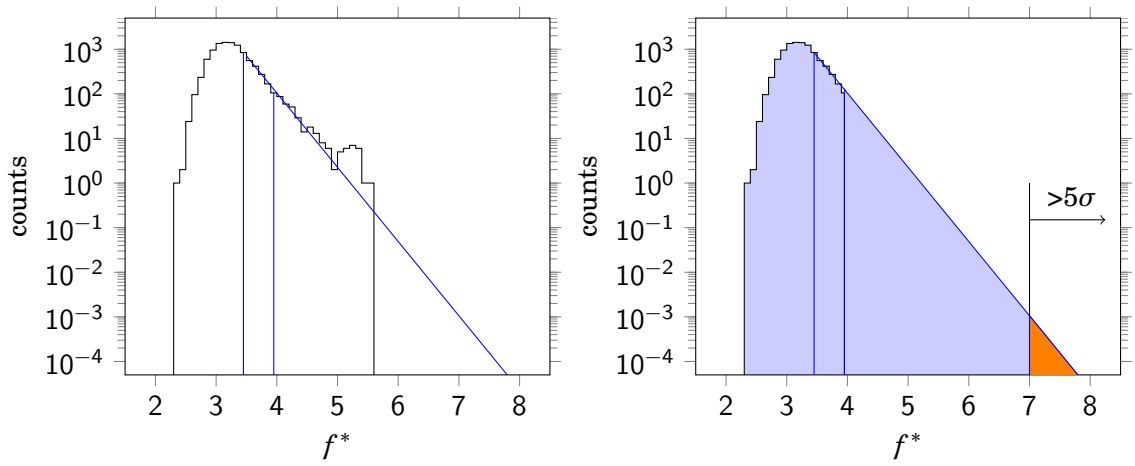

Figure 9.14: For $10^{14.5}$ eV showers thrown at a 1×1 array at 4 km altitude the background distribution of f^* (black) and the extension of the exponential tail (blue) (left), and the 5σ threshold for which the area (orange) is $2.87 \cdot 10^{-7}$ of the total area (blue + orange) (right). The two vertical blue lines depict the domain used for the fit to the exponential function.

For the same energy and altitude the resulting diagrams for the 1×1 alternate and the $\sqrt{2} \times \sqrt{2}$ filled arrays are shown in Figure 9.15. For these two cases the 5σ thresholds are at $f^* = 6.6$ and $f^* = 6.3$ respectively.

For 10^{15} eV showers at 2 km altitude the diagrams for the 1×1 filled and the $\sqrt{2} \times \sqrt{2}$ filled arrays are shown in Figure 9.16. For the latter two examples the 5σ thresholds are at $f^* = 6.9$ and $f^* = 6.5$ respectively.

For other energies and observation levels the 5σ thresholds are comparable. It therefore is decided to take $f^* = 7.0$ and $f^* = 6.5$ as the 5σ significance thresholds for the 1×1 array types and the $\sqrt{2} \times \sqrt{2}$ array types respectively.

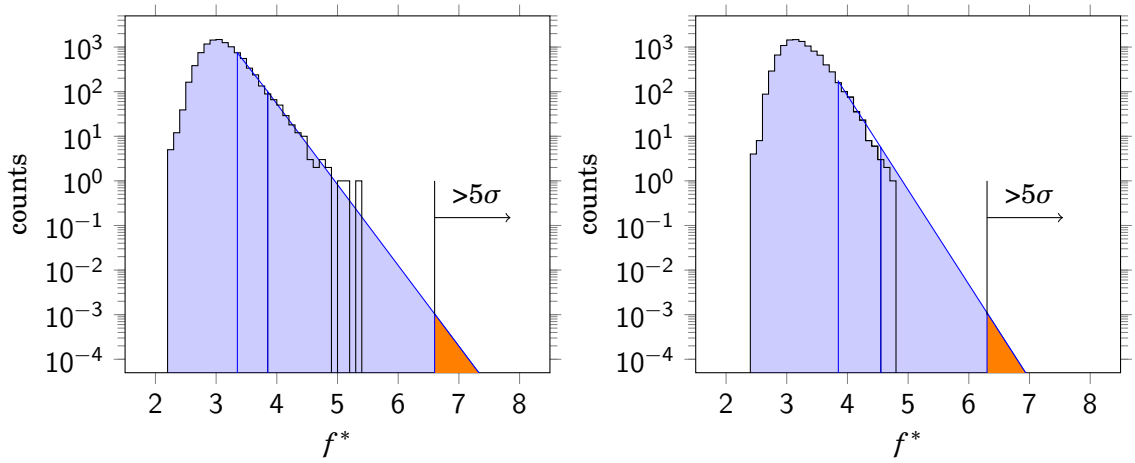

Figure 9.15: For $10^{14.5}$ eV showers thrown at a 1×1 alternate array (left) and at $\sqrt{2} \times \sqrt{2}$ filled array (right) at 4 km altitude the background distribution of f^* (black) and the extension of the exponential tail (blue), and the 5σ threshold (orange). The two vertical blue lines depict the domain of the exponential fit.

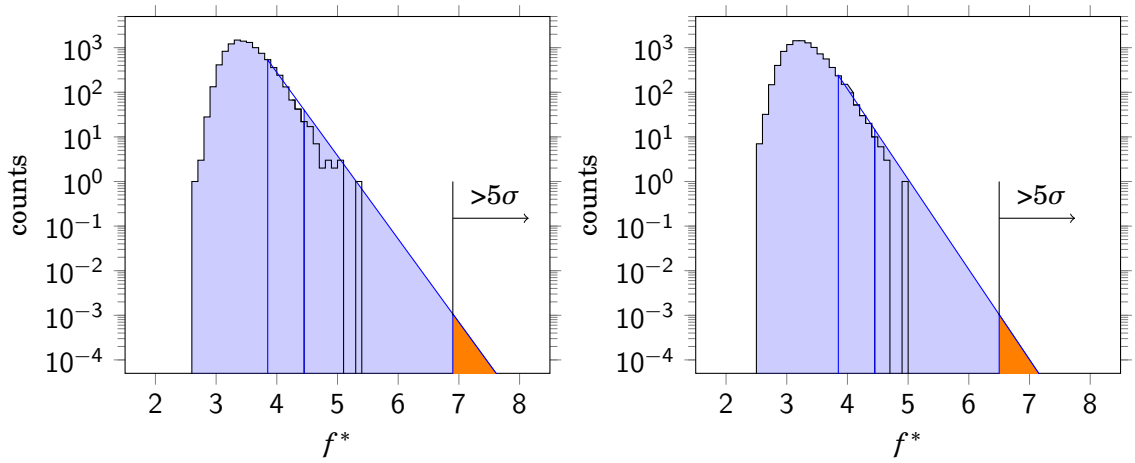

Figure 9.16: For 10^{15} eV showers thrown at a 1×1 filled array (left) and at $\sqrt{2} \times \sqrt{2}$ filled array (right) at 2 km altitude the background distribution of f^* (black) and the extension of the exponential tail (blue), and the 5σ threshold (orange). The two vertical blue lines depict the domain of the exponential fit.

10
Simulation results

10.1 Preliminary analysis

For each best sub core we have kept track of its distance r to the main core. For 10^{14} and $10^{14.5}$ eV showers without simulated jets and thrown on a 1×1 filled array at observation level of 4 km the distributions of best sub core distances are shown Figure 10.1.

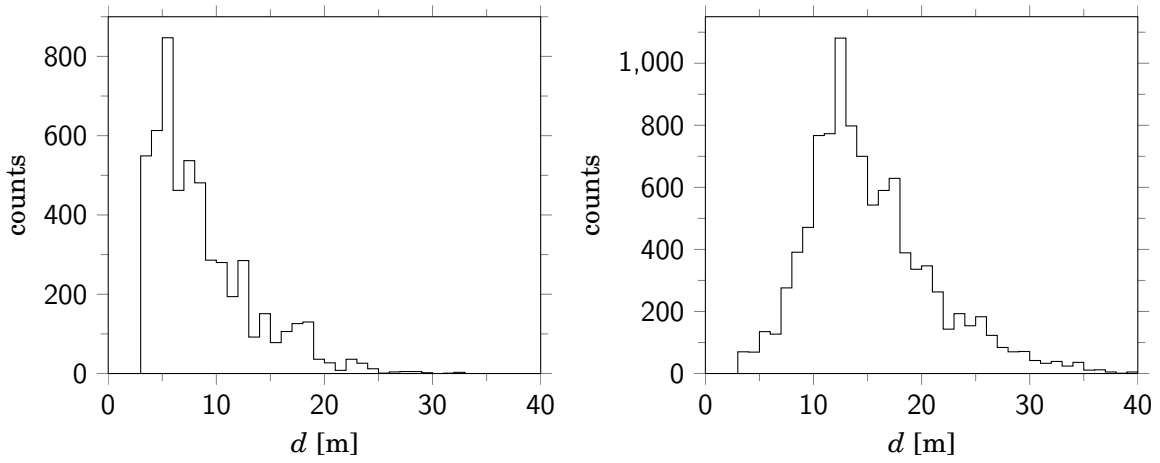

Figure 10.1: The distribution of the distances of best sub cores for 10^{14} eV showers (left) and $10^{14.5}$ eV showers (right) for a 1×1 array at 4 km altitude.

The distribution of distances of best sub cores extend to 30 and 40 m for 10^{14} eV showers and $10^{14.5}$ eV showers respectively. This increases to 50 m for 10^{15} eV showers. The signature of jets is expected around 10 m and decreases with shower energy. To verify this we now consider events with jets. The distribution of f^* and of the best core distances for a $10^{14.5}$ eV shower with $\widehat{p}_{\mathrm{T}} = 36\,\mathrm{GeV/c}$ at a 1×1 filled array at observation level of 4 km are shown in Figure 10.2.

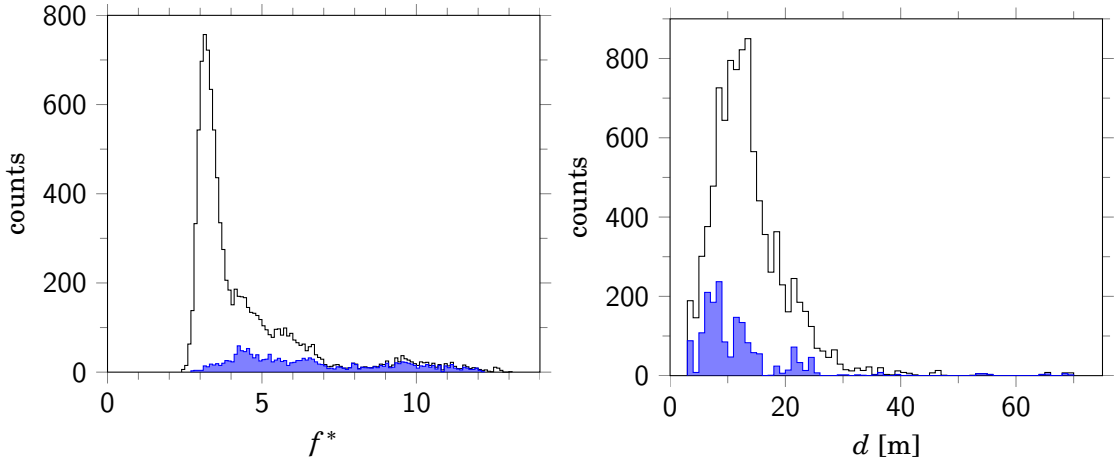

Figure 10.2: Left panel: the distribution of f^* (black) and the part of it matchable to simulated jets (blue). Right panel: the distribution of distances of best sub cores (black) and the part of it matchable to simulated jets (blue). Both panels for $10^{14.5}$ eV showers with $\widehat{p}_T = 36\,\mathrm{GeV/c}$ at a 1×1 filled array at observation level of 4 km.

About 20 % of the distribution is matchable to simulated jets. The distribution of f^* extends past the significance threshold up to 13. The part of it which has a best f value larger than $7.0\sigma(r)$ contributes to the effective area with $4.7 \cdot 10^2\,\mathrm{m}^2$. On the basis of the number of showers involved and the number of throws per shower the statistical uncertainty is estimated as $1.3 \cdot 10^2\,\mathrm{m}^2$. Above the threshold about 70 % of the distribution is caused by fluctuations matchable to simulated jets. That above a significance of $7.3\sigma(r)$ the distribution is dominated by matchable fluctuations is better visualized on a logarithmic scale, see Figure 10.3.

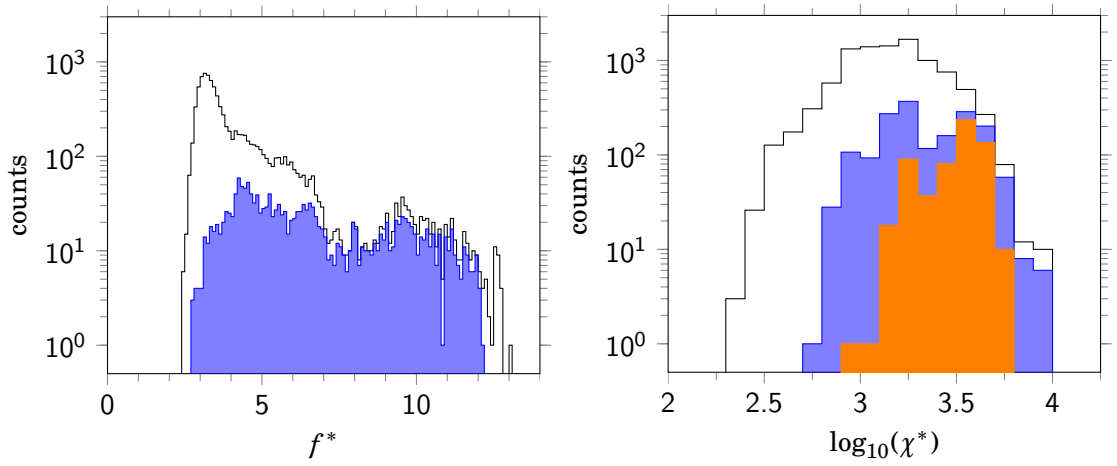

Figure 10.3: Left panel: the distribution of f^* (black) and the part of it matchable to simulated jets (blue). Right panel: the distribution of χ^* (black), the part of it matchable to simulated jets (blue) and the part of it matchable to simulated jets above the significance threshold (orange). Both panels for $10^{14.5}$ eV showers with $\widehat{p}_T = 36\,\mathrm{GeV/c}$ at a 1×1 filled array at observation level of 4 km.

Extremely large fluctuations cause a density larger than the core density. The algorithm than regards the fluctuation as the main core and the core as a fluctuation. This causes a bad matchability to jets if $f^* > 12$, see the left panel of Figure 10.3.

The physical observable χ^* is claimed to be proportional to the jet transverse momentum [116]. It is defined as

$$\chi^* = d\sqrt{\rho_1 \rho_2}\,, \tag{10.1}$$

where d is the distance to the main core in m, where ρ_1 is the density of the main core in m^{-2} and where ρ_2 is the density surplus of the sub core in m^{-2}. That is, $\rho_2 = \rho_{\mathrm{obs}} - \rho_{\mathrm{fit}}$. The distribution of χ^* is shown in the right panel of Figure 10.3. The distribution of χ^* tends to smaller values for smaller shower energy and to larger values for larger shower energy. For the part which could be matched with simulated jets, we can investigate the relation between χ^* and the jet transverse momentum. The distribution of χ^* versus jet p_{T} is shown in Figure 10.4. The density surplus, $\rho_{\mathrm{obs}} - \rho_{\mathrm{fit}}$, versus d is shown in the right panel of Figure 10.4.

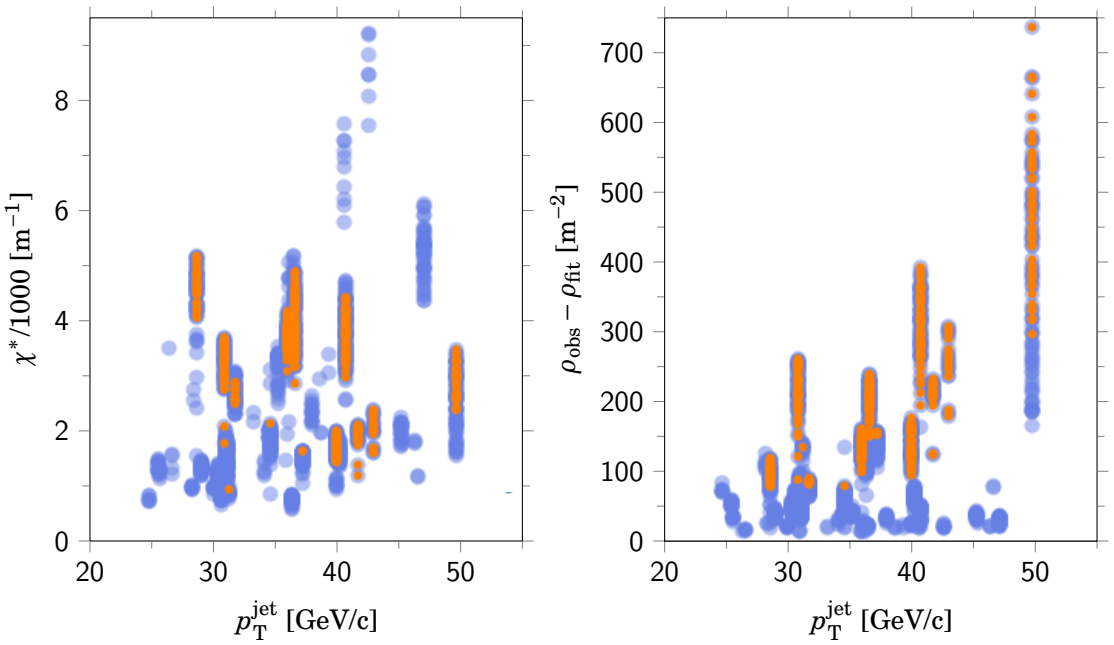

Figure 10.4: Left panel: χ^* versus jet transverse momentum for best sub cores (blue) and on top of it the part which meets the significance threshold (orange). Right panel: density surplus versus the jet transverse momentum for matching best sub cores (blue) and on top of it the part which meets the significance threshold (orange). Both panels for fluctuations matchable to simulated jets in $10^{14.5}$ eV showers with $\widehat{p}_{\mathrm{T}}$ = 36 GeV/c at a 1×1 filled array at observation level of 4 km.

The blue dots in the left panel suggest a slight relation between χ^* and $p_{\mathrm{T}}^{\mathrm{jet}}$, while the orange dots suggests no relation at all for the significant best sub cores. This implies that χ^* is not a particularly good predictor for the transverse jet momentum. This is probably due to the influ-

ence of the pseudorapidity. The right panel suggests the density surplus to be a better predictor for the transverse jet momentum. However, the relation vanishes when other $\hat{p}_T$ intervals are taken into consideration, see Figure 10.5.

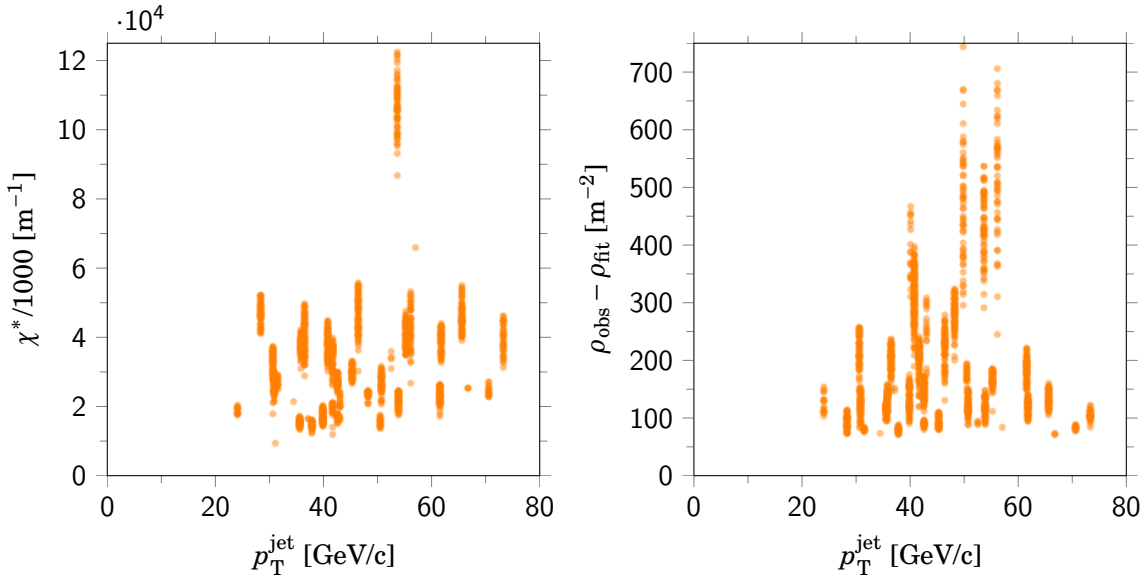

Figure 10.5: Left panel: χ^* versus jet transverse momentum for sub cores which meet the significance threshold. Right panel: density surplus versus the jet transverse momentum for sub cores which meets the significance threshold. Both panels for $10^{14.5}$ eV showers with $\hat{p}_T = 12$ through $\hat{p}_T = 60\,\mathrm{GeV/c}$ at a 1×1 filled array at observation level of 4 km.

Now both the correlation between χ^* and transverse jet momentum and between the density surplus and transverse jet momentum is poor. Next we consider the three energies 10^{14}, $10^{14.5}$ and 10^{15} eV. For each energy the χ^* of jet cores are plotted against the jet transverse momentum in Figure 10.6.

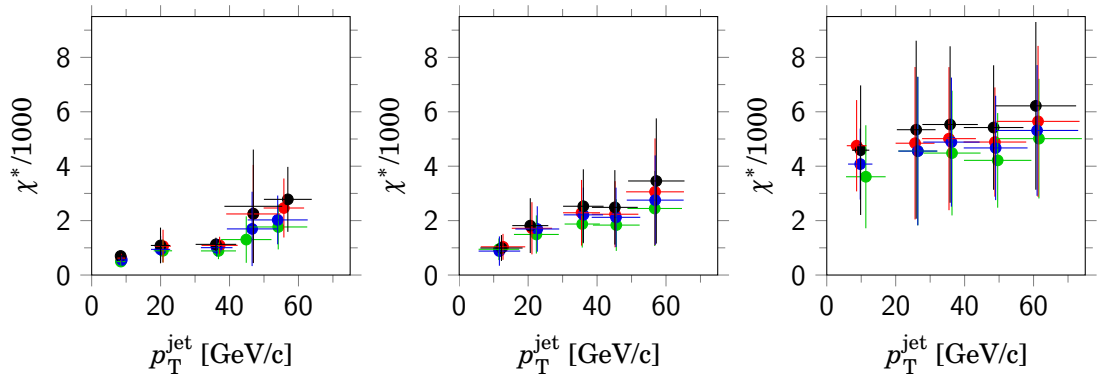

Figure 10.6: χ^* versus jet transverse momentum for 10^{14} eV (left), $10^{14.5}$ eV (middle) and 10^{15} eV (right) showers. All for the 1×1 filled array (black), 1×1 alternate array (red), $\sqrt{2} \times \sqrt{2}$ filled array (blue) and $\sqrt{2} \times \sqrt{2}$ alternate array (green) and for the observation level at 4 km altitude.

We see the relation between χ^* and transverse jet momentum is poor. The relation between χ^* and shower energy is already stronger. The overall conclusion is that χ^* is in general not a good measure for the jet transverse momentum. Attempts to find a better predictor for the jet transverse momentum in terms of observable quantities as d, ρ_1 and ρ_2 were not successful. For the remainder of the analysis we will focus on the effective area for jet observation at the three altitudes.

10.2 Results for 4 km altitude

For observation level at 4 km altitude we first show the results for 10^{15} eV showers thrown at the four kinds of arrays. In Figure 10.7 the effective area per shower is plotted against $\widehat{p}_{\mathrm{T}}$. Although a large $\widehat{p}_{\mathrm{T}}$ leads to a large effective area, its contribution to the flux of jet observations might still be small because of its small cross section. For the contribution to the flux of jet observations we have to consider the product of the effective area and the probability per shower to occur. The latter is the effective area per observational jet. It is plotted against $\widehat{p}_{\mathrm{T}}$ in the right panel of Figure 10.7.

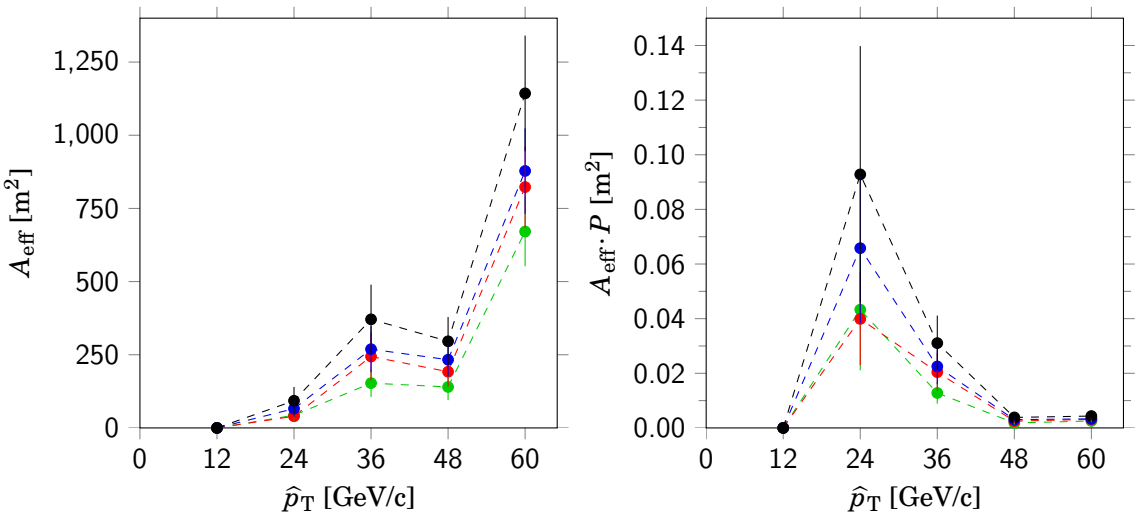

Figure 10.7: For 10^{15} eV showers the effective area per shower versus $\widehat{p}_{\mathrm{T}}$ (left) and the effective area per observational jet versus $\widehat{p}_{\mathrm{T}}$ (right) for the 1×1 filled array (black), 1×1 alternate array (red), $\sqrt{2} \times \sqrt{2}$ filled array (blue) and $\sqrt{2} \times \sqrt{2}$ alternate array (green) at 4 km altitude.

The effective area for observing a jet in a shower is reduced to less than 0.1 m^2. Similar results hold for $10^{14.5}$ and 10^{14} eV showers. At the latter energy an additional loss is observed due to the minimum density condition, see Figure 10.8.

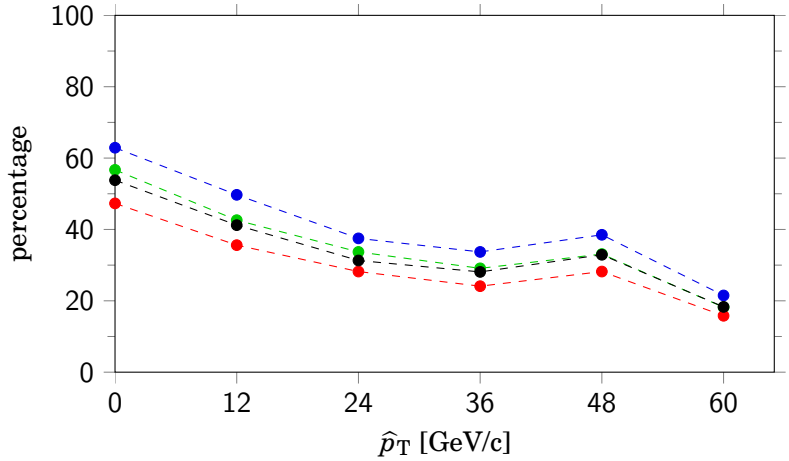

Figure 10.8: Percentages of showers which meet the minimum density conditions against $\widehat{p}_T$ for 10^{14} eV showers for the 1×1 filled array (black), 1×1 alternate array (red), $\sqrt{2}\times\sqrt{2}$ filled array (blue) and $\sqrt{2}\times\sqrt{2}$ alternate array (green) at 4 km altitude.

10.3 Results for 2 km altitude

For observation level at 2 km altitude 10^{15} eV showers show similar behavior as that observed at 4 km altitude, but with a factor 2 loss in effective area per shower, see Figure 10.9 for 10^{15} eV showers.

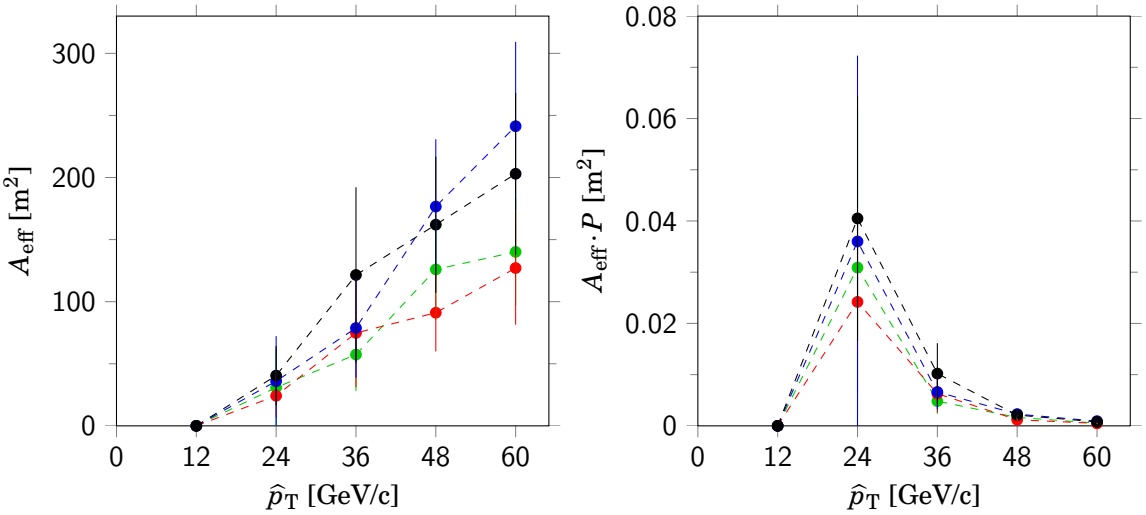

Figure 10.9: For 10^{15} eV showers the effective area per shower versus $\widehat{p}_T$ (left) and the effective area per observational jet versus $\widehat{p}_T$ (right) for the 1×1 filled array (black), 1×1 alternate array (red), $\sqrt{2}\times\sqrt{2}$ filled array (blue) and $\sqrt{2}\times\sqrt{2}$ alternate array (green) at 2 km altitude.

At lower energies the behavior becomes erratic due to the increased shower fluctuations, see Figure 10.10.

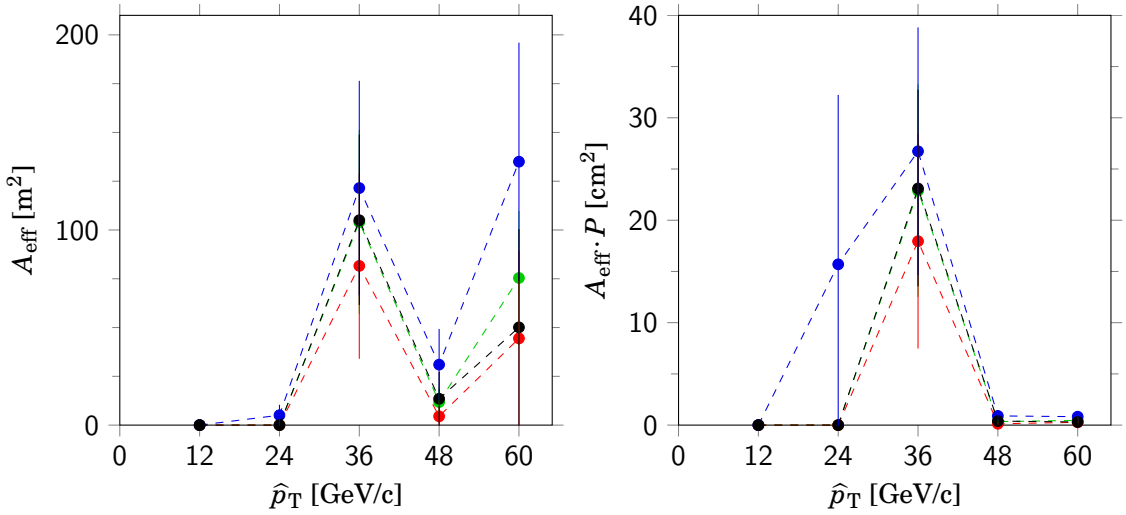

Figure 10.10: For $10^{14.5}$ eV showers the effective area per shower versus $\widehat{p}_{\text{T}}$ (left) and the effective area per observational jet versus $\widehat{p}_{\text{T}}$ (right) for the 1×1 filled array (black), 1×1 alternate array (red), $\sqrt{2} \times \sqrt{2}$ filled array (blue) and $\sqrt{2} \times \sqrt{2}$ alternate array (green) at 2 km altitude.

At 2 km altitude the minimum density requirement also reduces the statistics significantly at $E < 10^{15}$ eV, see Figure 10.11.

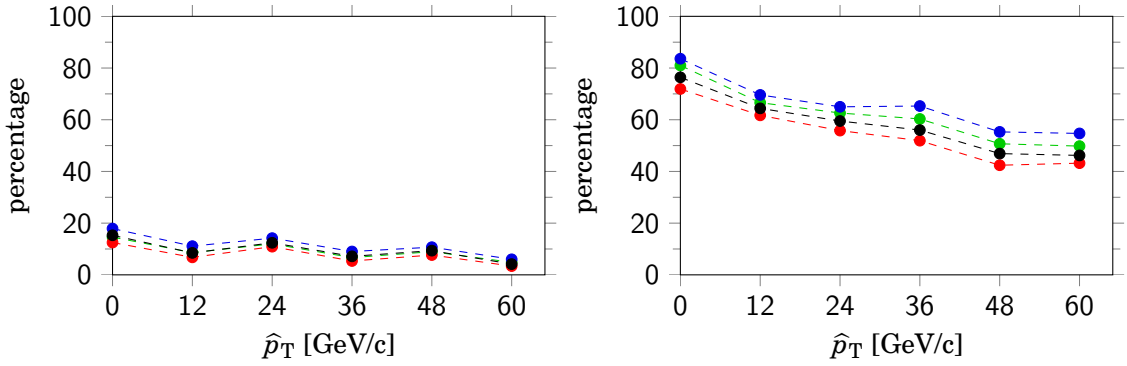

Figure 10.11: The percentages of showers which meet the minimum density conditions against $\widehat{p}_{\text{T}}$ for 10^{14} eV showers (left) and $10^{14.5}$ eV showers (right). Both for the 1×1 filled array (black), 1×1 alternate array (red), $\sqrt{2} \times \sqrt{2}$ filled array (blue) and $\sqrt{2} \times \sqrt{2}$ alternate array (green) at 2 km altitude.

10.4 Results for sea level

At sea level all 10^{14} eV showers fail the density criterium. Due to the further 2 km of atmosphere the showers have developed even further and the density of both core and sub cores decreases. Only around 10 % (70 %) of the showers pass the density criterium at $10^{14.5}$ eV (10^{15} eV). As a result the best effective areas per jet drop to below 100 cm^2.

For different altitudes and different energies the effective area per shower and per observational jet are tabulated in Appendix A. For each altitude and energy the total effective area per observational jet is shown in the last row of each table in Appendix A. To obtain the observational jet rate it has to be multiplied by the cosmic ray energy flux and by the solid angle in steradian. An estimation of the latter is derived in the next section.

10.5 Slant depth

The simulated showers are vertical showers. For non vertical showers there are four main differences. The first is a decrease of the lateral density with a factor $\cos\theta$ because of the projection on a horizontal observation level. The second is the increase of the signal with a factor $\sec\theta$. Both effects compensate each other. The third is a reduction of the effective area with a factor $\cos\theta$ because the probability for the main core to fall on the array is decreased. Alternatively, for inclined showers the plane of the array is not perpendicular to the direction. The fourth difference is a longer path to the observation level. The larger atmospheric depth is called the slant depth X':

$$X' = \frac{X}{\cos\theta} \tag{10.2}$$

for $\theta < 60°$. A slant depth decreases the fraction of showers which meets the density requirement at the observation level. To estimate it we consider the fraction of showers which meet the density condition of 100 particles per square meter for the main core. For 10^{14} eV showers at 4 km altitude the fractions are about 0.58 for the two types of filled arrays. The fraction is scattered against the atmospheric depth. For the few other occasions the scatter points are obtained in a similar way. The results are shown as colored dots in Figure 10.12.

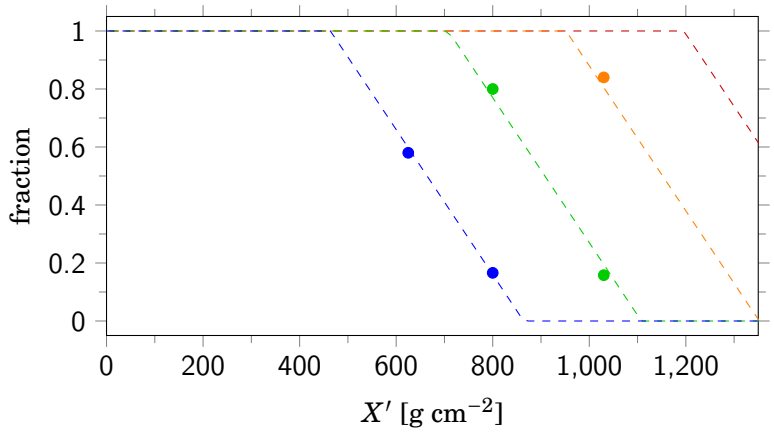

Figure 10.12: The fraction of showers meeting the density condition. The dashed curves are predictions as described in the text. Different colors correspond to different energies: 10^{14} eV (blue), $10^{14.5}$ eV (green),10^{15} eV (orange) and $10^{15.5}$ eV (red).

The line piece connecting the blue dots and the line piece connecting the green dots have approximately the same slope: $0.0025\,\mathrm{g}^{-1}\,\mathrm{cm}^2$. For this slope the equation for the descending part of the blue dashed curve is fraction $= 2.16 - 0.0025X'$. For the descending part of the green dashed curve this is fraction $= 2.76 - 0.0025X'$. This suggest for 10^{15} eV showers the equation: fraction $= 3.38 - 0.0025X'$. It turns out that this prediction is not far from the single dot for 10^{15} eV showers, see the orange dot and orange curve in Figure 10.12. For larger energies we assume the continuation also holds approximately. To be specific

$$f(X;E) \approx 1.22 \log_{10} E - 14.64 - 0.0025X' \,, \tag{10.3}$$

where E is the shower energy in eV. At this point we recall Equation 6.73. For $\theta = 0$ it reads

$$\log_{10} N_{e+\mu} = 1.205 \log_{10} E - 13.14 \,. \tag{10.4}$$

Comparison of the latter two equations suggest the fraction to be dependent on the logarithm of the number of particles $N_{e+\mu}$.

Since the fraction is limited by 0 and 1 the full footed curves in Figure 10.12 are given by

$$f(X;E) = \max\left(0,\, \min\left(1,\, 1.22 \log_{10} E - 14.64 - 0.0025X'\right)\right) \,. \tag{10.5}$$

The latter is a piecewise linear approximation of what in reality will look like a logistic curve. Substituting $X/\cos\theta$ for the slant depth we obtain for the fraction that reaches the observation level

$$f(\theta) = \max\left(0,\, \min\left(1,\, 1.22 \log_{10} E - 14.64 - \frac{0.0025X}{\cos\theta}\right)\right) \,. \tag{10.6}$$

For an observation plane perpendicular to the shower direction the average solid angle for showers to reach the observation level is obtained by integration:

$$\Omega = 2\pi \int_0^{\pi/2} f(\theta) \sin\theta \mathrm{d}\theta \,. \tag{10.7}$$

To account for the reduction of the probability for a core of an inclined shower to fall on a horizontal array the effective solid angle is

$$\Omega = 2\pi \int_0^{\pi/2} f(\theta) \cos\theta \sin\theta \mathrm{d}\theta \,. \tag{10.8}$$

For a cone limited by angle α the area of the surface of the segment of the sphere is given by

$$2\pi \int_0^{\alpha} \sin\theta \mathrm{d}\theta = 2\pi(1 - \cos\alpha) \,, \tag{10.9}$$

where α is half the cone angle; on average the limiting angle of the zenith angles. By means of the latter expression the average limiting angle can be expressed in terms of solid angle

$$\alpha = \arccos\left(1 - \frac{\Omega}{2\pi}\right) . \tag{10.10}$$

For different energies and observation levels the results are tabulated in Table 10.1. The estimates in Table 10.1 will be used to convert the energy flux of cosmic rays per steradian to the total energy flux from the hemisphere.

	4 km	2 km	0 km
10^{14} eV	(1.0 ± 0.4) sr , 33°	(0.2 ± 0.2) sr , 16°	0.00 sr 0.00°
$10^{14.5}$ eV	(1.9 ± 0.3) sr , 46°	(1.1 ± 0.5) sr , 35°	(0.2 ± 0.2) sr , 16°
10^{15} eV	(2.4 ± 0.2) sr , 51°	(1.9 ± 0.3) sr , 45°	(1.0 ± 0.4) sr , 33°
$10^{15.5}$ eV	(2.6 ± 0.1) sr , 54°	(2.2 ± 0.2) sr , 50°	(1.6 ± 0.2) sr , 42°
10^{16} eV	(2.7 ± 0.1) sr , 56°	(2.5 ± 0.1) sr , 53°	(2.0 ± 0.1) sr , 46°
$10^{16.5}$ eV	(2.8 ± 0.1) sr , 57°	(2.6 ± 0.1) sr , 55°	(2.3 ± 0.1) sr , 51°

Table 10.1: Effective average solid angle and average limiting angle for varius energies and varius altitudes. In brackets are the estimated systematic uncertainties due to the fitting procedure.

10.6 Alternative method

The previous method was based on a practical approach of finding in a fast way the center of the lateral density and the most significant fluctuation. The method is not optimal for two reasons. Firstly, it can occur that the density of a fluctuation exceeds the density of the main core. With the previous algorithm the sub core will act as the main core. An algorithm for finding the center of the lateral distribution, is complicated and time consuming. We do not need such an algorithm since the position of the shower core is known in simulations. We will mimic to a certain extent the realistic situation by inspecting around the known shower core position for the detector with the largest signal within a small range of 5×5 and 3×3 detectors for the 1×1 and $\sqrt{2} \times \sqrt{2}$ arrays respectively. For the alternate arrays this has to be done anyway. Secondly, a sub core may be spread out over more than one detector. It seems worthwhile to consider a small cluster of adjacent detectors. The relation $r \approx 0.07d$, as derived in Section 8.4, for the radius of the sub core gives an indication of the number of detectors in such a cluster as a function of distance to the main core. It suggests to consider as well a cluster of 3×3 detectors if $d \geq 14\,\text{m}$ for the 1×1 array and $d \geq 20\,\text{m}$ for the $\sqrt{2} \times \sqrt{2}$ array and a cluster of 5×5 detectors if $d \geq 25\,\text{m}$ for the 1×1 array and $d \geq 35\,\text{m}$ for the $\sqrt{2} \times \sqrt{2}$ array. The clusters are not applied to smaller jet distances than given above in order to avoid disturbing effects from the gradient

in the lateral density. Except for these two modifications, the alternative method is identical to the original method. Also the conditions are unaltered. To show an essential difference we consider the f^* and χ^* distributions for a $10^{14.5}$ eV shower at a 1×1 array at 4 km altitude, see Figure 10.13.

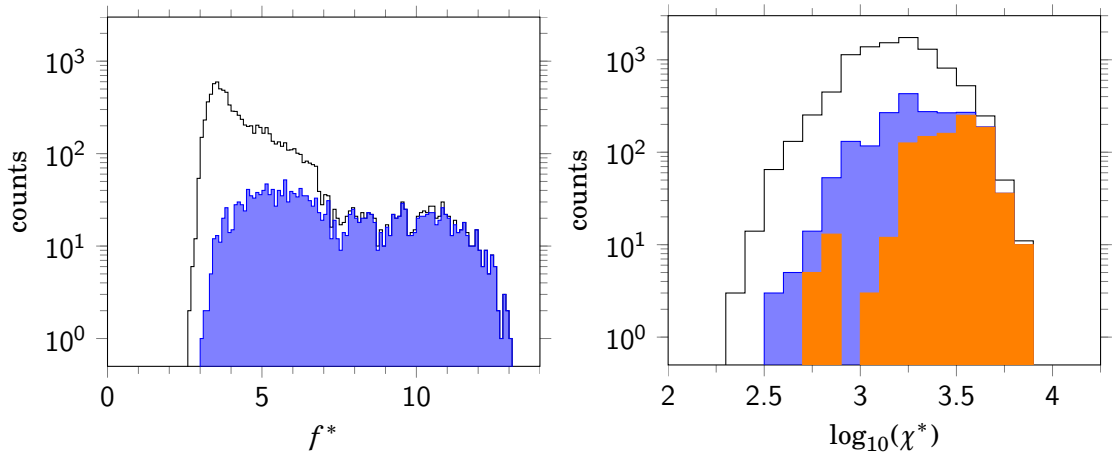

Figure 10.13: Left: the distribution of f^* (black) and the part of it matchable to simulated jets (blue). Right: the distribution of χ^* (black), the part of it which is matchable to simulated jets (blue) and the part which is matchable to simulated jets above the significance threshold (orange). Both panels for $10^{14.5}$ eV showers with $\widehat{p}_T = 36$ GeV/c at a 1×1 filled array at observation level of 4 km.

Now the part of the distribution of f^* that is matchable to simulated jets completely fills the total distribution of f^*. The same holds for the χ^* distribution; compare with Figure 10.3. The latter has only marginal effects on the diagrams as shown in Figure 10.6.

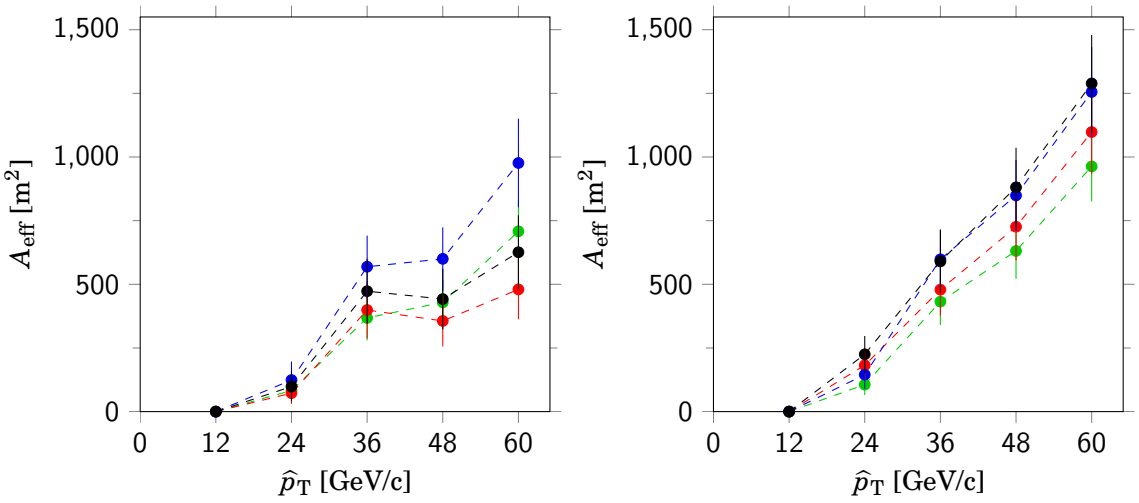

Figure 10.14: For $10^{14.5}$ eV showers the effective area per shower against $\widehat{p}_T$ by means of the previous method (left) and by means of the alternative method (right). Both for the 1×1 filled array (black), 1×1 alternate array (red), $\sqrt{2} \times \sqrt{2}$ filled array (blue) and $\sqrt{2} \times \sqrt{2}$ alternate array (green) at 4 km altitude.

To illustrate another difference we compare the diagrams of the effective area per shower for $10^{14.5}$ eV showers with $\widehat{p}_T$= 36 GeV/c at a 1×1 filled array at observation level of 4 km. For the previous method and the alternative method the diagrams are shown in the left panel and right panel respectively of Figure 10.14. The diagram is more regular and the effective areas are larger for the alternative method. The dip at $\widehat{p}_T = 48$ GeV/c in the left diagram is caused by jets for which the sub core is more spread out. They are recognized by the alternative method only. The given example is however an exception. Usually the effective area diagrams look close to one another. The effective areas per shower and per jet obtained with the alternative method are tabulated in Appendix B.

10.7 Jet rates

To obtain the jet rates for each energy the effective areas are multiplied with the solid angle in steradian and with the energy flux. For the observation level at 4 km altitude the result is shown in Figure 10.15. The observational jet rates are tabulated in Appendix C.

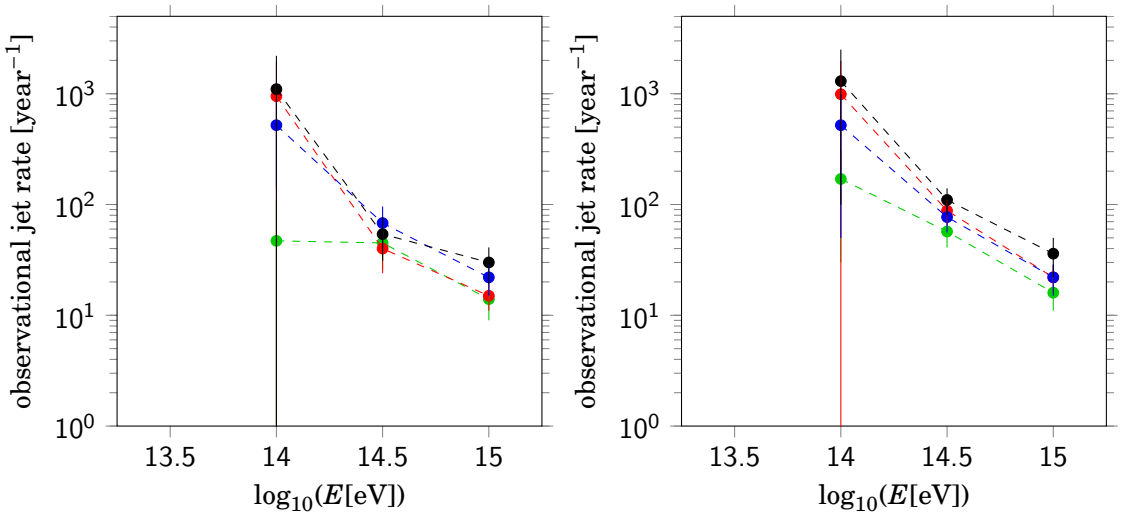

Figure 10.15: Observational jet rates at 4 km altitude versus shower energy for the original method (left) and the alternative method (right) for the 1×1 filled array (black), 1×1 alternate array (red), $\sqrt{2} \times \sqrt{2}$ filled array (blue) and $\sqrt{2} \times \sqrt{2}$ alternate array (green).

The observational jet rate at 4 km altitude is dominated by the showers with the smallest energy. The energy sum of the observational jet rate is, for both methods, of the order of 10^2 per month. This is comparable to the almost hundred jets a month observed with the ARGO-YBJ experiment [116]. The agreement should be considered as rather accidental because of the difference in the way a significance is ascribed to a best sub core and because the large uncertainty. Besides, if the factor α in the conversion from p-p to p-air jet rates is, say, 1.25 instead of 1 the obtained jet rates would have been $14.5^{0.25} \approx 2$ times larger.

For the observation level at 2 km altitude the jet rates are plotted versus shower energy for both methods in Figure 10.16.

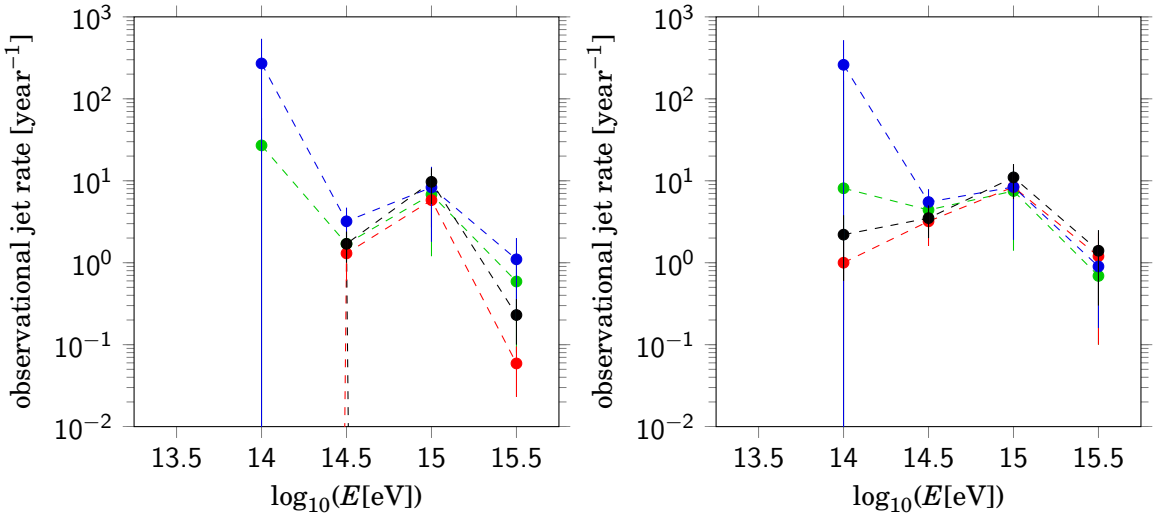

Figure 10.16: Observational jet rates at 2 km altitude versus shower energy for the original method (left) and the alternative method (right) for the 1×1 filled array (black), 1×1 alternate array (red), $\sqrt{2} \times \sqrt{2}$ filled array (blue) and $\sqrt{2} \times \sqrt{2}$ alternate array (green).

At 2 km altitude the observational jet rate is to a large extent determined by the type of array. The energy sum of the observational jet rate is, for both methods, of the order of 10^1 per year for the 1×1 type of arrays and of the order of 10^1 through 10^2 per year for the $\sqrt{2} \times \sqrt{2}$ type of arrays. In particular for the latter type of arrays the error bars are large.

For sea level the observational jet rates per energy are shown in Figure 10.17. The energy sum of the observational jet rates at sea level is, for both methods, about half a year. The energy sum of the observational jet rates are in the final row of each table in Appendix C.

Due to the quality cuts and the application of a minimum level for $\sigma(r)$ near the core the fluctuations in the background signal due to secondary hadronic interactions did not pass the significance threshold. However, an exception occurred in one of the $10^{15.5}$ eV showers at sea level generated with $\widehat{p}_{\text{T}} < 6\,\text{GeV/c}$. A high density sub core was induced at a distance of 10 m from the main core and with f^* values up to 9.5. From inspection it is found that a proton came out the first collision with 35 % of the primary energy; the leading particle effect. At a later stage of the shower the leading proton made a hard scatter with a jet as a result. The cone radius of the jet happens to be such small that significant sub cores are detected solely with the 1×1 array types. The effective areas were 43 and 20 m^2 for the 1×1 filled array and the 1×1 alternate array respectively. The alternative method delivered 42 and 23 m^2 respectively.

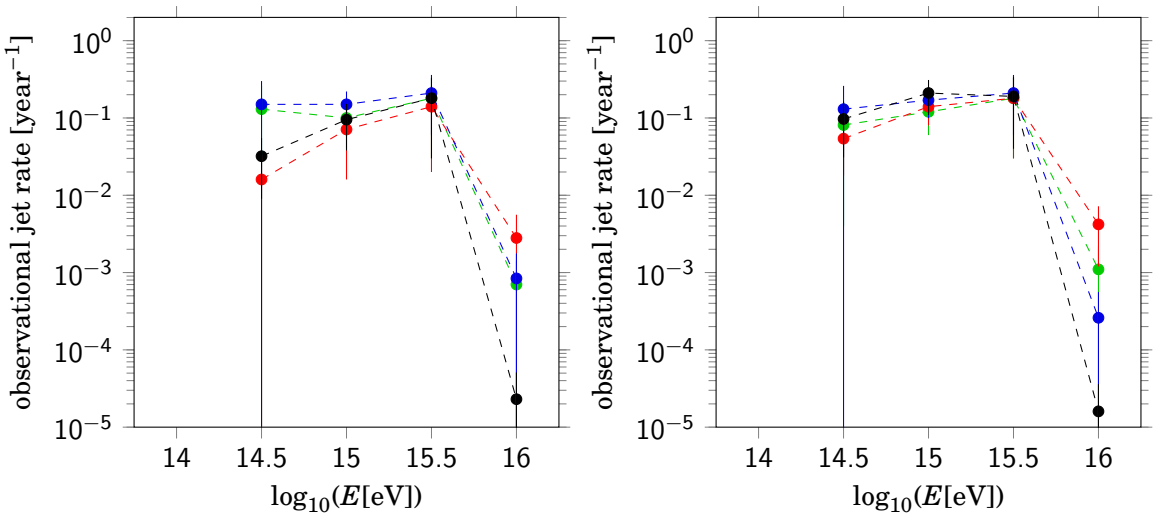

Figure 10.17: Observational jet rates at sea level versus shower energy for the original method (left) and the alternative method (right) for the 1×1 filled array (black), 1×1 alternate array (red), $\sqrt{2} \times \sqrt{2}$ filled array (blue) and $\sqrt{2} \times \sqrt{2}$ alternate array (green).

These effective areas per shower correspond with effective areas of about 30 and $15\,\text{m}^2$ per observational jet and to a jet rate of about 600 and 300 a year respectively. This is thousand times larger than the first collision jet rate at sea level. Of course one should keep in mind that the uncertainty is large. With the secondary jet included the latter two diagrams are as shown in Figure 10.18.

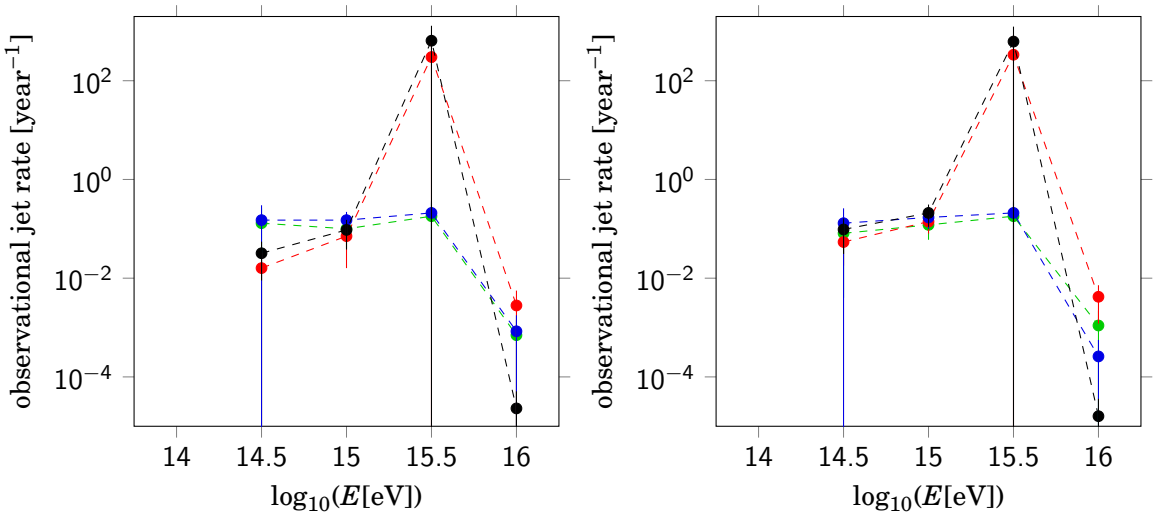

Figure 10.18: Observational jet rates at sea level versus shower energy for the original method (left) and the alternative method (right) for the 1×1 filled array (black), 1×1 alternate array (red), $\sqrt{2} \times \sqrt{2}$ filled array (blue) and $\sqrt{2} \times \sqrt{2}$ alternate array (green).

11

Jet directed data analysis

11.1 Introduction

The jet rates obtained with the simulation were for a large array of $5.6 \cdot 10^3$ m^2. For a thousand times smaller array the expected jet rate at sea level is less than once a year. Although the detection of jets at sea level is very unlikely, we have investigated the data from the SPA array for possible indications of jet activity. On 2014-09-29 station 510 was added to the Science Park Amsterdam cluster. The detectors of station 510 are positioned close to the detectors of station 501, see Figure 11.1.

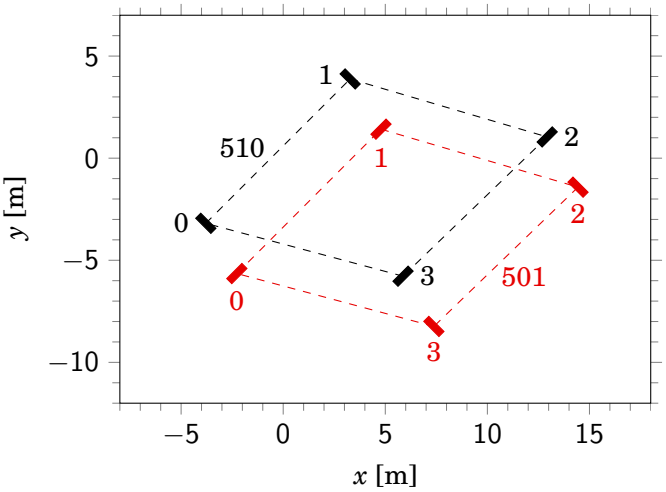

Figure 11.1: The layout of the detectors 0, 1, 2, 3 of stations 501 (red) and station 510 (black).

For both stations the detector positions are at the corners of a diamond shape. The shortest diagonal of the diamond is equal in length to the side of the diamond, 10 m. Detectors of station

501 and 510 with the same identifier will hereafter be denoted as a 'pair of detectors'. The distance, from center to center, of these pairs is 2.9 m. Since the detectors are close together, we expect a similar signal. In Figure 11.2 the signals of a pair of detectors are plotted versus one another. Clearly the signals from the two detectors are proportional.

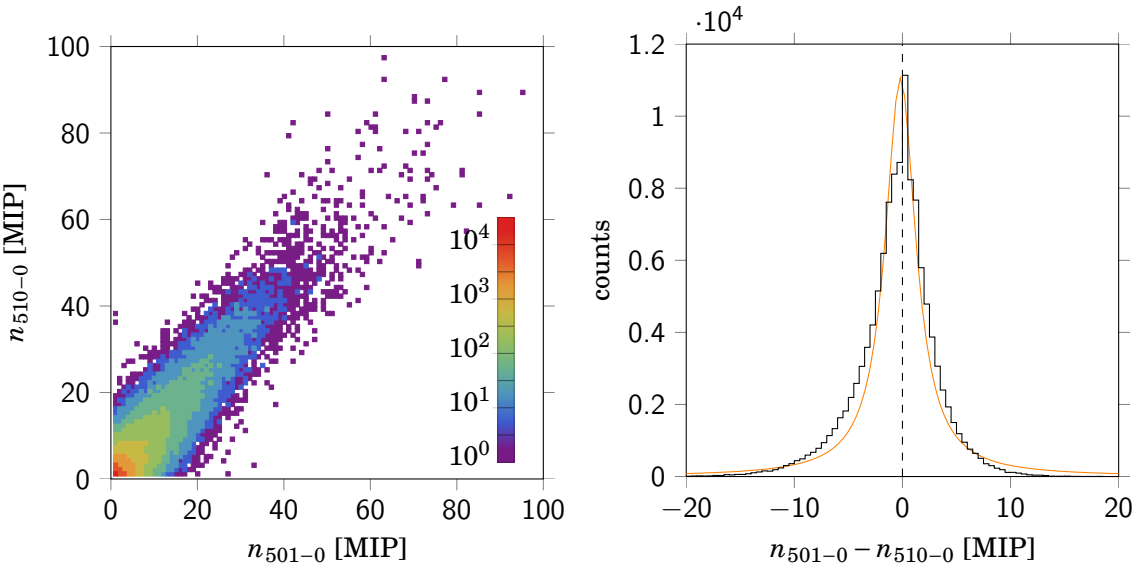

Figure 11.2: Density contour plot of the pulse integrals of detector 0 of station 510 versus the pulse integrals of detector 0 of station 501 for four-fold coincidences with stations 501, 502, 508, 510 participating (left); the Pearson-r value is 0.87. The pulse integral difference between detector 0 of station 510 and detector 0 of station 501 (right); the orange curve is a fit with the Cauchy function. Data taken between 2015-05-22, 00:00:00 and 2016-05-22, 00:00:00.

One can also look at differences between signals of detectors of the double station [122]. These differences can be fitted by the Cauchy function (or Lorentz function)

$$f(x;x_0,\gamma) = \frac{1}{\pi\gamma}\frac{\gamma^2}{(x-x_0)^2+\gamma^2}\,, \tag{11.1}$$

where x_0 is the location of the peak of the distribution and where 2γ is the FWHM of the peak. In Figure 11.2 the distributions of the differences between signals of detector 0 of station 501 and station 510 for the coincidences are considered. A fit with the Cauchy function delivers $x_0 = -0.181\,\text{MIP}$ and $\gamma = 1.722\,\text{MIP}$. The distribution of differences is not completely symmetric since the electronics in the PMT's in station 510 was updated with respect to those of station 501.

A 'double' station with 4 pairs of detectors increases the accuracy of the determination of the local density at observation level of electrons and muons. Being a sort of mini-array the double station is used for inspection for jets.

11.2 Preliminary analysis

To develop a method for inspection for jets we first consider fourfold coincidences with stations 501, 502, 508 and 510 participating for the 1 year period between 2015-05-22 through 2016-05-22. Monte Carlo studies show that fourfold coincidences with stations 501, 502, 508 and 510 participating are mainly caused by showers with energies around 10^{15} eV. Because of their proximity we assume that the density will be equal for each of the 8 detectors of station 501 and 510 if the main core is some distance away. Furthermore we regard the largest signal (pulse integral) of the 8 detectors separate from the 7 lower signals. The mean of the 7 lower signals is regarded as the density at station 501 and 510, while the largest signal is regarded as a fluctuation being due to Poisson statistics for the number of particles, energy loss statistics, or a jet. That is, the largest signal is regarded as N_{obs} and the mean of the other 7 signals as N_{fit}. Also here, the logarithm of the ratio of N_{obs} and N_{fit} is used for the inspection for jets:

$$f = \log_{10}(N_{\text{obs}}) - \log_{10}(N_{\text{fit}}) \ . \tag{11.2}$$

As for the simulation part, we assume the expectation value of f to be zero. Since we do not have a large array we can not derive experimentally the variation in f. Because of the gradient in the density, the distribution of f is complicated. To obtain an estimation for σ we assume N_{obs} and N_{fit} to be independent. According to the rules of error propagation the σ of f then is given by [123]

$$\sigma = \sqrt{\left[\frac{\partial f}{\partial N_{\text{obs}}}\sigma(N_{\text{obs}})\right]^2_{N_{\text{obs}}=E(N_{\text{obs}})} + \left[\frac{\partial f}{\partial N_{\text{fit}}}\sigma(N_{\text{fit}})\right]^2_{N_{\text{fit}}=E(N_{\text{fit}})}} \ , \tag{11.3}$$

where $E(N_{\text{obs}}) = N_{\text{fit}}$ and $E(N_{\text{fit}}) = N_{\text{fit}}$ are the expectation values of N_{obs} and N_{fit} respectively. Since N_{obs} and N_{fit} are based on 1 detector and 7 detectors respectively, we have for a pure Poisson distribution: $\sigma(N_{\text{obs}}) = \sqrt{N_{\text{fit}}}$ and $\sigma(N_{\text{fit}}) = \sqrt{N_{\text{fit}}/7}$. In combination with the instrumental uncertainty, $\sigma \approx 0.3\sqrt{N_{\text{fit}}}$, this is $\sigma(N_{\text{obs}}) = \sqrt{1.09 N_{\text{fit}}}$ and $\sigma(N_{\text{fit}}) = \sqrt{1.09 N_{\text{fit}}/7}$. Hence

$$\sigma = \frac{\sqrt{1.09}\sqrt{8/7}}{\ln(10)}\sqrt{\frac{1}{N_{\text{fit}}}} \approx \frac{0.4847}{\sqrt{N_{\text{fit}}}} \ . \tag{11.4}$$

As N_{fit} depends on r also σ depends on r. As before the value $f^* = f/\sigma(r)$ is used as a measure for fluctuations.

Fourfold coincidences with the double station participating are, from the reconstruction point of view, actually threefold coincidences. Core reconstruction is therefore not possible. If a large f^* value occurs there might be uncertainty about whether it is caused by a nearby core or by a fluctuation. We therefore distinguish between coincidences where the largest mean signal is in

double station 501/510 and where the largest mean signal was not in double station 501/510. For the first situation the core is in general closer to the double station than for the other situation. In a MC simulation a 10^{15} eV proton initiated shower with zenith angle 15° is thrown 100 000 times in an area of 62 500 m^2. For the fraction of it which caused fourfold coincidences with stations 502, 508, 501 and 510 participating, the core positions are shown in Figure 11.3. The core positions are differently colored for the situation where the largest mean signal was in the double station and where the largest mean signal was in either station 502 or station 508.

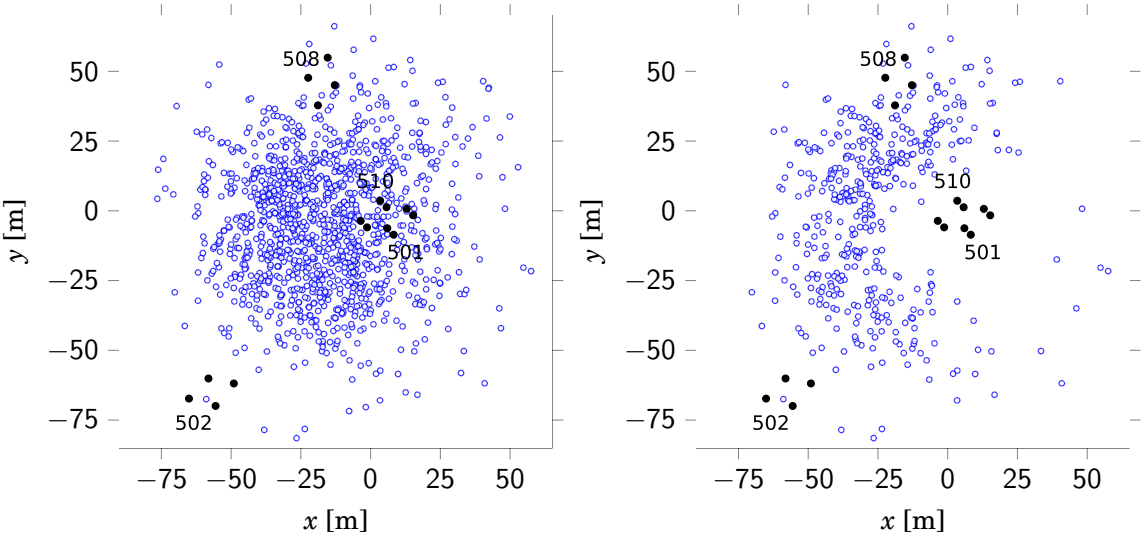

Figure 11.3: The core positions of 10^{15} eV showers with zenith 15° causing four-fold coincidences in station 501, 502, 508 and 510 (left) and the part of it for which the largest mean signal occurred not in the double station (right).

The core positions for which the largest mean signal was not in the double station are separately shown in the right panel of Figure 11.3. These core positions are mostly between 25 m and 50 m away from the double station. At these distances sub cores can be expected due to jets in showers with energies around 10^{15} eV. To analyse the data for it we consider fourfold coincidences for the SPA stations 501 through 506 and 508 through 510 in the period 2015-05-22, 00:00:00 through 2016-05-22, 00:00:00. Among the 286 636 fourfold coincidences there were 119 792 coincidences where station 501, 502, 508 and 510 participated and for which all four detectors of the participating stations were operational. In 68 793 of them the largest mean signal occurred in double station 501/510. In the other 50 999 cases the largest mean signal (7 detectors) occurred in either station 502 or in station 508. For both situations the largest detector signal is plotted against the mean signal in Figure 11.4. For both situations the distributions of f^* are shown in Figure 11.5.

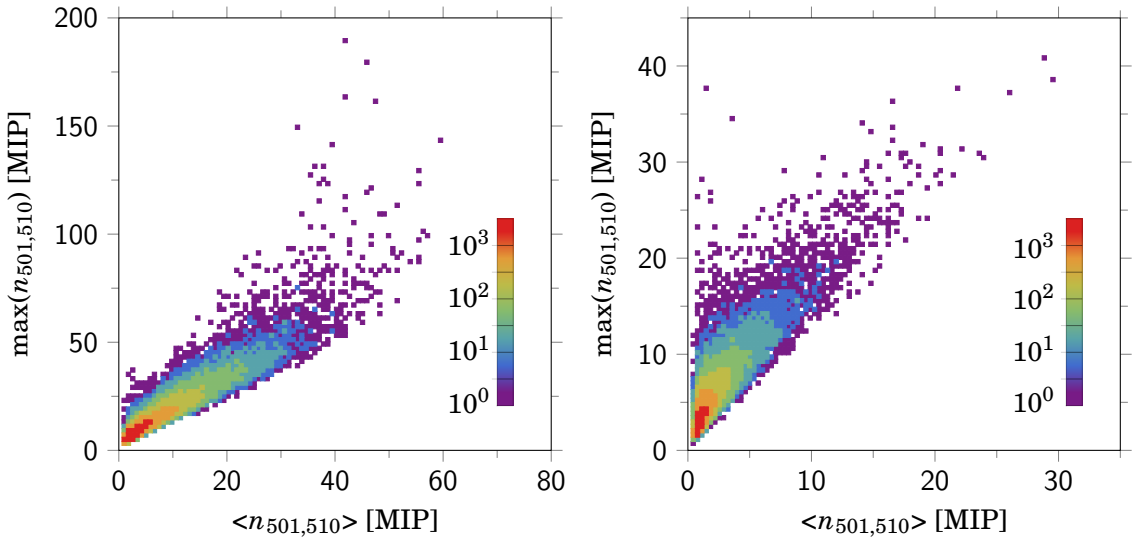

Figure 11.4: Density contour plot of the largest detector signal versus the mean of the other 7 detector signals in station 501/510 for the situation where the largest mean signal occurred in station 501/510 (left) and for the situation where the largest mean signal occurred in either station 502 or station 508 (right). Data taken between 2015-05-22, 00:00:00 and 2016-05-22, 00:00:00.

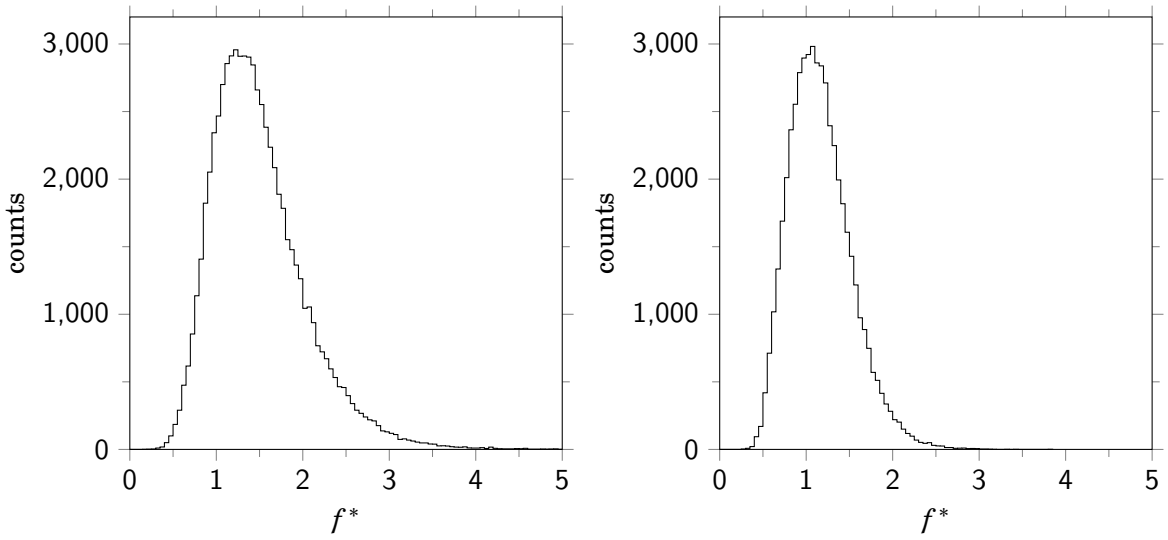

Figure 11.5: The distribution of f^* for the situation where the largest mean signal occurred in the double station (left) and for the situation where the largest mean signal occurred in either station 502 or station 508 (right). Data taken between 2015-05-22, 00:00:00 and 2016-05-22, 00:00:00.

They show a large similarity with the distributions obtained with simulations. To make visible the sparse large f^* values the distributions of f^* are plotted on a logarithmic scale in Figure 11.6.

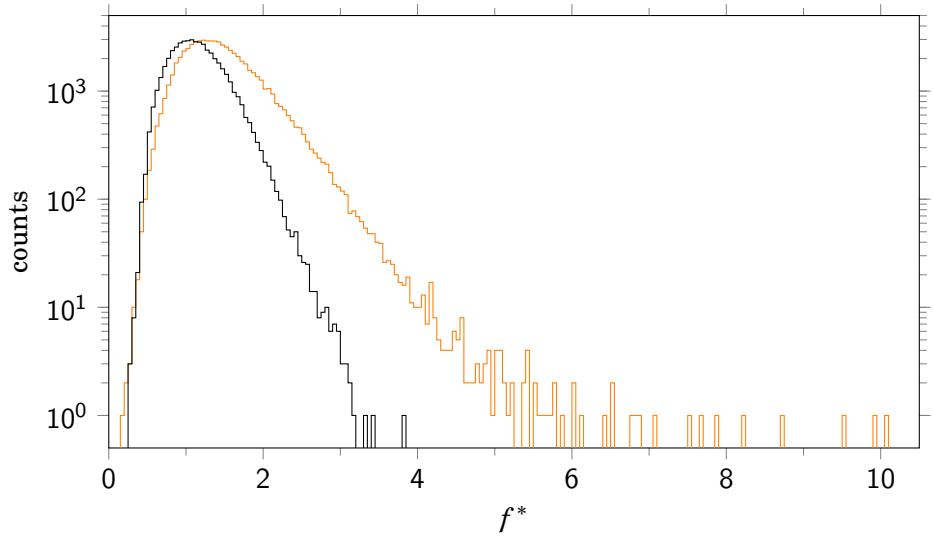

Figure 11.6: The distribution of f^* for the situation where the largest mean signal occurred in station 501/510 (orange) and for the situation where the largest mean signal occurred in either station 502 or station 508 (black). Data taken between 2015-05-22, 00:00:00 and 2016-05-22, 00:00:00.

As for the simulated distributions of f^* the tail is almost exponential.

For the situation where the largest mean signal occurred in the double station we see large f^* values. The largest one has $f^* = 10.1$. It occurred at 2015-05-24, 21:32:02 (timestamp 1432503122-394885806). The largest signal in the double station was 237.4 MIP in detector 0 of station 501, while the mean of the other seven detectors was 42.3 MIP. In detector 0 of station 510 the signal was 90.8 MIP. The mean of station 502 and 508 was 2.8 and 6.8 MIP respectively. What we have here is a shower with its core at or very close to, detector 0 of station 501. The other large f^* coincidences show a similar pattern. In conclusion, the large f^* values are caused by shower cores nearby the double station and not by a fluctuation.

For the situation where the largest mean signal occurred not in the double station we do not see large f^* values. The largest f^* value is 3.81. It occurred at 2015-12-13, 18:13:48 (timestamp 1450030428-447610312). The largest signal in the double station was 34.1 MIP in detector 1 of station 510, while the mean of the other seven detectors was 3.44 MIP. In detector 1 of station 501 the signal was 5.65 MIP. The mean of station 502 and 508 was 0.94 and 33.1 MIP respectively. Here we have a fluctuation in the double station while the shower core was near station 508. To ascribe it to a jet a 5σ threshold will be required. The 5σ threshold is determined

by extending the exponential fit of the tail of the distribution of f^*. The fit follows the tail when the fit domain is taken between the f^* value where the distribution is about 10 % of the maximum and 1 % of the maximum. For smaller data sizes larger percentages are taken for the domain.

11.3 Data analysis

With the results of the preliminary analysis in mind we turn to the analysis of the data of the SPA stations 501 through 506 and 508 through 511 taken from 2014-09-29 through 2016-05-22. Station 511 was operational at the SPA site since 2015-10-02. The maximum coincidence size therefore is 10. There were $7.4 \cdot 10^6$ coincidences with at least three participating stations. In $1.2 \cdot 10^6$ of them both station 501 and 510 participated. The f values are inspected for $n = 3$ through $n = 10$ coincidences where at least the stations 501 and 510 participated. For $n = 3$ we have a coincidence of the double station with just one of the other stations. For $n = 4$ we have a coincidence of the double station with two of the other stations, and so on. For these $n = 3$ and $n = 4$ coincidences for which the mean signal did not occur in the double station the energy of showers are about $10^{14.5} - 10^{15}$ eV. For these energies the jet distances to the main core are about $20 - 50$ m. These distances are comparable with the distances between the double station and the main core. Although extremely small the probability for finding a jet core is largest for these coincidences. For $n > 4$ coincidences the probability rapidly drops because the shower rate decreases with energy and because the fraction of showers for which the jet distance is comparable with the distance of the double station to the main core decreases with energy. Nevertheless, the data will be analyzed for $n = 3$ through $n = 10$ coincidences. From each set of $n = k$ coincidences a reduced set of coincidences is obtained for which the mean signal of the double station (7 detectors) is smaller than the mean signal of at least one of the other $k - 2$ stations. For each reduced set the distribution of f^* values is plotted. In the plots the exponential fits and some significance levels are depicted.

In the period considered the number of threefold through tenfold coincidences with the double station participating was 832 950, 241 804, 86 878, 36 271, 15 873, 6015, 2058 and 603 respectively. The number of threefold through tenfold coincidences with the double station participating and where the largest mean signal did not occur in the double station was 423 290, 114 064, 43 079, 18 082, 7445, 2435, 706 and 169 respectively. The distributions of f^* are shown for $n = 3$ and $n = 4$ coincidences in Figure 11.7, for $n = 5$ and $n = 6$ coincidences in Figure 11.8, for $n = 7$ and $n = 8$ coincidences in Figure 11.9 and for $n = 9$ and $n = 10$ coincidences in Figure 11.10.

For $n = 3$ coincidences the distribution of f^* falls off exponentially beyond its maximum as $e^{-4.7 f^*}$. The largest f^* value is 4.18, corresponding with a 5σ deviation from the mean. It

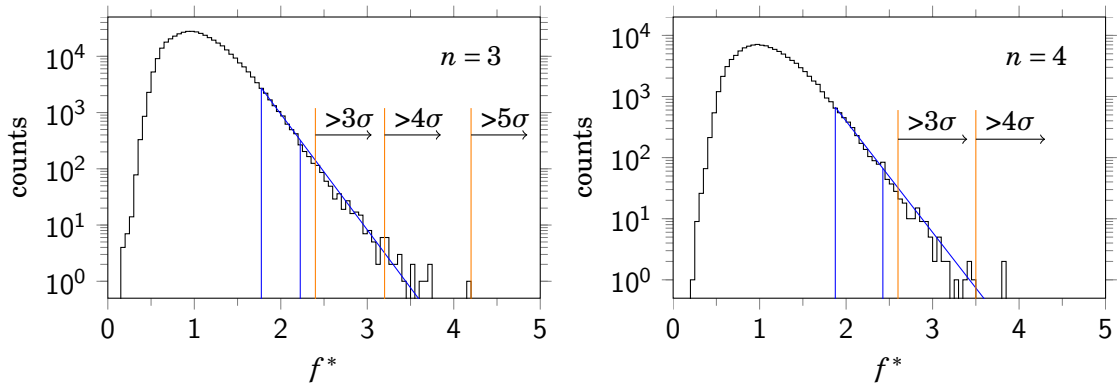

Figure 11.7: The distribution of f^* for threefold coincidences (left) and for fourfold coincidences (right) for which the mean signal in station 501/510 is not the largest one. The blue lines depict the exponential fit and the fit domain. Data taken between 2014-09-29 and 2016-05-22.

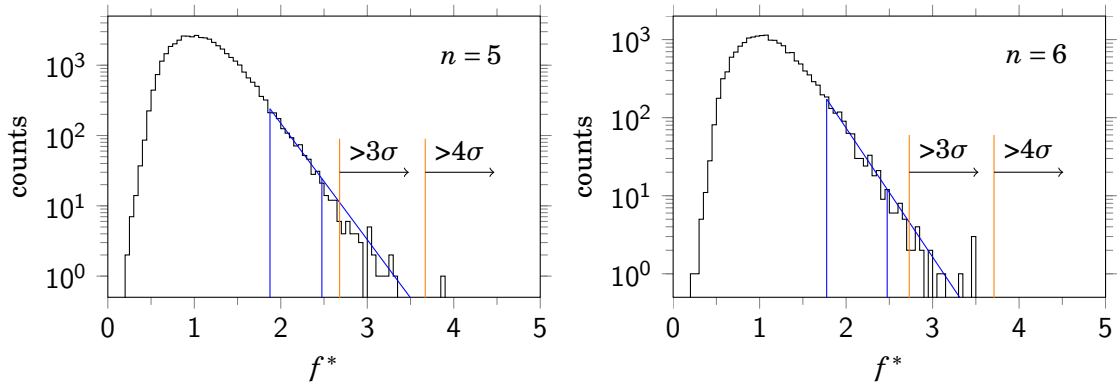

Figure 11.8: The distribution of f^* for fivefold coincidences (left) and for sixfold coincidences (right) for which the mean signal in station 501/510 is not the largest one. The blue lines depict the exponential fit and the fit domain. Data taken between 2014-09-29 and 2016-05-22.

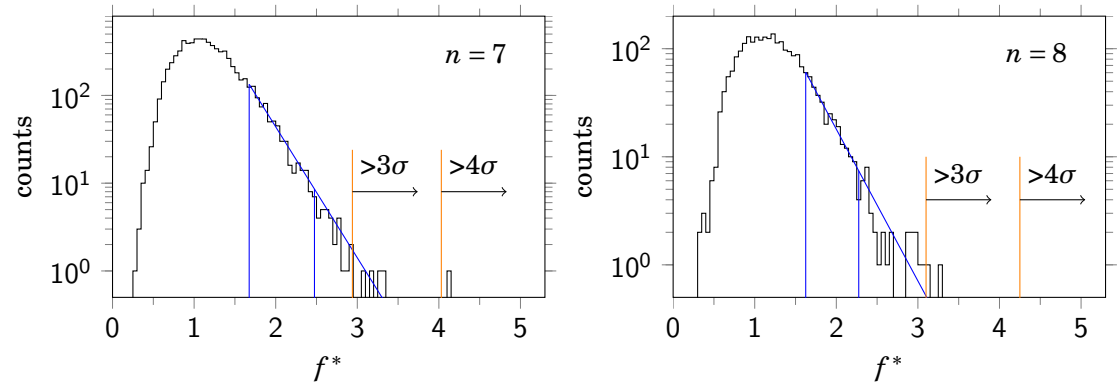

Figure 11.9: The distribution of f^* for sevenfold coincidences (left) and for eightfold coincidences (right) for which the mean signal in station 501/510 is not the largest one. The blue lines depict the exponential fit and the fit domain. Data taken between 2014-09-29 and 2016-05-22.

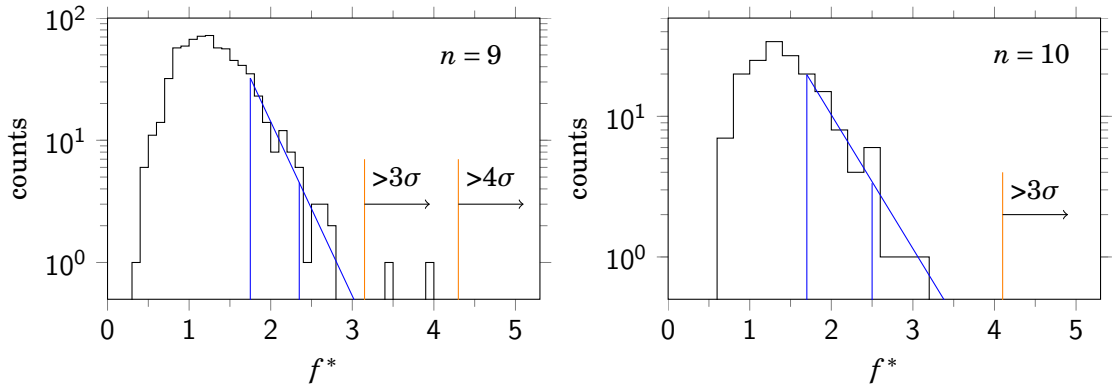

Figure 11.10: The distribution of f^* for ninefold coincidences (left) and for tenfold coincidences (right) for which the mean signal in station 501/510 is not the largest one. The blue lines depict the exponential fit and the fit domain. Data taken between 2014-09-29 and 2016-05-22.

occurred at 2015-10-21, 02:52:46 (timestamp 1445395966-341581832) with station 508 participating. The maximum signal in the double station is 40.2 MIP in detector 0 of station 510, while the signal in detector 0 of station 501 is 27.9 MIP. The mean of the six other detectors of the double station is 1.4 MIP. The mean signal of the double station (7 detectors) is 5.2 MIP, while the mean signal in station 508 is 7.6 MIP. The signals suggest a core closer to station 508 than to the double station and a sub core close to the detector 0 pair of the double station.

For $n = 4$ coincidences the distribution of f^* falls off exponentially beyond its maximum as $e^{-4.2f^*}$. The largest f^* value is 3.82, corresponding with a 4.3σ deviation. The next to largest f^* value is 3.81 and is the same coincidence we already met in the previous section.
For $n = 5$ coincidences the tail of the distribution of f^* falls off exponentially as $e^{-3.8f^*}$. The largest f^* value is 3.86, corresponding with a 4.2σ deviation.
For $n = 6$ coincidences the tail of the distribution of f^* falls off exponentially beyond its maximum as $e^{-3.8f^*}$. The largest f^* value is 3.47, corresponding with a 3.8σ deviation.
For $n = 7$ coincidences the tail of the distribution of f^* falls off exponentially beyond its maximum as $e^{-3.4f^*}$. The largest f^* value is 4.12, corresponding with a 4.1σ deviation.
For $n = 8$ coincidences the tail of the distribution of f^* falls off exponentially beyond its maximum as $e^{-3.2f^*}$. The largest f^* value is 3.26, corresponding with a 3.1σ deviation.
For $n = 9$ coincidences the tail of the distribution of f^* falls off exponentially beyond its maximum as $e^{-3.3f^*}$. The largest f^* value is 4.00, corresponding with a 3.8σ deviation.
For the $n = 10$ coincidences the exponential fit is inaccurate because of the small data size. The diagram shows no deviations larger than 3σ.

For all the deviations the probability to occur in the data of the given size is relatively large. Too large to ascribe it to a jet with a sufficient significance. For example, for the $f^* = 4.18$ event

in the $n = 3$ coincidences the expected number of f^* values larger than 4.18 is about 0.12. For this expectation value the Poisson probability to find an event is about 0.11. Translated to a Gaussian distribution this is a significance of about 1.2σ. By far not significant enough to ascribe it to a jet. Even worse significances are found for the other deviations.

11.4 Conclusion

With the double station as a mini-array it is possible to detect fluctuations. As expected the number of fluctuations with a f^* value above a given threshold decreases with coincidence size and thus with energy. The largest fluctuation observed in the 1.7 yr of data of the SPA stations occurred for a $n = 3$ coincidence. Although a 5σ deviation, the significance is very low. The coincidence size indicates a shower energy of approximately $10^{14.5}$ eV. The signal pattern indicates a main core roughly at a distance of 30 m to the double station. A jet core distance of 30 m is not unusual for a shower energy of $10^{14.5}$ eV. Even if the largest fluctuation would have been highly significant, one could still have doubts about this fluctuation since the main core position is not precisely detected. Besides, without a precise main core position there is no way to relate the physical observables to the transverse momentum of the jet. To detect the main core and a sub core simultaneously requires a large array of detectors; an array of the order of $5.6 \cdot 10^3$ m^2. Even for such a large array the observational rate of first interaction jets is extremely low, less than once a year at sea level. The observational rate of second interaction jets is about 10 per week at sea level. The latter is based on the leading particle effect in p-p collisions. For second interaction jets there is no way to relate the physical observables to the jet momentum and to the energy of the collision. Even for first interaction jets the prediction for the transverse jet momentum on the basis of the physical observables is highly uncertain. The investigation of jets becomes of more value if an accurate predictor is derived. For relatively large jet rates an observation level at an altitude of 4 km is preferable, although the observed jets are mainly in 10^{14} eV showers. For jets in showers with larger energy one has to decrease the altitude of the observation level at cost of the jet rate. At sea level the observed jets are mainly in $10^{15.5}$ eV showers. In the latter case the extremely low first interaction jet rate is overwhelmed by secondary interaction jet rates. As it stands now it is rather unlikely that one can observe first interaction hadronic jets by means of a large array at sea level.

12
Summary

Cosmic rays enter the atmosphere of the Earth in enormous quantities. When, for instance, a gamma ray enters the atmosphere it initiates an electromagnetic shower: a photon turns into an electron-positron pair (pair creation) and electrons and positrons radiate photons (Bremsstrahlung). The cascade of repeated electromagnetic interactions leads to a shower with a large number of electrons, positrons and photons. The shower size can be billions of particles for very high energy cosmic rays. Initially the shower size grows exponentially. The further the cascades develops the smaller the energy of the individual particles of the shower. As soon as the energy of an individual electron of the shower falls below the critical energy it stops generating new particles. This slows down the growth of the shower size. After reaching a maximum the shower size will decrease. The evolution of the shower size along atmospheric depth is called the longitudinal profile. There are several functions to model the longitudinal profile such as Heitler model, the Gaisser-Hillas function, the Gaussian in Age function and the Greisen function. They can be related to the level of accuracy of the underlying model [51].

Almost all primary cosmic rays are nuclei, among which the proton is the most likely. When such a cosmic ray collides (strong interaction) with the nucleus of an atom (most likely nitrogen or oxygen) in the air a multiplicity of secondary particles is created. The secondary particles are mostly pions. The neutral pions almost immediately decay into a pair of photons thereby initiating an electromagnetic sub shower. If their energy is large enough the charged pions also collide with nuclei in the air, else they will decay into a muon. The colliding pions generate a next multiplicity of particles. Showers dominated by hadronic interactions are called hadronic showers. Because of the large multiplicity hadronic showers reach their maximum shower size at smaller atmospheric depths than electromagnetic showers with the same energy. A discrete approximation of the cascade of hadronic interactions has been used to predict the depth of maximum for hadronic showers [52].

Extended air showers reach the surface of the Earth. The lateral density of the particles that reach the ground is a footprint of the shower. The larger the energy of the shower the larger the density. The density is largest at the core of the shower. The density decreases with the distance to the core. For vertical showers the lateral density is well described by the NKG function or suitable modifications of it. The NKG type of function for the SPA site of HiSPARC detectors is determined on the basis of simulations by means of CORSIKA without thinning. For inclined showers with a zenith angle smaller than 60° the density is approximately concentrical in the plane perpendicular to the shower direction. In a horizontal plane of observation the iso-density contours become elliptic. Moreover, the additional attenuation of the late part of the shower with respect to the early part of the shower leads to a shift of the center of the iso-density contours [60]. The NKG type of lateral density function including the modifications for the ellipticity and the shift are implemented in the analyses package SAPPHiRE for reconstructions of the size and energy of observed showers. The latter requires the direction of the shower which is determined from the arrival time differences between observation stations. For the direction reconstruction some fast methods have been implemented in SAPPHiRE.

The HiSPARC detectors observe the footprints of showers by means of the energy losses of the electrons and muons in their passage through the detector plate. The energy losses are transformed to PMT signals. The energy losses and their transformation to PMT signals is described and, to good approximation, implemented in SAPPHiRE for simulation purposes. By means of a Monte Carlo it is numerically investigated to which extend showers with a given energy and zenith will hit one or more stations. More specifically: for each situation the effective area is determined. The latter is, for instance, needed for the determination of the energy spectrum of cosmic rays.

In high-energy hadronic collisions jets can occur as a result of the hard scattering. Therefore this also occurs in the collision of a cosmic ray with a nucleus in an atom of the Earth's atmosphere. Jets in cosmic air showers cause density fluctuations which can be detected. However, the density of particles in a shower is full of 'background' fluctuations. Background fluctuations can be of statistical nature such as the Poisson statistics of the number of particles falling on a detector. They can also be of physical nature such as hadronic interactions in secondary collisions. An impression of the difficulty of finding a jet between all kinds of fluctuations is given in Figure 12.1. To distinguish a jet fluctuation from background fluctuations it should be very strong. Strong enough that the probability of being a background fluctuation is very small. As common in particle physics a 5σ level is applied. A jet is regarded as observable if its density fluctuation is at least 5σ.

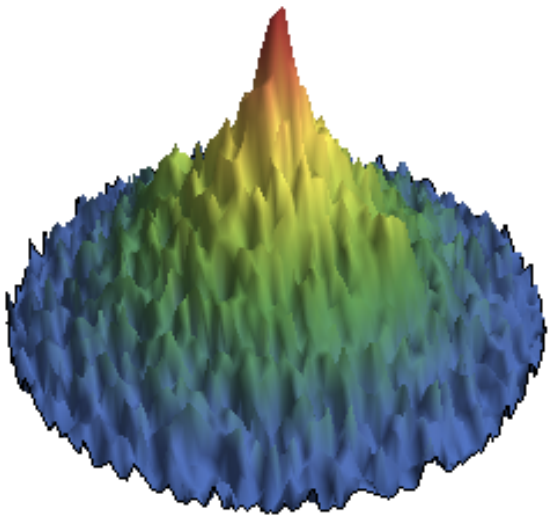

Figure 12.1: Impression of the lateral density, not to scale, plotted in vertical direction, with two jet fluctuations among many statistical fluctuations.

A large Monte Carlo is performed for the numerical investigation of jets in cosmic air showers. The jets are simulated for different energies and different transverse jet momentum. The p-air collisions in the first interaction are simulated as p-p collisions with PYTHIA. The output of PYTHIA is used as the input for CORSIKA to simulate the evolution of the shower. The latter results in lateral densities of particles at the desired observation level. These densities are randomly thrown on different types of large arrays. For each throw all the thousands of detectors are inspected for large fluctuations. As a result observational jet rates are obtained for observation levels at different altitudes. For 4 km altitude the jet rate obtained is comparable with the rate observed with the ARGO-YBJ experiment [116, 117]. For sea level the observational rate obtained for first collision jets is less than one per year. However, in very high energy showers jets are generated at secondary hadronic collisions at probably a thousand times larger rate. Another result from the investigation is that the transverse jet momentum can not be predicted well from physical observables as the main core density, the jet core density and the distance of the jet core to the main core.

The HiSPARC data for the stations at Science Park Amsterdam is analyzed for jet fluctuations. For this the double station is used as a mini-array. In one occasion the fluctuation reached the 5σ significance level. Still it is doubtful to ascribe it to a jet since we have no accurate information about the main core position of the shower. The core reconstruction method can not be applied because of the low number of station activated by the shower. Besides, even for a larger number of activated stations the uncertainty in the position of the main core is larger

than the distance of the jet core to the main core. A solution requires is a substantial increase of the number of stations.

In summary, at sea level observational jets are most probably generated in secondary collisions. The altitude of the interaction therefore is even more uncertain than for the first interaction. Since a predictor for the jet transverse momentum is based on the distance of the jet core to the main core and thus on the altitude of the interaction this further reduces the (already bad) accuracy of the prediction of the transverse jet momentum. That is, except from an experimental jet rate, jet observations do not provide information about the jet transverse momentum and thus not about the strong coupling constant. It therefore is not recommended to invest in detection capacity at sea level just for the purpose of jet observations.

A

Simulated effective areas

The effective areas per shower and per jet are tabulated per shower energy and per altitude. The tables are divided in three sections, one for each altitude. In the upper left corner of a table the energy and altitude are shown. In the upper row are the array types. In the first column are the $\widehat{p}_{\mathrm{T}}$. For each array type and $\widehat{p}_{\mathrm{T}}$ the upper and lower number are the effective areas per shower and per jet respectively. The statistical uncertainties are in brackets. The final row contains the sum of the effective area per jet.

A.1 Effective areas for 4 km altitude

10^{14} eV, 4 km	1×1	1×1 alt.	$\sqrt{2} \times \sqrt{2}$	$\sqrt{2} \times \sqrt{2}$ alt.
12 GeV/c	$1.4(1.4) \cdot 10^{1}$ $2.4(2.4) \cdot 10^{-1}$	$1.2(1.2) \cdot 10^{1}$ $2.0(2.1) \cdot 10^{-1}$	$6.2(4.8) \cdot 10^{0}$ $1.1(0.8) \cdot 10^{-1}$	$5.6(5.6) \cdot 10^{-1}$ $1.0(1.3) \cdot 10^{-2}$
24 GeV/c	$2.9(2.9) \cdot 10^{1}$ $2.3(2.3) \cdot 10^{-3}$	$1.1(1.2) \cdot 10^{1}$ $9.1(9.3) \cdot 10^{-4}$	$2.0(1.5) \cdot 10^{1}$ $1.6(1.2) \cdot 10^{-3}$	$9.6(7.1) \cdot 10^{0}$ $7.7(5.8) \cdot 10^{-4}$
36 GeV/c	$2.1(2.2) \cdot 10^{1}$ $9.2(9.3) \cdot 10^{-5}$	$7.9(8.2) \cdot 10^{1}$ $3.4(3.5) \cdot 10^{-5}$	$4.1(2.9) \cdot 10^{1}$ $1.8(1.3) \cdot 10^{-4}$	$2.1(2.2) \cdot 10^{1}$ $9.2(9.3) \cdot 10^{-5}$
48 GeV/c	$1.3(0.6) \cdot 10^{2}$ $5.8(2.7) \cdot 10^{-5}$	$8.3(4.2) \cdot 10^{1}$ $3.7(1.9) \cdot 10^{-5}$	$1.9(0.7) \cdot 10^{2}$ $8.5(3.2) \cdot 10^{-5}$	$1.6(0.6) \cdot 10^{2}$ $7.1(2.7) \cdot 10^{-5}$
60 GeV/c	$7.3(4.2) \cdot 10^{1}$ $4.6(2.7) \cdot 10^{-6}$	$3.3(2.4) \cdot 10^{1}$ $2.1(1.5) \cdot 10^{-6}$	$2.0(0.9) \cdot 10^{2}$ $1.3(0.6) \cdot 10^{-5}$	$1.7(0.8) \cdot 10^{2}$ $1.1(0.5) \cdot 10^{-5}$
$\sum A_{\mathrm{eff}}$ / jet	$2.4(2.4) \cdot 10^{-1}$	$2.0(2.1) \cdot 10^{-1}$	$1.1(0.8) \cdot 10^{-1}$	$1.0(1.3) \cdot 10^{-2}$

Table A.1: Effective area in m^2 per shower and per jet for 10^{14} eV showers at 4 km altitude.

$10^{14.5}$ eV, 4 km	1×1	1×1 alt.	$\sqrt{2} \times \sqrt{2}$	$\sqrt{2} \times \sqrt{2}$ alt.
12 GeV/c	0 0	0 0	0 0	0 0
24 GeV/c	$9.8(5.7) \cdot 10^{1}$ $3.1(1.8) \cdot 10^{-2}$	$7.3(4.2) \cdot 10^{1}$ $2.2(1.3) \cdot 10^{-2}$	$1.2(0.7) \cdot 10^{2}$ $3.9(2.2) \cdot 10^{-2}$	$8.3(4.8) \cdot 10^{1}$ $2.6(1.5) \cdot 10^{-2}$
36 GeV/c	$4.7(1.3) \cdot 10^{2}$ $1.0(0.3) \cdot 10^{-2}$	$4.0(1.1) \cdot 10^{2}$ $8.8(2.5) \cdot 10^{-3}$	$5.7(1.2) \cdot 10^{2}$ $1.3(0.3) \cdot 10^{-2}$	$3.7(0.9) \cdot 10^{2}$ $8.1(1.9) \cdot 10^{-3}$
48 GeV/c	$4.4(1.2) \cdot 10^{2}$ $1.3(0.3) \cdot 10^{-3}$	$3.6(1.0) \cdot 10^{2}$ $1.0(0.3) \cdot 10^{-3}$	$6.0(1.2) \cdot 10^{2}$ $1.7(0.4) \cdot 10^{-3}$	$4.3(0.9) \cdot 10^{2}$ $1.2(0.3) \cdot 10^{-3}$
60 GeV/c	$6.3(1.4) \cdot 10^{2}$ $3.8(0.8) \cdot 10^{-4}$	$4.8(1.2) \cdot 10^{2}$ $2.9(0.7) \cdot 10^{-4}$	$9.8(1.7) \cdot 10^{2}$ $6.0(1.1) \cdot 10^{-4}$	$7.1(1.2) \cdot 10^{2}$ $4.3(0.8) \cdot 10^{-4}$
$\sum A_{\text{eff}}$ / jet	$4.3(1.8) \cdot 10^{-2}$	$3.2(1.3) \cdot 10^{-2}$	$5.4(2.2) \cdot 10^{-2}$	$3.6(1.5) \cdot 10^{-2}$

Table A.2: Effective area in m^2 per shower and per jet for $10^{14.5}$ eV showers at 4 km altitude.

10^{15} eV, 4 km	1×1	1×1 alt.	$\sqrt{2} \times \sqrt{2}$	$\sqrt{2} \times \sqrt{2}$ alt.
12 GeV/c	0 0	0 0	0 0	0 0
24 GeV/c	$9.3(4.7) \cdot 10^{1}$ $9.3(4.7) \cdot 10^{-2}$	$4.0(1.7) \cdot 10^{1}$ $4.0(1.7) \cdot 10^{-2}$	$6.6(2.8) \cdot 10^{1}$ $6.6(2.8) \cdot 10^{-2}$	$4.3(2.2) \cdot 10^{1}$ $4.3(2.2) \cdot 10^{-2}$
36 GeV/c	$3.7(1.2) \cdot 10^{2}$ $3.1(1.0) \cdot 10^{-2}$	$2.4(0.8) \cdot 10^{2}$ $2.1(0.7) \cdot 10^{-2}$	$2.7(0.8) \cdot 10^{1}$ $2.3(0.7) \cdot 10^{-2}$	$1.5(0.5) \cdot 10^{1}$ $1.3(0.4) \cdot 10^{-2}$
48 GeV/c	$3.0(0.8) \cdot 10^{2}$ $3.8(1.0) \cdot 10^{-3}$	$1.9(0.5) \cdot 10^{2}$ $2.5(0.7) \cdot 10^{-3}$	$2.3(0.6) \cdot 10^{2}$ $3.0(0.8) \cdot 10^{-3}$	$1.4(0.5) \cdot 10^{2}$ $1.8(0.6) \cdot 10^{-3}$
60 GeV/c	$1.1(0.2) \cdot 10^{3}$ $4.3(0.8) \cdot 10^{-3}$	$8.2(1.4) \cdot 10^{2}$ $3.1(0.5) \cdot 10^{-3}$	$8.8(1.5) \cdot 10^{2}$ $3.3(0.6) \cdot 10^{-3}$	$6.7(1.2) \cdot 10^{2}$ $2.5(0.4) \cdot 10^{-3}$
$\sum A_{\text{eff}}$ / jet	$1.3(0.5) \cdot 10^{-1}$	$6.7(1.8) \cdot 10^{-2}$	$9.5(2.9) \cdot 10^{-2}$	$6.0(2.2) \cdot 10^{-2}$

Table A.3: Effective area in m^2 per shower and per jet for 10^{15} eV showers at 4 km altitude.

A.2 Effective areas for 2 km altitude

10^{14} eV, 2 km	1×1	1×1 alt.	$\sqrt{2} \times \sqrt{2}$	$\sqrt{2} \times \sqrt{2}$ alt.
12 GeV/c	0	0	$1.7(1.7) \cdot 10^{1}$	$1.7(1.9) \cdot 10^{0}$
	0	0	$2.9(2.9) \cdot 10^{-1}$	$2.9(3.3) \cdot 10^{-2}$
24 GeV/c	0	0	$3.4(3.6) \cdot 10^{0}$	0
	0	0	$2.7(3.0) \cdot 10^{-4}$	0
36 GeV/c	0	0	0	0
	0	0	0	0
48 GeV/c	0	0	$3.5(3.5) \cdot 10^{1}$	$2.1(2.2) \cdot 10^{2}$
	0	0	$1.6(1.6) \cdot 10^{-5}$	$1.0(1.0) \cdot 10^{-5}$
60 GeV/c	0	0	$3.9(3.9) \cdot 10^{1}$	$3.9(3.9) \cdot 10^{2}$
	0	0	$2.5(2.5) \cdot 10^{-6}$	$2.5(2.5) \cdot 10^{-6}$
$\sum A_{\text{eff}}$ / jet	0	0	$2.9(2.9) \cdot 10^{-1}$	$2.9(3.3) \cdot 10^{-2}$

Table A.4: Effective area in m^2 per shower and per jet for 10^{14} eV showers at 2 km altitude.

$10^{14.5}$ eV, 2 km	1×1	1×1 alt.	$\sqrt{2} \times \sqrt{2}$	$\sqrt{2} \times \sqrt{2}$ alt.
12 GeV/c	0	0	0	0
	0	0	0	0
24 GeV/c	0	0	$5.1(5.3) \cdot 10^{0}$	0
	0	0	$1.6(1.7) \cdot 10^{-3}$	0
36 GeV/c	$1.1(0.4) \cdot 10^{2}$	$8.2(4.8) \cdot 10^{1}$	$1.2(0.5) \cdot 10^{2}$	$1.0(0.5) \cdot 10^{2}$
	$2.3(0.9) \cdot 10^{-3}$	$1.8(1.0) \cdot 10^{-3}$	$2.7(1.1) \cdot 10^{-3}$	$2.3(1.0) \cdot 10^{-3}$
48 GeV/c	$1.4(1.4) \cdot 10^{1}$	$4.5(4.7) \cdot 10^{0}$	$3.1(1.8) \cdot 10^{1}$	$1.2(0.7) \cdot 10^{1}$
	$3.9(4.0) \cdot 10^{-5}$	$1.3(1.4) \cdot 10^{-5}$	$9.0(5.3) \cdot 10^{-5}$	$3.4(2.1) \cdot 10^{-5}$
60 GeV/c	$5.1(3.6) \cdot 10^{1}$	$4.4(4.5) \cdot 10^{1}$	$1.4(0.6) \cdot 10^{2}$	$7.5(3.4) \cdot 10^{1}$
	$3.1(2.2) \cdot 10^{-5}$	$2.7(2.7) \cdot 10^{-5}$	$8.2(3.8) \cdot 10^{-5}$	$4.6(2.1) \cdot 10^{-5}$
$\sum A_{\text{eff}}$ / jet	$2.3(0.9) \cdot 10^{-3}$	$1.8(1.0) \cdot 10^{-3}$	$4.4(2.0) \cdot 10^{-3}$	$2.4(1.0) \cdot 10^{-3}$

Table A.5: Effective area in m^2 per shower and per jet for $10^{14.5}$ eV showers at 2 km altitude.

10^{15} eV, 2 km	1×1	1×1 alt.	$\sqrt{2} \times \sqrt{2}$	$\sqrt{2} \times \sqrt{2}$ alt.
12 GeV/c	0 0	0 0	0 0	0 0
24 GeV/c	$4.1(2.4) \cdot 10^{1}$ $4.1(2.4) \cdot 10^{-2}$	$2.4(1.7) \cdot 10^{1}$ $2.4(1.7) \cdot 10^{-2}$	$3.6(3.6) \cdot 10^{1}$ $3.6(3.6) \cdot 10^{-2}$	$3.1(3.1) \cdot 10^{1}$ $3.1(3.1) \cdot 10^{-2}$
36 GeV/c	$1.2(0.7) \cdot 10^{2}$ $1.0(0.6) \cdot 10^{-2}$	$7.5(4.4) \cdot 10^{1}$ $6.3(3.7) \cdot 10^{-3}$	$7.9(4.0) \cdot 10^{1}$ $6.6(3.4) \cdot 10^{-3}$	$5.7(2.9) \cdot 10^{1}$ $4.8(2.5) \cdot 10^{-3}$
48 GeV/c	$1.6(0.5) \cdot 10^{2}$ $2.1(0.7) \cdot 10^{-3}$	$9.1(3.1) \cdot 10^{1}$ $1.2(0.4) \cdot 10^{-3}$	$1.8(0.5) \cdot 10^{2}$ $2.3(0.7) \cdot 10^{-3}$	$1.3(0.4) \cdot 10^{2}$ $1.6(0.5) \cdot 10^{-3}$
60 GeV/c	$2.0(0.7) \cdot 10^{2}$ $7.7(2.4) \cdot 10^{-4}$	$1.3(0.5) \cdot 10^{2}$ $4.8(1.7) \cdot 10^{-4}$	$2.4(0.7) \cdot 10^{2}$ $9.2(2.6) \cdot 10^{-4}$	$1.4(0.4) \cdot 10^{2}$ $5.3(1.6) \cdot 10^{-4}$
$\sum A_{\text{eff}}$ / jet	$5.4(2.5) \cdot 10^{-2}$	$3.2(1.7) \cdot 10^{-2}$	$4.6(3.6) \cdot 10^{-2}$	$3.8(3.1) \cdot 10^{-2}$

Table A.6: Effective area in m^2 per shower and per jet for 10^{15} eV showers at 2 km altitude.

$10^{15.5}$ eV, 2 km	1×1	1×1 alt.	$\sqrt{2} \times \sqrt{2}$	$\sqrt{2} \times \sqrt{2}$ alt.
12 GeV/c	0 0	0 0	0 0	0 0
24 GeV/c	$5.6(8.0) \cdot 10^{-1}$ $1.6(2.2) \cdot 10^{-3}$	0 0	$1.2(1.3) \cdot 10^{1}$ $3.5(3.5) \cdot 10^{-2}$	$6.8(7.0) \cdot 10^{0}$ $1.9(2.0) \cdot 10^{-2}$
36 GeV/c	$2.5(1.8) \cdot 10^{1}$ $6.2(4.5) \cdot 10^{-3}$	$6.8(5.2) \cdot 10^{0}$ $1.7(1.3) \cdot 10^{-3}$	$2.1(1.5) \cdot 10^{1}$ $5.2(3.8) \cdot 10^{-3}$	$1.2(1.3) \cdot 10^{1}$ $3.1(3.2) \cdot 10^{-3}$
48 GeV/c	$6.8(7.0) \cdot 10^{0}$ $3.2(3.4) \cdot 10^{-4}$	$3.9(4.2) \cdot 10^{0}$ $1.9(2.0) \cdot 10^{-4}$	$9.6(7.1) \cdot 10^{0}$ $4.6(3.4) \cdot 10^{-4}$	$4.5(3.0) \cdot 10^{0}$ $2.2(1.5) \cdot 10^{-4}$
60 GeV/c	$7.8(4.6) \cdot 10^{1}$ $1.1(0.6) \cdot 10^{-3}$	$3.2(2.3) \cdot 10^{1}$ $4.5(3.2) \cdot 10^{-4}$	$7.3(3.7) \cdot 10^{1}$ $1.0(0.5) \cdot 10^{-3}$	$2.9(1.5) \cdot 10^{1}$ $4.1(2.1) \cdot 10^{-4}$
72 GeV/c	$1.4(0.5) \cdot 10^{2}$ $6.4(2.2) \cdot 10^{-4}$	$5.3(2.0) \cdot 10^{1}$ $2.5(0.9) \cdot 10^{-4}$	$9.4(3.6) \cdot 10^{1}$ $4.4(1.7) \cdot 10^{-4}$	$3.8(1.5) \cdot 10^{1}$ $1.8(0.7) \cdot 10^{-4}$
$\sum A_{\text{eff}}$ / jet	$9.2(5.0) \cdot 10^{-3}$	$2.3(1.4) \cdot 10^{-3}$	$4.2(3.5) \cdot 10^{-2}$	$2.3(2.0) \cdot 10^{-2}$

Table A.7: Effective area in m^2 per shower and per jet for $10^{15.5}$ eV showers at 2 km altitude.

A.3 Effective areas for sea level

$10^{14.5}$ eV, 0 km	1×1	1×1 alt.	$\sqrt{2} \times \sqrt{2}$	$\sqrt{2} \times \sqrt{2}$ alt.
12 & 24 GeV/c	0 0	0 0	0 0	0 0
36 GeV/c	$1.1(0.8) \cdot 10^{1}$ $2.4(1.7) \cdot 10^{-4}$	$5.6(5.9) \cdot 10^{0}$ $1.2(1.3) \cdot 10^{-4}$	$4.8(4.8) \cdot 10^{1}$ $1.1(1.1) \cdot 10^{-3}$	$4.4(4.5) \cdot 10^{1}$ $1.0(1.0) \cdot 10^{-3}$
$\geq$ 48 GeV/c	0 0	0 0	0 0	0 0
$\sum A_{\text{eff}}$ / jet	$2.4(1.7) \cdot 10^{-4}$	$1.2(1.3) \cdot 10^{-4}$	$1.1(1.1) \cdot 10^{-3}$	$1.0(1.0) \cdot 10^{-3}$

Table A.8: Effective area in m^2 per shower and per jet for $10^{14.5}$ eV showers at sea level.

10^{15} eV, 0 km	1×1	1×1 alt.	$\sqrt{2} \times \sqrt{2}$	$\sqrt{2} \times \sqrt{2}$ alt.
12 $--$ 36 GeV/c	0 0	0 0	0 0	0 0
48 GeV/c	$4.6(4.6) \cdot 10^{1}$ $6.0(6.0) \cdot 10^{-4}$	$4.3(4.4) \cdot 10^{1}$ $5.6(5.7) \cdot 10^{-4}$	$7.7(5.5) \cdot 10^{1}$ $1.0(0.7) \cdot 10^{-3}$	$6.2(4.4) \cdot 10^{1}$ $8.1(5.8) \cdot 10^{-4}$
60 GeV/c	$8.9(5.2) \cdot 10^{1}$ $3.4(2.0) \cdot 10^{-4}$	$3.8(2.2) \cdot 10^{1}$ $1.4(0.8) \cdot 10^{-4}$	$1.3(0.6) \cdot 10^{2}$ $5.0(2.3) \cdot 10^{-4}$	$7.5(3.4) \cdot 10^{1}$ $2.9(1.3) \cdot 10^{-4}$
72 GeV/c	$5.8(3.4) \cdot 10^{1}$ $6.4(3.7) \cdot 10^{-5}$	$4.8(2.8) \cdot 10^{1}$ $5.3(3.1) \cdot 10^{-5}$	$4.6(2.7) \cdot 10^{1}$ $5.1(3.0) \cdot 10^{-5}$	$4.3(3.1) \cdot 10^{1}$ $4.8(3.4) \cdot 10^{-5}$
$\sum A_{\text{eff}}$ / jet	$1.0(0.6) \cdot 10^{-3}$	$7.5(5.8) \cdot 10^{-4}$	$1.6(0.7) \cdot 10^{-3}$	$1.1(0.6) \cdot 10^{-3}$

Table A.9: Effective area in m^2 per shower and per jet for 10^{15} eV showers at sea level.

$10^{15.5}$ eV, 0 km	1×1	1×1 alt.	$\sqrt{2} \times \sqrt{2}$	$\sqrt{2} \times \sqrt{2}$ alt.
12 & 24 GeV/c	0	0	0	0
	0	0	0	0
36 GeV/c	$3.0(3.0) \cdot 10^{1}$	$2.5(2.5) \cdot 10^{1}$	$3.2(3.2) \cdot 10^{1}$	$3.2(3.2) \cdot 10^{1}$
	$7.5(7.5) \cdot 10^{-3}$	$6.2(6.3) \cdot 10^{-3}$	$7.9(7.9) \cdot 10^{-3}$	$7.9(7.9) \cdot 10^{-3}$
48 GeV/c	$5.6(8.0) \cdot 10^{-1}$	0	$2.4(2.5) \cdot 10^{1}$	$6.2(6.5) \cdot 10^{0}$
	$2.7(3.8) \cdot 10^{-5}$	0	$1.2(1.2) \cdot 10^{-3}$	$3.0(3.1) \cdot 10^{-4}$
60 GeV/c	$1.2(0.6) \cdot 10^{2}$	$9.6(5.6) \cdot 10^{1}$	$9.8(7.0) \cdot 10^{1}$	$7.6(5.4) \cdot 10^{1}$
	$1.7(0.9) \cdot 10^{-3}$	$1.3(0.8) \cdot 10^{-3}$	$1.4(1.0) \cdot 10^{-3}$	$1.1(0.8) \cdot 10^{-3}$
72 GeV/c	$3.2(1.9) \cdot 10^{1}$	$1.4(0.8) \cdot 10^{1}$	$1.2(0.7) \cdot 10^{2}$	$9.8(5.7) \cdot 10^{1}$
	$1.5(0.9) \cdot 10^{-4}$	$6.3(3.9) \cdot 10^{-5}$	$5.5(3.2) \cdot 10^{-4}$	$4.6(2.7) \cdot 10^{-4}$
84 GeV/c	$4.8(2.5) \cdot 10^{1}$	$2.0(1.2) \cdot 10^{1}$	$2.1(1.1) \cdot 10^{1}$	$6.2(6.5) \cdot 10^{0}$
	$8.7(4.5) \cdot 10^{-5}$	$3.6(2.2) \cdot 10^{-5}$	$3.7(2.0) \cdot 10^{-5}$	$1.1(1.2) \cdot 10^{-5}$
$\sum A_{\text{eff}}$ / jet	$9.5(7.8) \cdot 10^{-3}$	$7.6(6.4) \cdot 10^{-3}$	$1.1(0.8) \cdot 10^{-2}$	$9.7(8.0) \cdot 10^{-3}$

Table A.10: Effective area in m^2 per shower and per jet for $10^{15.5}$ eV showers at sea level.

10^{16} eV, 0 km	1×1	1×1 alt.	$\sqrt{2} \times \sqrt{2}$	$\sqrt{2} \times \sqrt{2}$ alt.
12 −− 36 GeV/c	0	0	0	0
	0	0	0	0
48 GeV/c	0	$7.3(7.6) \cdot 10^{0}$	$2.3(2.5) \cdot 10^{0}$	$1.7(1.9) \cdot 10^{0}$
	0	$1.2(1.2) \cdot 10^{-3}$	$3.6(4.0) \cdot 10^{-4}$	$2.7(3.1) \cdot 10^{-4}$
60 GeV/c	0	0	0	$5.6(8.0) \cdot 10^{-1}$
	0	0	0	$2.4(3.4) \cdot 10^{-5}$
72 GeV/c	0	0	0	0
	0	0	0	0
84 GeV/c	$1.7(1.9) \cdot 10^{0}$	$1.1(1.4) \cdot 10^{0}$	$5.6(8.0) \cdot 10^{-1}$	$5.6(8.0) \cdot 10^{-1}$
	$1.0(1.2) \cdot 10^{-5}$	$7.0(8.5) \cdot 10^{-6}$	$3.5(5.0) \cdot 10^{-6}$	$3.5(5.0) \cdot 10^{-6}$
$\sum A_{\text{eff}}$ / jet	$1.0(1.2) \cdot 10^{-5}$	$1.2(1.2) \cdot 10^{-3}$	$3.6(4.0) \cdot 10^{-4}$	$3.0(3.1) \cdot 10^{-4}$

Table A.11: Effective area in m^2 per shower and per jet for 10^{16} eV showers at sea level.

B

Effective areas with the alternative method

See Appendix A for the description of the contents of the tables.

B.1 Effective areas for 4 km altitude

10^{14} eV, 4 km	1×1	1×1 alt.	$\sqrt{2} \times \sqrt{2}$	$\sqrt{2} \times \sqrt{2}$ alt.
12 GeV/c	$1.5(1.5) \cdot 10^{1}$	$1.2(1.2) \cdot 10^{1}$	$5.6(5.6) \cdot 10^{0}$	$1.7(1.8) \cdot 10^{0}$
	$2.6(2.6) \cdot 10^{-1}$	$2.0(2.0) \cdot 10^{-1}$	$9.5(9.5) \cdot 10^{-2}$	$2.9(2.9) \cdot 10^{-2}$
24 GeV/c	$1.1(0.5) \cdot 10^{2}$	$8.7(4.4) \cdot 10^{1}$	$1.3(0.5) \cdot 10^{2}$	$7.8(3.5) \cdot 10^{1}$
	$9.0(4.1) \cdot 10^{-3}$	$7.1(3.6) \cdot 10^{-3}$	$1.0(0.4) \cdot 10^{-2}$	$6.3(2.9) \cdot 10^{-3}$
36 GeV/c	$6.2(3.6) \cdot 10^{1}$	$5.0(2.9) \cdot 10^{1}$	$1.0(0.4) \cdot 10^{2}$	$6.5(3.0) \cdot 10^{1}$
	$2.7(1.6) \cdot 10^{-4}$	$2.1(1.2) \cdot 10^{-4}$	$4.4(1.7) \cdot 10^{-3}$	$2.8(1.3) \cdot 10^{-4}$
48 GeV/c	$3.1(0.8) \cdot 10^{2}$	$2.3(0.6) \cdot 10^{2}$	$4.0(0.9) \cdot 10^{2}$	$3.0(0.7) \cdot 10^{2}$
	$1.4(0.4) \cdot 10^{-4}$	$1.0(0.3) \cdot 10^{-4}$	$1.8(0.4) \cdot 10^{-4}$	$1.3(0.3) \cdot 10^{-4}$
60 GeV/c	$4.2(1.2) \cdot 10^{2}$	$3.4(2.4) \cdot 10^{2}$	$4.2(1.2) \cdot 10^{2}$	$3.3(0.9) \cdot 10^{2}$
	$2.7(0.8) \cdot 10^{-5}$	$2.2(0.6) \cdot 10^{-5}$	$2.7(0.8) \cdot 10^{-5}$	$2.1(0.6) \cdot 10^{-5}$
$\sum A_{\text{eff}}$ / jet	$2.7(2.6) \cdot 10^{-1}$	$2.1(2.1) \cdot 10^{-1}$	$1.1(1.0) \cdot 10^{-1}$	$3.6(2.9) \cdot 10^{-2}$

Table B.1: Effective area in m^2 per shower and per jet for 10^{14} eV showers at 4 km altitude.

$10^{14.5}$ eV, 4 km	1×1	1×1 alt.	$\sqrt{2} \times \sqrt{2}$	$\sqrt{2} \times \sqrt{2}$ alt.
12 GeV/c	0 0	0 0	0 0	0 0
24 GeV/c	$2.3(0.7) \cdot 10^{2}$ $7.0(2.2) \cdot 10^{-2}$	$1.8(0.6) \cdot 10^{2}$ $5.6(1.8) \cdot 10^{-2}$	$1.5(0.6) \cdot 10^{2}$ $4.5(1.7) \cdot 10^{-2}$	$1.1(0.4) \cdot 10^{2}$ $3.3(1.3) \cdot 10^{-2}$
36 GeV/c	$5.9(1.2) \cdot 10^{2}$ $1.3(0.3) \cdot 10^{-2}$	$4.8(1.0) \cdot 10^{2}$ $1.1(0.2) \cdot 10^{-2}$	$6.0(1.2) \cdot 10^{2}$ $1.3(0.3) \cdot 10^{-2}$	$4.3(0.9) \cdot 10^{2}$ $9.5(2.0) \cdot 10^{-3}$
48 GeV/c	$8.8(1.6) \cdot 10^{2}$ $2.6(0.4) \cdot 10^{-3}$	$7.3(1.3) \cdot 10^{2}$ $2.1(0.4) \cdot 10^{-3}$	$8.5(1.4) \cdot 10^{2}$ $2.5(0.4) \cdot 10^{-3}$	$6.3(1.1) \cdot 10^{2}$ $1.8(0.3) \cdot 10^{-3}$
60 GeV/c	$1.3(0.2) \cdot 10^{3}$ $7.9(1.1) \cdot 10^{-4}$	$1.1(0.2) \cdot 10^{3}$ $6.7(1.0) \cdot 10^{-4}$	$1.3(0.2) \cdot 10^{3}$ $7.7(1.1) \cdot 10^{-4}$	$9.6(1.4) \cdot 10^{2}$ $5.9(0.8) \cdot 10^{-4}$
$\sum A_{\text{eff}}$ / jet	$8.6(2.2) \cdot 10^{-2}$	$7.0(1.8) \cdot 10^{-2}$	$6.1(1.7) \cdot 10^{-2}$	$4.5(1.3) \cdot 10^{-2}$

Table B.2: Effective area in m^2 per shower and per jet for $10^{14.5}$ eV showers at 4 km altitude.

10^{15} eV, 4 km	1×1	1×1 alt.	$\sqrt{2} \times \sqrt{2}$	$\sqrt{2} \times \sqrt{2}$ alt.
12 GeV/c	0 0	0 0	0 0	0 0
24 GeV/c	$1.2(0.6) \cdot 10^{2}$ $1.2(0.6) \cdot 10^{-1}$	$6.6(2.6) \cdot 10^{1}$ $6.6(2.6) \cdot 10^{-2}$	$6.6(3.0) \cdot 10^{1}$ $6.6(3.0) \cdot 10^{-2}$	$5.0(2.3) \cdot 10^{1}$ $5.0(2.3) \cdot 10^{-2}$
36 GeV/c	$4.1(1.1) \cdot 10^{2}$ $3.4(0.9) \cdot 10^{-2}$	$2.8(0.8) \cdot 10^{2}$ $2.4(0.7) \cdot 10^{-2}$	$2.8(0.8) \cdot 10^{2}$ $2.3(0.7) \cdot 10^{-2}$	$1.8(0.5) \cdot 10^{2}$ $1.5(0.4) \cdot 10^{-2}$
48 GeV/c	$3.3(0.8) \cdot 10^{2}$ $4.3(1.0) \cdot 10^{-3}$	$2.4(0.6) \cdot 10^{2}$ $3.1(0.7) \cdot 10^{-3}$	$2.5(0.6) \cdot 10^{2}$ $3.3(0.8) \cdot 10^{-3}$	$1.6(0.4) \cdot 10^{2}$ $2.1(0.6) \cdot 10^{-3}$
60 GeV/c	$1.2(0.2) \cdot 10^{3}$ $4.6(0.7) \cdot 10^{-3}$	$9.1(1.4) \cdot 10^{2}$ $3.4(0.5) \cdot 10^{-3}$	$9.2(1.5) \cdot 10^{2}$ $3.5(0.6) \cdot 10^{-3}$	$6.5(1.2) \cdot 10^{2}$ $2.5(0.4) \cdot 10^{-3}$
$\sum A_{\text{eff}}$ / jet	$1.6(0.6) \cdot 10^{-1}$	$9.7(2.7) \cdot 10^{-2}$	$9.6(3.1) \cdot 10^{-2}$	$7.0(2.3) \cdot 10^{-2}$

Table B.3: Effective area in m^2 per shower and per jet for 10^{15} eV showers at 4 km altitude.

B.2 Effective areas for 2 km altitude

10^{14} eV, 2 km	1×1	1×1 alt.	$\sqrt{2} \times \sqrt{2}$	$\sqrt{2} \times \sqrt{2}$ alt.
12 GeV/c	0 0	0 0	$1.6(1.6) \cdot 10^{1}$ $2.8(2.8) \cdot 10^{-1}$	$5.1(5.3) \cdot 10^{0}$ $8.6(9.1) \cdot 10^{-2}$
24 GeV/c	$2.9(2.1) \cdot 10^{1}$ $2.3(1.7) \cdot 10^{-3}$	$1.4(1.0) \cdot 10^{1}$ $1.1(0.8) \cdot 10^{-3}$	$2.3(2.5) \cdot 10^{0}$ $1.8(2.0) \cdot 10^{-4}$	0 0
36 GeV/c	$5.6(8.0) \cdot 10^{-1}$ $2.4(3.4) \cdot 10^{-6}$	$5.6(8.0) \cdot 10^{-1}$ $2.4(3.4) \cdot 10^{-6}$	0 0	0 0
48 GeV/c	$7.9(4.6) \cdot 10^{1}$ $3.5(2.1) \cdot 10^{-5}$	$5.7(3.4) \cdot 10^{1}$ $2.6(1.5) \cdot 10^{-5}$	$9.3(4.7) \cdot 10^{1}$ $4.2(2.1) \cdot 10^{-5}$	$6.9(3.5) \cdot 10^{2}$ $3.1(1.6) \cdot 10^{-5}$
60 GeV/c	$4.5(3.2) \cdot 10^{1}$ $2.9(2.1) \cdot 10^{-6}$	$4.2(3.0) \cdot 10^{1}$ $2.7(1.9) \cdot 10^{-6}$	$5.3(3.1) \cdot 10^{1}$ $3.4(2.0) \cdot 10^{-6}$	$4.3(2.5) \cdot 10^{2}$ $2.8(1.6) \cdot 10^{-6}$
$\sum A_{\text{eff}}$ / jet	$2.3(1.7) \cdot 10^{-3}$	$1.1(0.8) \cdot 10^{-3}$	$2.8(2.8) \cdot 10^{-1}$	$8.6(9.1) \cdot 10^{-2}$

Table B.4: Effective area in m^2 per shower and per jet for 10^{14} eV showers at 2 km altitude.

$10^{14.5}$ eV, 2 km	1×1	1×1 alt.	$\sqrt{2} \times \sqrt{2}$	$\sqrt{2} \times \sqrt{2}$ alt.
12 GeV/c	0 0	0 0	0 0	0 0
24 GeV/c	$5,6(5.9) \cdot 10^{0}$ $1.7(1.8) \cdot 10^{-3}$	$5.6(5.9) \cdot 10^{0}$ $1.7(1.8) \cdot 10^{-3}$	$1.4(1.0) \cdot 10^{1}$ $4.2(3.1) \cdot 10^{-3}$	$9.6(7.1) \cdot 10^{0}$ $3.0(2.2) \cdot 10^{-3}$
36 GeV/c	$1.2(0.5) \cdot 10^{2}$ $2.7(1.1) \cdot 10^{-3}$	$1.1(0.5) \cdot 10^{2}$ $2.4(1.2) \cdot 10^{-3}$	$1.4(0.6) \cdot 10^{2}$ $3.0(1.2) \cdot 10^{-3}$	$1.2(0.5) \cdot 10^{2}$ $2.7(1.1) \cdot 10^{-3}$
48 GeV/c	$7.1(3.2) \cdot 10^{1}$ $2.1(0.9) \cdot 10^{-4}$	$5.2(2.4) \cdot 10^{1}$ $1.5(0.7) \cdot 10^{-4}$	$7.4(3.4) \cdot 10^{1}$ $2.2(1.0) \cdot 10^{-4}$	$5.6(2.6) \cdot 10^{1}$ $1.6(0.7) \cdot 10^{-4}$
60 GeV/c	$2.5(0.8) \cdot 10^{2}$ $1.5(0.5) \cdot 10^{-4}$	$1.9(0.6) \cdot 10^{2}$ $1.2(0.4) \cdot 10^{-4}$	$3.0(0.9) \cdot 10^{2}$ $1.8(0.5) \cdot 10^{-4}$	$1.9(0.5) \cdot 10^{1}$ $1.2(0.3) \cdot 10^{-4}$
72 GeV/c	$1.3(0.5) \cdot 10^{2}$ $2.2(0.9) \cdot 10^{-5}$	$8.2(3.2) \cdot 10^{1}$ $1.4(0.5) \cdot 10^{-5}$	$1.9(0.6) \cdot 10^{2}$ $3.2(1.0) \cdot 10^{-5}$	$1.1(0.4) \cdot 10^{1}$ $1.9(0.6) \cdot 10^{-5}$
$\sum A_{\text{eff}}$ / jet	$4.8(2.1) \cdot 10^{-3}$	$4.4(2.2) \cdot 10^{-3}$	$7.6(3.3) \cdot 10^{-3}$	$6.0(2.5) \cdot 10^{-3}$

Table B.5: Effective area in m^2 per shower and per jet for $10^{14.5}$ eV showers at 2 km altitude.

10^{15} eV, 2 km	1×1	1×1 alt.	$\sqrt{2} \times \sqrt{2}$	$\sqrt{2} \times \sqrt{2}$ alt.
12 GeV/c	0 0	0 0	0 0	0 0
24 GeV/c	$4.6(2.7) \cdot 10^{1}$ $4.6(2.7) \cdot 10^{-2}$	$3.7(2.2) \cdot 10^{1}$ $3.7(2.2) \cdot 10^{-2}$	$3.6(3.6) \cdot 10^{1}$ $3.6(3.6) \cdot 10^{-2}$	$3.4(3.4) \cdot 10^{1}$ $3.4(3.4) \cdot 10^{-2}$
36 GeV/c	$1.3(0.7) \cdot 10^{2}$ $1.1(0.6) \cdot 10^{-2}$	$8.3(4.2) \cdot 10^{1}$ $7.0(3.5) \cdot 10^{-3}$	$9.0(4.1) \cdot 10^{1}$ $7.6(3.4) \cdot 10^{-3}$	$6.3(2.9) \cdot 10^{1}$ $5.3(2.4) \cdot 10^{-3}$
48 GeV/c	$2.5(0.8) \cdot 10^{2}$ $3.3(1.0) \cdot 10^{-3}$	$1,7(0.6) \cdot 10^{2}$ $2.3(0.7) \cdot 10^{-3}$	$2.0(0.6) \cdot 10^{2}$ $2.6(0.8) \cdot 10^{-3}$	$1.6(0.5) \cdot 10^{2}$ $2.0(0.6) \cdot 10^{-3}$
60 GeV/c	$2.4(0.7) \cdot 10^{2}$ $9.0(2.6) \cdot 10^{-4}$	$1.6(0.5) \cdot 10^{2}$ $6.1(1.8) \cdot 10^{-4}$	$2.1(0.6) \cdot 10^{2}$ $8.1(2.2) \cdot 10^{-4}$	$1.2(0.3) \cdot 10^{2}$ $4.4(1.3) \cdot 10^{-4}$
72 GeV/c	$3.9(0.9) \cdot 10^{2}$ $4.3(1.0) \cdot 10^{-4}$	$2.9(0.7) \cdot 10^{2}$ $3.2(0.8) \cdot 10^{-4}$	$3.6(0.8) \cdot 10^{2}$ $3.9(0.9) \cdot 10^{-4}$	$2.5(0.7) \cdot 10^{2}$ $2.7(0.7) \cdot 10^{-4}$
$\sum A_{\text{eff}}$ / jet	$6.1(2.8) \cdot 10^{-2}$	$4.7(2.2) \cdot 10^{-2}$	$4.7(3.6) \cdot 10^{-2}$	$4.2(3.4) \cdot 10^{-2}$

Table B.6: Effective area in m^2 per shower and per jet for 10^{15} eV showers at 2 km altitude.

$10^{15.5}$ eV, 2 km	1×1	1×1 alt.	$\sqrt{2} \times \sqrt{2}$	$\sqrt{2} \times \sqrt{2}$ alt.
12 GeV/c	0 0	0 0	0 0	0 0
24 GeV/c	$1.5(1.5) \cdot 10^{1}$ $4.2(4.3) \cdot 10^{-2}$	$1.5(1.5) \cdot 10^{1}$ $4.1(4.2) \cdot 10^{-2}$	$1.0(1.0) \cdot 10^{1}$ $2.8(2.9) \cdot 10^{-2}$	$7.9(8.2) \cdot 10^{0}$ $2.2(2.3) \cdot 10^{-2}$
36 GeV/c	$3.8(2.7) \cdot 10^{1}$ $9.4(6.8) \cdot 10^{-3}$	$1.9(1.4) \cdot 10^{1}$ $4.8(3.5) \cdot 10^{-3}$	$2.0(1.4) \cdot 10^{1}$ $4.9(3.6) \cdot 10^{-3}$	$1.6(1.7) \cdot 10^{1}$ $4.1(4.1) \cdot 10^{-3}$
48 GeV/c	$7.9(8.2) \cdot 10^{0}$ $3.8(3.9) \cdot 10^{-4}$	$3.4(3.6) \cdot 10^{0}$ $1.6(1.7) \cdot 10^{-4}$	$1.1(0.8) \cdot 10^{1}$ $5.4(4.0) \cdot 10^{-4}$	$4.5(3.0) \cdot 10^{0}$ $2.2(1.5) \cdot 10^{-4}$
60 GeV/c	$8.1(4.7) \cdot 10^{1}$ $1.1(0.7) \cdot 10^{-3}$	$3.7(2.6) \cdot 10^{1}$ $5.1(3.7) \cdot 10^{-4}$	$6.5(3.3) \cdot 10^{1}$ $9.1(4.6) \cdot 10^{-4}$	$2.3(1.2) \cdot 10^{1}$ $3.2(1.7) \cdot 10^{-4}$
72 GeV/c	$1.4(0.5) \cdot 10^{2}$ $6.7(2.6) \cdot 10^{-4}$	$5.6(2.1) \cdot 10^{1}$ $2.6(1.0) \cdot 10^{-4}$	$1.1(0.4) \cdot 10^{2}$ $5.0(1.9) \cdot 10^{-4}$	$4.6(1.8) \cdot 10^{1}$ $2.1(0.8) \cdot 10^{-4}$
$\sum A_{\text{eff}}$ / jet	$5.4(4.4) \cdot 10^{-2}$	$4.7(4.2) \cdot 10^{-2}$	$3.5(2.9) \cdot 10^{-2}$	$2.7(2.3) \cdot 10^{-2}$

Table B.7: Effective area in m^2 per shower and per jet for $10^{15.5}$ eV showers at 2 km altitude.

B.3 Effective areas for sea level

$10^{14.5}$ eV, 0 km	1×1	1×1 alt.	$\sqrt{2} \times \sqrt{2}$	$\sqrt{2} \times \sqrt{2}$ alt.
12 & 24 GeV/c	0 0	0 0	0 0	0 0
36 GeV/c	$3.2(2.3) \cdot 10^{1}$ $6.9(5.0) \cdot 10^{-4}$	$1.7(1.2) \cdot 10^{1}$ $3.7(2.7) \cdot 10^{-4}$	$4.5(4.5) \cdot 10^{1}$ $1.0(1.0) \cdot 10^{-3}$	$2.6(2.6) \cdot 10^{1}$ $5.7(5.8) \cdot 10^{-4}$
48 GeV/c	$1.1(1.2) \cdot 10^{1}$ $3.3(3.3) \cdot 10^{-5}$	$1.1(1.2) \cdot 10^{1}$ $3.3(3.3) \cdot 10^{-5}$	$1.3(1.3) \cdot 10^{1}$ $3.8(3.8) \cdot 10^{-5}$	$1.2(1.2) \cdot 10^{1}$ $3.4(3.5) \cdot 10^{-5}$
60 GeV/c	$1.5(1.5) \cdot 10^{1}$ $8.9(9.0) \cdot 10^{-6}$	$1.5(1.5) \cdot 10^{1}$ $8.9(9.0) \cdot 10^{-6}$	$1.9(1.4) \cdot 10^{1}$ $1.1(0.8) \cdot 10^{-5}$	$1.6(1.6) \cdot 10^{1}$ $9.6(9.7) \cdot 10^{-6}$
72 GeV/c	0 0	0 0	0 0	0 0
$\sum A_{\text{eff}}$ / jet	$7.3(5.0) \cdot 10^{-4}$	$4.1(2.7) \cdot 10^{-4}$	$1.0(1.0) \cdot 10^{-3}$	$6.1(5.8) \cdot 10^{-4}$

Table B.8: Effective area in m^2 per shower and per jet for $10^{14.5}$ eV showers at sea level.

10^{15} eV, 0 km	1×1	1×1 alt.	$\sqrt{2} \times \sqrt{2}$	$\sqrt{2} \times \sqrt{2}$ alt.
12 GeV/c	0 0	0 0	0 0	0 0
24 GeV/c	$5.6(8.0) \cdot 10^{-1}$ $5.6(8.0) \cdot 10^{-4}$	0 0	0 0	0 0
36 GeV/c	0 0	0 0	0 0	0 0
48 GeV/c	$7.3(5.2) \cdot 10^{1}$ $9.4(6.7) \cdot 10^{-4}$	$7.3(4.2) \cdot 10^{1}$ $9.4(5.5) \cdot 10^{-4}$	$9.0(5.2) \cdot 10^{1}$ $1.2(0.7) \cdot 10^{-3}$	$7.3(4.3) \cdot 10^{1}$ $9.5(5.6) \cdot 10^{-4}$
60 GeV/c	$1.7(0.8) \cdot 10^{2}$ $6.5(2.9) \cdot 10^{-4}$	$1.2(0.5) \cdot 10^{2}$ $4.5(2.0) \cdot 10^{-4}$	$1.3(0.5) \cdot 10^{2}$ $5.0(2.0) \cdot 10^{-4}$	$7.7(3.2) \cdot 10^{1}$ $2.9(1.2) \cdot 10^{-4}$
72 GeV/c	$7.5(3.1) \cdot 10^{1}$ $8.3(3.5) \cdot 10^{-5}$	$7.1(3.0) \cdot 10^{1}$ $7.9(3.3) \cdot 10^{-5}$	$7.2(3.7) \cdot 10^{1}$ $7.9(4.0) \cdot 10^{-5}$	$7.1(3.6) \cdot 10^{1}$ $7.8(4.0) \cdot 10^{-5}$
$\sum A_{\text{eff}}$ / jet	$2.2(1.1) \cdot 10^{-3}$	$1.5(0.6) \cdot 10^{-3}$	$1.8(0.7) \cdot 10^{-3}$	$1.3(0.6) \cdot 10^{-3}$

Table B.9: Effective area in m^2 per shower and per jet for 10^{15} eV showers at sea level.

$10^{15.5}$ eV, 0 km	1×1	1×1 alt.	$\sqrt{2}\times\sqrt{2}$	$\sqrt{2}\times\sqrt{2}$ alt.
12 & 24 GeV/c	0	0	0	0
	0	0	0	0
36 GeV/c	$3.2(3.2)\cdot10^{1}$	$3.1(3.1)\cdot10^{1}$	$3.1(3.1)\cdot10^{1}$	$3.1(3.1)\cdot10^{1}$
	$7.9(7.9)\cdot10^{-3}$	$7.7(7.8)\cdot10^{-3}$	$7.7(7.8)\cdot10^{-3}$	$7.7(7.8)\cdot10^{-3}$
48 GeV/c	$5.6(8.0)\cdot10^{-1}$	0	$2.0(2.0)\cdot10^{1}$	$1.0(1.0)\cdot10^{0}$
	$2.7(3.8)\cdot10^{-5}$	0	$9.5(9.6)\cdot10^{-4}$	$4.9(5.0)\cdot10^{-4}$
60 GeV/c	$1.1(0.7)\cdot10^{2}$	$9.5(5.5)\cdot10^{1}$	$9.7(7.0)\cdot10^{1}$	$8.1(5.8)\cdot10^{1}$
	$1.6(0.9)\cdot10^{-3}$	$1.3(0.8)\cdot10^{-3}$	$1.4(1.0)\cdot10^{-3}$	$1.1(0.8)\cdot10^{-3}$
72 GeV/c	$1.0(0.5)\cdot10^{2}$	$8.2(4.2)\cdot10^{1}$	$1.1(0.6)\cdot10^{2}$	$9.4(5.4)\cdot10^{1}$
	$4.8(2.2)\cdot10^{-4}$	$3.9(2.0)\cdot10^{-4}$	$5.2(3.0)\cdot10^{-4}$	$4.4(2.5)\cdot10^{-4}$
84 GeV/c	$6.8(3.1)\cdot10^{1}$	$3.7(1.9)\cdot10^{1}$	$2.1(1.2)\cdot10^{1}$	$1.7(1.0)\cdot10^{1}$
	$1.2(0.6)\cdot10^{-4}$	$6.7(3.4)\cdot10^{-5}$	$3.7(2.2)\cdot10^{-5}$	$3.0(1.8)\cdot10^{-5}$
$\sum A_{\text{eff}}$ / jet	$1.0(0.8)\cdot10^{-2}$	$9.5(7.8)\cdot10^{-3}$	$1.1(0.8)\cdot10^{-2}$	$9.8(7.9)\cdot10^{-3}$

Table B.10: Effective area in m^2 per shower and per jet for $10^{15.5}$ eV showers at sea level.

10^{16} eV, 0 km	1×1	1×1 alt.	$\sqrt{2}\times\sqrt{2}$	$\sqrt{2}\times\sqrt{2}$ alt.
12 −− 36 GeV/c	0	0	0	0
	0	0	0	0
48 GeV/c	0	$1.1(0.8)\cdot10^{1}$	$5.6(8.0)\cdot10^{-1}$	$2.8(3.1)\cdot10^{0}$
	0	$1.8(1.3)\cdot10^{-3}$	$1.0(1.3)\cdot10^{-4}$	$4.5(4.9)\cdot10^{-4}$
60 GeV/c	0	0	0	$5.6(8.0)\cdot10^{-1}$
	0	0	0	$2.4(3.4)\cdot10^{-5}$
72 GeV/c	0	0	0	0
	0	0	0	0
84 GeV/c	$1.1(1.4)\cdot10^{0}$	$5.6(8.0)\cdot10^{-1}$	$1.1(1.4)\cdot10^{0}$	0
	$7.0(8.5)\cdot10^{-6}$	$3.5(4.9)\cdot10^{-6}$	$7.0(8.5)\cdot10^{-6}$	0
$\sum A_{\text{eff}}$ / jet	$7.0(8.5)\cdot10^{-6}$	$1.8(1.3)\cdot10^{-3}$	$1.1(1.3)\cdot10^{-4}$	$4.7(4.9)\cdot10^{-4}$

Table B.11: Effective area in m^2 per shower and per jet for 10^{16} eV showers at sea level.

C

Simulated jet rates

The simulated observational jet rates are tabulated per altitude. The altitude is depicted in the upper left corner of each table. In the upper row are the array types. In the first column are the shower energies. For each array type and energy the upper and lower number are the jet rates obtained with the original method and the alternative method respectively. The final row shows the energy sum of the jet rates, also with the upper and lower number for the original method and the alternative method respectively. The statistical uncertainties are in brackets.

4 km	1×1	1×1 alt.	$\sqrt{2} \times \sqrt{2}$	$\sqrt{2} \times \sqrt{2}$ alt.
$10^{13.5}$ eV	0 0	0 0	0 0	0 0
$10^{14.0}$ eV	$1.1(1.1) \cdot 10^3$ $1.3(1.2) \cdot 10^3$	$9.5(9.9) \cdot 10^2$ $9.9(9.9) \cdot 10^2$	$5.2(3.8) \cdot 10^2$ $5.2(4.7) \cdot 10^2$	$4.7(6.1) \cdot 10^1$ $1.7(1.4) \cdot 10^2$
$10^{14.5}$ eV	$5.4(2.3) \cdot 10^1$ $1.1(0.3) \cdot 10^2$	$4.0(1.6) \cdot 10^1$ $8.8(2.3) \cdot 10^1$	$6.8(2.8) \cdot 10^1$ $7.7(2.1) \cdot 10^1$	$4.5(1.9) \cdot 10^1$ $5.7(1.6) \cdot 10^1$
$10^{15.0}$ eV	$3.0(1.1) \cdot 10^1$ $3.6(1.4) \cdot 10^1$	$1.5(0.4) \cdot 10^1$ $2.2(0.6) \cdot 10^1$	$2.2(0.7) \cdot 10^1$ $2.2(0.7) \cdot 10^1$	$1.4(0.5) \cdot 10^1$ $1.6(0.5) \cdot 10^1$
$\sum$ jet rates	$1.2(1.1) \cdot 10^3$ $1.4(1.2) \cdot 10^3$	$1.0(1.0) \cdot 10^3$ $1.1(1.0) \cdot 10^3$	$6.1(3.8) \cdot 10^2$ $6.2(4.7) \cdot 10^2$	$1.1(0.6) \cdot 10^2$ $2.4(1.4) \cdot 10^2$

Table C.1: Observational jet rates per year at 4 km altitude.

2 km	1×1	1×1 alt.	$\sqrt{2} \times \sqrt{2}$	$\sqrt{2} \times \sqrt{2}$ alt.
$10^{14.0}$ eV	0	0	$2.7(2.7) \cdot 10^{2}$	$2.7(3.1) \cdot 10^{1}$
	$2.2(1.6) \cdot 10^{0}$	$1.0(0.8) \cdot 10^{0}$	$2.6(2.6) \cdot 10^{2}$	$8.1(8.6) \cdot 10^{1}$
$10^{14.5}$ eV	$1.7(0.7) \cdot 10^{0}$	$1.3(0.7) \cdot 10^{0}$	$3.2(1.5) \cdot 10^{0}$	$1.7(0.7) \cdot 10^{0}$
	$3.5(1.5) \cdot 10^{0}$	$3.2(1.6) \cdot 10^{0}$	$5.5(2.4) \cdot 10^{0}$	$4.4(1.8) \cdot 10^{0}$
$10^{15.0}$ eV	$9.7(4.5) \cdot 10^{0}$	$5.8(3.1) \cdot 10^{0}$	$8.3(6.5) \cdot 10^{0}$	$6.8(5.6) \cdot 10^{0}$
	$1.1(0.5) \cdot 10^{1}$	$8.4(4.0) \cdot 10^{0}$	$8.4(6.5) \cdot 10^{0}$	$7.5(6.1) \cdot 10^{0}$
$10^{15.5}$ eV	$2.3(1.3) \cdot 10^{-1}$	$5.9(3.6) \cdot 10^{-2}$	$1.1(0.9) \cdot 10^{0}$	$5.9(5.1) \cdot 10^{-1}$
	$1.4(1.1) \cdot 10^{0}$	$1.2(1.1) \cdot 10^{0}$	$9.0(7.4) \cdot 10^{-1}$	$6.9(5.9) \cdot 10^{-1}$
$\sum$ jet rates	$1.2(0.5) \cdot 10^{1}$	$7.2(3.2) \cdot 10^{0}$	$2.8(2.7) \cdot 10^{2}$	$3.6(3.2) \cdot 10^{1}$
	$1.8(0.6) \cdot 10^{1}$	$1.4(0.5) \cdot 10^{1}$	$2.7(2.6) \cdot 10^{2}$	$9.4(8.6) \cdot 10^{1}$

Table C.2: Observational jet rates per year at 2 km altitude.

0 km	1×1	1×1 alt.	$\sqrt{2} \times \sqrt{2}$	$\sqrt{2} \times \sqrt{2}$ alt.
$10^{14.5}$ eV	$3.2(2.3) \cdot 10^{-2}$	$1.6(1.7) \cdot 10^{-2}$	$1.5(1.5) \cdot 10^{-1}$	$1.3(1.3) \cdot 10^{-1}$
	$9.7(6.6) \cdot 10^{-2}$	$5.4(3.6) \cdot 10^{-2}$	$1.3(1.3) \cdot 10^{-1}$	$8.1(7.7) \cdot 10^{-2}$
$10^{15.0}$ eV	$9.5(5.7) \cdot 10^{-2}$	$7.1(5.5) \cdot 10^{-2}$	$1.5(0.7) \cdot 10^{-1}$	$1.0(0.6) \cdot 10^{-1}$
	$2.1(1.0) \cdot 10^{-1}$	$1.4(0.6) \cdot 10^{-1}$	$1.7(0.7) \cdot 10^{-1}$	$1.2(0.6) \cdot 10^{-1}$
$10^{15.5}$ eV	$1.8(1.5) \cdot 10^{-1}$	$1.4(1.2) \cdot 10^{-1}$	$2.1(1.5) \cdot 10^{-1}$	$1.8(1.5) \cdot 10^{-1}$
	$1.9(1.5) \cdot 10^{-1}$	$1.8(1.5) \cdot 10^{-1}$	$2.1(1.5) \cdot 10^{-1}$	$1.8(1.5) \cdot 10^{-1}$
$10^{16.0}$ eV	$2.3(2.8) \cdot 10^{-5}$	$2.8(2.8) \cdot 10^{-3}$	$8.4(9.3) \cdot 10^{-4}$	$7.0(7.2) \cdot 10^{-4}$
	$1.6(2.0) \cdot 10^{-5}$	$4.2(3.0) \cdot 10^{-3}$	$2.6(3.0) \cdot 10^{-4}$	$1.1(1.1) \cdot 10^{-3}$
$\sum$ jet rates	$3.1(1.6) \cdot 10^{-1}$	$2.3(1.3) \cdot 10^{-1}$	$5.1(2.2) \cdot 10^{-1}$	$4.1(2.1) \cdot 10^{-1}$
	$5.0(1.9) \cdot 10^{-1}$	$3.7(1.7) \cdot 10^{-1}$	$5.1(2.1) \cdot 10^{-1}$	$3.8(1.8) \cdot 10^{-1}$

Table C.3: Observational jet rates per year at sea level.

Samenvatting

Kosmische straling bestaat uit deeltjes, voornamelijk atoomkernen, die uit de ruimte komen. In de dampkring botsen ze met de atomen in de lucht. Daarbij ontstaan vele, soms zelfs honderden, secondaire deeltjes die op hun beurt ook weer kunnen botsen. Het gevolg is een lawine van deeltjes in de atmosfeer: de *cosmic air shower*. Bij elke botsing wordt de energie per deeltje steeds kleiner. Als de energie van een deeltje onder een bepaalde grenswaarde komt, verliest het deeltje zijn energie voornamelijk aan de ionisatie van luchtatomen en raakt het verloren voor de lawine. Dit heeft tot gevolg dat het aantal deeltjes van de lawine op een bepaalde hoogte een maximum bereikt om daarna weer af te nemen. Deze ontwikkeling kan worden beschreven met modellen van uiteenlopende complexiteit. Als de energie van het primaire kosmische deeltje voldoende groot is, kunnen lawinedeeltjes het aardoppervlak bereiken. Uit de voetafdruk daarvan kan de energie van het kosmische deeltje worden gereconstrueerd.

Kosmische lawines kunnen worden onderzocht met het HiSPARC (High School Project on Astrophysics Research with Cosmics). Het HiSPARC experiment heeft twee doelen. Enerzijds is het bedoeld om promovendi, leraren in onderzoek en studenten kosmische straling te laten onderzoeken. Anderzijds is het bedoeld om leerlingen in het voortgezet onderwijs deel te laten nemen aan wetenschappelijk onderzoek. De detectoren van HiSPARC zijn scintillatorplaten. Als er lawinedeeltjes doorheen gaan wordt een signaal afgegeven. Niet alleen de grootte, maar ook het tijdstip van het signaal wordt geregistreerd. Aan de hand van de aankomsttijden in verschillende detectoren kan de richting van het kosmische deeltje worden gereconstrueerd. Daarvoor zijn verschillende methoden ontwikkeld voor de verschillende situaties. Tevens is een methode ontwikkeld voor de reconstructie van het centrum van de lawine, in het bijzonder voor de situatie dat het centrum zich niet tussen de stations bevindt.

Kosmische deeltjes komen minder vaak voor naarmate ze een hogere energie hebben. De flux als functie van de energie is voor een aantal energieën op twee manieren bepaald. De ene manier is op basis van frequenties van showers van een bepaalde grootte. Deze werkt het best voor relatief kleine energieën waarvoor de frequenties groot zijn. De andere manier is door van elke shower de energie te reconstrueren. Voor beide manieren komt de door HiSPARC gemeten flux redelijk overeen met die van andere observatoria.

In deeltjesversnellers is waargenomen dat bij energierijke botsingen er botsingsproducten (deeltjes) zijwaarts bewegen ten opzichte van de richting waarin de oorspronkelijke deeltjes tegen elkaar aanbotsten. Soms hebben de zijwaarts bewegende deeltjes min of meer dezelfde richting.

Er is dan sprake van een bundel van deeltjes: de *jet*. Jets treden ook op als een kosmisch deeltje een sterke wisselwerking aangaat met een kern van een luchtatoom. Bij zeer energetische kosmisch deeltjes kan de botsingsenergie vele malen hoger zijn dan die in deeltjesversnellers. Als de energie van de jet in een kosmische lawine groot genoeg is, kan het leiden tot een lokale fluctuatie van de dichtheid van lawinedeeltjes op het observatieniveau. De vraag is in hoeverre die fluctuaties onderscheiden kunnen worden van toevallige fluctuaties. Dat is onderzocht met computersimulaties.

De computersimulaties zijn uitgevoerd voor de situatie waarbij duizenden detectoren naast elkaar staan opgesteld op bijvoorbeeld een voetbalveld. Het resultaat van die simulaties is dat men zo'n duizend jets per jaar zou kunnen observeren als de detectoren op 4 km hoogte staan. Deze waarde komt overeen met wat op die hoogte ook wordt waargenomen. Op 2 km hoogte wordt dat aantal tien tot honderd keer zo klein afhankelijk van de detector afmetingen. Op zeeniveau kan men waarschijnlijk minder dan één jet per jaar observeren die het gevolg is van de botsing van het kosmische deeltje in de atmosfeer. Echter, de deeltjes die bij de eerste botsing ontstaan kunnen op hun beurt ook weer botsen en daar kunnen dus ook jets bij ontstaan. De kans hierop is groter voor showers met veel energie en dat zijn juist de showers waarvan voldoende deeltjes het zeeniveau bereiken. Als we deze 'secondaire' jets meetellen, dan kan men mogelijk enkele honderden jets per jaar observeren op zeeniveau. Let wel, als er slechts een stuk of tien detectoren staan opgesteld op een klein veldje, dan daalt dit aantal tot nog maar enkele per jaar.

Tenslotte zijn de HiSPARC-meetgegevens van de stations in Science Park Amsterdam geanalyseerd. Daarbij zijn twee stations die tegen elkaar aan liggen beschouwd als het gedeelte waarin naar jet-fluctuaties wordt gekeken. Vanwege het geringe oppervlak van dit gedeelte is de kans op een jet-fluctuatie extreem klein. Ze zijn dan ook niet gevonden. Zelfs voor een grote fluctuatie is het twijfelachtig om die aan een jet toe te schrijven omdat er met zo weinig stations geen zekerheid is omtrent de positie van het centrum van de lawine. Bovendien is het verband tussen de waarnemingsgegevens van een fluctuatie en de kinematische eigenschappen van de jet die de fluctuatie heeft veroorzaakt vrij onzeker. Eenvoudig gesteld: jets kun je wel detecteren, maar je kan er weinig van leren. Gezien dit slechte verband en gezien het geringe aantal verwachte jet-observaties is een investering in een groot aantal detectoren op zeeniveau uitsluitend ten behoeve van jet onderzoek niet erg zinvol.

Bibliography

1. de Coulomb, C. A. Troisième mémoire sur l'Electricité et le Magnétisme. *Histoire de l'Académie Royale des Sciences,* 612–638 (1785).
2. Becquerel, H. Emission de radiations nouvelles par l'uranium metalique. *Comptes Rendus de l'Acad. des Sciences* **122,** 1086–1088 (1896).
3. Wulf, T. Über die in der Atmosphäre vorhandene Strahlung von hoher Durchdringungsfähigkeit. *Phys. Zeit* **1,** 152–157 (1909).
4. Pacini, D. La radiazione penetrante alla superficie ed in seno alle acque. *Nuovo Cim.* **VI/3,** 93–100 (1912).
5. Hess, V. F. Über Beobachtungen der durchdringenden Strahlung bei sieben Freiballonfahrten. *Phys. Zeit.* **13,** 1084–1091 (1912).
6. Hess, V. F. Über den Ursprung der durchdringenden Strahlung. *Phys. Zeit* **14,** 612–617 (1913).
7. Kolhörster, W. Messungen der durchdringenden Strahlung im Freiballon in grösseren Höhen. *Phys. Zeit.* **14,** 1153–1156 (1913).
8. Millikan, R. A. & Bowen, I. S. Penetrating radiation at high altitudes. Minutes of the Pasadena Meeting, May 5, 1923. *Phys. Rev.* **22,** 198 (1923).
9. Millikan, R. A. & Cameron, G. H. High frequency rays of cosmic origin III. Measurements in snow-fed lakes at high altitudes. *Phys. Rev.* **28,** 851–868 (1926).
10. Clay, J. Penetrating radiation. *Acad. Amsterdam Proc.* **30,** 1115–1127 (1927).
11. Clay, J. Penetrating radiation II. *Acad. Amsterdam Proc.* **31,** 1091–1097 (1928).
12. Rossi, B. Directional Measurement on the Cosmic Rays near the Geomagnetic Equator. *Phys. Rev.* **45,** 212–214 (1934).
13. Greisen, K. End to the cosmic-ray spectrum? *Physical Review Letters* **16,** 748 (1966).
14. Zatsepin, G. & Kuzmin, V. Upper Limit of the Spectrum of Cosmic Rays. *Journal of Experimental and Theoretical Physics Letters* **4,** 78–80 (1966).
15. Cronin, J., Swordy, S. & Gaisser, T. Cosmic rays at the energy frontier. *Sci.Am.* **276,** 32–37 (1997).
16. <http://astroparticle.uchicago.edu/siteold/cosmic_ray_spectrum_picture.htm>.
17. <www.physics.utah.edu/~whanlon/spectrum.html>.

18. Abraham, J *et al.* Correlation of the highest-energy cosmic rays with the positions of nearby active galactic nuclei. *Astroparticle Physics* **29,** 188–204 (2008).

19. Abreu, P. *et al.* Update on the correlation of the highest energy cosmic rays with nearby extragalactic matter. *Astroparticle Physics* **34,** 314–326. ISSN: 0927-6505 (2010).

20. Abbasi, R. *et al.* Indications of Intermediate-Scale Anisotropy of Cosmic Rays with Energy Greater Than 57 EeV in the Northern Sky Measured with the Surface Detector of the Telescope Array Experiment. *The Astrophysical Journal Letters* **790,** L21 (2014).

21. He, H.-N., Kusenko, A., Nagataki, S., Yang, R.-Z. & Fan, Y.-Z. The Possible Extragalactic Source of Ultra-High-Energy Cosmic Rays at the Telescope Array Hotspot. *arXiv preprint arXiv:1411.5273* (2014).

22. Auger, P., Ehrenfest, P., Maze, R., Daudin, J. & Fréon, R. A. Extensive Cosmic-Ray Showers. *Rev. Mod. Phys.* **11,** 288–291 (3-4 1939).

23. Hinton, J. A., collaboration, H., *et al.* The status of the HESS project. *New Astronomy Reviews* **48,** 331–337 (2004).

24. Aharonian, F *et al.* Energy spectrum of cosmic-ray electrons at TeV energies. *Physical Review Letters* **101,** 261104 (2008).

25. Griffiths, D. *Introduction to elementary particles* (John Wiley & Sons, 2008).

26. Altarelli, G. & Parisi, G. Asymptotic freedom in parton language. *Nuclear Physics B* **126,** 298–318 (1977).

27. Dokshitzer, Y. L. Zh. ETF 71 (1977) 1216; Soy. Phys. *JETP* **46,** 461 (1977).

28. Gribov, V. & Lipatov, L. Phys. Letters 1971; 37B. 78 [CrossRef]. *Soviet J. Nucl. Phys* **15,** 672 (1972).

29. Sjöstrand, T. & Prestel, S. PYTHIA 8 Merging Tutorial.

30. Sjöstrand, T., Mrenna, S. & Skands, P. PYTHIA 6.4 physics and manual. *Journal of High Energy Physics* **2006,** 026 (2006).

31. 2012. <http://home.thep.lu.se/~torbjorn/pythiaaux/present.html>.

32. Sciutto, S. *AIRES: A System for air shower simulations. User's guide and reference manual. Version 2.2.0* (1999). arXiv: astro-ph/9911331 [astro-ph].

33. Engel, R., Gaisser, T., Stanev, T. & Lipari, P. *Air Shower Calculations with the New version of SIBYLL* in *Proceedings of the 26*th *ICRC* (Salt Lake City, 1999).

34. Heitler, W. *The Quantum Theory of Radiation* ISBN: 9780486645582 (Dover Publications, 1954).

35. Rossi, B. & Greisen, K. Cosmic-Ray Theory. *Rev. Mod. Phys.* **13,** 240–309 (4 1941).

36. Carlson, J. F. & Oppenheimer, J. R. On Multiplicative Showers. *Phys. Rev.* **51,** 220–231 (4 1937).
37. Nishimura, J. Handbuch der Physik XLVI/2. *COSMIC RAYS II', Springer-Verlag* **1** (1967).
38. Greisen, K. The extensive air showers. *Progress in cosmic ray physics* **3** (1956).
39. Matthews, J. A Heitler model of extensive air showers. *Astroparticle Physics* **22,** 387–397 (2005).
40. Heck, D., Knapp, J., Capdevielle, J., Schatz, G. & Thouw, T. *Report FZKA 6019* (1998). <http://www-ik.fzk.de/corsika/physics_description/corsika_phys.html>.
41. Ostapchenko, S. QGSJET-II: towards reliable description of very high energy hadronic interactions. *Nuclear Physics B-Proceedings Supplements* **151,** 143–146 (2006).
42. Fesefeldt, H. Report PITHA-85/02. *RWTH Aachen* **647** (1985).
43. Grupen, C. *Astroparticle physics* ISBN: 9783540253129 (Springer, 2005).
44. <http://www.hisparc.nl>.
45. <http://docs.hisparc.nl/sapphire/>.
46. <https://github.com/HiSPARC/sapphire>.
47. <https://www.ikp.kit.edu/corsika/>.
48. Olive, K. *et al.* Particle data group collaboration. *Chin. Phys. C* **38,** 090001 (2014).
49. <http://pdg.lbl.gov/2009/AtomicNuclearProperties/>.
50. Gaisser, T. K. *Cosmic Rays and Particle Physics* ISBN: 0 521 33931 6 (Cambridge University Press, 1990).
51. Montanus, J. M. C. Intermediate models for longitudinal profiles of cosmic showers. *Astroparticle Physics* **35,** 651–659 (2012).
52. Montanus, J. M. C. An extended Heitler–Matthews model for the full hadronic cascade in cosmic air showers. *Astroparticle Physics* **59,** 4–11 (2014).
53. Novotny, V., Nosek, D. & Ebr, J. A branching model for hadronic air showers. *arXiv preprint arXiv:1509.00364* (2015).
54. Nishimura, J. & Kamata, K. On the theory of cascade showers, I. *Progress of Theoretical Physics* **7,** 185–192 (1952).
55. Landau, L. *J. Phys. U.S.S.R.* **3,** 889 (1950).
56. Nagano, M & Watson, A. A. Observations and implications of the ultrahigh-energy cosmic rays. *Reviews of Modern Physics* **72,** 689 (2000).
57. Apel, W. *et al.* Comparison of measured and simulated lateral distributions for electrons and muons with KASCADE. *Astroparticle Physics* **24,** 467–483 (2006).

58. Cillis, A & Sciutto, S. Air showers and geomagnetic field. *Journal of Physics G: Nuclear and Particle Physics* **26,** 309 (2000).

59. Greisen, K. Cosmic ray showers. *Annual Review of Nuclear Science* **10,** 63–108 (1960).

60. Montanus, J. M. C. The center of lateral iso-density contours for inclined cosmic air showers. *Experimental Astronomy* **41,** 159–184 (2016).

61. Galstad, E. *et al. Nagios: The Industry Standard in IT Infrastructure Monitoring* 1999–. <http://www.nagios.org/>.

62. <http://data.hisparc.nl/>.

63. <http://data.hisparc.nl/api/>.

64. <http://data.hisparc.nl/media/jsparc/data_retrieval.html>.

65. <http://data.hisparc.nl/data/download/>.

66. Nakamura, K *et al.* Review of Particle Physics. *Journal of Physics G: Nuclear and Particle Physics* **37,** 075021 (2010).

67. Leo, W. R. *Techniques for nuclear and particle physics experiments. A how-to approach* (Springer, 1994).

68. Sternheimer, R. M. The density effect for the ionization loss in various materials. *Physical Review* **88,** 851 (1952).

69. Paul, J. The density effect and rate of energy loss in common plastic scintillators. *Nuclear Instruments and Methods* **96,** 51–59 (1971).

70. <http://physics.nist.gov/PhysRefData/XrayMassCoef/tab2.html>.

71. <http://pdg.lbl.gov/2013/AtomicNuclearProperties/HTML_PAGES/216.html>.

72. <http://physics.nist.gov/cgi-bin/Star/e_table.pl>.

73. <http://vlado.fmf.uni-lj.si/texceh/kako/tex2pdf/ex/maria-1.pdf>.

74. Blunck, O & Leisegang, S. Zum energieverlust schneller elektronen in dünnen schichten. *Zeitschrift für Physik* **128,** 500–505 (1950).

75. Vavilov, P. Ionization losses of high-energy heavy particles. *Soviet Phys. JETP* **5** (1957).

76. Landau, L. On the energy loss of fast charged particles. *J. Phys. USSR* **8,** 201–205 (1944).

77. <http://meroli.web.cern.ch/meroli/>.

78. Kölbig, K. & Schorr, B. A program package for the Landau distribution. *Computer Physics Communications* **31,** 97–111. ISSN: 0010-4655 (1984).

79. Borsch-Supan, W. On the Evaluation of the Function.. *J. of Research of NBS* **65** (1961).

80. Elo, A.-M. & Arvela, H. *Direction distributions of air showers observed with the Turku air shower array* in *International Cosmic Ray Conference* **2** (2001), 598.

81. Pennink, D. in *FOM verslag LIO's 2009 – 2010* (FOM, 2010).

82. Fokkema, D. *The HiSPARC experiment* PhD thesis (2012).

83. Steijger, J. HiSPARC Internal note. (2010).

84. Buisman, H. in *FOM verslag LIO's 2010 – 2011* (FOM, 2011).

85. Abbasi, R *et al.* Calibration and characterization of the IceCube photomultiplier tube. *Nuclear Instruments and Methods in Physics Research Section A: Accelerators, Spectrometers, Detectors and Associated Equipment* **618,** 139–152 (2010).

86. De Laat, A. *Lineariteit PMT.* HiSPARC Internal note, (2015).

87. Apel, W. *et al.* The KASCADE-Grande experiment. *Nuclear Instruments and Methods in Physics Research Section A: accelerators, spectrometers, detectors and associated equipment* **620,** 202–216 (2010).

88. Melcarne, A. C., Perrone, L, Surdo, A, *et al.* Time structure of the extensive air shower front with the ARGO-YBJ experiment. *Proc. 31st ICRC* (2009).

89. Svanidze, M. & Verbetsky, Y. G. Improved method of the Extensive Air Shower arrival direction estimation. *arXiv preprint arXiv:0804.1751* (2008).

90. Jaranowski, P. & Krolak, A. Optimal solution to the inverse problem for the gravitational wave signal of a coalescing compact binary. *Physical Review D* **49,** 1723 (1994).

91. Cavalier, F. *et al.* Reconstruction of source location in a network of gravitational wave interferometric detectors. *Physical Review D* **74,** 082004 (2006).

92. Ashton, F *et al. Determining the Arrival Directions of Extensive Air Showers from Fast Timing Measurements* in *International Cosmic Ray Conference* **12** (1979), 371.

93. Steijger, J. J. M. & Montanus, J. M. C. *Direction reconstruction in HiSPARC.* HiSPARC Internal note. (2012).

94. Kamata, K. & Nishimura, J. The lateral and the angular structure functions of electron showers. *Progress of Theoretical Physics Supplement* **6,** 93–155 (1958).

95. <http://mathforum.org/library/drmath/view/51836.html>.

96. Montanus, J. M. C. in *FOM verslag LIO's 2009–2010,* 45–58 (FOM, 2010).

97. Ciampa, D & Clay, R. The zenith angle distribution of extensive air showers at sea level: a measure of shower development. *Journal of Physics G: Nuclear Physics* **14,** 787 (1988).

98. Iyono, A *et al. Zenith Angle Distribution and Atmospheric Effect for EAS with LAAS experiments* in *International Cosmic Ray Conference* **4** (2008), 47–50.

99. Elo, A.-M. *The effect of timing inaccuracy on the shower arrival direction* in *International Cosmic Ray Conference* **5** (1999), 328.

100. Cacciari, M., Salam, G. P. & Soyez, G. The anti-kt jet clustering algorithm. *Journal of High Energy Physics* **2008,** 063 (2008).

101. Collaboration, A. *et al.* Measurement of the inelastic proton-proton cross-section at [radic] s= 7 TeV with the ATLAS detector. *Nature Communications* **2,** 463 (2011).

102. Antchev, G *et al.* Measurement of proton-proton inelastic scattering cross-section at. *EPL (Europhysics Letters)* **101,** 21003 (2013).

103. ATLAS-CONF-2015-038. Measurement of the inelastic proton-proton cross section at sqrt (s) = 13 TeV with the ATLAS detector at the LHC. *cds.cern.ch/record/2045064* (2015).

104. Abelev, B. *et al.* Measurement of inelastic, single-and double-diffraction cross sections in proton–proton collisions at the LHC with ALICE. *The European Physical Journal C* **73,** 1–20 (2013).

105. Abreu, P. *et al.* Measurement of the proton-air cross section at s= 57 tev with the pierre auger observatory. *Physical Review Letters* **109,** 062002 (2012).

106. Fagundes, D. A., Grau, A., Pancheri, G., Srivastava, Y. N. & Shekhovtsova, O. *p–air production cross-section and uncorrelated mini-jets processes in pp-scattering* in *EPJ Web of Conferences* **90** (2015), 03002.

107. Poniatowski, T. Measuring the Inelastic and Total Cross-Sections for p-Air and pp Collisions at s˜ 44 TeV Using HiRes Stereo Data (2003).

108. Cronin, J. *et al.* Production of hadrons at large transverse momentum at 200, 300, and 400 GeV. *Physical Review D* **11,** 3105 (1975).

109. Antreasyan, D *et al.* Production of hadrons at large transverse momentum in 200-, 300-, and 400-GeV p- p and p-nucleus collisions. *Physical Review D* **19,** 764 (1979).

110. Accardi, A. Cronin effect in proton-nucleus collisions: a survey of theoretical models. *arXiv preprint hep-ph/0212148* (2002).

111. Aglietta, M *et al.* Study of jet production in p–N interactions at s 500 GeV in EAS multicore events. *Physics Letters B* **460,** 474–483 (1999).

112. Brown, B *et al.* Production of high-transverse-energy events in p-nucleus collisions at 400 GeV/c. *Physical Review Letters* **50,** 11 (1983).

113. Rice, J. & Fermilab, E. 609 Collab., et al. *Nucl. Phys. A* **418,** 315c (1984).

114. Miettinen, H. *et al.* Jet production from nuclei at 400 GeV/c. *Physics Letters B* **207,** 222–226 (1988).

115. Stewart, C *et al.* Production of high-p t jets in hadron-nucleus collisions. *Physical Review D* **42,** 1385 (1990).

116. MA, X. Study on Multicore Extensive Air Showers in the ARGO-YBJ Experiment. *Proceedings of the 31st ICRC* (2009).

117. ZHAO, J. & MA, X. Multicore Cosmic Shower in the ARGO-YBJ experiment. *Proceedings of the 32nd ICRC, HE3* **1** (2011).

118. Stanev, T. *High Energy Cosmic Rays* ISBN: 3 540 40653 0 (Springer-Praxis, 2004).

119. Hazen, W. *et al.* Subcores in cosmic-ray air showers and high transverse momentum. *Journal of Physics G: Nuclear Physics* **7,** 1285 (1981).

120. Engler, J *et al.* A warm-liquid calorimeter for cosmic-ray hadrons. *Nuclear Instruments and Methods in Physics Research Section A: Accelerators, Spectrometers, Detectors and Associated Equipment* **427,** 528–542 (1999).

121. Antoni, T *et al.* Geometric structures in hadronic cores of extensive air showers observed by KASCADE. *Physical Review D* **71,** 072002 (2005).

122. Steijger, J. *The signal strength in stations 501 and 510 compared* (2015).

123. Cowan, G. *Statistical data analysis* (Oxford University Press, 1998).

Dankwoord

De aanloop naar dit proefschrift begon eigenlijk al op 1 augustus 2009. Op het Nikhef bij de afdeling HiSPARC begon ik als leraar in onderzoek (LIO), op basis van één dag per week, mij in te lezen in een onderwerp waar ik op dat moment nagenoeg niets van wist: kosmische straling en de lawines van deeltjes die daardoor in de dampkring worden veroorzaakt. Geboeid door het onderwerp ging ik er al snel meer tijd in stoppen dan die ene dag per week. Bovendien kreeg ik de vrijheid om me te richten op de meer wiskundige aspecten; ik was immers bijna twintig jaar eerder overgestapt van leraar Natuurkunde naar leraar Wiskunde. Het beviel mij uitstekend en ik was dan ook verheugd dat ik het schooljaar daarop weer LIO mocht zijn. Er werd een onderzoeksvoorstel 'Jets in cosmic air showers' gedaan voor een promotiebeurs voor leraren. Eind 2011 werd de beurs toegekend waarmee ik gedurende de schooljaren 2012 tot en met 2016 twee dagen per week van lesgeven zou worden vrijgehouden om onderzoek kon verrichten. Bob wil ik bedanken voor het feit dat hij mij op een promotietraject heeft gezet.

Ondanks dat ik in de drie aanloopjaren als LIO al behoorlijk wat onderzoek had gedaan, had ik toch enigszins mijn twijfels over de toereikendheid van die twee dagen. Door mijn aanstellingsomvang op school wat te verlagen heb ik er effectief drie dagen van gemaakt. Dat betekent niet dat het onderzoek tot drie werkdagen per week beperkt bleef. Vrijwel alle schoolvakanties zijn besteed aan onderzoek. Voorzover tijd en energie het toelieten werkte ik ook 's avonds en in het weekend, zoals een reguliere promovendus dat ook doet. Dat het uiteindelijk heeft het geresulteerd in dit proefschrift is niet het resultaat van alleen mijn inspanningen. Het is zeker ook te danken aan de hulp die mij daarbij is geboden.

Vlak voor het promotieonderzoek aanving werd mij geadviseerd om over te stappen op een Apple. Dat was een goed advies, maar het was ook wel 'even wennen'. Met name bij installeren van wetenschappelijke software deden zich soms lastige problemen voor. De toenmalige promovendi David en Arne waren dan zeer behulpzaam. Het softwarepakket SAPPHiRE, voornamelijk het werk van David en Arne, was onmisbaar voor het onderzoek. David en Arne wil ik bedanken voor al hun hulp. En Bon wil ik bedanken voor zijn hulp bij ROOT.

In de afgelopen jaren hebben veel LIO's een bijdrage geleverd aan HiSPARC en daarmee indirect ook aan mijn onderzoek. Met een aantal van hen heb ik een werkkamer gedeeld. De LIO's Niek, Wim, Machiel, Dorrith, Niels, Henk, Remon, Daniel, Sjoerd, Wytse, Paul, Rickie, Matthijs, Norbert, Gilbert, Sabine, Tom en Gideon wil ik bedanken voor de samenwerking.

Tijdens mijn onderzoek was het mijn gewoonte om telkens schriftelijk rapportages aan het HiSPARC team te sturen over een deelonderwerp wat ik had bestudeerd. Die rapportages noemde Jos 'pamfletten'. Het was de gewoonte van Jos om die pamfletten, en later het proefschrift, zo ongeveer per omgaande van uitgebreid commentaar te voorzien. Correcties konden

zo snel worden aangebracht. Jos wil ik bedanken voor deze efficiënte begeleiding.

Sommige van mijn pamfletten zijn uitgegroeid tot manuscripten. Goede herinneringen heb ik aan de sessies met Jan-Willem over de inhoud van die manuscripten. Met een scherp oog voor detail en de helderheid van formuleringen zijn de manuscripten en dit proefschrift onder de loep genomen. Zijn commentaar was altijd heel waardevol. Jan-Willem wil ik bedanken voor al zijn inspanningen als promotor.

De eerste ruwe versie van mijn thesis was grotendeels een bundeling van pamfletten en manuscripten. Aanwijzingen van Paul om de tekst te snoeien, te herschikken en waar nodig te herschrijven zijn de presentatie in de thesis zeer ten goede gekomen. Dankzij de begeleiding van Paul kwam er ook meer convergentie in het onderzoek. Paul wil ik bedanken voor zijn bereidheid om promotor te zijn van een deeltijd-promovendus.

Zoals alles komt ook een thesis makkelijker tot stand naarmate de randvoorwaarden beter zijn. Een goede randvoorwaarde is een eigen bureau in een werkkamer. Alle jaren heeft Nikhef mij daarvan voorzien. Een goede randvoorwaarde is de medewerking van de middelbare school. Het Oostvaarders College heeft altijd medewerking verleend aan mijn 'buitenschoolse activiteiten'. Een goede randvoorwaarde is ook de financiering van het onderzoek door NWO middels de promotiebeurs voor leraren. Alle personen en instanties die hebben bijgedragen aan goede randvoorwaarden wil ik daarvoor bedanken.

De afgelopen jaren heb ik gemerkt dat het goed is om af en toe van gedachten te wisselen over het onderzoek met iemand die geen 'insider' is. Met name gold dit voor de gesprekken met mijn vriend en oud-studiegenoot Ron en mijn vriend en collega Rins. Ron en Rins wil ik bedanken voor hun belangstelling voor het onderzoek en voor hun bereidheid om paranimf te zijn.

Het is mijn echtgenote Daniële (†16-09-2016) en mijn dochters Jenny en Romy niet ontgaan dat promotieonderzoek intensief en tijdrovend is. Regelmatig heb ik 'social events' aan mij voorbij laten gaan. En bij de gelegenheden waar ik wel aanwezig was, was ik er soms geestelijk niet bij. De gedachten dwaalden dan af naar bijvoorbeeld een wiskundig probleem dat ik nog op wilde lossen. Zij zijn hiermee omgegaan als ware het een vanzelfsprekendheid.

Hans Montanus,
Augustus 2016